CVD Diamond Sensors for Particle Detection and Tracking

Dissertation
by
Dirk Meier
CERN, Geneva, January 1999

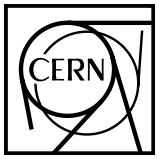

Fachliche Betreuung:

Dr. P. Weilhammer,
CERN, Geneva
Prof. H. Kagan,
Ohio State University,
Columbus

Gutachter:

Prof. B. Povh,
Max-Planck Institut für Kernphysik,
Heidelberg
Prof. K. Tittel,
Universität Heidelberg

contact: Dirk.Meier@cern.ch

Zusammenfassung

Die vorliegende Arbeit beschreibt Untersuchungen an CVD Diamanten zur Spurbestimmung elektrisch geladener Teilchen (CVD ist die Abkürzung für chemical vapor deposition). Die Strahlenhärte ist Voraussetzung für Detektoren, die nahe am Wechselwirkungsbereich der Experimente ATLAS und CMS am Large Hadron Collider am CERN arbeiten sollen. Detektoren auf Diamantbasis könnten eine strahlenharte Option für Pixel und Streifendetektoren in diesem Bereich sein.

Die Arbeit enthält vier wesentliche Resultate. Erstens wurde die Detektorqualität der Diamantproben eines Herstellers von 30 μm charge collection distance auf 200 μm verbessert. Zweitens wurden zum ersten mal Mikrosteifendetektoren auf Diamantbasis betrieben: Diamantstreifendetektoren erreichten ein Signal-Rauschverhältnis von 50-zu-1 am Scheitelpunkt der Signalverteilung bei einem wahrscheinlichsten Ladungssignal von 5000 e. Der Fehler in der Spurvorhersage lag zwischen 12 μm und 16 μm. Die Detektoreffizienz lag typischerweise nahe 100 % für Signalschwellen unter 1000 e. Als drittes Resultat wurde festgestellt, daß Inhomogenitäten in den CVD Diamanten die Signalverteilung verbreitern. Das ist nicht verwunderlich, da CVD Diamanten polykristallin sind. Der vierte wichtige Punkt sind die Bestrahlungen von CVD Diamanten, die zum ersten Mal mit Protonen, Neutronen und Pionen mit einer Dosis zum Teil oberhalb der am LHC zu erwartenden Dosis durchgeführt wurden. Die hier untersuchten Diamantproben sind je nach Teilchensorte und Dosis strahlenhart. Ich habe diese Arbeit als Mitglied in der ATLAS/SCT Gruppe am CERN innerhalb des Detektor Forschungsprojekts RD42 durchgeführt.

Stichworte: Diamant, Chemical Vapor Deposition, Kristall, Silizium, Detektor, Streifendetektor, Teilchenspur, Teleskop, Ladungssammlung, RD42, LHC, ATLAS, CMS, Elektronik, Strahlenhärte

Abstract

This thesis describes recent research aimed at developing chemical vapor deposition (CVD) diamonds for charged particle detection and tracking. Radiation hardness is required for detectors located near the beam interaction region at the future experiments, ATLAS and CMS, at the Large Hadron Collider at CERN. Detectors based on CVD diamond could be a radiation hard option for pixel and strip detectors very close to the interaction region.

There are four important results of this work. Firstly the CVD diamond sensor quality was improved in samples produced by one manufacturer from 30 μm charge collection distance to now typically 200 μm charge collection distance. Secondly a large number of CVD diamond microstrip sensors were operated for the first time under beam test conditions. The diamond strip sensors reached a most probable signal to noise ratio of 50-to-1 at a typical most probable signal charge of 5000 e. The spatial track resolution was between 12 μm and 16 μm. The hit finding efficiency was typically close to 100 % for thresholds below 1000 e. The third important result is that the material uniformity contributes to the width of the observed charge distribution. This is not surprising since CVD diamond is polycrystalline in nature. Fourthly for the first time CVD diamond samples have been irradiated with pions, protons and neutrons with fluences above those expected at LHC. The samples under study here were radiation hard depending on the particle type and fluence. I performed this work as a member of the ATLAS/SCT group at CERN together with the detector research and development project RD42.

Keywords: diamond, chemical vapor deposition, crystal, silicon, detector, strip detector, particle track, telescope, charge collection, RD42, LHC, ATLAS, CMS, radiation hardness

Contents

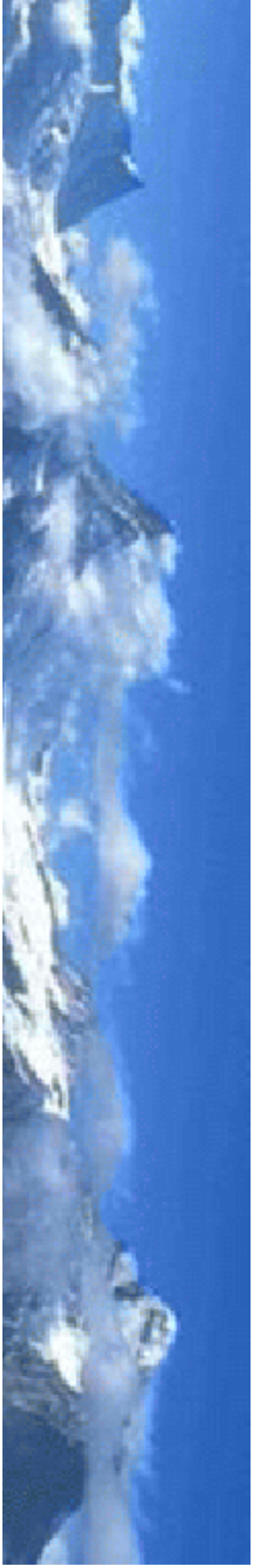

CVD Diamond Sensors for Particle Detection and Tracking

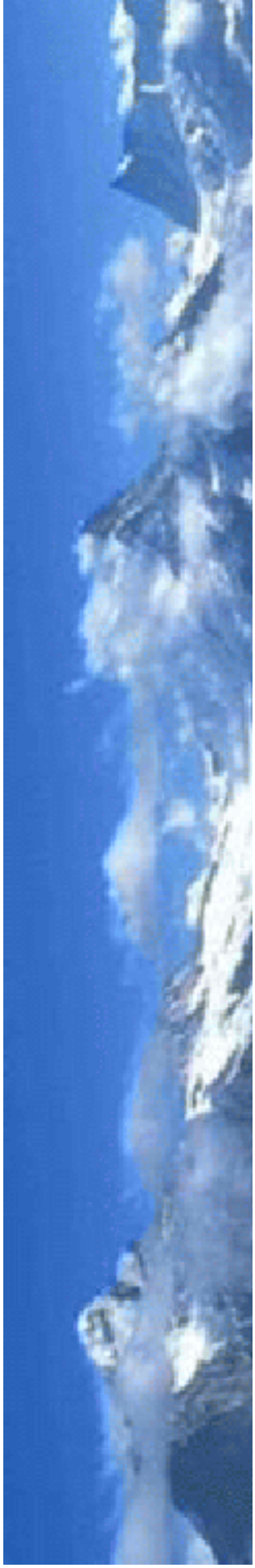

Inaugural-Dissertation
zur
Erlangung der Doktorwürde
der
Naturwissenschaftlich-Mathematischen Gesamtfakultät
der
Ruprecht-Karls-Universität Heidelberg

vorgelegt von
Dipl.-Phys. Dirk Meier
aus Düsseldorf
Tag der mündlichen Prüfung: 11. Februar 1999

CVD Diamond Sensors for Particle Detection and Tracking

Gutachter:

Prof. Bogdan Povh,
Max-Planck Institut für Kernphysik, Heidelberg
Prof. Klaus Tittel,
Universität Heidelberg

CVD Diamond Sensors for Particle Detection and Tracking

Dissertation
by
Dirk Meier
CERN, Geneva, January 1999

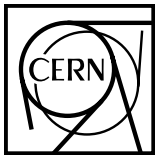

Fachliche Betreuung:

Dr. P. Weilhammer,
CERN, Geneva
Prof. H. Kagan,
Ohio State University,
Columbus

Gutachter:

Prof. B. Povh,
Max-Planck Institut für Kernphysik,
Heidelberg
Prof. K. Tittel,
Universität Heidelberg

contact: Dirk.Meier@cern.ch

Zusammenfassung

Die vorliegende Arbeit beschreibt Untersuchungen an CVD Diamanten zur Spurbestimmung elektrisch geladener Teilchen (CVD ist die Abkürzung für chemical vapor deposition). Die Strahlenhärte ist Voraussetzung für Detektoren, die nahe am Wechselwirkungsbereich der Experimente ATLAS und CMS am Large Hadron Collider am CERN arbeiten sollen. Detektoren auf Diamantbasis könnten eine strahlenharte Option für Pixel und Streifendetektoren in diesem Bereich sein.

Die Arbeit enthält vier wesentliche Resultate. Erstens wurde die Detektorqualität der Diamantproben eines Herstellers von 30 μm charge collection distance auf 200 μm verbessert. Zweitens wurden zum ersten mal Mikrosteifendetektoren auf Diamantbasis betrieben: Diamantstreifendetektoren erreichten ein Signal-Rauschverhältnis von 50-zu-1 am Scheitelpunkt der Signalverteilung bei einem wahrscheinlichsten Ladungssignal von 5000 e. Der Fehler in der Spurvorhersage lag zwischen 12 μm und 16 μm. Die Detektoreffizienz lag typischerweise nahe 100 % für Signalschwellen unter 1000 e. Als drittes Resultat wurde festgestellt, daß Inhomogenitäten in den CVD Diamanten die Signalverteilung verbreitern. Das ist nicht verwunderlich, da CVD Diamanten polykristallin sind. Der vierte wichtige Punkt sind die Bestrahlungen von CVD Diamanten, die zum ersten Mal mit Protonen, Neutronen und Pionen mit einer Dosis zum Teil oberhalb der am LHC zu erwartenden Dosis durchgeführt wurden. Die hier untersuchten Diamantproben sind je nach Teilchensorte und Dosis strahlenhart. Ich habe diese Arbeit als Mitglied in der ATLAS/SCT Gruppe am CERN innerhalb des Detektor Forschungsprojekts RD42 durchgeführt.

Stichworte: Diamant, Chemical Vapor Deposition, Kristall, Silizium, Detektor, Streifendetektor, Teilchenspur, Teleskop, Ladungssammlung, RD42, LHC, ATLAS, CMS, Elektronik, Strahlenhärte

Abstract

This thesis describes recent research aimed at developing chemical vapor deposition (CVD) diamonds for charged particle detection and tracking. Radiation hardness is required for detectors located near the beam interaction region at the future experiments, ATLAS and CMS, at the Large Hadron Collider at CERN. Detectors based on CVD diamond could be a radiation hard option for pixel and strip detectors very close to the interaction region.

There are four important results of this work. Firstly the CVD diamond sensor quality was improved in samples produced by one manufacturer from 30 μm charge collection distance to now typically 200 μm charge collection distance. Secondly a large number of CVD diamond microstrip sensors were operated for the first time under beam test conditions. The diamond strip sensors reached a most probable signal to noise ratio of 50-to-1 at a typical most probable signal charge of 5000 e. The spatial track resolution was between 12 μm and 16 μm. The hit finding efficiency was typically close to 100 % for thresholds below 1000 e. The third important result is that the material uniformity contributes to the width of the observed charge distribution. This is not surprising since CVD diamond is polycrystalline in nature. Fourthly for the first time CVD diamond samples have been irradiated with pions, protons and neutrons with fluences above those expected at LHC. The samples under study here were radiation hard depending on the particle type and fluence. I performed this work as a member of the ATLAS/SCT group at CERN together with the detector research and development project RD42.

Keywords: diamond, chemical vapor deposition, crystal, silicon, detector, strip detector, particle track, telescope, charge collection, RD42, LHC, ATLAS, CMS, radiation hardness

Contents

Chapter 1

Introduction

Solid state tracking devices have become one of the mainstays of general purpose high energy physics detectors. Fig. 1.1 shows the DELPHI silicon vertex detector as an example. Detectors in future high energy collider experiments will be exposed to high radiation levels. In experiments at the Large Hadron Collider (LHC) at the European Laboratory for Particle Physics (CERN) detectors very close to the beam interaction region are expected to receive a fluence above 10^{15} particles/cm^2 *during 10 years of operation. Few detector materials are able to survive this radiation level. Strip or pixel devices based on CVD diamond are a possible choice for radiation hard tracking detectors.*

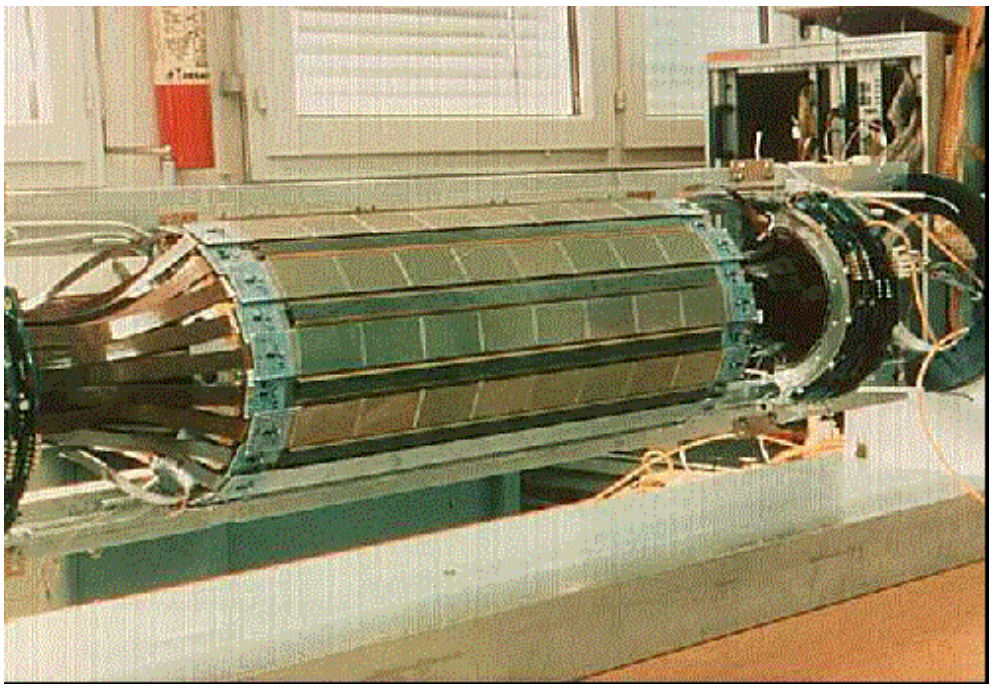

Figure 1.1: Photograph of the DELPHI vertex detector. The purpose of this vertex detector is to measure particle tracks from e^+e^- collisions at LEP. In particular production- and decay-vertices are reconstructed from the hit measurements in the silicon sensor planes. The detector consists of three layers of silicon strip sensors which detect the passage of charged particles. The layers encircle the colliding beams at radii of 6.6 cm, 9.2 cm and 10.6 cm. The outer layer can be seen in this photo. The track position is determined with a precision of 8 μm in each plane perpendicular to the beam axis [1].

Contents

1.1 Introduction to CVD Diamond Sensors

This thesis describes the properties of chemical vapor deposition (CVD) diamond sensors for particle detection and tracking. An introduction to CVD diamond is given below. The order of the subsections in this introduction reflects the structure of the thesis. The radiation hardness of CVD diamond and particle tracking with CVD diamond strip sensors are the most important sections in this thesis. The foundations for these sections include the applications at LHC experiments and basic material and electrical properties of CVD diamond.

1.1.1 Material Properties of CVD Diamond

Diamond is a crystal that can be found in nature as well as produced under certain conditions in laboratories and industry. A diamond consists of carbon atoms in a diamond lattice structure. It is interesting to note that the carbon atoms in the diamond lattice structure have the highest atomic number density of any matter on earth: the atomic number density of diamond is 1.75×10^{23} atoms/cm^3 corresponding to a molar volume [1] of 3.44 cm^3/mol. For comparison, a silicon crystal has an atomic number density of about 5×10^{22} atoms/cm^3 corresponding to 12.05 cm^3/mol. The nucleon density in diamond is 2.11×10^{24} nucleons/cm^3. Carbon is a relatively light atom. Its proton number is 6 and the nucleon number is 12. The weight of the carbon atom is 12.011 u. In fact the atomic mass unit is defined by the weight of carbon isotopes with atomic number 12 [2]. The mass density of diamond is 3.515 g/cm^3. Therefore a diamond sensor with a size of 2×4 cm^2 and a thickness of 500 μm would weigh 1.4 g corresponding to 7 ct [3]. In the periodic table of elements carbon ($^{12}_{6}$C) is located next to boron ($^{11}_{5}$B) and nitrogen ($^{14}_{7}$N) which are common impurities in natural diamond. Elements in the same group of the periodic table include silicon ($^{28}_{14}$Si) and germanium ($^{73}_{32}$Ge) which are commonly used in electronic devices and sensors. A unique feature of carbon atoms in the diamond lattice is the strength of their bonds. The cohesive energy in diamond is 5.8×10^{-19} J/bond, corresponding to 3.62 eV/bond or 7.24 eV/atom [2] [4]. The strength of bonds is important in applications of diamond for machine tools, but it is also the reason for the relatively high energy necessary to displace an atom from its lattice site under particle irradiation.

The work described in this thesis uses diamonds produced by industry in the low pressure, low temperature chemical vapor deposition process. It is amazing that diamond can be produced under low pressure and low temperature conditions considering the natural process of formation which results in diamonds being found in vulcanic residues. A few of the principles of the diamond synthesis are reviewed in Sec. 2.1. The morphology of the CVD diamond samples used was studied by scanning electron microscopy verifying the interesting result that the grain size increases during growth. Other work using X-ray diffraction and Raman spectroscopy in Sec. 2.3 and Sec. 2.4 investigates the crystal structure, the orientation of crystal growth and the material quality [5].

[1] The unit *mol*: 1 mol = 6.0221367×10^{23} atoms.
[2] The unit *unified atomic mass*: 1 u = $m(^{12}\text{C})/12 = 1.6603 \times 10^{-27}$ kg.
[3] The unit *karat*: 1 ct = 200 mg, (do not confuse with 24 carat gold = 100 % gold in alloy).
[4] The unit *electron volt*: 1 eV = 1.602×10^{-19} J, unit of energy.
[5] In this thesis we distinguish the material quality (determined by impurities, defects and stress) from the electrical quality (determined by the mobility, lifetime, signal charge).

1.1.2 Charged Particle Detection using CVD Diamond

Charged particle detection in its most general sense means obtaining a response in a sensor during or after illumination with charged particles. An easy experiment to perform (10 minutes long) is the 'glooming experiment': A CVD diamond[6] is exposed in darkness to ionizing radiation from a β-source. A dose of 10 rad is sufficient[7]. At the same time one heats an iron plate to a temperature of about 300 °C. The procedure has to be performed in darkness and the eye of the observer should be well adapted to the darkness. The diamond is removed from the β-source and put on the heated iron plate to heat the diamond to 300 °C. As the diamond heats one observes the emission of green light from the diamond. The diamond glooms (emits luminescence light) after exposure to the ionizing radiation. The intensity of the luminescence light decreases with time and lasts approximately five to ten seconds. This effect, thermoluminescence, is known[8] and is used with other materials (for example with lithium) in dosimetry.

Particle detection in this thesis means the measurement of the induced charge on the electrodes of a diamond sensor due to the motion of charge carriers after traversal of a charged particle. The energy necessary for creation of an electron-hole pair in diamond is 13 eV. This energy determines the ionization yield for a given amount of energy deposited by a particle. The electrical properties of diamond, namely the charge carrier mobility and the charge carrier lifetime, are most important for single particle detection. The mobility of electrons and holes in diamond is high and, in particular, for holes is 2.5 times higher than in silicon. A high carrier mobility enables faster charge collection in diamond sensors than in silicon. The mobility depends only on the bending of the energy bands and the time between electron-phonon scattering. We will see in Sec. 3.1 that the lifetime depends mainly on defects and impurities. It is shown in Sec. 3.3 that the average charge collection distance in an inhomogenous diamond crystal is proportional to the mobility and the lifetime and that it is the important quantity that determines the induced charge on the electrodes of the sensor. The typical current voltage characteristic, the charge signal readout and the response to ionizing radiation from a β-source are discussed in Sec. 3.2 and Sec. 3.4. The measurements in CVD diamond show a very low bulk leakage current of the order of 0.2 pA/mm^2 at room temperature and a mean signal charge of the order of 8000 e corresponding to a charge collection distance of 222 μm. An important result is that the charge collection distance increases along the direction of growth from the nucleation side to the growth side.

The properties of natural diamond and silicon which are of interest for sensor applications are listed in Table 1.1.

1.1.3 Tracking with CVD Diamond Detectors

One of the main goals of this work was to investigate the ability of CVD diamond sensors to measure charged particle tracks. A track is the interpolation of hit positions as measured by several sensors. The position precision of a hit measurement is an important characteristic of a position sensitive device. A small position error can be achieved by a device with the highest possible signal charge and the lowest possible noise. CVD diamond microstrip sensors were therefore tested in pion beams for their charge signal response on strips, their noise and

[6] This experiment was specifically performed with CVD diamonds described in this thesis, but any CVD diamond will do.

[7] The unit *rad*: 100 rad $\equiv$ 1 Gy = 1 J/kg, unit of the absorbed dose.

[8] Reported by Sir Robert Boyle on October 28, 1663 to the Royal Society in London: "I also brought it [the diamond] to some kind of glimmering light by taking it into bed with me, and holding it a good while upon a warm part of my naked body..".

spatial resolution. The detailed description of the experimental method using a silicon beam telescope for track prediction and the results on diamond sensors are reported in Chapter 4.

1.1.4 Radiation Hardness of CVD Diamond

Results on the radiation hardness of CVD diamond samples are given in Chapter 5. CVD diamond samples were irradiated with 300 MeV/c pions, 1 MeV neutrons and 24 GeV/c protons. These irradiations are a continuation of a series of irradiations performed by the RD42 collaboration [9] in the past [3, 4, 5]: CVD diamond sensors were irradiated in 1993 with photons using a ^{60}Co gamma source at the Argonne National Laboratory. The samples were irradiated up to an absorbed dose of 10 Mrad [6]. No decrease in charge collection distance was observed. In an electron irradiation in 1995 at Société AERIAL with 2.2 MeV electrons from a Van de Graaf accelerator CVD diamond samples absorbed a dose of up to 100 Mrad [7]. No decrease in charge collection distance was observed. Proton irradiations were performed on CVD diamond samples in 1994 and 1995 at TRIUMF, Vancouver, Canada using protons with a kinetic energy of 500 MeV reaching a fluence of 1×10^{14} p/cm^2 at a maximum flux of 8×10^8 $p/\mathrm{cm}^2/\mathrm{s}$ [8]. As in electron and gamma irradiations no decrease in charge collection distance was observed.

The results in Chapter 5 try to establish where the limits in radiation hardness of CVD diamond sensors may be. A decrease of charge collection distance was observed after several 10^{14} neutrons/cm^2, after several 10^{14} pions/cm^2 and after several 10^{15} protons/cm^2. If CVD diamond sensors prove to be sufficiently radiation hard and if the signal charge is sufficiently high then CVD diamond sensors will be of interest for high luminosity experiments at the LHC since radiation hard sensors will better serve to achieve the physics goals set for the LHC.

Before describing CVD diamond sensors it is of interest to review the physics goals at LHC and the conditions relating to the radiation environment close to the region of proton-proton collisions.

[9] The members of the RD42 collaboration are given in the acknowledgements on page 234.

		silicon [a]		natural diamond [b]	
proton number	[ ]	14		6	
atomic number	[ ]	28.0855	[9]	12.011	[9]
lattice constant	[Å]	5.4310	[10]	3.5668	[10]
mass density	$[\mathrm{g\,cm^{-3}}]$	2.329	[10]	3.515	[10]
cohesive energy	[eV/atom]	4.63	[11]	7.37	[11]
melting point	[K]	1685	[10]	4100 [c]	[10]
band gap	[eV]	1.124	[10]	5.48	[10]
relative dielectric constant [d]	[ ]	11.9	[10]	5.7	[10]
resistivity	[Ωcm]	20×10^3 [e]		$> 10^{13}$	[11]
	[Ωcm]	5×10^{11} [f]	[3.2.3]	$> 10^{14}$ [g]	[3.2.3]
breakdown field	$[\mathrm{V/\mu m}]$	30		1000	
electron mobility	$[\mathrm{cm^2\,V^{-1}\,s^{-1}}]$			1500..	[12]
		1450	[10]	..2400	[13]
hole mobility	$[\mathrm{cm^2\,V^{-1}\,s^{-1}}]$			1000..	[12]
		≈ 440	[10]	..2100	[13]
electron saturation velocity	[cm/s]			2×10^7	[13]
hole saturation velocity	[cm/s]			10^7	[13]
thermal expansion coefficient	$[10^{-6}\mathrm{K^{-1}}]$	2.59	[10]	0.8..1.0	[14]
thermal conductivity	$[\mathrm{W\,cm^{-1}\,K^{-1}}]$	1.4		20..23	[14]
energy to create *eh*-pair	[eV]	3.6	[15, 16]	13	[13, 17]
radiation length	[cm]	9.4	[9]	12.03	[3.75]
specific ionization loss	[MeV/cm]	3.9	[3.3.1]	6.2	[3.3.1]
ave. no. of *eh*-pairs/*mip*	[pairs/100 μm]	9000	[3.3.5]	3600	[11]
ave. no. of *eh*-pairs/*mip*	[pairs/300 μm]	27000	[3.3.5]	11850	[3.3.5]

Table 1.1: Properties of silicon and natural diamond that are of interest when considering the material for use as a particle detector. The properties depend on temperature and pressure. The values are valid under normal conditions: for temperature around 298 K and a pressure of 1 atm. A reference to an entry in the bibliography or to a section or an equation in this thesis is given in rectangular brackets.

[a] The column gives values for single crystal silicon.
[b] Selected natural diamond, type IIa, see footnote on page 96.
[c] Diamond melts at 4100 K and 12.5 GPa., it graphitizes at ≈ 1200 K and 1 atm under oxygen [2].
[d] Vacuum has the dielectric constant (permittivity) $\epsilon_0 = 8.854$ pF/m [9].
[e] This is the intrinsic resistivity of silicon.
[f] This is the resistance of a reversed biased silicon diode.
[g] This is the resistivity of a CVD diamond.

1.2 The Large Hadron Collider (LHC)

The study of particle interactions and particle decay behaviour is one the fundamental goals of high energy phyiscs. The creation of new particles at high energies with high production rate is necessary to attain this goal. The aim of a particle collider is to accelerate particles to energies necessary for the production of new particles. Another goal is to have a sufficient number of particles in the beam in order to attain a high interaction rate. A collider accelerates charged particles by means of alternating electric fields. Acceleration increases the kinetic energy of the particles. The particles move in opposite directions inside the ring guided by magnetic fields. The ring is made of one beam pipe or two separate beam pipes, depending on the type of particles used. The particles are brought into collision at certain locations around the ring. The LHC is a collider that will accelerate 'bunches' of protons or heavy ions in two separate circular beams. It will be built inside the existing LEP tunnel [10] and will become operational for physics experiments in the year 2005. One of the major challenges of the LHC project is the cryogenics system along the beam line designed to keep the temperature at 1.9 K necessary to cool the superconducting beam bending magnets. Another challenge is to realize the high particle energy and luminosity required by the physics goals.

1.2.1 Beam Luminosity

Inelastic interaction of two beam particles causes the production of particles. One aims for a high particle rate of inelastic proton-proton interactions. Given the energy dependent inelastic cross section, σ, and the beam luminosity, $\mathcal{L}$, the particle production rate is [18]

$$\frac{\mathrm{d}N}{\mathrm{d}t} = \sigma\mathcal{L}. \tag{1.1}$$

High luminosity is required to obtain a high interaction rate. The luminosity $\mathcal{L}$ is the number of interactions per area A and time. In a circular collider it is [18]

$$\mathcal{L} = \nu\, n\, \frac{N_1\, N_2}{A} \qquad \text{and} \qquad L \stackrel{\text{def}}{=} \int \mathcal{L}\,\mathrm{d}t. \tag{1.2}$$

The LHC accelerates $n = 2835$ bunches along the ring, with a revolution frequency $\nu = 11.2455$ kHz. Each bunch contains $N_1 = N_2 \approx 10^{11}$ particles [19]. In past and present colliders the luminosity culminates around $\mathcal{L} = 10^{32}/\mathrm{cm}^2/\mathrm{s}$. During the first 3 years the LHC will operate at a luminosity of $\mathcal{L} = \mathcal{L}_0 \stackrel{\text{def}}{=} 10^{33}/\mathrm{cm}^2/\mathrm{s}$ (referred to as 'low' luminosity). Later the LHC will operate at a luminosity of $\mathcal{L} = 10 \times \mathcal{L}_0 = 10^{34}/\mathrm{cm}^2/\mathrm{s} = 10^7$ /mb/s (referred to as 'high' luminosity) [12]. The time separation between bunches is 25 ns which is very short relative to a beam cross over (BCO) of approximatively 5 μs at LEP. From these values it follows that the transverse area A is about 50 μm $\times$ 50 μm corresponding to a Gaussian standard deviation of 15 μm in both directions. The interaction area can be measured by displacing the beams with respect to each other, while monitoring the proton-proton interaction rate. Eq. 1.2 gives the definition of the integrated luminosity L. The annual luminosity for continuous running would be 3.15×10^4 /pb in the 'low' luminosity period. The LHC will be on for about 8 months a year of which 2 months will be dedicated to

[10] *LEP*: **L**arge **E**lectron **P**ositron Collider, circumference of 26.66 km [9], first particle injection in 1989.
[12] The unit *barn*: 1 b $= 10^{-28}$ m^2 $\Longrightarrow$ 1 mb $= 10^{-27}$ cm^2.

machine studies and 6 months for physics data taking. Effectively about 4 months at 100 % optimal beam conditions are considered for physics. This gives about 116 days (=10^7 s) [20, 21] of continuous running. The effective 'annual' luminosity is then $10^7 \cdot 10^{33}/\mathrm{cm}^2 = 1 \times 10^4/\mathrm{pb}$ for the 'low' luminosity period and $1 \times 10^5/\mathrm{pb}$ for the 'high' luminosity of $10 \times \mathcal{L}_0$. The accumulated annual luminosity during 10 years of operation starting with a low luminosity period of 3 years followed by a high luminosity period of 7 years yields $7.3 \times 10^5/\mathrm{pb}$. Calculations by the LHC experiments, ATLAS and CMS, assume an integrated fluence of $5 \times 10^5/\mathrm{pb}$ in 10 years of LHC operation [21, 22].

1.2.2 Beam Energy

The beam energy for an accelerator is (ideally) based on two physics principles. The first one is the *mass scale* of particles under study. In order to create new particles with mass M, a sufficient kinetic energy has to be provided for their production:

$$\sqrt{s} \geq M\,c^2. \tag{1.3}$$

The center of mass energy, $\sqrt{s}$, of two colliding beam particles ($i = 1, 2$) with four momenta $p_i = (E_i, \vec{p}_i)$ is [23]

$$\sqrt{s} = \sqrt{(p_1 + p_2)^2} \qquad \overset{\text{see text}}{\Longrightarrow} \qquad \sqrt{s} = 2E_{\mathrm{beam}}. \tag{1.4}$$

In case of two collinear colliding relativistic particles with the same rest mass and same energy $E_{\mathrm{beam}} = E_1 = E_2$ one obtains the second expression for the center of mass energy. The production of the Z^0-Boson, for example, requires a center of mass energy exceeding the rest mass m_{Z^0} which means that $E_{\mathrm{beam}} \geq \frac{1}{2} m_{Z^0} c^2$ [(13)].

The second principle is the *length scale* which one wants to explore. The 'accessible' length scale, λ, in an experiment is related to the momentum, $\vec{p}$, of the probing (beam) particle by de Broglie's equation

$$\lambda = \frac{2\,\pi\,\hbar\,c}{|\vec{p}|\;c}, \tag{1.5}$$

where $\hbar\,c = 197.327$ MeV fm. The momentum in Eq. 1.5 is given by the rest mass, m_0, and the energy, E, of the beam particles:

$$E^2 = \vec{p}^{\,2}\,c^2 + m_0^2\,c^4. \tag{1.6}$$

A typical energy for probing the nucleus on a length scale of femtometers (fermi [14]) is therefore several 100 million electron volts. Probing nucleons requires much higher energies. LEP operated at various energies between $\sqrt{s} = 70$ GeV and $\sqrt{s} \approx 190$ GeV, necessary for Z^0 or $W^\pm$ pair production ($m_{Z^0} = 91.187$ GeV/c^2 and $m_{W^\pm} = 80.22$ GeV/c^2 [9]) which probed a distance scale of the order of 1×10^{-2} fm. The proton beam energy at the LHC will reach 7 TeV which implies from Eq. 1.4 a center of mass energy of 14 TeV. The length scale attainable at the LHC is more complex to describe than at LEP since the energy of 7 TeV is that of the beam protons. Protons are composed of quarks/partons. A parton carries $\approx 1/10$ of the energy of the proton. Eq. 1.5 and Eq. 1.3 apply to the quarks/partons in the proton. This implies that the LHC will reach a length scale of 10^{-4} fm and a mass scale of 1.4 TeV/c^2. This is just the region where new physics is expected to occur.

[13] The Z_0 has a line width of several GeV such that production occurs already below $m_{Z^0} c^2$. The production probability peaks at $m_{Z^0} c^2$.

[14] The unit *fermi*: 1 fm = 10^{-15} m.

1.3 High Luminosity Experiments (ATLAS and CMS)

ATLAS [15] *and CMS* [16] *are general-purpose experiments for recording proton-proton collisions at the LHC. The detectors have been designed to answer "one of the most fundamental questions in physics: what is the origin of the different particle masses?" [24].*

1.3.1 Common Physics Goals

The interaction of electrically charged particles is described in quantum electrodynamics by photon exchange. The photon is massless and has infinite range (the potential decreases like 1/distance). Transition probabilities of electrons in the atomic shell or electromagnetic cross sections between two scattering charges can be calculated using the model of photon exchange between both objects. The cross section for photon absorption is proportional to the fine structure constant $\alpha = e^2/(4\pi\epsilon_0\,\hbar c) \approx 1/137$. Cross sections for single photon exchange are proportional to α^2. The probability for the next higher order process (for example Bremsstrahlung) is proportional to α^3.

The interaction of neutrinos with electrons requires a different model, as given by Fermi's theory of the weak interaction [25]. This model was first applied to the β-decay of the neutron. In analogy with photon exchange, Fermi assumed the exchange of charge via a 'charged weak field' with a very short range (point-like interaction). Fermi postulated a contact interaction which described the decay probability of neutrons. The probability is proportional to the constant $G_{\mathrm{F}}^2 = (1.02 \times 10^{-5}\,\hbar c\,(\hbar/(m_{\mathrm{p}}c))^2)^2$ [18] and was measured in β-decays [17], where $m_{\mathrm{p}} = 938.27$ MeV/c^2 is the rest mass of the proton. However, Fermi's theory predicts a linearly increasing cross section for neutrino-electron scattering (that is the inverse of the β-decay) as the center of mass energy, $\sqrt{s}$, increases. Such behaviour of cross sections is not observed in nature. In addition processes like neutrino-neutrino scattering require a 'neutral weak field' which also would give infinite cross section for a point-like description of their interaction. The limits of cross sections are given by partial wave theory. In an elastic scattering one finds that the intensity of the scattered wave can not exceed the intensity of the incoming wave, an observation, which is called the *principle of unitarity*. The principle of unitarity sets an upper limit to Fermi's cross section for the weak interaction. One finds that for energies $\sqrt{s_{W,Z}} < 700$ GeV, Fermi's cross section is smaller than the maximum possible value as obtained from wave theory [18]. This argument was used to limit the maximum possible mass of the W, Z to be 350 GeV/c^2. In order to limit the cross sections of weak interactions one redefines G_{F} such that it depends on the momentum transfer of the interacting particles (like for the electromagnetic interaction). In addition one introduces a mass for the 'weak field'. This is a technical 'trick' which limits the cross section for weak interaction to a finite value.

The unification of the electromagnetic and weak interaction was developed by Glashow, Salam and Weinberg in 1961 to 1968 and is today known as the *standard model of the electroweak interaction* [26, 27]. The model unified the electro-magnetic and weak interactions by four gauge bosons. Mixed states of these gauge bosons are the photon, Fermi's 'charged weak fields',$W^{\pm}$, and the 'neutral weak field', Z^0. The standard model predicted the masses of $W^{\pm}$ and Z^0 bosons [18]

[15] *ATLAS* abbreviation for **A** **T**oroidal **L**HC **A**pparatu**s**.

[16] *CMS* abbreviation for **C**ompact **M**uon **S**olenoid.

[17] The probability also depends on the number of possible angular momentum states of the decay products [18].

$$m_{W,Z} \approx \frac{4\pi\alpha}{\sqrt{G_{\rm F}}} \approx 90 \text{ GeV}/c^2. \tag{1.7}$$

This prediction allowed the design of experiments which then measured the mass of $W^{\pm}$ and Z^0 and their decay channels at the SPS at CERN in 1983. However, the introduction of masses has no explanation in the standard model. Technically one can explain the masses of $W^{\pm}$ and Z^0 by introducing new particles, namely the Higgs bosons [18] (Higgs-mechanism). The Higgs mechanism gives mass to $W^{\pm}$ and Z^0. The standard model predicts a single mixing state of the Higgs as a real particle with mass $m_{\rm H}$. An upper limit to the Higgs mass is given by the unitarity limit [18]:

$$m_H < \sqrt{4\pi\sqrt{2}/G_{\rm F}} = 1.2 \text{ TeV}/c^2. \tag{1.8}$$

A lower mass limit of 120 GeV/c^2 for the Higgs is given by the measurements of the Z^0 and $W^{\pm}$ masses at LEP.

ATLAS and CMS are going to look for Higgs particles. In the mass range from $m_{\rm H} =$ (80 GeV/c^2 to 150 GeV/c^2) one expects to observe Higgs decaying to photons or to bottom quarks. At the higher mass range 130 GeV/c^2 $< m_{\rm H} <$ 600 GeV/c^2 the most appropriate search would focus on leptonic or hadronic decays:

$$H \to \gamma\gamma \qquad \text{or} \qquad H \to b\bar{b} \qquad \text{or} \qquad H \to 4 \text{ charged leptons} \tag{1.9}$$

where the last decay may go via ZZ, ZZ^*, WW or directly. Several other Higgs decay channels are possible within the Standard Model. Other decay channels are predicted by the Minimal Super-symmetric Standard Model (MSSM in SUSY); they are essentially the same as for the standard model, though with different production rates. ATLAS and CMS are designed to search for one (or more) Higgs bosons in the predicted mass range.

Both experiments will also study symmetry-breaking mechanisms: the symmetries C (particle-antiparticle interchange) and P (space inversion) hold for strong and electro-magnetic interactions. Originally the P symmetry was believed to be conserved by the weak interaction as well but was experimentally observed to be violated. The combination of C and P symmetry is the CP symmetry. CP symmetry is observed to be violated (broken) in kaon decays to pions via the weak interaction. CP symmetry breaking is anticipated for B^0 decays as well, but requires experimental confirmation [9]. Also high-precision measurements of the third quark family such as the top-quark mass and decay properties will be performed [28]. The program also includes searches for super-symmetric particles, new gauge bosons, leptoquarks, and quark and lepton compositeness indicating extensions to the Standard Model and new physics beyond it [29].

The inelastic proton-proton cross section at 14 TeV is about 70 mb [9][18]. Using Eq. 1.1 one obtains for the nominal luminosity of $10 \times \mathcal{L}_0$ a primary particle interaction rate of 7×10^8/s which imply on average $n_{\rm BCO} = (18 \pm 5)$ interactions per bunch (the error is the 1 σ variation of the number of interactions per bunch crossing as given in ATLAS [28]). Estimates from the standard model for Higgs production give total cross sections ranging from 0.2 pb to 1 pb depending on the Higgs mass and the decay channels [24]. Such cross sections are 11 to 12 orders of magnitude smaller than the total proton-proton cross section and lead to a rough production rate of less than 1 Higgs in 10 minutes at the LHC. Such estimates depend on many assumptions described in references [24, 22]. The actual number of Higgs particles

[18] The non-diffractive cross section at $\sqrt{s} = 14$ TeV should be between 65 mb and 70 mb. More conservative calculations for expected radiation levels assume 80 mb [22].

which will be detected is lower and depends on the efficiency and acceptance of the detector for the decay channel and the associated background.

1.3.2 The Radiation Environment

Proton-proton interactions have been simulated based on the inelastic cross section and the proton beam energy [24, 22]. The simulation predicts the primary multiplicities per event and the scattering of particles into a specific interval of the solid angle. A particle emerges at the angle Θ from the interaction point. Θ depends on the energy, E, of the particle and its momentum, p_z, in direction of the beam as given by the approximation

$$\frac{1}{2}\ln\left(\frac{E+p_z}{E-p_z}\right) \approx -\ln\left(\tan\frac{\Theta}{2}\right) \stackrel{\text{def}}{=} \eta. \tag{1.10}$$

The left side is the *rapidity* and the right side defines the *pseudo-rapidity*, η, [9]. The pseudo-rapidity can be measured for any particle according to Eq. 1.10 by measuring Θ with the tracking system. For particles with $\Theta \to 0$ one finds $\eta \to \infty$ and for $\Theta = 90^\circ$ one finds $\eta = 0$. Fig. 1.2 shows the distribution of η for charged particles as simulated by ATLAS and CMS for a single inelastic proton-proton interaction (overlayed from the references [28, 22]). The total number (multiplicity) of charged particles can be read from the figure as the sum of entries in the distribution. The multiplicity is ≈ 92 charged particles (mainly hadrons) and ≈ 60 neutral particles per event. The number of entries in each bin varies by a maximum of 0.5 entries depending on the event generator used (DTUJET, DPMJET-II or PHYTIA-5.7). The curves from ATLAS and CMS agree within this error. It should be noted that this distribution does not depend on the luminosity. In order to normalize to the number of proton-proton interactions interactions per bunch, each entry would have to be multiplied by $n_{\text{BCO}} = 18$ which then depends on the luminosity.

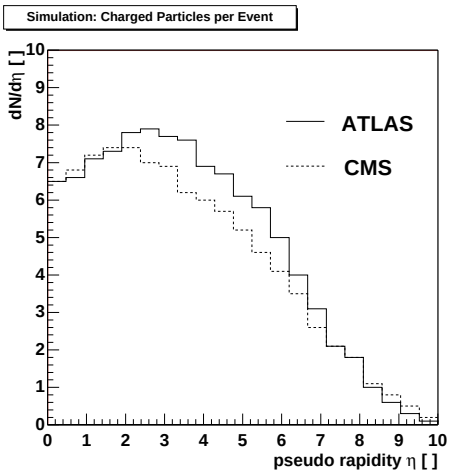

Figure 1.2: Distribution of the pseudo-rapidity of charged particles in a single inelastic proton-proton collision as simulated by ATLAS and CMS. The data are taken from references [28, 22].

particle type	multiplicity/event
$\pi^{\pm}$	71.7
p,$\bar{\text{p}}$	9.0
$\text{K}^{\pm}$	7.1
other charged	3.8
total charged	91.6
π^0	40.7
n,$\bar{\text{n}}$	8.4
photon	1.3
other neutral	10.6
total neutral	61.0
total	152.6

Table 1.2: Average particle multiplicities from the primary proton-proton interaction as simulated by CMS in reference [22]. The same values can be assumed for ATLAS.

The mean number of different particle types in an inelastic interaction is listed in Table 1.2 [22]. The majority of charged particles are pions which amount for 78 % of the total number of charged hadrons. Protons (p and $\bar{\text{p}}$) amount for 10 % of the total number of

charged hadrons. The multiplicity would increase significantly above the mean values when jets are produced.

The simulated distribution [Fig. 1.2] allows a 'naive' [22] estimate of the primary charged particle flux. The flux is the number $\mathrm{d}N^{\mathrm{c}}$ of charged particles in the area of size $\mathrm{d}A$ in the time $\mathrm{d}t$,

$$\phi^{\mathrm{c}} \equiv \frac{\mathrm{d}N^{\mathrm{c}}}{\mathrm{d}A\,\mathrm{d}t} \approx \frac{N^{\mathrm{c}}_{\eta}}{2\,\pi\,r^2\,\cos\frac{\Theta}{2}}\,\frac{n_{\mathrm{BCO}}}{\tau_{\mathrm{BCO}}}. \tag{1.11}$$

The primary flux near the interaction region can be estimated using $N^{\mathrm{c}}_{\eta} \approx 7$ for $|\eta| < 2.5$ as read from Fig. 1.2 and the beam cross over time $\tau_{\mathrm{BCO}} = 25$ ns. Eq. 1.11 is an estimate for the primary flux since it does not account for secondary particle production as it occurs via decay or by interaction or showering in material of the detector and the beam pipe. Results of this calculation are shown for four different radii and angles, Θ, in Table 1.3.

radius		angle	charged flux	'annual' fluence ($= 10^7$ s)		
				charged	primary neutral	total
r	$r_\perp$	Θ	$\phi^{\mathrm{c}} \pm 28$ %	$\Phi^{\mathrm{c}} \pm 28$ %	$\Phi^{\mathrm{n}} \pm 28$ %	$\Phi^{\mathrm{t}} \pm 28$ %
[cm]	[cm]	[°]	[10^6/cm^2/s]	[10^{13}/cm^2]	[10^{13}/cm^2]	[10^{13}/cm^2]
4.0	2.8	45.0	54.4	54.4	36.3	90.7
4.0	4.0	90.0	70.2	70.2	46.8	117.0
11.0	7.8	45.0	7.2	7.2	4.8	12.0
11.0	11.0	90.0	9.4	9.4	6.3	15.7
20.0	20.0	90.0	2.8	2.8	1.9	4.7
50.0	50.0	90.0	0.5	0.5	0.3	0.8

Table 1.3: Results of the 'naive' model for the primary charged hadron flux ϕ^{c} close to the beam interaction point at nominal luminosity of 10^{34}/cm^2/s. The fluence for charged particles is derived from the flux by multiplication with 10^7 s. The primary neutral fluence is 2/3 of the charged fluence [Table 1.2]. The sum of the charged fluence and the primary neutral fluence gives the total fluence. The values were obtained using Eq. 1.11. The error is the statistical 1 σ variation of 28 % in the uncertainty of n_{BCO}.

The neutral flux is assumed to be 2/3 of the charged flux as demonstrated by the simulation of CMS in Table 1.2. The calculation from the 'naive model' gives a charged hadron flux of 9.4×10^6/cm^2/s under $\Theta = 90°$ at $r = 11$ cm. Assuming an effective annual period of 10^7 s running at a luminosity of $10 \times \mathcal{L}_0$ one obtains the charged hadron fluence of 0.9×10^{14}/cm^2 at 11 cm.

Another way to obtain fluences is a full detector simulation which takes into account the different materials, secondary particle interactions, secondary particle production and the magnetic field. Such simulations were done in ATLAS and CMS. Simulated charged particle fluences from CMS are shown in Fig. 1.3. The figure shows charged hadron fluences as a function of z along the beam axis at different radii $r_\perp = r \sin\Theta$. It is important to note that the year is defined as the time until the integrated luminosity reaches 1×10^5/pb [22] which corresponds to 10^7 s of running at nominal luminosity of $10 \times \mathcal{L}_0$ as described in Sec. 1.2.1. The CMS simulation was performed for a continuous beam luminosity of 10^{34}/cm^2 and inelastic proton-proton cross section of 80 mb. This simulation finds at a distance of 11 cm parallel to the beam an annual fluence of 1.1×10^{14} charged hadrons/cm^2 which agrees with the fluence of 0.9×10^{14} charged hadrons/cm^2 from the naive model. No significant difference is expected for ATLAS at the same luminosity. The simulated data might be slightly higher

than the data obtained by the naive model since the simulation takes into account decays and interactions and also low energy particles which loop several times through the detector due to the magnetic field. The flux for neutral particles and neutrons in particular is not shown here. The neutral flux also depends on the experimental setup as discussed in [20, 30].

The naive calculation and the simulation demonstrate that flux and fluence will be extremely high and in excess of any value seen in the past in other experiments (though the number of tracks will be comparable to 'heavy ion events' in present experiments such as NA49). This situation is of great concern, since silicon detectors and readout electronics degrade and eventually stop working due to radiation damage (see Sec. 5.4).

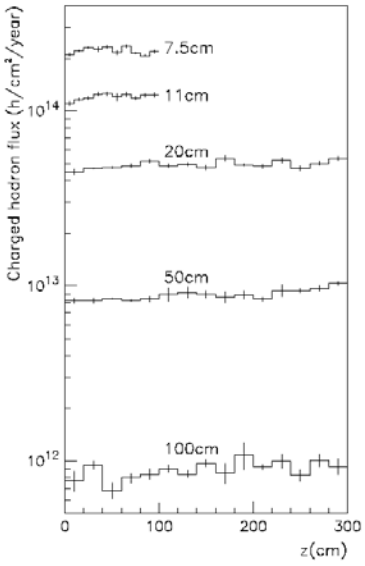

Figure 1.3: Simulation of the annual charged hadron fluence (1 'year' = 100 days) from proton-proton interaction at a luminosity of $10^{34}/\mathrm{cm}^2/\mathrm{s}$. z is the coordinate along the beam axis. The simulation was prepared for the inner tracking region of CMS, however, same radiation levels apply for ATLAS as well. This figure was prepared by CMS [22].

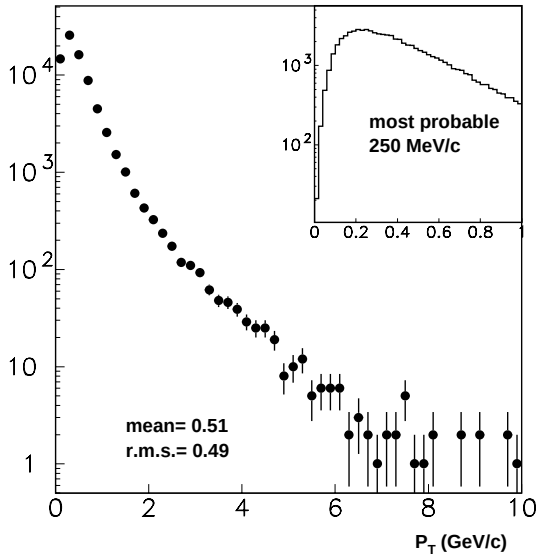

Figure 1.4: Distribution of the transverse momentum, p_T, of charged particles from an inelastic proton-proton collision as simulated by CMS [31].

The p_T momentum distribution of primary charged particles is relevant from the radiation point of view: scattered or created particles emerging from the interaction have the *transverse momentum* $p_\mathrm{T} = \sqrt{p_x^2 + p_y^2}$, where p_x and p_y are the momentum components along $\vec{e}_x$ and $\vec{e}_y$ which are perpendicular to the beam axis ($r\phi$-plane). Fig. 1.4 shows the distribution of the transverse momentum for charged hadrons in inelastic proton-proton events. It is important to notice that the transverse momentum peaks between 200 MeV/c and 300 MeV/c. The total momentum of charge particles is therefore between 200 MeV/c and 400 MeV/c in the central region for $|\eta| < 1$. Radiation damage due to 300 MeV/c charged pions is known to be particularly severe since pions of that momentum interact in resonance with nucleons.

The momentum distribution is also of interest for particle tracking. A charged particle traversing a detector plane is scattered by many small-angle scatters, mainly in the Coulomb potential of nuclei. The effect is called multiple Coulomb scattering. The distribution of (outgoing) track angles projected into a plane relative to the incident tracks depends on the detector thickness, x, its radiation length, X_0 (given in Eq. 3.75), and the particle energy

and momentum. This angle distribution has a standard deviation of [9]

$$\Delta\Theta = 0.0136 \text{ GeV}/c^2 \frac{E}{p^2} z \sqrt{\frac{x}{X_0}} \left[1 + 0.038 \ln\left(\frac{x}{X_0}\right)\right] \tag{1.12}$$

with the energy, E, the momentum, p, and the charge number, z, of the incident particles. Particles with low momentum are likely scattered in larger angles than particles with high momentum. It is important to note that Eq. 1.12 gives the standard deviation of the scattering angles projected into a plane. The standard deviation in space is higher by a factor $\sqrt{2}$ [9]. Fig. 1.5 shows $\Delta\Theta$ evaluated for pions traversing 300 μm thick silicon, diamond and G10 printed circuit board as a function of the pion momentum. Pions with momenta between 200 MeV/c and 300 MeV/c scatter on average with 0.1 mrad which causes a 10 μm error at a 10 cm distance. The standard deviation in space is 14 μm at a 10 cm distance. The experiments will have several layers of detectors and support mechanics which causes multiple scattering. It is therefore important to reduce the amount of material with short radiation length (that means high proton number).

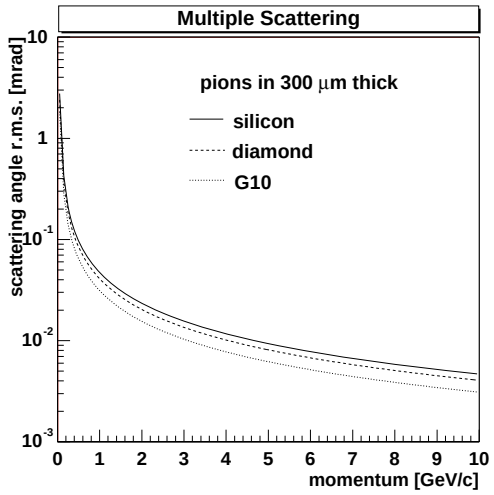

Figure 1.5: Variation (root mean square, rms) of the track angles due to multiple (Coulomb) scattering for pions in 300 μm thick silicon, diamond and G10 (printed circuit board) as a function of the pion momentum. The standard deviation is given for the projection of scattering angles into a plane perpendicular to the detector plane.

1.4 The ATLAS Spectrometer

ATLAS is the acronym for **A T***oroidal* **L***HC* **A***pparatu***s**. *It is outlined in the proposal [24] and described in detail in the technical design reports of the various detector components. A brief overview and essentials of the silicon strip and pixel tracker are given below.*

1.4.1 Overview

The ATLAS detector is a spectrometer, containing detector components for calorimetry, particle identification and particle tracking. The overall detector will have a length of 50 m, a diameter of 25 m and a weight of 7000 tons. The ATLAS detector includes an inner tracking detector inside a super-conducting solenoid which generates a 2 T magnetic field along the beam axis [19] , [20], electro-magnetic and hadronic calorimeters outside the solenoid and muon spectrometers in the forward, barrel and end-cap regions. A spectrometer measures

[19] For comparison, the magnetic field of the super-conducting solenoid in DELPHI is 1.23 T [32].
[20] The unit *tesla*: 1 T = 1 kg/As^2.

momentum and energy. The particle energy is measured in calorimeters. The momentum is measured from the bending radius r in the magnetic field. The particle tracking system must measure at least three points in order to determine the radius. The transverse momentum of a particle with charge, q, is measured from its bending radius, r, in the beam axial magnetic field $\vec{B}$:

$$p_{\mathrm{T}} = q\, r\, |\vec{B}| \qquad \Longrightarrow \qquad r\,[\mathrm{m}] \approx \frac{10}{3}\,\frac{p_{\mathrm{T}}\,[\mathrm{GeV}/c]}{|\vec{B}|\,[\mathrm{T}]}, \tag{1.13}$$

where the radius r is obtained by the particle tracking system. Eq. 1.13 is solved for r which allows one to quickly calculate the bending radius at given p_{T}: a particle with a momentum of 300 MeV/c (or 8 GeV/c) would curl in a magnetic field of 2 T with a radius of 0.5 m (or 13.3 m).

The ATLAS inner detector from the outside to the inside consists of a transition radiation tracker (TRT), the semi-conductor tracker (SCT, barrel and forward direction) and an inner pixel detector for tracking. Fig.1.6 shows a simulated event in the ATLAS barrel inner detector with the view along the beam axis. The outer radius of the inner detector is 115 cm (limited by the surrounding cryostat), the total length is 7 m limited by the position of the end-cap calorimetry. The TRT is made of straw-tubes (a straw-tube has a diameter of 4 mm, length 150 cm). It identifies electrons and rejects hadrons from their different ionization loss and transition radiation in the $Xe/CF_4/CO_2$ gas filling. A straw-tube has a central anode wire which collects electrons from ionizations by traversing particles. The TRT has a characteristic position resolution of 170 μm for $p_{\mathrm{T}} = 10$ GeV/c muons. The inner detector will be cooled with coolant at a temperature of -15 °C in order to keep the semi-conductor tracker at -7 °C.

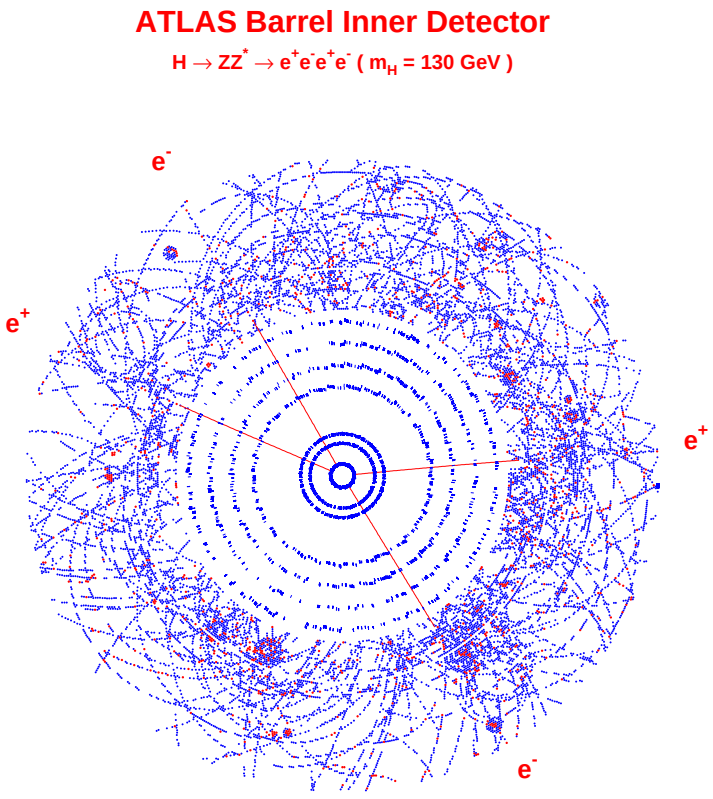

Figure 1.6: Display of a simulated event in the ATLAS barrel inner detector with the view along the beam axis. The simulated process is the Higgs decay $H \rightarrow ZZ^* \rightarrow e^+e^-e^+e^-$ for a Higgs mass $m_{\mathrm{H}} = 130$ GeV/c^2 at the nominal luminosity of $10^{34}/\mathrm{cm}^2/\mathrm{s}$. Hits are shown for $0 < \eta < 0.7$; TRT hits are shown in the barrel for $z > 0$; Fitted tracks, with $p_{\mathrm{T}} > 5$ GeV/c and $0 < \eta < 0.7$, are shown just in the precision tracker so as not to obscure the TRT hits. The picture is taken from reference [28].

1.4.2 ATLAS Semi-conductor Tracker (SCT)

The SCT is composed of 4 barrel layers of silicon (total area 34.4 m^2) and 9 end-cap wheels (total area 26.7 m^2) on each side. The barrel layers will have a radial spacing of 10 cm with the innermost layer at a radius of 30 cm. The four layers are visible in the event display Fig. 1.6. The total number of readout channels will be 6.2×10^6. Using a strip pitch of 80 μm the spatial resolution will be ≈ 16 μm in the $r\varphi$ coordinate and ≈ 580 μm in the z-coordinate [28]. The detector acceptance depends on the angle, Θ, between the outgoing particle and the beam axis. This angle is commonly converted to pseudo-rapidity using Eq. 1.10. The SCT barrel part will cover the interval $|\eta| < 1.4$ and together with the end-cap wheels up to $|\eta| < 2.5$ which corresponds to an angle coverage of $\Theta \approx 9^\circ$ to 171° (for comparison, the DELPHI detector covers 15° to 165° [32]). The barrel silicon tracker is designed to reconstruct isolated lepton tracks with $p_T > 5$ GeV/c (>1 GeV/c) with an efficiency better than 95 % (90 %) in the range $|\eta| < 2.5$. The number of reconstructed fake tracks should be below 1 % (10 %) which means looping tracks, such as low momentum (< 1 GeV/c) leptons which circulate around the magnetic field lines and pass the barrel several times, have to be reconstructed in three dimensions in order to be suppressed in the analysis [28]. The spatial resolution of the barrel layers has to be better than 20 μm, in order to measure tracks with $\Delta p_T/p_T < 0.3$ at $p_T = 500$ GeV/c. In practice one combines the track predictions from all detectors to form an overall track fit. Exact specifications for pattern recognition, particle identification and errors for the secondary vertex measurements are listed in reference [28].

1.4.3 ATLAS Pixel System

The ATLAS pixel system consists of 3 barrel layers and 8 disk layers (four on each side of the barrel). The barrel layers (as visible in Fig. 1.6) will be located between the radii from 4.15 cm to 13.75 cm, the four disks are planned from $|z| = 49$ cm to $|z| = 103.5$ cm. The innermost radius is limited by the beam pipe which will have a radius between 2.5 cm and 3.0 cm. The total number of channels to be read out will be 140×10^6 channels exceeding by more than one order of magnitude the number of channels of the SCT. The nominal spatial resolution is given as 12 μm in $r\phi$ direction and 66 μm in z direction. The pixel system will be sensitive for tracks with $|\eta| < 2.5$. Pixels are favored in the high flux regions very near to the beam pipe, since their hit occupacy is lower than that of strips at this location. The *hit occupancy* is defined as

$$o \stackrel{\text{def}}{=} \phi \, \tau \, A_D \qquad ; \qquad A_D = P_u \cdot P_v \tag{1.14}$$

where τ is the single strip/pixel deadtime before it can receive a new hit and A_D the sensitive area. The particle flux, ϕ, can be the primary flux as defined in Eq. 1.11 or the flux including particle interaction and decays. The sensitive area, A_D, is assumed as given in Eq. 1.14 with the pixel pitch P_u and P_v along both directions in the detector plane. For strip detectors, P_v is the length of the strip. Typical strips of the SCT barrel will have a pitch $P_u = 80$ μm and a length $P_v = 12$ cm whereas typical pixels will have a pitch $P_u = 50$ μm and $P_v = 400$ μm. Assuming both sensors would be exposed to the same particle flux, having the same deadtime, one obtains an occupancy 220 times higher for the strips compared to the pixels. The deadtime for a single pixel must stay below 0.5 μs (2.5 μs) in the B-layer (pixel barrel) as specified in reference [28]. Assuming $\tau \approx 0.5$ μs one obtains for the B-layer at 4 cm with the charged hadron flux given in Table 1.3 a single pixel occupancy of 0.7 % and 1.4 % for the case of tracks that cause response on two pixels. The occupancy decreases

with decreasing flux for increasing η. The occupancy should stay below several percent since otherwise trackfinding becomes too complex to separate real tracks from fake tracks. The purpose of the pixel system is to increase the precision of impact parameter measurements of secondary vertices very close to the interaction region. The pixel system improves b-tagging and allows rejection of light-quark jets. Also tagging of other relatively heavy particles (τ or charm containing hadrons) is improved with an efficient pixel system. The error on the impact parameter measurements of secondary vertices decreases by a factor of 2 with the B-layer included compared to a situation without B-layer and demonstrates its importance for physics [28]. The innermost barrel layer (B-layer at 4.15 cm) will be removable since it may need replacement because of radiation damage.

1.5 The CMS Spectrometer

CMS is the acronym for **C***ompact* **M***uon* **S***pectrometer. The experiment is outlined in the proposal [22] and described in detail in the technical design reports of the various detector components. A brief overview and informations about the silicon strip and pixel tracker are given below.*

1.5.1 Overview

CMS is a general purpose detector with emphasis on muon identification and muon momentum measurement, precise photon and electron identification and calorimetry and central tracking for momentum measurement and vertex finding of charged particles. The overall detector will have a length of ≈ 22 m, a height of ≈ 15 m and a weight of 11500 tons. A muon sees four muon stations over most of the solid angle. Each of the four barrel muon stations consists of 12 planes of aluminum drift tubes. Efficient muon tracking will be possible up to $|\eta| = 2.4$ for $p_{\mathrm{T}} > 4$ GeV/c. CMS has a superconducting solenoid with a beam axial magnetic field of 4 T. The magnet iron yoke is part of the muon system. CMS will have high (energy) resolution crystal electromagnetic calorimeters (ECAL, made of $PbWO_4$) in the barrel and endcap regions. The ECAL is sourrounded by the barrel and endcap hadron calorimeter (HCAL, made of copper/scintillator layers). A very forward (iron/gas) hadron sampling calorimeter extends the coverage up to $|\eta| = 5$. The CMS central tracking is based on pixels, silicon strips (SST) and microstrip gas chambers. Fig. 1.7 shows the CMS central tracking region (sideview) together with the ECAL in a GEANT event simulation. The physics event (leptonic Higgs decay $H \rightarrow ZZ^* \rightarrow 2e^+2e^-$) is the same as in the ATLAS simulation in Fig. 1.6 and illustrates the huge amount of tracks.

1.5.2 CMS Silicon Strip Tracker (SST)

The CMS silicon strip tracker is based on microstrip-silicon sensors (all 300 μm thick, single sided, p^+ in n bulk, total area of ≈ 70 m^2) in 5 barrel layers from $r_\perp =$ (22 cm to 60 cm), 3 silicon mini-disks and 10 end-cap disks on either side. The SST has a length of 5.6 m and covers the pseudo-rapidity range of $|\eta| < 2.5$. Isolated tracks are expected to be reconstructed with efficiencies greater than 98 % and fake tracks below 1 % at a momentum resolution better than $\Delta p_{\mathrm{T}} < 0.15$ GeV/c over $|\eta| < 2.5$. Non-isolated tracks with p_{T} inside jets are required to be identified with an efficiency better than 90 % at a fake rate below 1 %. As in ATLAS the relevant constraints are the radiation environment and aim to reduce material in order to avoid unwanted interactions and multiple scattering.

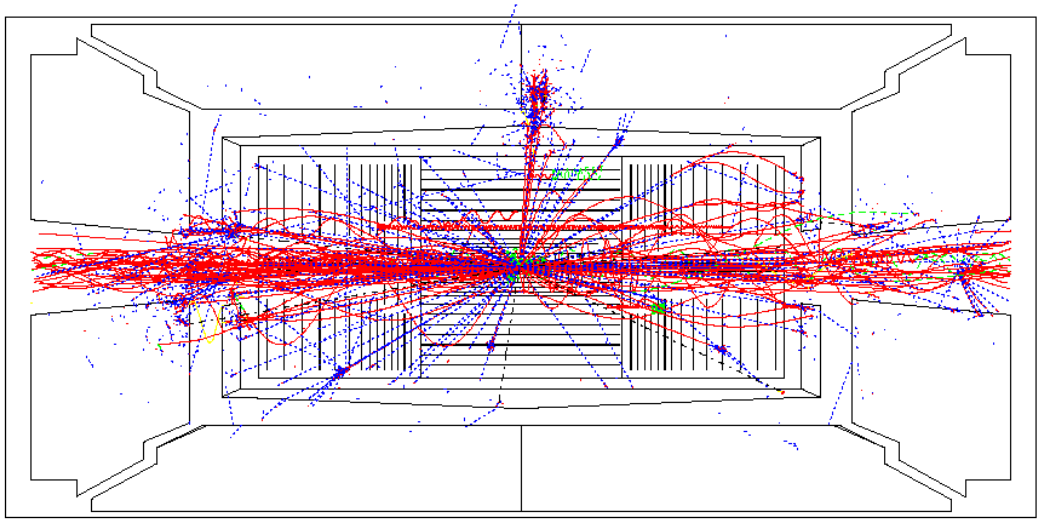

Figure 1.7: GEANT simulation of $H \rightarrow ZZ^* \rightarrow e^+e^-e^+e^-$ at $m_{\mathrm{H}} = 150$ GeV/c^2 in the CMS tracker. From inside to outside: silicon pixel and silicon strip detectors, microstrip gas chambers and crystal electromagnetic calorimeter. The event is taken from CMS, reference [22].

1.5.3 CMS Pixel System

The CMS pixel system will consist of 3 barrel layers and 4 disk layers (two on each side of the barrel). The barrel layers will be located between the radii from ≈ 4.0 cm to 11.5 cm, the two disks are planned at $|z| = 32.5$ cm and $|z| = 46.5$ cm [31]. The purpose of the pixel system is the same as for ATLAS: exact determination of the vertex and rejection of background from jets and beam beam interaction. Pixels make it possible to extrapolate track candidates from the outer layers to the vertex. The main issues appart from high resolution, large efficiency, acceptance and occupancy are mechanical constrains (complete coverage, lowest amount of material), electronics design of suitable fast and lowest possible noise readout electronics and radiation hardness of the whole system (electronics and detectors). It is anticipated that the innermost layer will need replacement at least once during the experiment.

Chapter 2

CVD Diamond

The material aspects of chemical vapor deposition (CVD) diamond will be presented in this chapter. Standard characterization techniques for crystals, scanning electron microscopy, X-ray diffraction and Raman spectroscopy were used, in order to obtain information about the material quality of the CVD diamond samples. The diamond samples presented in this chapter were obtained from two manufacturers [33, 34] and results may be different for other manufacturers. The figure below shows the image from the surface of a CVD diamond as seen through a scanning electron microscope. The surface is unprocessed and shows crystal grains.

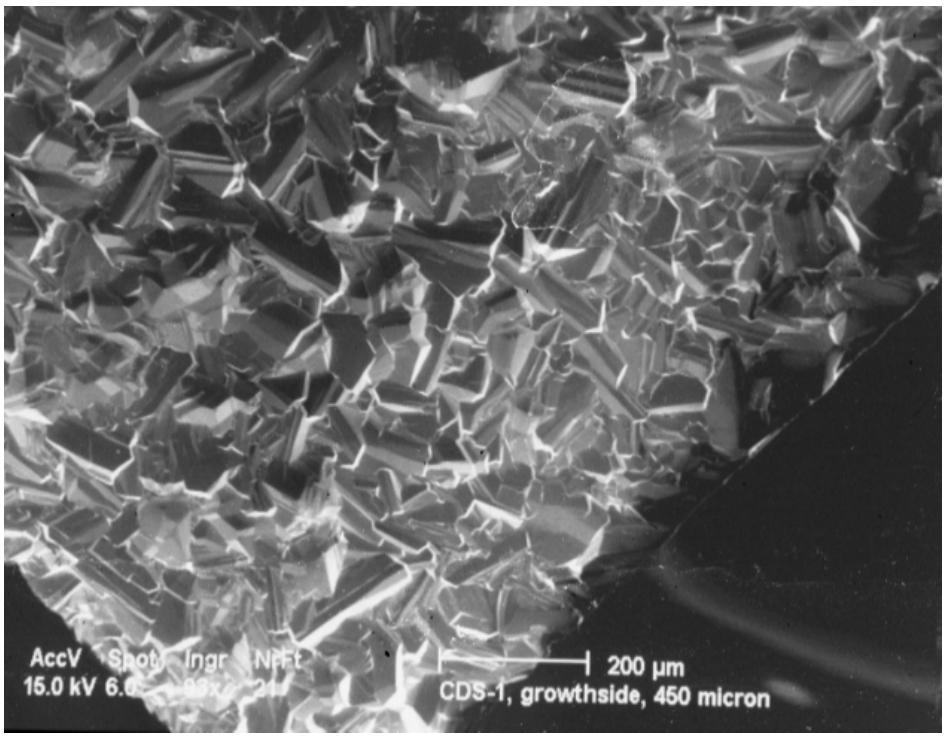

Figure 2.1: Scanning electron micrograph from the growth side of a CVD diamond sample (CDS-1, one of the first diamond samples obtained for characterization as a sensor for charged particles [34]). The picture shows a corner of the unprocessed surface.

Contents

2.1 Diamond Synthesis

The practical use of diamond as a detector material has been made possible by advances in the chemical vapor deposition (CVD) growth process. This process allows diamond to be produced economically over a large area and with high purity. A description of the diamond lattice and a production method is given below.

2.1.1 The Diamond Lattice

A diamond crystal is formed of carbon atoms in a diamond lattice structure. The diamond lattice consists of two face centered cubic lattices, displaced along the diagonal of the (cubic) unit cell by one quarter the length of the diagonal [35]. In an equivalent definition one can say: the diamond structure is one face centered cubic lattice (*fcc*) with two atoms per primitive unit cell [36]. A face centered cubic lattice can be described by a four point basis

$$fcc \quad : \quad \text{four point basis} \quad \left\{\vec{0}, \vec{a}_1, \vec{a}_2, \vec{a}_3\right\} \stackrel{\text{def}}{=} \left\{\vec{0},\ \tfrac{a}{2}(\vec{e}_1+\vec{e}_2), \tfrac{a}{2}(\vec{e}_2+\vec{e}_3), \tfrac{a}{2}(\vec{e}_1+\vec{e}_3)\right\} \tag{2.1}$$

where $\vec{e}_i$, $i = 1, 2, 3$, are the orthogonal unit vectors along the corners of the cubic cell. Each atom of the *fcc* structure can therefore be reached by a linear combination of primitive vectors:

$$\vec{R} = m_i\, \vec{a}_i \qquad ; \qquad m_i \in N. \tag{2.2}$$

Fig. 2.2 shows a unit cell of the diamond crystal structure and one way to describe the positions of atoms in the unit cell: one carbon atom of the primitive cell is placed at the origin, $\vec{0}$, of an orthogonal coordinate system, $\{\vec{e}_1, \vec{e}_2, \vec{e}_3\}$. The second atom of the primitive cell is situated at $(\vec{e}_1 + \vec{e}_2 + \vec{e}_3)\, a/4$ along the body diagonal of the unit cell at a distance of one quarter of the diagonal length. The diamond lattice is therefore described as

$$\text{diamond} \quad : \quad fcc \ \text{ and two point basis} \quad \left\{\vec{d}_1, \vec{d}_2\right\} \stackrel{\text{def}}{=} \left\{\vec{0}\,, (\vec{e}_1+\vec{e}_2+\vec{e}_3)\, a/4\right\}. \tag{2.3}$$

The primitive cell chosen here has the volume $V = \vec{a}_1 \circ (\vec{a}_2 \times \vec{a}_3) = a^3/4$, one quarter of the volume of the unit cell. One could choose other primitives cells to describe the diamond lattice (for example the Wigner Seitz cell). The lattice constant, $a = 3.56$ Å, is the corner length of the cubic cell. The distance from one atom to its nearest neighbour, which is drawn as a line between the carbon atoms, is $|\vec{d}_2| = a\sqrt{3}/4 = 1.54$ Å.

For the description of X-ray diffraction, Raman spectra and electric conduction it is useful to define the reciprocal lattice. The basis vectors of a primitive cell in the reciprocal lattice are

$$\vec{b}_i \equiv \frac{\pi}{V}\, \varepsilon_{ijk}\, \vec{a}_j \times \vec{a}_k \qquad , \quad V = \frac{1}{6}\, \vec{a}_i \circ (\varepsilon_{ijk}\, \vec{a}_j \times \vec{a}_k) = \frac{1}{4}\, a^3 \qquad ; \quad i,j,k \in \{1,2,3\} \tag{2.4}$$

where the $\vec{a}_i$ span the primitive cell in the unit cell of the direct lattice, as defined in Eq. 2.1. A primitive cell in the reciprocal lattice is called a Brillouin zone. In general one distinguishes the first Brillouin zone from higher Brillouin zones. The first Brillouin zone is the Wigner Seitz cell of the primitive lattice. The Brillouin zone used here is a higher order primitive

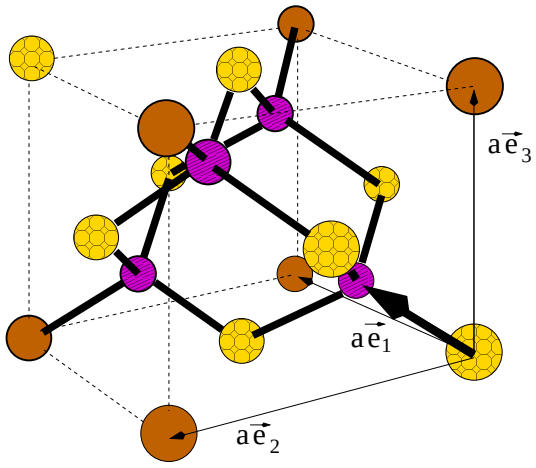

Figure 2.2: The cubic unit cell of the diamond lattice. The corner atoms of the primitive cell are marked with small circles on a light gray background. Those atoms of the diamond lattice which are missing in a face centered cubic lattice are shaded with dashed lines on a dark gray background. The four nearest neighbour bonds for each atom are drawn with solid lines. The origin of the coordinate system $\{\vec{e}_1, \vec{e}_2, \vec{e}_3\}$ is located at one corner atom of the unit cell. The unit cell has corner lengths a. The distance to nearest neighbours is $a\sqrt{3}/4$.

cell. A vector, $\vec{G}$, of the reciprocal lattice is then a linear combination of reciprocal basis vectors

$$\vec{G} = n_i \, \vec{b}_i \qquad \text{with} \qquad n_i \in N. \tag{2.5}$$

The n_i are called the *Miller indices*.

2.1.2 Diamond Phase Diagram

Synthetic diamond can be formed by two techniques, one using a high-temperature (> 1000 °C), high-pressure ($> 10^5$ atm) liquid and the other using a gas at lower temperature (< 1000 °C) and low pressures (≈ 0.1 atm)[1]. The high-pressure process takes advantage of the phase diagram of carbon, shown in Fig. 2.3. At 1 atm, graphite is the most stable form of carbon, but as the pressure is increased, the diamond phase becomes more stable [37]. At 298 K and 1 atm pressure, the difference in free energy between diamond and graphite is 0.03 eV per atom, which is of the order of $k_B T = (1/40)$ eV at room temperature. However, there is a large activation barrier inhibiting the transformation of graphite to diamond [38]. Since graphite (2.26 g/cm^3) is less dense than diamond (3.5 g/cm^3) [from Table 1.1] the 'first' phase of carbon formation out of a super-saturated carbon gas is graphite and not diamond. The transformation of graphite into diamond is a slow process due to the activation barrier; high temperatures and catalysts (nickel, iron or cobalt) are usually required [37].

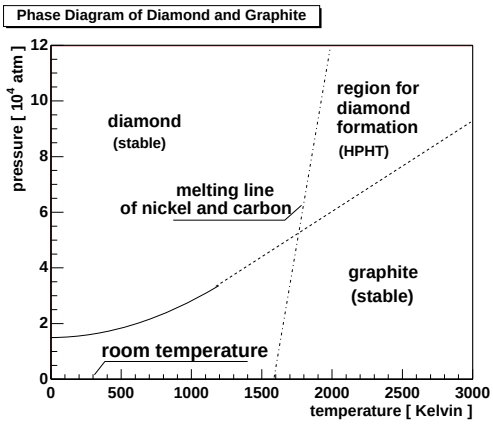

Figure 2.3: Pressure versus temperature phase diagram for carbon [37]. The line labeled with nickel and carbon denotes the conditions utilized for diamond growth using metallic catalysts [39]. More precise pressure versus temperature phase diagrams can be found in reference [40].

[1]The unit *atmospheric pressure*: 1 atm = 760 mmHg = 760 Torr = 1.013×10^5 N/m^2, 1 bar = 10^5 N/m^2 = 10^5 Pa.

2.1.3 Chemical Vapor Deposition of Diamond

The second production technique uses a non-equilibrium process to form diamond. The diamond is grown in a mixture of gases containing carbon, hydrogen, and oxygen. Fig. 2.4 shows the principle of a hot filament chemical vapour deposition reactor. Carbon deposits in the form of graphite and diamond on a heated (600 °C to 1000 °C) surface (substrate) from decomposition of carbon containing gases (for example methane, CH_4). Graphite usually deposits much faster than diamond, however, graphite is etched by hydrogen and oxygen atoms and OH radicals while diamond is comparatively inert. Under the best possible conditions any deposited graphite will be etched while diamond continues to be deposited [37]. The main difficulty in the synthesis of diamond by the CVD method is preventing the deposition of carbon in its stable form (graphite). Therefore all studies of the growth of large or thick diamond films are essentially developments of methods of removing graphite or preventing its formation.

Chemical vapor deposition can be separated into two steps: nucleation and growth. The exact process of nucleation in the CVD process is difficult to model and it is an active field of research [38]. The nucleation is thought to begin by adsorption of carbon from the gas phase on the substrate material. This is difficult since it requires a suitable atomic site for the carbon atom on the substrate surface. The nucleation can be achieved on non-diamond substrates like silicon or metals (for example molybdenum) which can form a carbide. The nucleation process is usually enhanced by providing nucleation centers on the substrate. Nucleation centers can be defects on the substrate which can be obtained by polishing the substrate using grit materials such as silicon carbide, alumina or diamond powder [41]. Nucleation may involve the intermediate formation of graphite. The electron structure of a carbon atom on the surface can be an sp^2-hybrid or an sp^3-hybrid. The sp^2-bonded carbon can be etched by atomic hydrogen, desorb or eventually convert from an sp^2-hybrid to an sp^3-hybrid. In graphite, the carbon atoms are arranged in parallel hexagonal layers, having strong sp^2-bonds within each layer and only weak Van der Waals bonds between layers. The cohesion between layers is relatively low. Once an sp^2-bond is broken carbon atoms on the surface can be hydrogenated by atomic hydrogen and then act as a site for diamond growth [38].

Diamond growth requires large amounts of atomic hydrogen provided by the decomposition of molecular hydrogen in the heated reaction region. The hydrogen serves two functions. Firstly the atomic hydrogen can remove (etch) sp^2-bonded carbon (graphite). Secondly hydrogen can terminate the surface of an existing diamond or graphite structure. A hydrogen terminated diamond surface itself is stable. A carbon radical can replace a hydrogen termination on the surface. Diamond growth is then a competition between the formation of graphite and the etching of graphite. The growth of diamond requires tuning of the growth parameters in order to obtain the correct rate between the breaking of sp^2-bonded carbon (graphite) and making of sp^3-bonded carbon (diamond).

The possible reaction processes are summarized in reference [38]. Fig. 2.5 shows the triangular diagram with atomic hydrogen, oxygen and carbon at each corner. Mixtures with certain ratios of these elements are located inside the triangle. The diamond growth is only possible for ratios in the narrow region from hydrogen to CO (along the carbon monoxide line, 'CO-line'). This information was obtained by analysis of C-O-H gas compositions and is independent of the particular CVD growth method [42]. The triangular diagram contains no information about the temperature or pressure. However, substrate temperature and pressure are important parameters. It was found that the region of possible diamond growth narrows with increasing substrate temperature [42].

Diamond from a CVD process is polycrystalline in nature with a columnar structure of

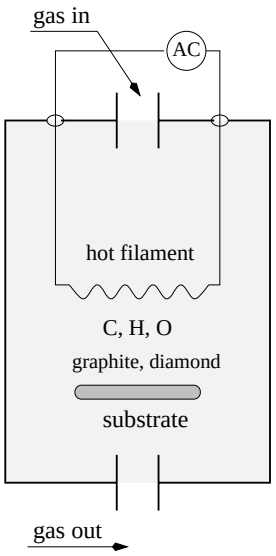

Figure 2.4: Schematic diagram of a hot-filament chemical vapour deposition reactor [38].

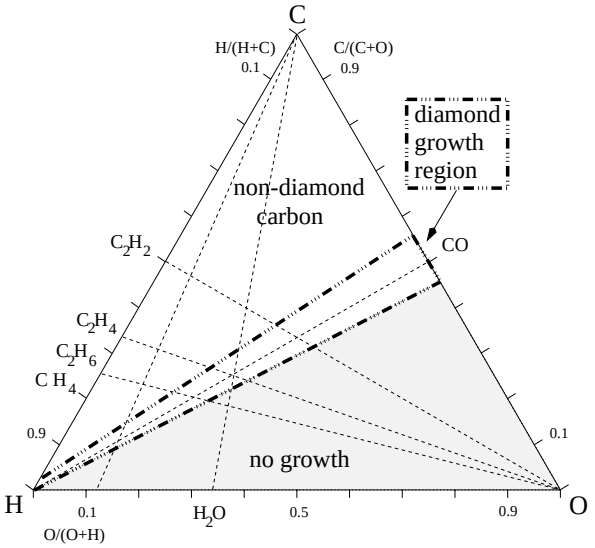

Figure 2.5: Diagram for diamond deposition from hydrogen-oxygen-carbon gas mixtures. Diamond growth is possible in the narrow region from hydrogen to CO. Taken from reference [42].

grains. The columns typically increase in size from the nucleation side to the growth side. Polycrystalline CVD diamond has grain boundaries between columns. Once nucleation has been established the orientation of crystal growth can be controlled by the growth conditions (gas composition, density of nucleation sites, temperature and pressure) in the reactor. Different combinations of growth parameters produce diamond. CVD diamond can be grown with texture which means that its crystal planes are oriented with respect to a fixed direction.

2.1.4 History of Diamond CVD

Diamond synthesis by chemical vapour deposition was first achieved at Union Carbide in 1952 [43] using a methane flow over a heated diamond grid. The growth rate was low and significant amount of graphite was present. This first chemical vapor deposition was achieved before the first high-pressure high-temperature diamond synthesis in 1953. Without knowledge of the first CVD synthesis new efforts started in 1956 and 1961 and were later documented in references [44, 45]. An important step was the synthesis of CVD diamond on non-diamond substrates in 1976 [46], 1981 [47, 48] together with new production techniques in microwave plasma reactors in 1983 [49].

2.1.5 Example of Diamond CVD

A relatively simple experimental setup of a diamond synthesis by a DC plasma chemical vapour deposition can be found in reference [50]. Inside a metallic chamber (pressure $\approx$ 200 Torr), decomposition of the gas (methane/hydrogen, 0.9 % to 3.8 %) and partial ionization (plasma) was achieved between two electrodes which were at a voltage of $\approx$ 1000 V. No hot filament was necessary in this configuration. The electrical current at plasma glow was 2.5 A. Polycrystalline diamond of several 100 μm thickness was deposited at the anode on a time scale of several hours. Both anode and cathode were water cooled and the anode (substrate) temperature was typically 1000 °C. A good overview of other diamond synthesis techniques

can be found in reference [41].

2.2 Scanning Electron Micrographs

A scanning electron microscope (SEM) was used to obtain magnified topographical images of CVD diamond surfaces. The SEM can produce images from surfaces with greater magnification and greater depth of focus than optical microscopes due to the short de Broglie wave length of electrons. The magnifications used here, were between ×50 and ×5000. The polycrystalline structure of CVD diamond was studied under various view angles. The micrographs allowed the measurement of grain sizes on the nucleation side and on the growth side.

2.2.1 Principle of the Electron Microscope

In an SEM, an electron beam is generated and scans the sample. Electrons are emitted from a cathode and accelerate in a vacuum to the anode. They pass the anode and travel with a typical *kinetic* energy of 15 keV to the sample (specimen). Magnetic fields focus and steer the electron beam over the specimen. Electrons interact with the atoms on the surface of the specimen. The relevant interactions for topographic images are electron backscattering and secondary electron production (other interactions like X-rays emission, Auger electron emission or cathodoluminescence occur and can be used to obtain information about atomic surface composition or electrical surface characteristics). The smallest distance which can be resolved by an electron microscope is given by [51]

$$d = 0.61 \frac{\lambda}{\sin \alpha_0} \tag{2.6}$$

where $\alpha_0 \approx 0.34\,^\circ$ is a realistic value for the aperture angle and λ the de Broglie wave length for electrons (see Eq. 1.5). A typical electron energy of 15 keV, corresponding to a wave length of $\lambda = 0.01$ nm, gives the resolution of $d \approx 1$ nm which is smaller by 3 orders of magnitude than the resolution of optical light microscopes.

The yield of electrons emitted from the specimen surface depends on the incident angle between the beam and the specimen surface. Lateral topographic changes on the surface are therefore detected as a change in electron yield from the surface as the beam scans over the specimen. The electron yield from the surface is typically measured using a scintillator read out by a photomultiplier, mounted next to the sample. The electron beam scans over the sample while the yield is measured. The topographic image of the surface is the yield as a function of the position on the surface.

2.2.2 Experimental Method

The CVD diamond samples had a size of 1×1 cm^2 and thickness between 400 μm to 650 μm. They had electrical contacts of 5 mm in diameter on both sides (from electrical characterizations described in Chapter 3), the remaining area had the bare 'as grown' surface. A small amount of conductive plasticine, containing graphite, was used in order to electrically connect the one contact with the other contact. The plasticine also conducted charges from the sample to the grounded sample holder preventing charging of the sample. Non-conductive samples tend to accumulate charges in the electron beam which would deflect the scattered electrons and cause image distortion (charging effect). The charging effect was observed several times. Moving the plasticine or changing the view angle helped and good images

were obtained. The micrographs where taken using the scanning electron microscope at the department of biology at the University of Florence [52].

2.2.3 Observations and Results

Fig. 2.6 shows an electron micrograph from growth and nucleation side of a CVD diamond. This sample was produced by reference [33]. Diamond grains are visible on both sides and illustrate the polycrystalline morphology of CVD diamond. The growth side contains grains with a size up to 100 μm, while the nucleation side shows smaller grains of the order of 1 μm. The nucleation side has small gaps in between grains, while no gaps are observed on the growth side. Small reflecting contaminations, with a size smaller than 5 μm, appear on the growth side. They were only observed on this sample and could not be removed by cleaning. They may be remainders of gold from the electrical contact fabrication.

Fig. 2.7 shows the electron micrographs from the growth and the nucleation side of a CVD diamond sample produced by reference [34]. The growth side shows grains on the same scale as Fig. 2.6 with typical grain sizes up to 100 μm. The grains are striated compared to grains in Fig. 2.6 an observation which was made on CDS samples in general. The nucleation side of CDS-1 is shown on a ten micron scale. No grains can be observed but rather a curled structure on a ten micron scale.

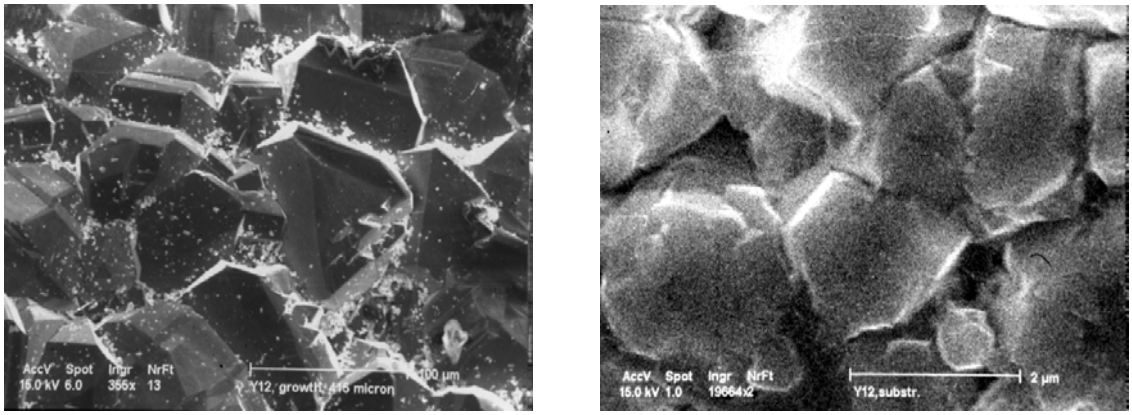

Figure 2.6: Electron micrographs from the growth side (left, scale 100 μm) and the nucleation side (right, scale 2 μm) of the CVD diamond sample TD1150-Y12. The sample was grown by reference [33].

The average grain size on the nucleation and growth side can be obtained from SEM images. The method used here was suggested by the American Society of Material Testing and described in reference [11]. One counts the number, N, of grains in the area, A, of the image. In case of gaps between grains one estimates the gap area, A', inside the area A. The *average grain size* is then given by

$$g^{\perp} = \sqrt{\frac{A - A'}{N}}. \tag{2.7}$$

Table 2.1 lists samples and their average grain size on the growth and nucleation side. The average grain size on the growth side ranges from 50 μm to 100 μm. The grain size on the nucleation side was measured on the sample Y12, with clearly visible grains. The grain size on the nucleation side of CDS samples could not be estimated because of the curly structure.

Fig. 2.8 shows the grain size from the growth side versus the thickness of the CDS samples. It can be seen that the grain size increases linearly in the measured thickness

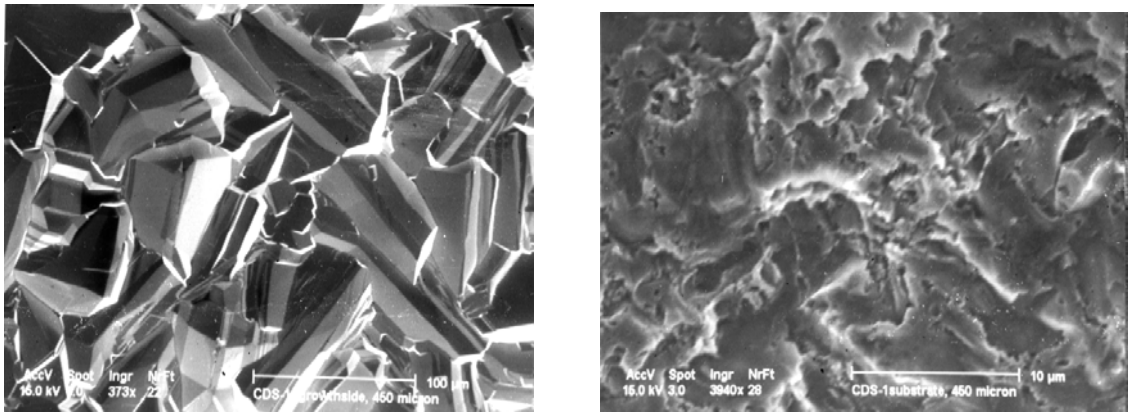

Figure 2.7: Electron micrograph from the growth side (left, scale 100 μm) and the nucleation side (right, scale 10 μm) of the CVD diamond sample CDS-1. This sample was grown by reference [34].

sample	thickness [μm]	$g^{\perp}_{\text{growth}}$ [μm]	$g^{\perp}_{\text{nucleation}}$ [μm]
CDS-1	450	49 ± 8	-
CDS-2	485	77 ± 8	-
CDS-7	593	98 ± 10	-
CDS-8	645	94 ± 10	-
CDS-9	608	88 ± 11	-
CDS-10	469	61 ± 7	-
TD1150-Y12	415	70 ± 8	1.4 ± 0.2

Table 2.1: Average grain-sizes, $g^{\perp}_{\text{growth}}$ and $g^{\perp}_{\text{nucleation}}$, on growth and nucleation side of CVD diamond samples measured by electron microscopy using the method explained by Eq. 2.7. The '-' means that no grain size could be measured.

interval from 450 μm to 645 μm for these samples. It was observed in the past that the grain size on the nucleation side is of the order of a few microns [11]. The SEM from the nucleation side of TD1150-Y12 confirms this observation. It is therefore reasonable to approximate the measured data by a function that intersects zero and the line fit to the data is forced to intersect 0. The linear fit (solid line) has a slope of 0.14. It has been shown on other samples that the grain size increases linearly with thickness [11]. The slope of the linear increase depends on the growth conditions as found by studying the slope for multiple growths. The number of measured data points here is too sparse in order to obtain information about multiple growths. The measured data is consistent with a linear increase of grain size for a single growth condition.

Fig. 2.9 shows a typical cross-section of a CVD diamond. The upper edge is the growth side of the diamond, the lower edge is close to the nucleation side. The columnar structure of diamond growth can be recognized. This cross section is free of voids.

2.2.4 Summary and Discussion

The increase of grain size from the nucleation side to the growth side was observed on CVD diamond samples from three other manufacturers as presented by S. Zhao in reference [11]. The increase of grain size from the nucleation side to the growth side seems to be a general property of diamond produced by chemical vapour deposition. In reference [11], the grain size on the nucleation side was observed to be between 1 μm to 3 μm with gaps of similar size in between grains. The nucleation side of sample Y12 agrees with this observa-

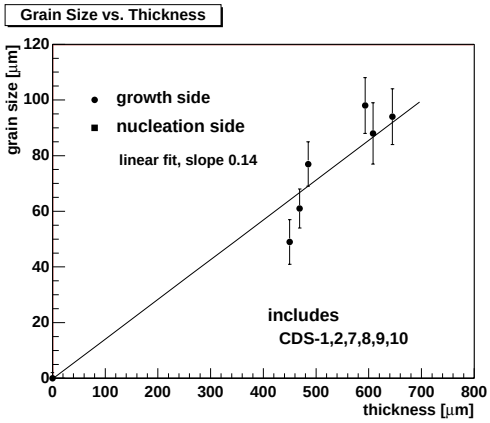

Figure 2.8: Grain-size as a function of the thickness. The measurement includes samples CDS-1,2,7,8,9,10.

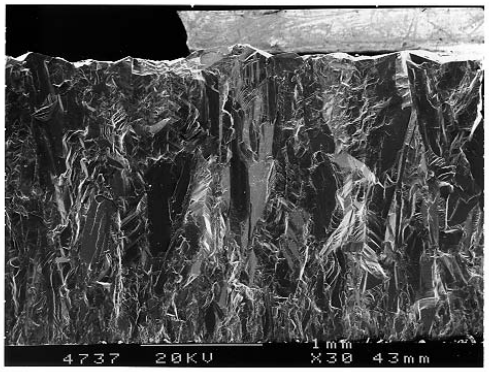

Figure 2.9: Typical cross-section of high quality CVD diamond optical material, (courtesy of De Beers Industrial Diamond Division (UK) Ltd) [53].

tion. The nucleation side of CDS samples shows no single grains. Their nucleation side may consist of grains with a size below the scale of the pictures taken on these samples. It also could be that the nucleation side contains a non-diamond structure or that the structure contains defects due to the surface of the substrate on which it was produced. The observation is plausible since different manufacturers initiate the nucleation on different substrates (for example tungsten, molybdenum or silicon) and use different growing techniques. The grain size on the growth side of these CDS samples is larger than on those samples in reference [11] which may reflect the progress made by the manufacturers.

The observation of gaps and curly non-diamond structures on the nucleation side suggests material removal (polishing or lapping) before electrical contacts are prepared. Gaps could cause charge loss and non-diamond regions on the nucleation side have different electrical properties than the bulk. As a result samples for diamond strip or pixel detectors were normally lapped on the nucleation side before metallization. Also the growth side was lapped for tracker preparation in order to obtain a smooth surface. Visual inspection (using a light microscope) showed normally very few remaining gaps on both sides after lapping.

2.3 X-Ray Diffraction

Crystals have a lattice structure with inter-atomic distances, ranging from several Angstroms to several tens of Angstroms. X-rays have typical wave lengths of inter-atomic distances and have been used to measure lattice orientations in CVD diamond samples. Orientations of lattice planes in polycrystalline CVD diamond samples (the texture) have been quantified. Other parameters like the lattice constant of diamond or the mass density were verified from the measurements.

2.3.1 The Principle of X-ray Diffraction

Fig. 2.10 shows two lattice planes a distance, d, apart with X-rays incident with wave vector, $\vec{k}$, and outgoing waves with wave vector, $\vec{k}'$. Incoming waves are elastically scattered

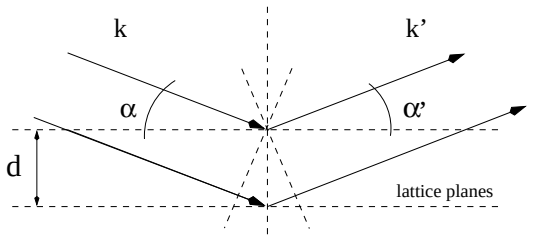

Figure 2.10: Principle of X-ray diffraction. An X-ray wave front is incident with wave vector $\vec{k}$ under the Bragg angle α onto two lattice planes. The lattice planes are a distance d apart. The incident wave is elastically deflected into the outgoing wave with wave vector $\vec{k}'$.

such that $|\vec{k}| = |\vec{k}'|$. The wavelength, λ, of the incident and outgoing waves is then $\lambda = 2\pi/|\vec{k}| \equiv 2\pi/|\vec{k}'|$. Constructive interference of elastically scattered waves is possible if the path length difference from all scatters is an integral number of the wavelength:

$$n\lambda = d\,\sin\alpha + d\,\sin\alpha'. \tag{2.8}$$

Using the condition of elastic scattering and constructive interference one derives the magnitude of the difference between the outgoing and the incoming wave vectors [2]

$$|\vec{k}' - \vec{k}| = \frac{2\,\pi\,n}{d\,\cos([\alpha' - \alpha]\,/2)}. \tag{2.9}$$

Under the experimental condition of $\alpha' = \alpha$ one obtains the *Laue condition* for X-ray diffraction

$$|\vec{k}' - \vec{k}| = \frac{2\,\pi\,n}{d}. \tag{2.10}$$

An alternative formulation, the *Bragg condition*, can be read from Eq. 2.8, again using the experimental condition $\alpha' = \alpha$:

$$\sin\alpha = \frac{n}{d}\cdot\frac{\lambda}{2}. \tag{2.11}$$

Using the definition $\vec{K} \stackrel{\text{def}}{=} \vec{k}' - \vec{k}$ one can generalize the Laue condition: for constructive interference the 'momentum transfer', $\vec{K}$, has to be equal to a reciprocal lattice vector, $\vec{G}$,

[2] The following relations are useful to proof Eq. 2.9: $\sin\left(\frac{\alpha'+\alpha}{2}\right) = \pm\sqrt{\frac{1-\cos(\alpha'+\alpha)}{2}}$ and $\sin\alpha + \sin\alpha' = 2\,\sin\left(\frac{\alpha+\alpha'}{2}\right)\,\cos\left(\frac{\alpha-\alpha'}{2}\right)$.

$$\vec{K} = \vec{G} \equiv n_i \, \vec{b}_i \qquad \text{with} \qquad n_i = (h,k,l)_i \in N. \tag{2.12}$$

The reciprocal lattice vector is defined in Eq. 2.5 with Miller indices, n_i and the basis vectors, $\vec{b}_i$, of the Brillouin zone [Eq. 2.4]. The general Laue condition, Eq. 2.12, can be formed into the general Bragg condition

$$\sin\alpha = \frac{\sqrt{h^2+k^2+l^2}}{a} \cdot \frac{\lambda}{2}. \tag{2.13}$$

The number of combinations for Miller indices is finite since the sine on the left side is bounded by one. The intensity, I, of scattered X-rays is proportional to the square of the scattering amplitude from the primitive cell

$$I(\vec{K}) \propto |S(\vec{K})|^2. \tag{2.14}$$

The scattering amplitude, $S(\vec{K})$, is called the *geometrical structure factor*. It is the sum over amplitudes from the scatterers in the primitive cell

$$S = \sum_{j:\ d_j \text{ in } fcc} S_{\rm d}\, e^{+i\,\vec{K}\cdot\vec{d}_j} = S_{\rm d} \cdot S_{fcc}. \tag{2.15}$$

The primitive cell of the *fcc* contains 8 atoms, at locations which were shown in Fig. 2.2. These atoms are the centers for scattering and contribute to the scattering amplitude of the *fcc* lattice. The primitive cell of the *fcc* has one carbon atom inside which gives a structure to the primitive cell. This structure is described by the structure factor, $S_{\rm d}$, in the sum of Eq. 2.15. If a primitive cell contains different types of atoms one would require an atomic form factor. Such factor is not necessary in the mono-atomic diamond lattice. The scattering amplitude can be calculated for the diamond lattice using Eq. 2.4, Eq. 2.12 and the locations of scatterers from Eq. 2.3. One finds

$$\begin{aligned} S_{fcc} &= \sum_{j:\ d_j \text{ in } fcc} e^{+i\,\vec{K}\cdot\vec{d}_j} \\ &= 2 + e^{i\pi(h+k)} + e^{i\pi(h+l)} + e^{i\pi(k+l)} + \left(e^{i\pi h} + e^{i\pi k} + e^{i\pi l}\right) \cdot \left(e^{i\pi(h+k+l)}\right) \end{aligned} \tag{2.16}$$

and

$$S_{\rm d} = \sum_{j:\ d_j \text{ in diamond}} e^{+i\,\vec{K}\cdot\vec{d}_j} = 1 + e^{i\frac{\pi}{2}(h+k+l)}. \tag{2.17}$$

The peak intensities for the possible combinations of Miller indices can then be calculated using Eq. 2.14. Fig. 2.11 shows the result of this calculation: it gives the intensities as a function of $2\,\alpha$, where α is obtained from Eq. 2.13 for the wave length $\lambda = 1.5406$ Å and the lattice constant $a = 3.5668$ Å. The wave length is the K_{α_1} transition wave length for copper as it will be used in the measurement below. The open circles give the calculated intensities for the *fcc* structure only. The solid circles are the calculated intensities for diamond. The figure contains all combinations of Miller indices which are possible at this wave length for diamond. Only a few combinations show constructive diffraction: diamond peaks appear at (111), (220), (311), (400), and (331). They exist already for the *fcc* structure. All other combinations are suppressed in diamond. Some of them are already suppressed by the *fcc* structure (like (100), (110), (210), ...). Others are still present for a *fcc* structure but are suppressed by the additional atom inside the primitive diamond cell ((200), (222) and (420)).

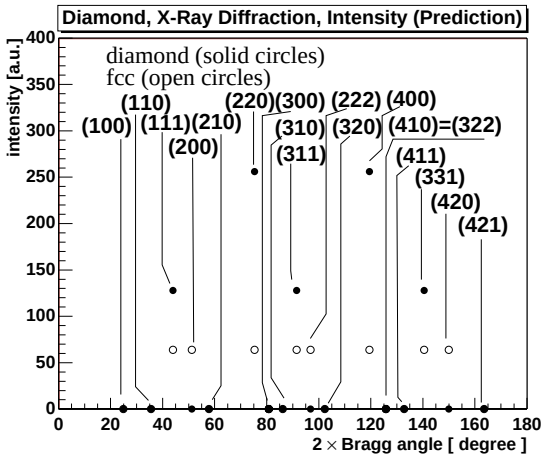

Figure 2.11: Calculated intensities and angles for Bragg peaks in the monoatomic diamond lattice (solid circles) and for a face centered cubic lattice, *fcc* (open circles). The calculation was done with the lattice constant $a = 3.5668$ Å and the K_{α_1} X-ray wave length of copper. The Miller indices (*hkl*) are given for each angle. The Bragg angles and intensities were calculated using Eq. 2.13 and Eq. 2.14.

It is important to note that the scattering amplitude is not the only source of $\vec{K}$ dependence to the intensity. Further dependence comes from ordinary angular dependence of any electromagnetic scattering and also on angular dependent absorption of X-rays in the diamond. Therefore the structure factor alone can not predict the absolute intensity in a Bragg peak. However, it can serve as a selection rule for diffraction angles. At the calculated angle with non-vanishing intensity one therefore expects to observe peaks in the X-ray diffraction measurement. Where the calculation predicts zero intensity one can not measure a peak.

Table 2.2 lists the lattice orientations and the corresponding Bragg angles from diamond powder taken from reference [54]. The diamond powder contains small grains (of the order of 10 μm in diameter) in a randomly distributed orientation. One therefore expects to see diffraction at all angles which are allowed by the selection rule [Eq. 2.15]. A comparison between the calculated Bragg angles in Fig. 2.11 and the angles in the table verifies that the given selection rule and the calculated angles are correct. The table also lists the diffraction intensities, I_{hkl}^{powder}, for the peaks. The intensities are different for different peaks although the powder can be assumed to contain equal amounts from all orientations. The peaks are not equal since the acceptance of the diffractometer is different for different angles.

(*hkl*)		(111)	(220)	(311)	(400)	(331)
$2\alpha_1$	[°]	43.92	75.30	91.50	119.53	140.60
I_{hkl}^{powder}	[a.u.]	100	25	16	8	16

Table 2.2: The intensities, I_{hkl}^{powder}, and Bragg angles, $2\alpha_1$, of X-ray diffraction peaks from diamond powder. The angles are given for the incident wave length of 1.5405 Å (K_{α_1} transition in copper). The values are taken from the measurement in reference [54].

2.3.2 Experimental Method

An X-ray diffractometer contains an electron tube that accelerates electrons towards an anode. The electron beam strikes the anode and ionizes atoms of the anode material and a vacant electron state remains in the atomic 'shell'. The probability for ionization of the innermost atomic shell, the K-shell, is higher compared to outer shells. The vacant electron state in the K-shell will be re-occupied from an outer shell electron, this transition causes X-

ray emission. The X-ray energy is the difference between electron binding energies before and after transition. The shell energies are split due to the angular momentum of electrons in the electric field of the nucleus. The L shell generally splits into three energy levels: $L_{\mathrm{I}}, L_{\mathrm{II}}, L_{\mathrm{III}}$. Two transitions with photon emission are possible between the L- and the K-shell: K_{α_1} between K and L_{III} and K_{α_2} between K and L_{II}. In copper, the K_{α_1}-transition emits X-rays with a wave length of $\lambda_{\alpha_1} = 1.540562$ Å. The K_{α_2}-transition emits a wave length of $\lambda_{\alpha_2} = 1.544390$ Å.

Fig. 2.12 shows a schematic of the setup for the X-ray diffraction measurement. The setup contained an X-ray source, a goniometer and an X-ray scintillation counter for measuring the intensity of scattered X-rays. X-rays were produced by an electron beam from a fixed copper (Cu) anode with the wave lengths, λ_{α_1} and λ_{α_2}, as given above. The electron beam had an energy of 40 keV and an electron current of 20 mA. The goniometer was mounted next to the X-ray tube. It contained the sample holder that could be turned by a motor around one axis with respect to the incident X-rays. The angle between the sample holder and the axis of incident X-rays is the Bragg angle, α. The X-ray detector rotated around the same axis as the sample holder. The detector was rotated with twice the angular velocity of the sample holder such that its angle was always 2α with respect to the incident X-rays. The angle reproducibility in 2α was $\pm 0.001°$ over the entire angular range, as given by the manufacturer of the diffractometer. A continuous angle scan covered the 2α range from 17.5° to 72.5°. The measurements were carried out using the X-ray diffraction setup at the department of mechanics at the University of Florence [55].

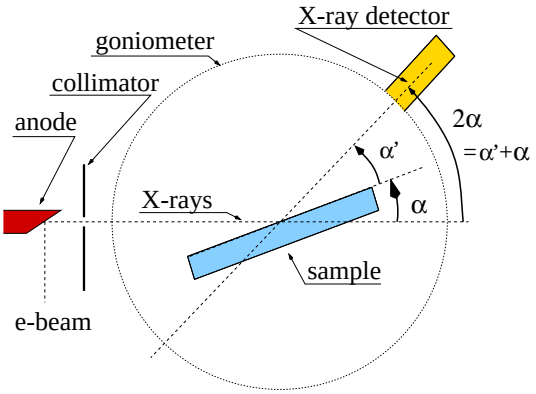

Figure 2.12: Schematic of the diffractometer setup. A sample was mounted in the center inside the goniometer (not drawn to scale). The sample was turned slowly by a motor such that its surface was always in the turning axis. The intensity of scattered X-rays was measured by an X-ray detector. The experimental condition forced the observation under the angle $\alpha' = \alpha$.

The calibration of the diffractometer was verified using a silicon pellet that was delivered by the manufacturer. The silicon pellet consisted of silicon grains. The Bragg peak position in silicon was calculated, as described above for diamond, using the lattice constant $a_{\mathrm{Si}} = 5.43102$ Å and was compared with the measurement of Bragg angles. Fig. 2.13 shows the intensity from a calibration angle scan with the silicon pellet in the diffractometer. The peak with the highest intensity is at (111) and is normalized to 100 arbitrary units. The exact peak positions were determined from magnifications of the peaks as shown for the (331) orientation in Fig. 2.14. Each peak is in fact a doublet since the X-rays contain both wave lengths from the K_{α_1} and the K_{α_2} transitions. The intensities of each peak are Gaussian distributed. The exact maxima were found from a *Gaussian fit to the measured intensity*

$$\hat{I}(2\alpha) = \hat{I}_0 + \hat{I}_1\, e^{(2\alpha - 2\,\alpha_1)^2/\left(2\sigma_1^2\right)} + \hat{I}_2\, e^{(2\alpha - 2\,\alpha_2)^2/\left(2\sigma_2^2\right)} \tag{2.18}$$

where $\hat{I}_0$ is the background intensity and $\hat{I}_1$, $\hat{I}_2$ are the intensities at the peaks. Each orientation peaks at the Bragg angles $2\alpha_1$ and $2\alpha_2$. The width of each peak is given by the standard deviations σ_1 and σ_2. The widths of the (331) peak in silicon [Fig. 2.14] are $\sigma_1 = 0.048\,°$ and

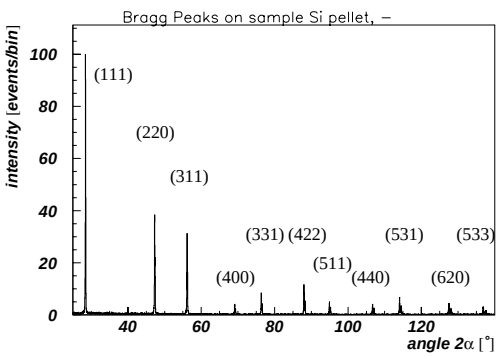

Figure 2.13: Intensities of X-ray diffraction peaks from a silicon pellet versus the angle 2α. The orientation of planes are characterized by their Miller indices (hkl). The silicon pellet was provided by the manufacturer of the diffractometer as a standard and was used to verify the correct calibration of the setup.

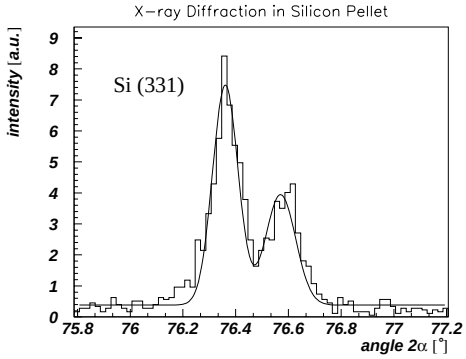

Figure 2.14: Measured Bragg peak of the (331) orientation in silicon. The peak is a doublet since the X-rays consist of two wave lengths from K_{α_1} and K_{α_1} transitions. The measured data is fitted with the sum of two Gaussian functions.

$\sigma_2 = 0.057\,^\circ$. The widths determine the *error of the measured Bragg angles*

$$\sqrt{\left\langle (2\alpha_i)^2 \right\rangle} = \sqrt{\frac{\sigma_i}{\sqrt{2\pi}\hat{I}_i}} \quad ; \quad i = 1, 2. \tag{2.19}$$

The intensity, $\hat{I}$, as measured in the diffractometer is in fact a spectral intensity

$$\frac{\mathrm{d}I}{\mathrm{d}(2\alpha)}(2\alpha) = \hat{I}(2\alpha). \tag{2.20}$$

Integration of the spectral intensity gives the intensity of X-rays scattered by grains with the lattice orientation (hkl)

$$I_{hkl} = \int_{2\alpha_{\mathrm{lower}}}^{2\alpha_{\mathrm{upper}}} \hat{I}(2\alpha)\,\mathrm{d}(2\alpha). \tag{2.21}$$

The limits $2\alpha_{\mathrm{lower}} \approx 2\alpha_1 - 3\sigma_1$ and $2\alpha_{\mathrm{upper}} \approx 2\alpha_2 + 3\sigma_2$ were used for measuring I_{hkl}. Table 2.3 gives the result of the calibration and compares the measured Bragg angles and the intensities with the values given by the manufacturer. The calibrated angles agree within the errors with the angles given by the manufacturer. Also the measured intensities, I_{hkl}, agree within 10 % with the values given by the manufacturer.

The CVD diamond samples were mounted like silicon in the sample holder. They were aligned in plasticine with their surface parallel to the sample holder and in the turning axis. The fixation with plasticine insured that the surface under study was in the turning axis even though the samples had different thicknesses.

2.3.3 Results: Orientations of Lattice Planes

Fig. 2.15 shows X-ray diffraction peaks from the growth and nucleation side of the CVD diamond sample CDS-7. On the nucleation side four diamond peaks are visible: (111), (220), (311) and (331). The angles were predicted from Fig. 2.11. The relative intensities from the nucleation side are close to those for diamond powder [Table 2.2]. The (400) orientation

	from manufacturer		measured here	
(hkl)	$2\alpha_1$ [°]	I_{hkl} [a.u.]	$\left(2\alpha_1 \pm \sqrt{\left\langle (2\alpha_i)^2 \right\rangle}\right)$ [°]	$I_{hkl} \pm 10\%$ [a.u.]
(111)	28.443	100.0	28.445 ± 0.004	100.0 ± 10
(220)	47.304	55.0	47.292 ± 0.005	54.7 ± 5
(311)	56.122	39.4	56.126 ± 0.005	40.2 ± 4
(400)	69.132	7.1	69.114 ± 0.02	8.4 ± 1
(331)	76.380	12.5	76.355 ± 0.02	13.5 ± 1

Table 2.3: Calibration: Bragg angles, $2\alpha_1$, from the silicon powder pellet using the Cu K_{α_1} X-ray wave length and intensities, I_{hkl}, in the Bragg peaks. The values in the left column were given by the manufacturer of the diffractometer. The values in the right column are the result of the calibration measurement.

is not observed. The peak below 40 ° is due to diffraction from the gold contact. Low intensity gold diffraction peaks were observed at various Bragg angles since the diamond samples had gold contacts on both sides. The growth side has one principal peak for the (220) orientation. The other diffraction peaks are negligibly small and nearly invisible on this scale. The presence of only one peak means that the corresponding crystal orientation dominates over other orientations. The dominance of one orientation is called *texture*. The change from the powder-like orientations on the nucleation side to the (220) orientation on the growth side indicates a prefered direction of growth for this sample and a strong texture.

sample name	side	measured I_{hkl} ±10%				
		(111)	(220)	(311)	(400)	(331)
Di-powder	-	100	25.0	16.0	8.0	16.0
CDS-1	g	100	7.3	18.6	1.6	23.8
	n	100	19.7	11.7	1.1	12.5
CDS-2	g	100	254.0	9.4	15.7	254.0
	n	100	178.5	11.2	4.0	68.6
CDS-7	g	100	1244.5	24.2	5.2	37.9
	n	100	32.2	7.7	0.6	11.9
CDS-8	g	100	7000.0	25.3	13.0	266.6
	n	100	184.9	10.5	2.8	113.1
CDS-10	g	100	742.5	27.6	4.8	147.9
	n	100	82.0	8.9	0.8	18.6
TD1150-Y12	g	100	3.9	12.1	1.4	5.1
	n	100	4.2	9.0	1.7	9.5

Table 2.4: Measured X-ray intensities I_{hkl} at the Bragg peak in diamond powder and CVD diamond samples. The intensities are normalized to the intensity in the (111) orientation. The lattice orientations are characterized by their Miller indizes (hkl).

Table 2.4 gives the intensities, I_{hkl}, of Bragg peaks from all samples measured. The intensity for the (111) orientation is normalized to be 100 arbitrary units. It is not yet possible to extract the abundance of orientations from this table since the intensities given are not corrected for the acceptance of the diffractometer. By normalizing to the abundance

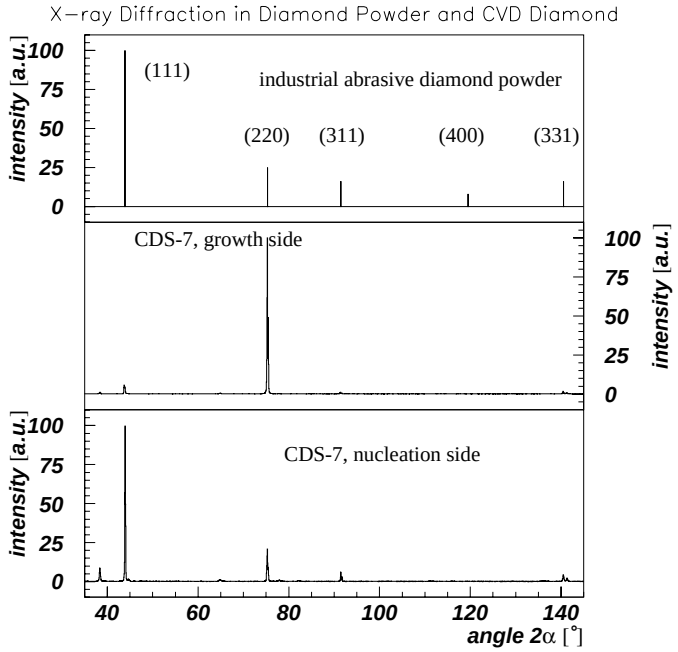

Figure 2.15: Measured X-ray diffraction peaks from the growth (middle) and nucleation side (bottom) of the CVD diamond sample CDS-7. The peaks from diamond powder (top), as taken from reference [54], are given for comparison.

of orientations in the diamond powder one obtains the *percentage of oriented grains* [56]

$$p_{hkl} = \frac{I_{hkl}^{\mathrm{CVD}}}{I_{\mathrm{total}} I_{hkl}^{\mathrm{powder}}} \qquad \text{with} \qquad I_{\mathrm{total}} = \sum_{hkl} I_{hkl}^{\mathrm{CVD}} / I_{hkl}^{\mathrm{powder}}, \tag{2.22}$$

where I_{hkl}^{CVD} is the intensity in the Bragg peak of the CVD diamond sample at (hkl) and $I_{hkl}^{\mathrm{powder}}$ the intensity from the diamond powder in Table 2.2. The summation for the total intensity is performed over the five orientations with Miller indices (111), (220), (311), (400) and (331). The intensity for the orientation (400) is included here since a Bragg peak is expected for this orientation. However it does not significantly contribute since the intensity of the (400) peak was measured to be relatively small. Table 2.5 gives the percentage of oriented grains. All samples are textured on the growth side. On the nulceation side of CDS-1 and CDS-7 the relative intensities are similar to the powder diffraction peaks which means no texture. The samples CDS-2 and CDS-8 nucleate mainly with the orientation (220). The samples CDS-1 and Y12 are textured but they do not change the direction of growth from the nulceation to the growth side.

2.3.4 Results: Lattice Constants of CVD Diamond

Fig. 2.16 shows the Bragg peaks for the (111) and (220) planes from the nucleation and growth side of CDS-7. As in silicon the Bragg peaks of the CVD diamond samples are split in two Gaussian distributions as described by Eq. 2.18. The peak from the (111) growth side is shifted with respect to the nucleation side. The cause of this shift requires further investigation. Alternatively one could fit for three peaks instead of two. Two peaks can be seen on the growth side and nucleation side at the same angles. The third peak appears at

sample name	side	measured p_{hkl} [%] ±10%				
		(111)	(220)	(311)	(400)	(331)
Di-powder	-	20	20	20	20	20
CDS-1	g	24	7	28	5	36
	n	29	23	21	4	23
CDS-2	g	3	34	2	7	54
	n	7	52	5	4	32
CDS-7	g	2	90	3	1	4
	n	28	36	13	2	21
CDS-8	g	3	93	0.5	0.5	6
	n	6	45	4	2	43
CDS-10	g	2	70	4	1	22
	n	16	54	9	2	19
TD1150-Y12	g	42	7	31	7	13
	n	40	6	22	8	23

Table 2.5: Percentage, p_{hkl}, of oriented grains in diamond powder and CVD diamond samples.

43.7° and 75.1° which is 0.2° smaller than the K_{α_1} peak. The assumption of three peaks removes the difficulty of explaining the peak shift but raises the question of the cause of the third peak. The data measured here was fitted with two peaks only where the positions were free parameters of the fit (not fixed). The fit function allowed the extraction of the peak positions at $2\alpha_1$ and at $2\alpha_2$ and the lattice constant using Eq. 2.13. The separation between the two peaks was normally larger for the (220) orientation compared to the (111) orientation which indicates a higher angular resolution for the measurment at the (220) orientation. The measurement of the lattice constant is therefore preferrably done using the (220) orientation. The measurements using (111) were also done for completeness but one has to consider their possible systematic error due to a shift in the peak position or due to a poor fit for the case of three peaks.

Table 2.6 summarizes the measured lattice constants. The statistical error of the lattice constant measurement is obtained from Eq. 2.13 as the derivative of a with respect to 2α

$$\sigma_{a_i} \equiv \frac{\partial a}{2\,\partial\alpha}\sqrt{\left\langle (2\alpha_i)^2 \right\rangle} = \frac{1}{2\,\tan\alpha_i}\sqrt{\left\langle (2\alpha_i)^2 \right\rangle}. \tag{2.23}$$

The measurement on the growth side of CDS-8 has the smallest error. The measured lattice constant is (3.56604 ± 0.0006) Å in good agreement with the value of 3.5668 Å from a natural sample [10].

The Bragg peaks have the width σ_1 and σ_2. The width is due to instrumental broadening, finite grain size and structural defects [11]. The peak widths in the CVD diamond samples as obtained from the average of σ_1 and σ_2 are listed in Table 2.6 as well. The width is, within variation, equal to the width obtained from the silicon pellet. It is likely that the width is dominated by the instrumental broadening.

The mass density of diamond can be calculated from the measured lattice constant. With $n = 8$ atoms per unit cell, the relative atomic mass of carbon, $m_{\bar{\mathrm{C}}} = 12.011$ u, and the measured lattice constant, $a = 3.56604$ Å, one obtains the mass density of diamond

$$\varrho = \frac{n\, m_{\bar{\mathrm{C}}}}{a^3} = (3.518 \pm 0.002)\ \mathrm{g/cm^3}. \tag{2.24}$$

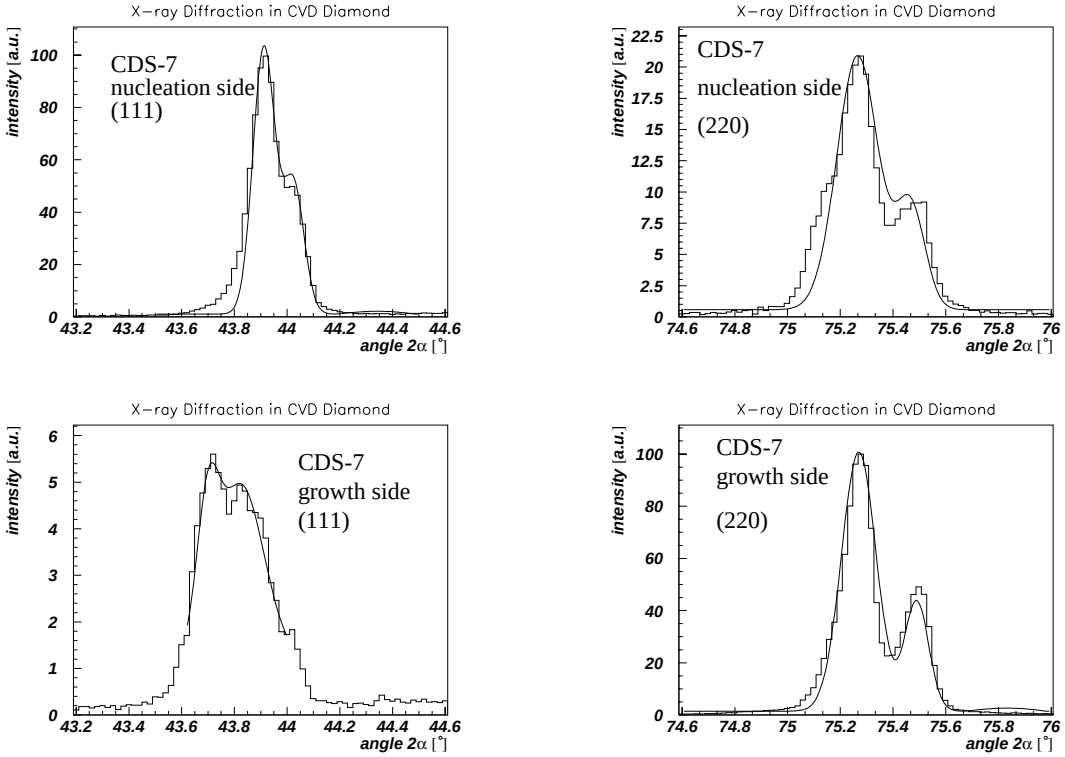

Figure 2.16: X-ray diffraction peaks of the (111) and (220) lattice plane from the growth and from the nucleation side of CVD diamond sample (CDS-7).

The measured mass density agrees with the density of 3.515 g/cm^3 as given in reference [10].

2.3.5 Summary and Discussion

The crystal structure of CVD diamond samples has been studied using X-ray diffraction. The Bragg angles with non-vanishing Bragg peaks were calculated under the assumption of the position of atoms in the diamond cubic cell [Fig. 2.2]. Diffraction peaks were found at the expected Bragg angles. No diffraction peak was seen for the plane orientation (400). The diffraction on a natural diamond type IIa was measured for comparison. The natural diamond used was cut with the goal to obtain a lattice orientation of (400). No diffraction peak was observed from the natural diamond. The missing (400) orientation is therefore not specific to the CVD diamonds measured here. The measurement of the (400) orientation may require further tests. Grains on the nucleation side are oriented differently from the equal distribution of oriented grains in a powder. The preferred orientation on the nucleation side on these samples was (111) or (220). As the diamond grows a certain orientation may decrease in favor of another orientation. The growth side shows typically one single peak for the (111) or (220) lattice planes. The diamond growth side is highly oriented and textured.

The CVD diamond lattice constant was measured to be (3.5660 ± 0.0006) Å which gives the mass density of (3.518 ± 0.002) g/cm^3. The mass density is of relevance for charged particle detection since the energy loss of particles in matter is proportional to the mass density.

The effect of X-ray absorption in diamond was not discussed here. However, it would be important to confirm that X-ray diffraction only probes the diamond surface up to a

		(111) plane		(220) plane	
sample	side	lattice constant (a $\pm\sigma_a$) [Å]	width σ [°]	lattice constant (a $\pm\sigma_a$) [Å]	width σ [°]
CDS-1	g	3.57575±0.005	0.0955	3.57275±0.007	0.0522
	n	3.56846±0.002	0.0448	3.56622±0.015	0.0566
CDS-2	g	3.57515±0.024	0.0830	3.56994±0.003	0.0830
	n	3.56729±0.007	0.0425	3.56766±0.002	0.0572
CDS-7	g	3.57534±0.010	0.0718	3.56790±0.0009	0.0545
	n	3.56842±0.002	0.0409	3.56850±0.003	0.0667
CDS-8	g	no peak		3.56604±0.0006	0.0518
	n	3.56475±0.005	0.0432	3.56809±0.002	0.0697
CDS-10	g	3.60262±0.063	0.8	3.56800±0.001	0.0551
	n	3.56919±0.003	0.0416	3.57024±0.003	0.0838
TD1150-Y12	g	3.57257±0.003	0.0804	3.57408±0.025	0.1901
	n	3.57590±0.002	0.0305	3.57083±0.011	0.0794

Table 2.6: Measured lattice contants and peak width from the growth (g) and nucleation (n) side of CVD diamond samples. The lattice constants were calculated from the (111) or from the (220) diffraction peak. The peak width σ is the average of the widths from the K_{α_1} and the K_{α_2} peaks.

several micrometers depth in order to draw conclusions on the texture on the surface. It was shown in reference [11] that typical X-ray attenuation lengths in diamond range from 4 μm to 33 μm depending on the diffraction peak. Therefore X-rays diffraction indeed only probes the diamond surface and does not give bulk properties.

2.4 Raman Spectroscopy

Elastic Rayleigh scattering of light from molecules or from solids leaves the frequency of the scattered outgoing light unchanged compared to the incident light. Besides the effect of elastic scattering, inelastic Raman scattering occurs which changes the frequency of the scattered light compared to the incident light. The probability for Raman scattering is typically 4 orders of magnitude smaller than for Rayleigh scattering. The energy difference between the incident and the scattered light allows phonon creation or annihilation. From the change of the energy of the scattered light the energy of the phonon can be measured. The phonon energy is characteristic for the diamond or non-diamond structures. The lifetime of the phonon is limited by stress in the crystal where the stress is determined by impurities, defects and dislocations in the lattice. The later determine the crystal material quality. Raman spectroscopy is a method to quantify the material quality of CVD diamond by measuring the phonon lifetime. The material quality of several diamond samples has been studied using Raman spectroscopy by measuring the phonon lifetime. Results are reported below.

2.4.1 Principle of Raman Spectroscopy

Atoms in a crystal vibrate in an oscillating motion about the central atomic lattice site. The motions of many atoms in a crystal are coupled. The collective motion is a vibration mode of the lattice and can be described as a plane wave with frequency, $\omega/2\pi$, and momentum $\hbar\vec{q}$. Its energy, $\hbar\omega(\vec{q})$, is quantized. The lattice vibration mode is called a *phonon*. Electrons or photons interact with phonons and create or annihilate phonons. As an example, the finite velocity of charge carriers in electrical conduction is explained by electron-phonon scattering and the subsequent energy loss of electrons after a scattering event. If a crystal is illuminated with light of energy, E, phonons can be created or annihilated as well under the condition of energy conservation:

$$E' - E = \pm\hbar\omega(\vec{q}) \tag{2.25}$$

where E and E' are the energies of the photon before and after scattering. The positive sign describes the case of phonon annihilation, the negative sign the case of phonon creation. Fig. 2.17 illustrates the three types of photon scattering from a solid. The first is the elastic Rayleigh scattering with $E' = E$. The second type illustrates the creation of a phonon under partial or full energy loss of the photon. Energy loss means that the frequency of the scattered light is smaller then the frequency of the incident light. This type of scattering is called the Stokes Raman scattering where Raman spectroscopy shows a spectral line at the energy difference between the incident and the scattered light. This spectral line is called the Stokes Raman line. The third type is the annihilation of the phonon under energy gain of the photon, corresponding to a frequency gain, that is called the anti-Stokes Raman scattering. The corresponding spectral line at the energy difference is called the anti-Stokes Raman line. The difference, in energy, wave length or wave number, between the incident and the outgoing light is called the Raman shift.

In addition to the energy conservation, momentum has to be conserved. Momentum conservation is given in generalization of Eq. 2.12 as

$$\hbar\vec{K} = \hbar\vec{G} \pm \hbar\vec{q}. \tag{2.26}$$

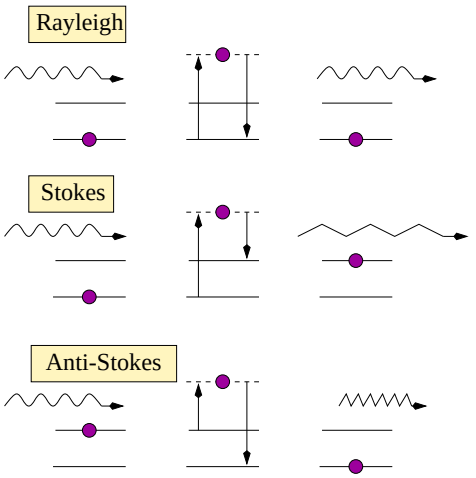

Figure 2.17: Three types of photon scattering are shown: Rayleigh scattering and Raman scattering (Stokes and anti-Stokes). A photon is incident from the left and excites a phonon from a phonon-state to a virtual phonon-state. Depending on the phonon decay channel the outgoing photon has the same, higher or lower frequency (energy). The photon energy gain or loss is called the Raman shift [51].

where $\vec{K} = \vec{k}' - \vec{k}$ and $\vec{G} = n_i \vec{b}_i$ a vector of the reciprocal lattice in the conventions of Sec. 2.3. The positive sign corresponds again to the phonon annihilation and the negative sign to phonon creation.

As an example we consider the following: a typical photon energy of blue light is $2\pi\hbar c/(400\text{ nm}) \approx \pi$ eV that corresponds to a photon momentum of π eV$/c$. A typical reciprocal lattice vector has the length corresponding to the size of the Brillouin zone that gives $\hbar|\vec{G}| \approx 2\pi\hbar/a \approx 3.5$ keV$/c$ which is 3 orders of magnitude larger than the photon momentum or any change of the photon momentum. Therefore the photon momentum transfer can be neglected in Eq. 2.26 and on obtains the *phonon selection rule*

$$\hbar\vec{G} \approx \mp\hbar\vec{q}, \tag{2.27}$$

that means that phonon creation or annihilation is only possible for phonon wavelengths which match a reciprocal lattice vector.

An estimate of the phonon energy can be found from the phonon velocity, $\vec{v}$

$$\vec{v} \equiv \frac{\partial\omega}{\partial\vec{q}} \quad \overset{\text{Eq. 2.27}}{\Longrightarrow} \quad \hbar\omega \approx \hbar|\vec{G}||\vec{v}|. \tag{2.28}$$

The approximation to the right assumes that $\vec{v}$ does not depend too strongly on $\vec{q}$. The phonon velocity is actually the velocity of sound which depends on the direction of the phonon propagation in the crystal. The phonon velocity is of the order of 10^6 cm/s in natural diamond [40]. Taking this value one estimates a phonon energy of $\hbar\omega \approx 0.13$ eV. Eq. 2.25 allows one to calculate the frequency shift for Raman photon scattering from diamond that is usually expressed as a wave length or wave number. One obtains the Raman shift for diamond to be $2\pi c\hbar/\hbar\omega = ac/|\vec{v}| \approx 10$ μm corresponding to a wave number of ≈ 1000/cm.

The phonon probability amplitude, $p(t)$, decreases exponentially in time. The spectral probability amplitude, $\tilde{p}(w)$, is given as the Fourier transform of the time dependent probability amplitude

$$p(t) \propto e^{-t/\tau} \quad \Longrightarrow \quad \tilde{p}(w) \propto \int_0^\infty e^{t/\tau + iwt}\,\mathrm{d}t. \tag{2.29}$$

The intensity of scattered light is therefore

$$I \propto |\tilde{p}(w)|^2 \propto \frac{1}{\tau^{-2} + w^2} \quad \text{with} \quad w = E' - E \mp \hbar\omega. \tag{2.30}$$

Using the definition $\Gamma \stackrel{\text{def}}{=} 2\hbar/\tau$ one obtains the intensity of the scattered light as a function of the phonon energy

$$I(\hbar\omega) \propto \frac{1}{\Gamma^2/4 + (E' - E \mp \hbar\omega)^2}. \tag{2.31}$$

The intensity has the shape of a Lorentz resonance curve that peaks at the phonon energy $\pm\hbar\omega = E' - E$. The intensity curve has a full width at half maximum (FWHM), Γ, that is explained by the phonon lifetime: a narrow intensity curve indicates a longer lifetime than a wide curve[3]. The phonon lifetime is naturally limited by phonon scattering. The width of the intensity can be understood from the various scattering processes, k, which contribute each with their specific width, Γ_k, such that the measured *width of the Raman line* becomes

$$\Gamma = \sum_k \Gamma_k = 2\hbar \sum_k \frac{1}{\tau_k}. \tag{2.32}$$

Possible processes which determine the Raman line width are impurities such as non-diamond carbon compositions, graphite or amorphous carbon, structural defects, lattice distortions, finite grain sizes, stress in the lattice and also chemical impurities.

In analogy to a resonance circuit one defines the *material quality of the crystal*

$$Q \stackrel{\text{def}}{=} \frac{E' - E}{\Gamma} = \frac{\omega\tau}{2}. \tag{2.33}$$

The material quality is proportional to the phonon energy and more importantly proportional to the phonon lifetime. For a given crystal lattice structure the phonon energy is fixed. Hence the material quality depends on the lifetime only. The phonon lifetime is limited by stress in the lattice where the stress is caused by impurities, defects and dislocations.

On pure crystalline diamonds a Raman peak can be measured which is centered around 1332 cm^{-1} with FWHM typically between (2.5 to 3.2) cm^{-1} depending on the material quality of the crystal [14]. Between (1400 to 1600) cm^{-1} CVD diamond broad Raman structures have been reported in addition to the diamond Raman peak. This is attributed to double- or triple bonded carbon [14].

The Raman line width and crystal material quality have been measured from the intensity of the scattered light from CVD diamond and were compared to that of natural diamond in order to verify the material quality of our diamond samples for detector applications.

2.4.2 Experimental Method

The measurements where carried out in one of the Raman laboratories at LENS in Florence [58]. A micro-Raman setup was used which allows beside the 'normal' Raman measurements to study the position resolved Raman response. The micro-Raman setup contained three principal components: a light source, a microscope and a spectrometer. Fig. 2.18 shows the schematic of the micro-Raman setup that was used to measure the Raman line on diamond samples. The light source was a monochromatic 5 Watt argon laser. An argon laser emits a green laser light with a wave length of $\lambda_{\text{Ar}} = 514.5$ nm. A narrow, monochromatic light from a laser is preferred compared to a wide-band light source since the wave number of the Raman line can lie relatively close to the wave number of the incident light. The laser light was guided via lenses and a mirror onto the diamond sample. The laser beam was focused such that the illuminated region was below 1 mm in diameter. The

[3] Eq. 2.31 assumes a constant phonon dispersion curve. Otherwise it requires integration over all phonon momenta, $\vec{q}$, in the Brillouin zone as explained in reference [57].

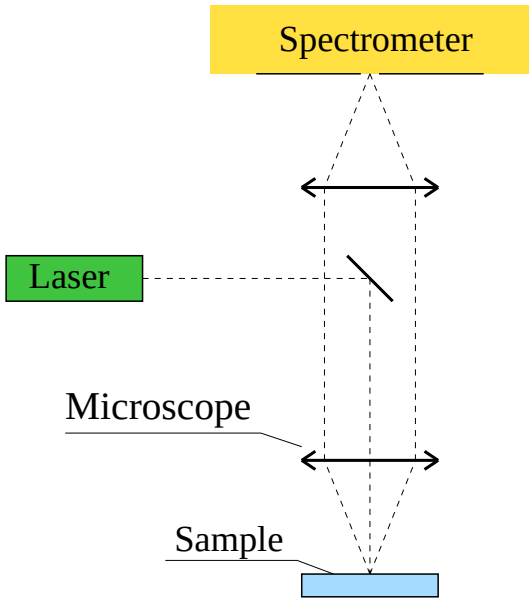

Figure 2.18: Schematic of the Raman spectrometer for this measurement. Monochromatic laser light is directed onto the surface of the sample. The scattered light is focused into a spectrometer.

total laser power onto the sample was about 50 mW. The illuminated spot could be observed through the microscope with a typical magnification of 50 and a spatial resolution of 0.5 μm. The scattered light was deflected through the microscope into a grating spectrometer. The grating inside the spectrometer could turn and gave a wave number resolution of 0.15/cm. The spectrum could be measured either by a scintillator or by a liquid nitrogen cooled CCD-camera.

The calibration of the spectrometer was performed using a mercury (Hg) lamp. The Hg-lamp emits light from which two emission lines are at $\lambda_{\mathrm{Hg},1} = 546.07348$ nm and at $\lambda_{\mathrm{Hg},2} = 576.95982$ nm. The expected difference in wave numbers relative to the argon laser line is therefore $\lambda_{\mathrm{Ar}}^{-1} - \lambda_{\mathrm{Hg},1}^{-1} = 1123.789$/cm and $\lambda_{\mathrm{Ar}}^{-1} - \lambda_{\mathrm{Hg},2}^{-1} = 2104.116$/cm. The spectrometer was adjusted to match these shifts under illumination from the Hg-lamp. After calibration, the spectrometer measured the line shift between argon and mercury at 1124.2/cm and 2104.5/cm which indicates a systematic deviation of 0.4/cm towards higher wave numbers. The aperture at the spectrometer entrance determined the spectral resolution: it was adjusted to give a FWHM of 0.5/cm for both Hg-lines. Under the assumption that the Hg-line has 'zero' width, the instrumental line broadening was given by the measured Hg-line width of 0.5/cm FWHM.

The diamond samples were put under the microscope in the focus of the laser beam and the microscope. All measurements were made with the samples at room temperature [4]. The Raman line was measured on the growth and nucleation side of CVD diamonds and on one natural diamond with the following results.

2.4.3 Results: Diamond Raman Line

Fig. 2.19(left) shows two diamond Raman lines from a natural diamond as measured on both sides (1 and 2) of the sample. The line peaks for both sides at ≈ 1333.1/cm which gives ≈ 1332.7 after correction for the systematic shift. This result corresponds to the diamond line of 1332/cm normally given in literature [14]. The statistical error from the number of counts and the line width is 0.03/cm. An additional error of ≈ 0.15/cm is introduced due to the stepping of the grating. The measured line width from the natural sample is 2.0/cm which is large compared to the instrumental broadening. The measured width is therefore

[4] Temperature dependent Raman spectroscopy is reported in reference [59].

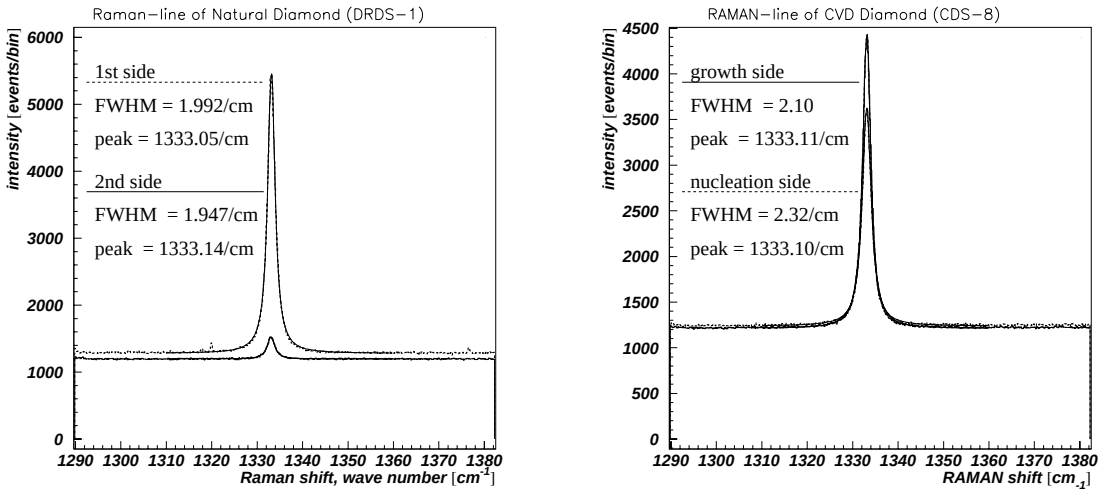

Figure 2.19: Left: Diamond Raman lines from both sides of a natural diamond. Right: Diamond Raman lines from the nucleation and from the growth side of CVD diamond sample CDS-8. All measurements are fitted with the Lorentz function Eq. 2.31 and a constant background term. No difference between the fits and the measured data are observed on this scale.

the 'true' width of the natural diamond Raman line.

Fig. 2.19(right) shows two diamond Raman lines from CVD diamond sample CDS-8. One line was measured from the nucleation side, the other line from the growth side. Both lines peak within the error of ≈ 0.15/cm at the same wave number of 1332.6/cm (after subtraction of 0.4/cm from the systematic shift). The line width is 2.7/cm on the nucleation side and 2.9/cm on the growth side which is slightly wider than on the natural diamond. The line width can be converted from a wave number to an energy using the phonon velocity is 10^6 cm/s which then allows to estimate the phonon lifetime. A typical phonon lifetime is then 0.1 μs.

Table 2.7 summarizes the line peak position and the line width from several CVD diamond samples and the natural sample. The lines peak on average at 1332.7/cm which agrees with the literature values of 1332/cm at room temperature. The systematic error of 0.4/cm from the Hg-line calibration has been subtracted from the measured line position. The line width of the natural diamond is about 2/cm. The line width of all measured CVD diamonds is below 2.9/cm. The material quality can be read from the table as the ratio of the Raman shift to the line width according to Eq. 2.33. The natural diamond has the highest material quality of ≈ 666, followed by TD1150-Y12 and CDS-8 with ≈ 600. The most likely cause for the higher material quality of natural diamond is the mono-crystalline lattice structure. CVD diamond is polycrystalline with grain boundaries which may limit the phonon lifetime. Also impurities limit the phonon lifetime. The most likely impurities in the natural diamond are boron and nitrogen and different carbon isotopes. The phonon lifetime is apparently more limited by the stress in the CVD diamond than by the impurities in the natural diamond. The width of the Raman line from the nucleation side is slightly bigger than from the growth side indicating a lower crystal material quality on the nucleation side compared to the growth side.

The Raman shift $1/\lambda_{\text{diamond}}$ allows an estimation for the velocity of sound

$$v = \frac{a\,c}{\lambda_{\text{diamond}}} = 1.4 \times 10^6 \text{ cm/s} \tag{2.34}$$

sample name	side	Raman shift [cm^{-1}] ±0.15 cm^{-1}	width [cm^{-1}] ±0.1 cm^{-1}
CDS-1	g	1332.40	2.899
	n	1332.67	2.687
CDS-2	g	1332.68	2.260
	n	1332.67	2.249
CDS-7	g	1332.70	2.514
	n	1332.73	2.637
CDS-8	g	1332.70	2.096
	n	1332.70	2.323
CDS-9	g	1332.90	2.279
	n	1332.70	2.589
CDS-10	g	1332.68	2.765
	n	1332.75	2.853
TD1150-Y12	g	1332.78	2.111
	n	1332.70	2.296
DRDS-1	1	1332.65	1.947
(natural)	2	1332.74	1.991
Hg-line	-	-	0.5

Table 2.7: Width and position of the Raman line from CVD diamond samples and a natural diamond sample. The values were measured on the growth (g) and on the nucleation (n) side. The values for CDS-8 and the natural sample can also be read from the fit parameters in Fig. 2.19. The Raman shifts in this table has been corrected for the systematic offset of 0.4/cm as measured using a Hg-lamp. The ratio of the Raman shift to the line width gives the diamond material quality, Q, according to Eq. 2.33. The measurement was done at room temperature. The measured width of a mercury line is given for comparison.

which is in good agreement to the values of 1.28×10^6 cm/s and 1.83×10^6 cm/s for transversal and longitudinal acoustic waves given in reference [40].

2.4.4 Results: Extended Raman Spectra

Fig. 2.20 shows extended spectra from a natural diamond (to the left) and from two CVD diamond samples CDS-1 and TD1150-Y12 (to the right, both samples are from different manufacturers). The diamond Raman line is visible at $\approx$ 1332.7/cm relative to the argon laser line. The range extends from 16700/cm to 18150/cm corresponding to a wave length range from $\lambda_{\text{start}} = 598.8$ nm to $\lambda_{\text{stop}} = 550.9$ nm and a light energy from $2\pi\hbar c\lambda_{\text{start}}^{-1} = 2.07$ eV to $2\pi\hbar c\lambda_{\text{stop}}^{-1} = 2.247$ eV. The extended spectra were taken in order to investigate the range where graphite impurities were reported. Graphite would cause a broad band in the range from 1400/cm to 1600/cm [39]. Such band does not exist in the natural diamond and could not be observed in the measured CVD diamonds here. The measurements show that the diamond Raman peaks sit on a broad background. This background is constant for both CVD diamonds. The constant background is 200 counts/bin in CDS-1 and 300 counts/bin in TD1150-Y12. The measurement on the natural diamond shows a background as well. The background in the natural diamond increases linearly from 200 counts/bin at 16800 /cm to 300 counts/bin at 18100 /cm. The range above Raman shifts of 2000/cm (2000/cm and higher, corresponding to -2000/cm and lower values in Fig. 2.20) was reported to emit

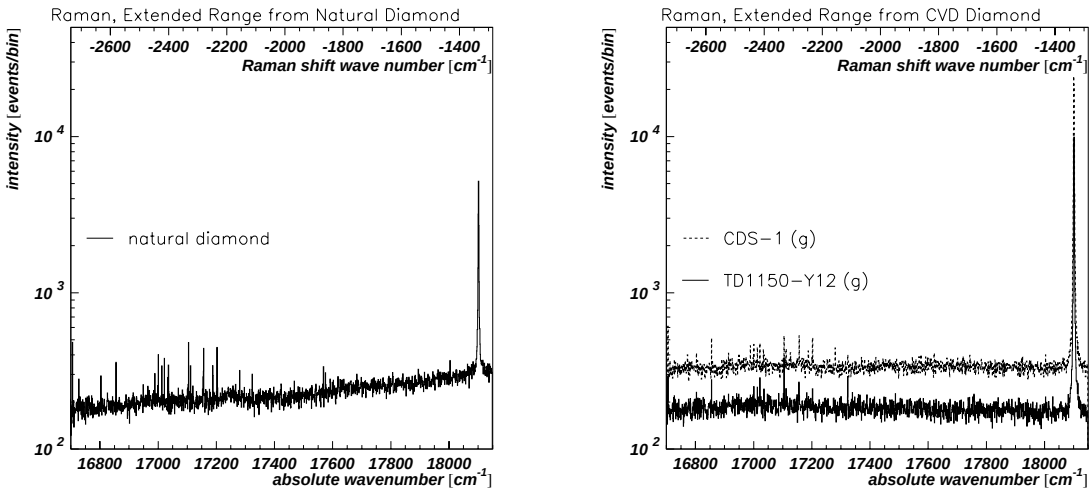

Figure 2.20: Extended Raman spectra from a natural diamond (left) and from two CVD diamonds (right). The abscissa is given in absolute wave numbers of light on the bottom axis and as the Raman shift on the top axis. The Raman shift is labeled with negative values because of technical reasons in the display.

photoluminescence light for some samples [11]. The background measured here is considered to be low compared to photoluminescence background reported in literature.

2.4.5 Summary and Discussion

The diamond Raman line position and width have been measured on several CVD diamond and one natural diamond. The diamond Raman line was observed close to the expected wave number as estimated from the velocity of sound and the diamond lattice constant. The measured diamond Raman shift was on average (1332.7 ± 0.15)/cm at room temperature after correction for the systematic error. The width of the diamond Raman line is explained by the phonon lifetime. The phonon lifetime is limited by stress and impurities in the crystal which determine the material quality. The CVD diamonds had slightly wider line width than the natural diamond. The natural diamond measured here had the highest material quality compared to the CVD diamonds. The natural diamond had the least stress in the lattice since it is a mono-crystal. The polycrystalline structure of CVD diamond introduces grain boundaries, lattice defects and dislocations which could cause stress. The stress limits the phonon lifetime. The line width from CVD diamond was wider on the nucleation side than on the growth side which may be due to the smaller grain size on the nucleation side. The CVD diamond material quality, according to the definition Eq. 2.33, was typically close to that of natural diamond. The line on both sides of CDS-1 is wider than on other samples. This may be due to a treatment with particles by the vendor.

The samples measured here did not show bands which could be associated with graphite. The photoluminescence background was negligibly low in the range from 2450/cm to 1300/cm. The peak from the natural diamond appeared to be on a light background whereas the intensity from the CVD diamonds did not change over the measured range. The sensitivity of the spectrometer was observed to be constant in this range. This was confirmed by measuring the spectral intensity from a tungsten lamp and normalizing with the spectrum from a black body at the same temperature. The background intensity may be due to luminescence from impurities. The Raman measurements should be extended to a larger range in order to gain

more information about luminescence emission and impurities. Extended Raman spectra from 100 nm to 3000 nm can be found in reference [14] and show a silicon vacancy defect in CVD diamond. The silicon Raman line appears at 520/cm [57]. Extending the measurement in Fig. 2.20 to this Raman shift could give information about the substrate on which the CVD diamonds were grown. The sensitivity to non-diamond phases could improve with longer incident wave lengths from 633 nm to 1060 nm [14].

The line widths measured here should be compared to the Raman measurements by S. Zhao in reference [11]: his work includes diamonds with line widths ranging from 2.4/cm to 11.5/cm. The highest material quality diamonds available for his work are comparable to the diamond material quality measured here. The lines measured here are typically equal or narrower than lines from the samples available to him[5].

Diamond characterization using Raman spectroscopy is of relevance for diamond detector applications since the line width gives a 'selection rule' for sensors: samples with line widths above ≈ 3.5/cm are likely bad sensors. On the other side, samples with narrow (< 3.5/cm) Raman line width do not correlate with charge collection properties [11]. It is assumed that the crystal material quality of the CVD diamond here is characteristic for other diamonds which were delivered later from the same manufacturers.

[5]S. Zhao used a spectrometer resolution of 2/cm. The spectrometer resolution here was lower than 0.5/cm; this may explain the different width for the natural diamond sample which is 0.4/cm higher in his work than measured here.

Chapter 3

Particle Detection

A charged particle that traverses a CVD diamond sensor creates pairs of charge carriers in the diamond bulk. These charge carriers move under the influence of the applied external electric field and their movement induces a current on the contact electrodes. This chapter introduces the charged particle detection properties of CVD diamond sensors. Fig. 3.1 shows five detector grade CVD diamond samples and one silicon diode. The CVD diamond samples are metallized with electrical contacts to study their bulk response to charged particles.

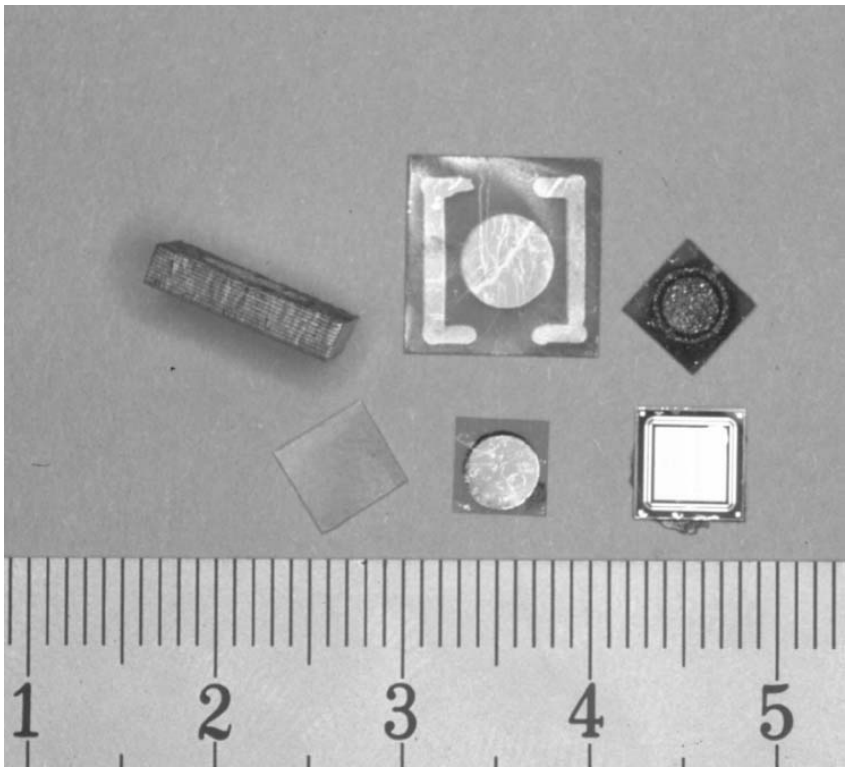

Figure 3.1: Photo of five CVD diamond sensors and one silicon diode (bottom right). The samples have a size of 5×5 mm^2 and 10×10 mm^2. The thickness of the diamond samples ranges from 400 μm to 2.6 mm. The lower left sample is lapped on both sides and is transparent. The other samples are unprocessed and have electrical contacts with a variety of geometries. The sample to the very left stands vertically on one edge.

Contents

3.1 Electrical Model of Diamond

The intrinsic electrical properties of a crystal are determined by the energy band gap between the valence band and the conduction band and the band bending. Diamond has a large band gap and no intrinsic conductivity is expected at room temperature. However, diamond is not completely insulating due to the presence of defects and impurities. Defects and impurities introduce additional energy levels in the band gap which may contribute to conduction. The lifetime of charge carriers in the bands is then limited by re-trapping and recombination. The following reviews the basic model of electric conduction in a crystal.

3.1.1 Description of a Single Electron in the Crystal

Electrons are the 'carriers' of the electric current in solids. The description of electric current therefore starts with a model for the electron transport. An electron in the crystal is described as a wave with amplitude, Ψ. In the *single electron approximation* the electron wave is the solution of Schrödinger's equation

$$\left(-\frac{\hbar^2}{2m}\partial_{\vec{r}}^2 + U(\vec{r})\right)\Psi(\vec{r}) = E\Psi(\vec{r}) \tag{3.1}$$

where m is the rest mass and E the total energy of the electron [1]. The waves are modulated by the potential, $U(\vec{r})$. The periodicity of the lattice implies periodicity of the potential and is expressed as

$$U(\vec{r}) = U(\vec{r}+\vec{R}) \qquad ; \qquad \forall\ \vec{R} \ \text{ from Eq. 2.2.} \tag{3.2}$$

A solution of Schrödinger's equation can be found by using the method of linear combination of atomic orbitals (LCAO-method) [35]. The solutions of Schrödinger's equation are plane waves

$$\Psi_n(\vec{r}) = u_n(\vec{r})e^{i\vec{k}\circ\vec{r}} \tag{3.3}$$

where $u(\vec{r})$ is a periodic function of the position such that $u(\vec{r}+\vec{R}) = u(\vec{r})$ [2]. An electron state is characterized by the energy quantum number n and the wave vector $\vec{k}$. The wave function has the form

$$\Psi_n(\vec{r}+\vec{R}) = e^{i\vec{k}\circ\vec{R}}\Psi_n(\vec{r}) \tag{3.4}$$

which is just Bloch's theorem for electron waves in the crystal. This equation holds for any $\vec{k}' = \vec{k}+\vec{K}$ under the condition that $\vec{K}\circ\vec{R} = 2\pi\cdot\text{integer}$ [35]. This is possible, if $\vec{K}$ is a vector of the reciprocal lattice:

$$\vec{K} = \vec{G} \tag{3.5}$$

where the reciprocal lattice vector, $\vec{G}$, is defined in Eq. 2.5. The electron energy levels in the periodic potential are the eigenvalues of Schrödinger's equation. Also the energy has periodicity in the reciprocal lattice: $E_n(\vec{k}+\vec{G}) = E_n(\vec{k})$.

The single electron approximation in the periodic potential assumes no interactions of the electron with the phonons or other electrons. This assumption is 'good' for the description

[1] The notation of the partial differentiation: $\partial_{\vec{r}} \equiv \partial/\partial\vec{r}$.

[2] The *inner product* : $\vec{a}\circ\vec{b} = a_i\,b_i \equiv \sum_i a_i\,b_i$.

of electrical conductivity in crystals as long as the electron moves like a free particle. Under the influence of interactions one can still assume that the electron moves like a free particle in the time between interactions.

3.1.2 Electron Energy Bands

A free carbon atom has 2 core electrons in a helium configuration (two $1s$ orbitals written as $1s^2$) and 4 valence electrons in the $2s^2p^2$ configuration. The electrons in the atom have discrete energy levels and are localized in atomic orbitals, where s and p denote the angular momentum quantum numbers. The N separated carbon atoms have $2N$ electrons in $1s$ orbitals, $2N$ electrons in $2s$ and $2N$ electrons in $2p$ orbitals.

Fig. 3.2 shows $4N$ energy levels of N carbon atoms as a function of the interatomic distance. At large interatomic distance the $4N$ states degenerate into two energy levels, $2s$ and $2p$. As the carbon atoms get closer the degeneracy is removed due to the interaction of the electrons with the nearby atoms. The interaction causes the energy levels to coagulate in two quasi-continuous bands[3]. The energy levels of the $2N$ core electrons form another quasi-continuous band which is not shown in the figure. The highest energy band is called the conduction band (CB) and the next lower band is called the valence band (VB). The region between the bands is called the band gap (BG).

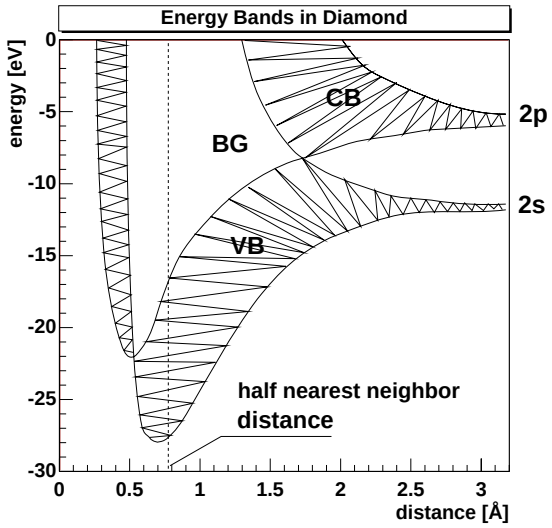

Figure 3.2: Energy levels of the $2s$ and $2p$ states in diamond as a function of the distance (separation between atoms). The valence band (VB) and the conduction band (CB) are 'quasi' continuous energy levels. They are separated by the band gap (BG) [60].

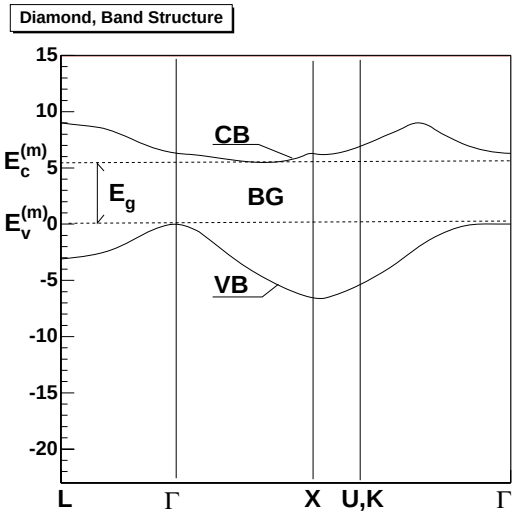

Figure 3.3: Electron energy levels along a path of wave vectors in the Brioullin zone. The upper graph represents the lowest energies of the conduction band (CB), the lower graph represents the highest energies of the valence band (VB). The point Γ corresponds to $\vec{k} = \vec{0}$ in diamond. The highest point of the VB is set arbitrarily to 0 eV [10].

Fig. 3.3 shows two dispersion curves of energies as a function of the wave vector obtained from linear combination of atomic orbitals (LCAO) for the diamond crystal [10]. The upper graph is the lowest energy branch of the CB, the lower graph is the highest energy branch of the VB. Both energies are separated by the BG. The energy is periodic in $\vec{k}$, such that it

[3] One can also say that the energy levels in the crystal are split into bands.

is sufficient to display an interval of wave vectors inside the Brioullin zone. The dispersion curve is shown for wave vectors along a path in the Brioullin zone. Here the path is described by the wave vectors L, Γ, X, U and K which are points in the Brioullin zone [10]. The wave vector $\vec{0}$ corresponds to the point Γ in the center of the Brioullin zone. The energy of the VB at Γ is the highest energy in the VB and arbitrarily assigned to be 0 eV. The energy difference between the highest energy, $E_{\mathrm{v}}^{(\mathrm{m})} \equiv E_{\mathrm{v}}(\vec{k}_{\mathrm{v}}^{(\mathrm{m})})$, of the VB and the lowest energy, $E_{\mathrm{c}}^{(\mathrm{m})} \equiv E_{\mathrm{c}}(\vec{k}_{\mathrm{c}}^{(\mathrm{m})})$, of the CB is the band gap energy, E_{g}. The energies are labeled as 'm' in order to emphasize that they are fixed values (meaning 'maximum' or 'minimum'). The wave vectors, $\vec{k}_{\mathrm{v}}^{(\mathrm{m})}$ and $\vec{k}_{\mathrm{c}}^{(\mathrm{m})}$, denote the wave vectors where the energy is a maximum in the VB and a minimum in the CB. The band gap energy of natural diamond is $E_{\mathrm{g}} = 5.48$ eV [10]. Fig. 3.3 only shows the N highest energies of the VB. There exist three more branches with $3N$ energy levels in the VB. The other three branches of the VB have lower energies and are partially separated from the curve that is shown [10]. Also the CB has three more branches with states above the one which is shown in the figure. The electrical properties of the crystal are determined by the lowest energy levels of the CB and the highest levels of the VB. Generally an energy transition of an electron from a state in the VB to the CB requires that momentum is conserved. This is possible if the transition is 'vertical' corresponding to no change in the wave vector of the electron. In diamond the highest energy level in the VB is at a different wave vector than the lowest energy in CB: $\vec{k}_{\mathrm{v}}^{(\mathrm{m})} \neq \vec{k}_{\mathrm{c}}^{(\mathrm{m})}$. A transition into the lowest energy of the CB is only possible if the electron can acquire additional momentum in order to reach the energy minimum in the CB. A phonon can transfer the additional momentum to the electron in order to realize the transition. A transition which requires a phonon is called an *indirect transition* and a vertical transition is called a *direct* transition. Diamond and silicon are indirect semi-conductors whereas germanium for example is a direct semi-conductor.

Solids are classified by the energy difference between the VB and the CB. Solids may have a separation or an overlap between the bands. Fig. 3.4 shows three classes of solids: the conductor, the semi-conductor and the insulator. The conductor has either overlap between VB and CB or a partially filled CB. The insulator has a large band gap, E_{g}, of several electron volts. The insulator has no partially filled bands. The semi-conductor also has a band gap but electrons from the VB occupy levels in the CB. They leave the same number of vacancies in the VB such that the sum of occupied levels in the CB is equal to the number of vacancies in the VB. The vacancies in the VB are called holes.

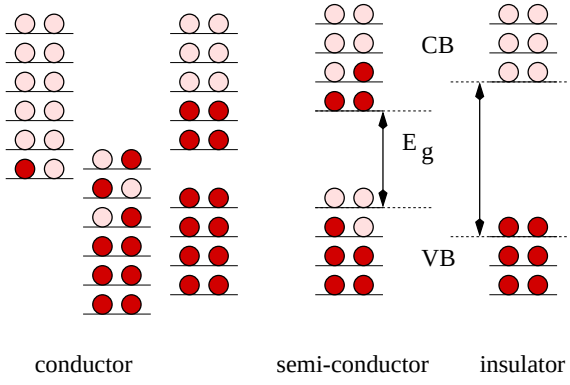

Figure 3.4: Schematic energy levels of the conduction band (CB) and the valence band (VB) of a conductor, a semi-conductor and an insulator. The charge carriers in the VB are marked with open circles, charge carriers in the CB are solid circles. The energy bands in the conductor overlap or are partially filled. In the semi-conductor charge carriers from the VB occupy states in the CB and leave vacancies in the VB. The insulator has bands which are completely occupied by the same type of charge carriers in other words, the insulator has no partially filled bands. The VB and the CB are separated by the band gap (BG). The energy difference between CB and the VB is the band gap energy, E_{g} [61].

An important property of a semi-conductor or of an insulator is the number, n_c, of electrons per unit volume in the CB and the number, p_v, of vacancies per unit volume in the VB:

$$n_c = \int_{E_c^{(m)}}^{\infty} dE \, \frac{g_c(E)}{e^{(E-E_F)/(k_B T)} + 1} \quad ; \quad p_v = \int_{-\infty}^{E_v^{(m)}} dE \, \frac{g_v(E)}{e^{(E_F-E)/(k_B T)} + 1} \tag{3.6}$$

where g_c and g_v are the densities of energy states in the CB and the VB [35]. The integration for electrons starts from the lowest energy, $E_c^{(m)}$, of the CB and the integration for vacancies ends at the highest energy, $E_v^{(m)}$, of the VB. The integrand contains the temperature dependent probability, the Fermi function or the Fermi statistical factor, of an energy state to be occupied. The probability depends on the difference between the energy, E, and the Fermi energy, E_F. The energy E_F is also called the chemical potential [35]. For the case of large energy difference, $(E - E_F)/(k_B T) \gg 1$, the Fermi statistical factor can be approximated by the Boltzmann factor such that

$$n_c = N_c(T) \, e^{-\left(E_c^{(m)} - E_F\right)/(k_B T)} \quad ; \quad p_v = P_v(T) \, e^{-\left(E_F - E_v^{(m)}\right)/(k_B T)} \tag{3.7}$$

where the concentrations N_c and P_v can be calculated under the assumption that the density of states increases as the square root of the energy [35]:

$$N_c = 2 \left(\frac{m_c^* k_B T}{2 \pi \hbar^2} \right)^{3/2} \quad ; \quad P_v = 2 \left(\frac{m_v^* k_B T}{2 \pi \hbar^2} \right)^{3/2} . \tag{3.8}$$

The m_c^* and m_v^* are the effective masses of electrons in the conduction band and electrons in the valence band (as explained below).

Electrons and holes are called intrinsic when the electrons in the CB have come from a formerly occupied state in the VB and leave vacancies in the VB. The number of intrinsic electrons and holes are equal and the number, n_i, of intrinsic carriers per unit volume, the *intrinsic carrier concentration*, is

$$p_v = n_c \equiv n_i \implies n_i(T) = \sqrt{N_c(T) \, P_v(T)} \, e^{-E_g/(2 k_B T)} . \tag{3.9}$$

The factors N_c and P_v are of the order of 10^{19} cm^{-3} at room temperature. They vary less than the exponential factor as a function of temperature [35]. Using the band gap energy, $E_g^{(di)} = E_c^{(m,di)} - E_v^{(m,di)} = 5.48$ eV, in diamond [Table 1.1] and the band gap energy, $E_g^{(si)} = E_c^{(m,si)} - E_v^{(m,si)} = 1.124$ eV, in silicon [10] one obtains at room temperature, $k_B T = (1/40)$ eV, the intrinsic concentrations of 10^{-29} cm^{-3} in diamond and 10^{+9} cm^{-3} in silicon. At room temperature the intrinsic carrier concentration in diamond is negligibly small. This is the reason why diamond is classified as an insulator at room temperature.

3.1.3 Charge Carrier Equation of Motion

Intrinsic charge carriers, as they abundantly exist in silicon at room temperature, can move in the CB and in the VB [4]. Here a *charge carrier* in a band is defined as the *pair of an occupied electron state and a vacant electron state*. The model chosen here is that it is the electron which moves. A vacant state is necessary to allow the motion.

[4] The same formalism that is described here will be used later in order to describe the motion of charge carriers from excitation by ionizing radiation.

Predictions about the movement of a charge carrier in the crystal are made in the semi-classical model of conduction [35]. No collisions between carriers or carriers and phonons are assumed at this stage. Then the energy quantum number, n, is conserved. The velocities, $\vec{v}_\mathrm{c}$ and $\vec{v}_\mathrm{v}$, of a carrier with quantum number n and energy $E_\mathrm{c}(\vec{k})$ in the CB and $E_\mathrm{v}(\vec{k})$ in the VB are [35]

$$\vec{v}_\mathrm{c} \equiv \frac{\partial E_\mathrm{c}(\vec{k})}{\hbar\,\partial\vec{k}} \quad \text{and} \quad \vec{v}_\mathrm{v} \equiv \frac{\partial E_\mathrm{v}(\vec{k})}{\hbar\,\partial\vec{k}}. \tag{3.10}$$

In order to find the velocity for a carrier one expands its energy in a Taylor series around the band extremum at $\vec{k} = \vec{0}$ (the Γ point in Fig. 3.3) [61]

$$E(\vec{k}) = E(\vec{0}) + \frac{1}{2}\left(\frac{\mathrm{d}^2E}{\mathrm{d}\vec{k}^2}\right)_{\vec{k}=\vec{0}} \cdot \vec{k}^2 + ... \tag{3.11}$$

Differentiation of Eq. 3.11 with respect to $\vec{k}$ gives the velocities, $\vec{v}_\mathrm{c}$ and $\vec{v}_\mathrm{v}$, for a carrier in the CB and in the VB

$$\begin{aligned} \vec{v}_\mathrm{c} &\approx \frac{1}{\hbar^2}\left(\frac{\mathrm{d}^2E_\mathrm{c}}{\mathrm{d}\vec{k}^2}\right)_{\vec{k}=\vec{0}} \cdot \hbar\,\vec{k} \stackrel{\mathrm{def}}{=} +\frac{\hbar\,\vec{k}}{m_\mathrm{c}^*} \\ \vec{v}_\mathrm{v} &\approx \frac{1}{\hbar^2}\left(\frac{\mathrm{d}^2E_\mathrm{v}}{\mathrm{d}\vec{k}^2}\right)_{\vec{k}=\vec{0}} \cdot \hbar\,\vec{k} \stackrel{\mathrm{def}}{=} -\frac{\hbar\,\vec{k}}{m_\mathrm{v}^*} \end{aligned} \tag{3.12}$$

where the last expressions define the masses of a charge carrier in the CB and in the VB. $1/m_\mathrm{c}^*$ and $1/m_\mathrm{v}^*$ are tensors of effective masses. The coordinate system of the Brillouin zone can be chosen such that the tensors are diagonal. The diagonal elements in the tensor can be equal and then $1/m_\mathrm{c}^*$ and $1/m_\mathrm{v}^*$ are real numbers. The second derivative of the CB is bigger than zero at the energy minimum and the sign for the effective mass of a charge carrier in the CB is chosen to be positive. For the VB the second derivative is negative. The convention is to choose the sign such that the effective masses of charge carriers are positive [35]. A charge carrier has a non-zero velocity only in the case of partially filled bands since any change in $\vec{k}$ requires a free energy level in the band. An external electric field $\vec{E}(\vec{r},t)$ causes a force on the charge $-e$ of the charge carrier according to the *equation of motion* [35]

$$\hbar\,\partial_t\vec{k} = -e\,\vec{E}(\vec{r},t). \tag{3.13}$$

Both Eq. 3.12 and Eq. 3.13 are the equations of motion for charge carriers in the CB and in the VB. It should be noted that the Taylor series in Eq. 3.11 is developed around $\vec{0}$. It can be seen from Fig. 3.3 that in diamond the extremum of the VB is at $\vec{k}_\mathrm{v}^{(\mathrm{m})} = \vec{0}$ and the extremum of the CB is at $\vec{k}_\mathrm{c}^{(\mathrm{m})} \neq \vec{0}$. Hence one should develop $E_\mathrm{c}(\vec{k})$ around $\vec{k}_\mathrm{c}^{(\mathrm{m})}$ for a precise description of the electron transport.

3.1.4 Model of Electrical Conductivity

Integration of Eq. 3.13 and insertion in Eq. 3.12 gives the velocity which increases linearly in time. Linear increase of carrier velocities is macroscopically not observed. Instead, charge carriers scatter with phonons in the lattice. Continuous scattering limits the velocity of charge carriers to a constant value. The motion of a charge carrier is therefore described as an acceleration as a free particle for a certain path length by Eq. 3.13 and a deceleration due to scattering. The equation of motion for charge carriers in the CB and in the VB are then [61]

$$m_{\mathrm{c}}^{*}\left(\partial_t \vec{v}_{\mathrm{c}} + \frac{\vec{v}_{\mathrm{c}}}{\tau_{\mathrm{c}}^{(\mathrm{S})}}\right) = -e\vec{E} \quad ; \quad m_{\mathrm{v}}^{*}\left(\partial_t \vec{v}_{\mathrm{v}} - \frac{\vec{v}_{\mathrm{v}}}{\tau_{\mathrm{v}}^{(\mathrm{S})}}\right) = +e\vec{E} \tag{3.14}$$

where m_{c}^{*} and m_{v}^{*} are the effective masses for charge carriers in CB and VB. The constants $\tau_{\mathrm{c}}^{(\mathrm{S})}$ and $\tau_{\mathrm{v}}^{(\mathrm{S})}$ are the relaxation times for charge carriers between scattering events. The superscript 'S' indicates that the time is taken between scattering events. The solutions to Eq. 3.14 are constant *drift velocities*

$$\vec{v}_{\mathrm{c}} = -\frac{e\,\tau_{\mathrm{c}}^{(\mathrm{S})}}{m_{\mathrm{c}}^{*}}\,\vec{E} \quad ; \quad \vec{v}_{\mathrm{v}} = -\frac{e\,\tau_{\mathrm{v}}^{(\mathrm{S})}}{m_{\mathrm{v}}^{*}}\,\vec{E}. \tag{3.15}$$

The terms with $1/\tau_{\mathrm{c}}^{(\mathrm{S})}$ and $1/\tau_{\mathrm{v}}^{(\mathrm{S})}$ in Eq. 3.14 are interpreted as a form of friction. If the external force, $-e\vec{E}$, would be switched off, the drift velocities, $\vec{v}_{\mathrm{c}}$ and $\vec{v}_{\mathrm{v}}$, would decline in time like $|\vec{v}_{\mathrm{c}}(t)| \propto e^{-t/\tau_{\mathrm{c}}^{(\mathrm{S})}}$ and $|\vec{v}_{\mathrm{v}}(t)| \propto e^{-t/\tau_{\mathrm{v}}^{(\mathrm{S})}}$. Eq. 3.15 describes the motion of charge carriers in the VB and in the CB with positive masses and negative charge signs and the carriers in the VB move the same direction as the carriers in the CB. An alternative interpretation would be to imagine electrons (with negative charge, positive mass) in the CB and holes (with positive charge and positive mass) in the VB. Then the electrons move in a direction opposite to the direction of motion of the holes. Eq. 3.15 suggests that the *mobilities of charge carriers* should be defined

$$\mu_{\mathrm{c}} \stackrel{\mathrm{def}}{=} \frac{e\,\tau_{\mathrm{c}}^{(\mathrm{S})}}{m_{\mathrm{c}}^{*}} \quad ; \quad \mu_{\mathrm{v}} \stackrel{\mathrm{def}}{=} \frac{e\,\tau_{\mathrm{v}}^{(\mathrm{S})}}{m_{\mathrm{v}}^{*}}. \tag{3.16}$$

The mobility for carriers in the CB differs from that of carriers in the VB since the effective masses are different due to different bending of the energy bands in Eq. 3.12. Also the scattering time for carriers in the CB can be different from that of carriers in the VB. The mobilities can be tensors in a non-isotropic media where the direction of current flow deviates from the direction of the electric field.

The current densities, $\vec{j}_{\mathrm{c}}$ and $\vec{j}_{\mathrm{v}}$, for charge carriers in the CB and VB are given by the number of electrons, $\mathrm{d}\#_{\mathrm{c}}$, in the CB and the number of vacancies, $\mathrm{d}\#_{\mathrm{v}}$, in the VB which pass through an imaginary surface area $\mathrm{d}\vec{A}$ in the time interval $\mathrm{d}t$. The charges have the velocities $\vec{v}_{\mathrm{c}}$ and $\vec{v}_{\mathrm{v}}$ and are displaced by $\mathrm{d}\vec{x}_{\mathrm{c}}$ and $\mathrm{d}\vec{x}_{\mathrm{v}}$ in the time interval $\mathrm{d}t$. The number of charges in the displacement volumes, $\mathrm{d}V_{\mathrm{c}} = \mathrm{d}\vec{x}_{\mathrm{c}} \circ \mathrm{d}\vec{A}$ and $\mathrm{d}V_{\mathrm{v}} = \mathrm{d}\vec{x}_{\mathrm{v}} \circ \mathrm{d}\vec{A}$, and the velocities define the *current densities for charge carriers*

$$\begin{aligned} \vec{j}_{\mathrm{c}} &= -e\,n_{\mathrm{c}}\,\vec{v}_{\mathrm{c}} \quad ; \quad n_{\mathrm{c}} \stackrel{\mathrm{def}}{=} \frac{\mathrm{d}\#_{\mathrm{c}}}{\mathrm{d}V_{\mathrm{c}}} \\ \vec{j}_{\mathrm{v}} &= -e\,p_{\mathrm{v}}\,\vec{v}_{\mathrm{v}} \quad ; \quad p_{\mathrm{v}} \stackrel{\mathrm{def}}{=} \frac{\mathrm{d}\#_{\mathrm{v}}}{\mathrm{d}V_{\mathrm{v}}}. \end{aligned} \tag{3.17}$$

The current density is the sum of current densities from the CB and the VB

$$\vec{j} = \vec{j}_{\mathrm{c}} + \vec{j}_{\mathrm{v}}. \tag{3.18}$$

Fig. 3.5 illustrates the transport of charge carriers in the VB and in the CB. The charge carriers follow the force of the applied external electric field. An intrinsic charge carrier has come from the dissociation of an electron and a vacancy. Therefore, the carrier concentrations in the CB and in the VB are equal which allows one to define the *intrinsic carrier concentration*

$$n_{\mathrm{c}} = p_{\mathrm{v}} \stackrel{\mathrm{def}}{=} n_{\mathrm{i}} \tag{3.19}$$

which then gives the *intrinsic current density*

$$\vec{j} = e\, n_\mathrm{i}\, (\mu_\mathrm{v} + \mu_\mathrm{c})\, \vec{E}. \tag{3.20}$$

The *mobility sum* is defined as

$$\mu \overset{\mathrm{def}}{=} \mu_\mathrm{v} + \mu_\mathrm{c}. \tag{3.21}$$

The intrinsic current density depends on the temperature as the intrinsic carrier concentration is temperature dependent according to Eq. 3.9. The current increases with temperature in contrast to metals where the current decreases with temperature. The *electrical conductivity* is defined as

$$\sigma \overset{\mathrm{def}}{=} e\, n_\mathrm{i} \mu \overset{\text{Eq. 3.16}}{=} e^2\, n_\mathrm{i} \left(\frac{\tau_\mathrm{c}^{(\mathrm{S})}}{m_\mathrm{c}^*} + \frac{\tau_\mathrm{v}^{(\mathrm{S})}}{m_\mathrm{v}^*} \right) \tag{3.22}$$

which allows one to rewrite the current density in the form of *Ohm's law*:

$$\vec{j} = \sigma\, \vec{E}. \tag{3.23}$$

Ohm's law describes the magnitude of the current as linearly increasing with $|\vec{E}|$. In reality the current increases up to a certain value corresponding to a saturation velocity, $\vec{v}_\mathrm{sat}$, at the field strength, E_sat. The reason is that the mobility decreases for high electric field above E_sat like $1/|\vec{E}|$ due to additional scattering with optical mode phonons.

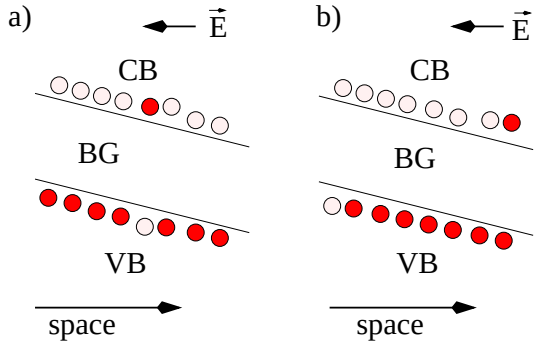

Figure 3.5: Model of intrinsic conduction in the valence band (VB) and in the conduction band (CB). Both bands are separated by the band gap (BG). The left figure illustrates two charge carriers at a time t_0. The right figure illustrates the charge carriers at the time $t > t_0$ [61].

The variation of carrier velocities at thermal equilibrium is [35, 62]

$$v_\mathrm{th} \overset{\mathrm{def}}{=} \sqrt{\langle v^2 \rangle} = \sqrt{3 k_\mathrm{B} T / m^*} \tag{3.24}$$

which determines the velocity where the drift velocity saturates

$$|\vec{v}_\mathrm{sat}| \approx v_\mathrm{th}. \tag{3.25}$$

The saturation of the drift velocity determines the *saturation field strength*

$$|\vec{E}_\mathrm{sat}| = \frac{1}{\mu}\, |\vec{v}_\mathrm{sat}|. \tag{3.26}$$

Assuming an effective carrier mass of $m^* = 511$ keV$/c^2$, the electron rest mass, one obtains the saturation velocity of 1.2×10^7 cm/s for charge carriers at room temperature which agrees with measurements shown in reference [63]. Using the mobility of 2100 cm^{2}V^{-1}s^{-1} for carriers in the VB in diamond from Table 1.1 one finds the field strength of 0.5 V/μm above which velocity saturation in the VB sets in [5]. The velocity of charge carriers in the CB saturates at about the same field strength since their mobility is 2400 cm^{2}V^{-1}s^{-1} [Table 1.1]. The typical *transition time* for a charge carrier to travel through a 400 μm thick diamond sensor is then about 4 ns.

At this point one can summarize the following: the basic intrinsic electrical properties of a (crystalline) semi-conductor or insulator are determined by the band gap and by the bending of the energy bands. The band gap and the temperature determine the intrinsic carrier concentration. The band bending determines the effective mass and therefore the carrier velocity between scattering events. The scattering effect of charge carriers from phonons introduces a (phenomenological) relaxation time between scattering events which limits the velocity to a constant drift velocity.

3.1.5 Conductivity in the Presence of Charge Traps

The previous section describes the intrinsic semi-conductor which only contains electrons and vacancies with energies in the VB or in the CB. However, real semi-conductors have defects, either by nature or due to intentional doping. Defects introduce energy levels between the VB and the CB. Fig. 3.6 illustrates a model of the BG [62]: active electron states (AES) with concentration N, of which n are filled with electrons, are located at the energy $E_\mathrm{c} - E_\mathrm{n}$ below the CB energy. Deep electron states (DES) with concentration H, of which h are filled with electrons, are located slightly above the middle of the BG. Deep vacancy states (DVS) of concentration M, of which m are vacant states, are located slightly below the middle of the BG. The Fermi energy is located near middle of the energy gap.

At a given temperature, there are electron transitions between the AES and the CB. The transitions are indicated in Fig. 3.6 by arrows. A transition from the AES into the CB is a de-trapping transition (DT), the transition back into the AES is a re-trapping transition (RT). The transition into a deep state is a recombination (RC). The average transition times are [65, 62]

$$\tau_\mathrm{c}^{(\mathrm{RT})} = \frac{1}{(N-n)\, v_\mathrm{th}\sigma_\mathrm{n}} \quad ; \quad \tau_\mathrm{c}^{(\mathrm{RC})} = \frac{1}{m\, v_\mathrm{th}\sigma_\mathrm{m}} \quad ; \quad \tau_\mathrm{c}^{(\mathrm{DT})} = \frac{e^{+(E_\mathrm{c}-E_\mathrm{n})/k_\mathrm{B}T}}{N_\mathrm{c}\, v_\mathrm{th}\sigma_\mathrm{n}}. \quad (3.27)$$

The transition times depend on the cross section, σ_n and σ_m, of an energy state and on the concentration of states at the destination. The de-trapping transitions proceed at a rate determined by the thermal energy and the energy, $E_\mathrm{c} - E_\mathrm{n}$, of the AES through the Boltzmann factor. Similar transition times can be given for the transition between the VB and the AVS. The transition times are generally much larger than the scattering times, $\tau_\mathrm{c}^{(\mathrm{S})}$ and $\tau_\mathrm{v}^{(\mathrm{S})}$. There are additional transitions between the CB and the DES and the VB and the DVS which are not shown in Fig. 3.6. The rates of these transitions are negligibly small: de-trapping transitions from deep levels are suppressed through the Boltzmann factor and

[5] The mobilities for charge carriers in the CB and VB depend on the carrier concentration. For carrier concentrations below 10^{14}/cm^3 the mobility sum is about 4000 cm^{2}V^{-1}s^{-1} for carriers in the VB and CB in diamond [64]. Typical carrier concentrations in diamond after ionization from a minimum ionizing particle are of the order of $(36/\pi)/\mu\mathrm{m}^3 \approx 10^{13}/\mathrm{cm}^3$ where 36 electron-hole pairs are created per 1 μm distance travelled by the minimum ionizing particle.

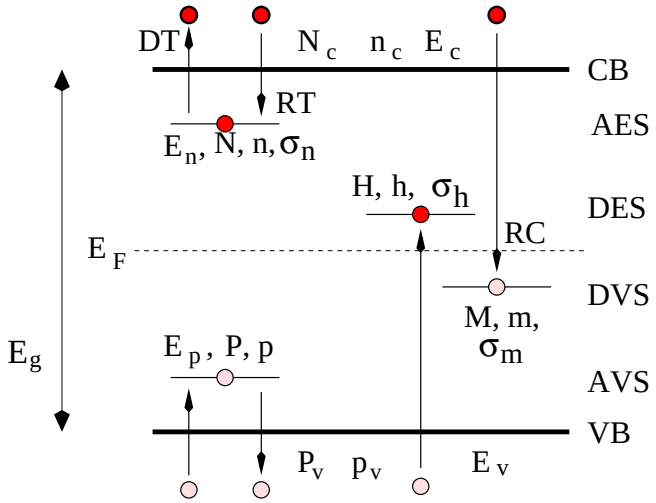

Figure 3.6: Model of energy states between the valence band (VB) and the conduction band (CB). Both bands are separated by the band gap (BG) with an energy difference E_g. The active electron state (AES) and active vacancy state (AVC) are energetically close to the CB and the VB. The deep electron state (DES) and deep vacancy states (DVS) are close to the Fermi energy E_F. After reference [62].

re-trapping transitions of electrons from the CB in the DES are suppressed since the DES is filled with electrons. There are also no significant re-trapping transitions of vacancies from the VB to the DVS since the DVS is filled with vacancies. The model presented in Fig. 3.6 only considered electron and vacancy states at a fixed energy. In reality there can be states at various energies.

The following considers the CB and the AES only, but the method to derive the rate equations for the VB and an AVS is the same. The change in the carrier concentration in the CB due to the three transitions, DT, RT and RC, in an infinitesimal time, dt, is [35]

$$n_\mathrm{c}(t+\mathrm{d}t) = \left(1 - \frac{\mathrm{d}t}{\tau_\mathrm{c}^{(\mathrm{RT})}} - \frac{\mathrm{d}t}{\tau_\mathrm{c}^{(\mathrm{RC})}}\right) n_\mathrm{c}(t) + \frac{\mathrm{d}t}{\tau_\mathrm{c}^{(\mathrm{DT})}}\, n(t). \tag{3.28}$$

The first term on the right expresses the destruction of charge carriers in the CB through re-trapping and recombinations by the fractions $\mathrm{d}t/\tau_\mathrm{c}^{(\mathrm{RT})}$ and $\mathrm{d}t/\tau_\mathrm{c}^{(\mathrm{RC})}$. The second term on the right expresses the creation through thermal de-trapping. The change of concentrations in the AES due to the two transitions, DT and RT, is

$$n(t+\mathrm{d}t) = \left(1 - \frac{\mathrm{d}t}{\tau_\mathrm{c}^{(\mathrm{DT})}}\right) n(t) + \frac{\mathrm{d}t}{\tau_\mathrm{c}^{(\mathrm{RT})}}\, n_\mathrm{c}(t) \tag{3.29}$$

where the first term on the right expresses destruction of an electron in the AES through de-trapping and the second term expresses creation due to re-trapping. Both Eq. 3.28 and Eq. 3.29 can be rewritten in differentials $\mathrm{d}n_\mathrm{c}/\mathrm{d}t \equiv [n_\mathrm{c}(t+\mathrm{d}t) - n_\mathrm{c}(t)]/\mathrm{d}t$ and $\mathrm{d}n/\mathrm{d}t \equiv [n(t+\mathrm{d}t) - n(t)]/\mathrm{d}t$ and one obtains the *rate equation for re-trapping, de-trapping and recombination*

$$\frac{\mathrm{d}n_\mathrm{c}}{\mathrm{d}t} = -\frac{\mathrm{d}n}{\mathrm{d}t} - \frac{n_\mathrm{c}}{\tau_\mathrm{c}^{(\mathrm{RC})}} \tag{3.30}$$

and

$$\frac{\mathrm{d}n}{\mathrm{d}t} = -\frac{n}{\tau_\mathrm{c}^{(\mathrm{DT})}} + \frac{n_\mathrm{c}}{\tau_\mathrm{c}^{(\mathrm{RT})}}. \tag{3.31}$$

The rate equations form a set of first-order, non-linear, coupled differential equations. It is not possible to decouple them and give an analytical solution. In order to proceed one usually assumes *quasi-equilibrium* [62]:

$$\frac{\mathrm{d}n_\mathrm{c}}{\mathrm{d}t} \ll \frac{n_\mathrm{c}}{\tau_\mathrm{c}^{(\mathrm{RC})}} \tag{3.32}$$

which means that any change in the number of carriers is small compared to the number of free charge carriers. It is difficult to justify the quasi-equilibrium assumption as discussed in reference [62]. The transitions are then described by the *rate equation of the quasi-equilibrium approximation*:

$$\frac{\mathrm{d}n}{\mathrm{d}t} \approx -\frac{n_\mathrm{c}}{\tau_\mathrm{c}^{(\mathrm{RC})}} \quad \text{and Eq. 3.31} \tag{3.33}$$

which can be solved for the concentration of charge carriers in the CB

$$n_\mathrm{c} = n\,\frac{\tau_\mathrm{c}^{(\mathrm{R})}}{\tau_\mathrm{c}^{(\mathrm{DT})}} \qquad \text{with} \qquad \frac{1}{\tau_\mathrm{c}^{(\mathrm{R})}} = \frac{1}{\tau_\mathrm{c}^{(\mathrm{RC})}} + \frac{1}{\tau_\mathrm{c}^{(\mathrm{RT})}}. \tag{3.34}$$

The right side depends on the concentration, n, of occupied AES. It also depends on the ratio between the transition times for the destruction of a charge carrier, $\tau_\mathrm{c}^{(\mathrm{R})}$, and the creation time $\tau_\mathrm{c}^{(\mathrm{DT})}$. In analogy one obtains for the concentration of charge carriers in the VB

$$p_\mathrm{v} = p\,\frac{\tau_\mathrm{v}^{(\mathrm{R})}}{\tau_\mathrm{v}^{(\mathrm{DT})}} \qquad \text{with} \qquad \frac{1}{\tau_\mathrm{v}^{(\mathrm{R})}} = \frac{1}{\tau_\mathrm{v}^{(\mathrm{RC})}} + \frac{1}{\tau_\mathrm{v}^{(\mathrm{RT})}}. \tag{3.35}$$

The destruction and creation times of a charge carrier in the VB are obtained in analogy to those for the CB from Fig. 3.6. The time for carrier destruction in the CB and the VB can be generalized for the case of different processes where each process, k, is characterized by a transition time $\tau_\mathrm{c}^{(k)}$ and $\tau_\mathrm{v}^{(k)}$

$$\frac{1}{\tau_\mathrm{c}^{(\mathrm{R})}} = \sum_k \frac{1}{\tau_\mathrm{c}^{(k)}} \qquad \text{and} \qquad \frac{1}{\tau_\mathrm{v}^{(\mathrm{R})}} = \sum_k \frac{1}{\tau_\mathrm{v}^{(k)}}. \tag{3.36}$$

These relations are known as a 'Matthiessen-like'[6] sum-rule [35, 36].

The current densities from Eq. 3.17 can be rewritten

$$\vec{j}_\mathrm{c} = -e\,n\,\frac{\tau_\mathrm{c}^{(\mathrm{R})}}{\tau_\mathrm{c}^{(\mathrm{DT})}}\,\vec{v}_\mathrm{c} \qquad ; \qquad \vec{j}_\mathrm{v} = -e\,p\,\frac{\tau_\mathrm{v}^{(\mathrm{R})}}{\tau_\mathrm{v}^{(\mathrm{DT})}}\,\vec{v}_\mathrm{v}. \tag{3.37}$$

Using the lifetime for de-trapping from Eq. 3.27 which contains the concentrations N_c and P_v one can define the *non-intrinsic carrier concentrations*

$$\tilde{n}_\mathrm{c} \stackrel{\mathrm{def}}{=} N_\mathrm{c}(T)\,e^{-(E_\mathrm{c}^{(\mathrm{m})}-E_\mathrm{n})/(k_\mathrm{B}T)} \qquad \text{and} \qquad \tilde{p}_\mathrm{v} \stackrel{\mathrm{def}}{=} P_\mathrm{v}(T)\,e^{-(E_\mathrm{p}-E_\mathrm{v}^{(\mathrm{m})})/(k_\mathrm{B}T)} \tag{3.38}$$

and one arrives at the current densities

$$\vec{j}_\mathrm{c} = -e\,\tilde{n}_\mathrm{c}\,v_\mathrm{th}\,\sigma_\mathrm{n}\,\tau_\mathrm{c}^{(\mathrm{R})}\vec{v}_\mathrm{c} \qquad \text{and} \qquad \vec{j}_\mathrm{v} = -e\,\tilde{p}_\mathrm{v}\,v_\mathrm{th}\,\sigma_\mathrm{p}\,\tau_\mathrm{v}^{(\mathrm{R})}\vec{v}_\mathrm{v}. \tag{3.39}$$

[6] Precisely, the Matthiessen sum-rule expresses the reciprocal mobility as the sum over reciprocal mobilities of independent processes, (see reference [35] for the limitations).

The main dependence on the temperature is expressed through $\tilde{n}_c$ and $\tilde{p}_v$ which depend on the temperature through the exponential Boltzmann factor and which are proportional to $T^{3/2}$ as given by Eq. 3.8. The product $v_{th}\tau_{c,v}^{(R)}$ is independent of the temperature since the thermal velocity cancels which can be seen from Eq. 3.27.

3.1.6 The Carrier Drift Length

The product of the drift velocity and the time for destruction defines the *mean drift lengths* for charge carriers in the CB and in the VB

$$s_c \stackrel{\text{def}}{=} \tau_c^{(R)}|\vec{v}_c| \qquad \text{and} \qquad s_v \stackrel{\text{def}}{=} \tau_v^{(R)}|\vec{v}_v|. \tag{3.40}$$

Using the expression Eq. 3.15 for the drift velocity and the carrier mobility one finds

$$s_c = \tau_c^{(R)}\,\mu_c\,|\vec{E}| \qquad \text{and} \qquad s_v = \tau_v^{(R)}\,\mu_v\,|\vec{E}|. \tag{3.41}$$

The sum of the mean drift lengths is defined as the *carrier drift length*

$$s \stackrel{\text{def}}{=} s_c + s_v. \tag{3.42}$$

The carrier drift length is the distance that charge carriers in the CB and in the VB drift apart until they are trapped. Using the mobility sum, μ, from Eq. 3.21, one can define the *mobility weighted lifetime*

$$\tau \stackrel{\text{def}}{=} \frac{\tau_v^{(R)}\mu_v + \tau_c^{(R)}\mu_c}{\mu}, \tag{3.43}$$

and rewrite the carrier drift length as

$$s = \tau\mu|\vec{E}|. \tag{3.44}$$

The carrier drift length is proportional to the applied electric field when $|\vec{E}| < E_{sat}$. The carrier drift length saturates at the field strength E_{sat} when the velocity, $\mu\vec{E}$, saturates. An alternative introduction of the carrier drift length via the lifetime weighted mobility can be found in reference [12].

In practice the lifetime of charge carriers can depend on their position in the crystal. This is normally the case in silicon devices where intentional doping concentrations change along a *pn*-junction for example. In CVD diamond the lifetime depends on the position along the direction of growth due to a decrease in impurities and defects from the nucleation to the growth side. This may be explained by the increase in grain size from the nucleation side to the growth side but does not have to. The lifetime may also depend laterally on the position perpendicular to the columnar grains. It may also be that the lifetime depends on the position relative to the grain boundaries. For the case that the lifetime only depends on the position along the direction of growth, the lifetime may be parameterized as a function $\tau(z)$ where z is the position parameter. The lifetime distribution is $\mathrm{d}A/\mathrm{d}\tau$ as a function of τ, where $\mathrm{d}A$ is the number of lifetimes in the interval from τ to $\tau + \mathrm{d}\tau$. The average lifetime over the material thickness, D, is then the first moment of the lifetime distribution

$$\bar{\tau} = \frac{1}{A}\int_{-\infty}^{+\infty} \tau\,\frac{\mathrm{d}A}{\mathrm{d}\tau}(\tau)\,\mathrm{d}\tau \qquad \text{with} \qquad A \stackrel{\text{def}}{=} \int_{-\infty}^{+\infty} \frac{\mathrm{d}A}{\mathrm{d}\tau}(\tau)\,\mathrm{d}\tau \tag{3.45}$$

using

$$\frac{\mathrm{d}A}{\mathrm{d}\tau} = \frac{\mathrm{d}A}{\mathrm{d}z}\frac{\mathrm{d}z}{\mathrm{d}\tau} = \frac{A}{D}\frac{\mathrm{d}z}{\mathrm{d}\tau} \tag{3.46}$$

one finds

$$\bar{\tau} = \frac{1}{D}\int_{-\infty}^{+\infty} \tau(z)\,\mathrm{d}z \overset{\text{Eq. 3.44}}{=} \frac{1}{D}\int_{-\infty}^{+\infty} \frac{s(z)}{\mu\,|\vec{E}|}\,\mathrm{d}z. \tag{3.47}$$

Under the assumption that the electric field does not depend on z one obtains the *average carrier drift length*

$$\bar{s} = \bar{\tau}\,\mu\,|\vec{E}| \qquad \text{with} \qquad \bar{s} = \frac{1}{D}\int_{-\infty}^{+\infty} s(z)\,\mathrm{d}z. \tag{3.48}$$

Fig. 3.7 illustrates $s(z)$ as a function of the position in the material. Since $s(z)$ is a property of the material it is defined for all positions z between $-D/2$ and $+D/2$. Outside of the material s is zero. The limits of the integration in Eq. 3.48 and Eq. 3.47 can therefore be changed to $-D/2$ and $+D/2$.

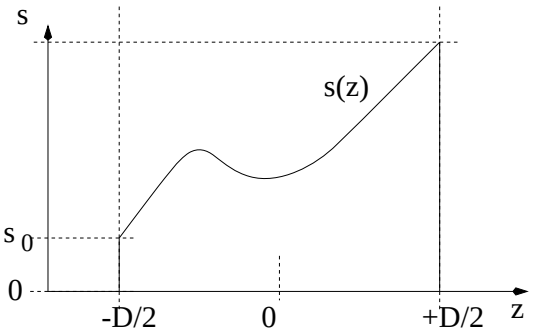

Figure 3.7: Illustration of arbitrary carrier drift length, s, as a function of the position, z, in the material.

3.1.7 Charge Carrier Excitation

Electromagnetic radiation can excite electrons from the VB into the CB leaving a vacant state in the VB. Fig. 3.8 illustrates the excitation process of an electron from the VB to the CB. The vacant state forms an excess carrier in the VB and the electron is an excess carrier in the CB. Both carriers exist 'in excess' of the concentration of carriers at thermal equilibrium. The generation rate of charge carriers in the CB and in the VB is

$$g(t) = \frac{E}{\epsilon\,D}\,f \qquad \text{with} \qquad f = \frac{N^{(\gamma,q)}}{\Delta A \Delta t} \tag{3.49}$$

where E is the energy of the illuminating radiation and ϵ is the specific energy necessary for the excitation of an electron from the VB to the CB. The flux, f, is the number, $N^{(\gamma,q)}$, of photons or charged particles which illuminate a unit area, ΔA, per unit time Δt. It is assumed that the energy transfer is sufficiently high ($E > \epsilon$, see Sec. 3.3.5). The excitation creates the concentration, $n_0 = N^{(\gamma,q)}E/(\epsilon V)$, of charge carriers in the CB and $p_0 = N^{(\gamma,q)}E/(\epsilon V)$ charge carriers in the VB where $V = D\Delta A$ is the uniformly illuminated volume. One could describe a short illumination at the time, t_0, using a delta function or using a Gaussian function [12]

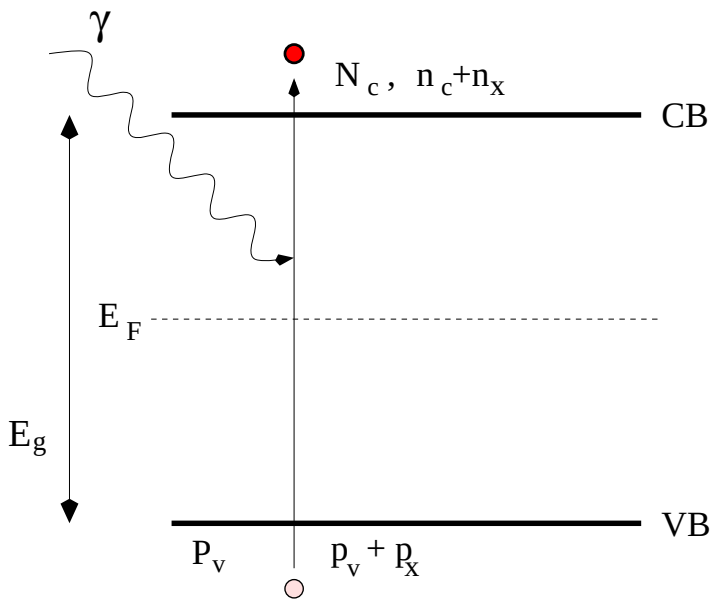

Figure 3.8: Model of charge carrier generation by particle excitation. The electromagnetic radiation γ can be understood as the virtual photon from the traversing charged particle. The virtual photon excites an electron from the VB to the CB leaving a vacant state in the VB.

$$f(t) = \frac{N^{(\gamma,q)}}{\Delta A}\delta(t-t_0) \qquad \text{or} \qquad f(t) = \frac{N^{(\gamma,q)}}{\Delta A\sqrt{2\pi\,\sigma_t^2}}\,e^{-(t-t_0)^2/(2\sigma_t^2)}. \tag{3.50}$$

The standard deviation of the Gaussian function is given by the time of the illumination: for charged particles traversing the material the standard deviation is few picoseconds. Excess charge carriers can participate in the de-trapping and re-trapping process and can undergo recombination with deep traps as it is shown in Fig. 3.6. The transitions for carrier destruction limit the carrier lifetime. If n_x is the concentration of excess carriers in the CB and p_x the concentration of excess carriers in the VB, then one can write the rate equation for the excess carriers [12]

$$\frac{\mathrm{d}n_\mathrm{x}}{\mathrm{d}t} = -\frac{n_\mathrm{x}}{\tau_\mathrm{c}^{(\mathrm{R})}} + g(t) \qquad \text{and} \qquad \frac{\mathrm{d}p_\mathrm{x}}{\mathrm{d}t} = -\frac{p_\mathrm{x}}{\tau_\mathrm{v}^{(\mathrm{R})}} + g(t) \tag{3.51}$$

where $\tau_\mathrm{c}^{(\mathrm{R})}$ and $\tau_\mathrm{v}^{(\mathrm{R})}$ are the lifetimes as given in Eq. 3.36. The initial conditions at the time t_0 are $n_\mathrm{x}(t_0) = n_0$ and $p_\mathrm{x}(t_0) = p_0$. For the case of an excitation by a delta function the solutions are exponentially decreasing concentrations of excess carriers for the time $t > t_0$

$$n_\mathrm{x}(t) \overset{\text{Eq. 3.51}}{=} n_0\,e^{-(t-t_0)/\tau_\mathrm{c}^{(\mathrm{R})}} \qquad \text{and} \qquad p_\mathrm{x}(t) \overset{\text{Eq. 3.51}}{=} p_0\,e^{-(t-t_0)/\tau_\mathrm{v}^{(\mathrm{R})}}. \tag{3.52}$$

These solutions need modification for the case of a Gaussian excitation as they can be found in reference [12].

The lifetimes, $\tau_\mathrm{c}^{(\mathrm{R})}$ and $\tau_\mathrm{v}^{(\mathrm{R})}$, are indeed the first moments (mean values) of the time distributions $|\mathrm{d}n_\mathrm{x}/\mathrm{d}t|$ and $|\mathrm{d}p_\mathrm{x}/\mathrm{d}t|$

$$\frac{1}{n_0}\int_{t_0}^{\infty} t\left|\frac{\mathrm{d}n_x}{\mathrm{d}t}\right|\mathrm{d}t \overset{\text{Eq. 3.52}}{=} t_0 + \tau_\mathrm{c}^{(\mathrm{R})} \qquad \text{and} \qquad \frac{1}{p_0}\int_{t_0}^{\infty} t\left|\frac{\mathrm{d}p_x}{\mathrm{d}t}\right|\mathrm{d}t \overset{\text{Eq. 3.52}}{=} t_0 + \tau_\mathrm{v}^{(\mathrm{R})}. \tag{3.53}$$

where the normalization is

$$n_0 \overset{\text{Eq. 3.52}}{=} \int_{t_0}^{\infty} \left| \frac{\mathrm{d}n_x}{\mathrm{d}t} \right| \mathrm{d}t \quad \text{and} \quad p_0 \overset{\text{Eq. 3.52}}{=} \int_{t_0}^{\infty} \left| \frac{\mathrm{d}p_x}{\mathrm{d}t} \right| \mathrm{d}t. \tag{3.54}$$

3.2 Conductivity

The dark current has been measured on CVD diamond samples. Typical current-voltage curves are shown below.

3.2.1 Experimental Method: Sample Preparation

Fig. 3.1 and Fig. 3.9 show several CVD diamond samples and a silicon diode for comparison. The samples were obtained from references [33] and [34]. The samples were cut from CVD diamond disks (similar to the disk in Fig. 4.21) to a typical size between 5×5 mm^2 and 10×10 mm^2. The sample thickness was typically between 400 μm and 700 μm. The diamond samples were metallized on both sides with ohmic contacts using chromium and gold. Chromium and gold were evaporated onto the clean diamond surface. The chromium had a typical thickness of 600 Å. The gold had a typical thickness of 2000 Å and covered the chromium in order to avoid oxidation of the chromium. The contacts were annealed for 5 minutes at 400 °C in a N_2 atmosphere in order to form chromium-carbide. The carbide gives an ohmic contact between the metal and the diamond. The metallization technique is described also in reference [11].

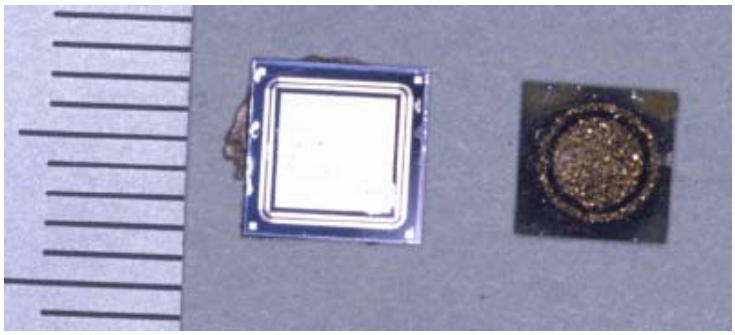

Figure 3.9: Photograph of a silicon diode (left) and of a CVD diamond sample (right). The diamond sample is metallized with ohmic contacts on both sides. The nucleation side has a single circular contact, the growth side a circular contact and a guard ring. The scale is in millimeters.

3.2.2 Experimental Method: Current Measurement

Fig. 3.10 shows the setup for measuring electrical currents in CVD diamond samples. The sample was mounted inside an electrically shielded and light tight aluminium box. A voltage between -1100 V to +1100 V was applied to one contact on the diamond with respect to the other contact using a voltage source (Keithley 237 or Keithley 6517 [66]). The current was measured in series with the diamond bulk. For the case where the sample had a guard structure (ring), the current was also measured in the guard ring. A guard ring around the central contact allows one to measure the bulk current independent of the surface current. Currents for the central contact and the guard ring were measured simultaneously as a function of the applied voltage. The currents were measured under normal conditions and in darkness [7].

[7] *normal conditions*: here (298 ± 3) °K, atmospheric air pressure and humidity.

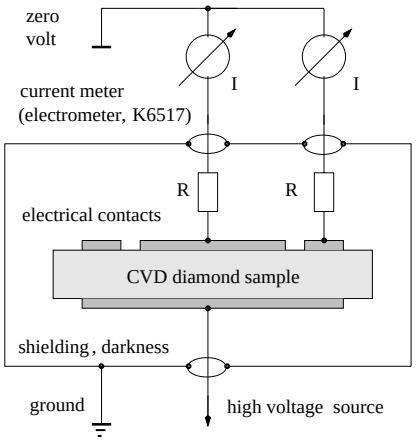

Figure 3.10: Setup for measuring the current in diamond samples with electrical contacts on both sides. The diamond sample was fixed inside an electrically shielded and light tight box. The current was measured using an electrometer (Keithley 6517 [66]), as a function of the high voltage which was supplied by the same instrument.

The contacts on both sides form a plate capacitor with the diamond of thickness, D, between. The electrical field strength between the contacts is

$$|\vec{E}| = \frac{U}{D} \tag{3.55}$$

where U is the applied voltage. The field strength is assumed to be independent of the position in the diamond between the contacts. The direction of the field lines is assumed to be perpendicular to the electrical contacts. In a current measurement, the voltage was slowly increased in steps starting at 0 V, stepping up to 1 V/μm and then decreasing to -1 V/μm and back to 0 V. The voltage was increased with 100 V per step at a rate of one step in 120 s. The current was measured at the end of each time interval, before changing to the next voltage. The currents were acquired automatically using a PC with GPIB interface to the voltage source and the current meter. The acquisition software was written in Labview [67].

3.2.3 Results: Typical Current-Voltage Characteristics

Fig. 3.11 shows the current measured in darkness from two 710 μm thick CVD diamond samples. The current was measured on the central contact (solid markers) and simultaneously on the guard ring (open markers). The smooth curve represents a fit to the average currents and is provided to guide the eye. The current is symmetric for both polarities of the electric field. The current from the center electrode is roughly linear in the electric field interval from -1 V/μm to $+1$ V/μm. The measured current on the central contact was ± 1 pA at ± 1 V/μm in both samples. The central contact had a diameter of 3 mm which allows one to deduce the current density of 0.14 pA/mm^2. The bulk resistivity is

$$\rho \equiv \frac{1}{\sigma} \overset{\text{Eq. 3.23}}{=} \frac{|\vec{E}|}{|\vec{j}|}. \tag{3.56}$$

Assuming a linear relation between the current and the electric field one obtains a resistivity of $\rho = 7 \times 10^{14}$ Ωcm. The current on the guard ring is higher by about one order of magnitude. For $|E| > \pm 0.5$ V/μm the guard ring current increases non-linearly with the electric field.

The current-voltage characteristic of a typical diamond sample can be compared with the typical characteristic of a silicon diode. A diode has a *pn*-junction that works as a current rectifier in contrast to the ohmic (linear) conduction considered so far. The current-voltage characteristic of a diode has an exponential increase of the current in the forward direction (with negative potential applied to the *n*-side). A typical reverse biased current-voltage characteristic from a diode is shown in Fig. 5.30 in Sec. 5.3 (the diode has an implant area of

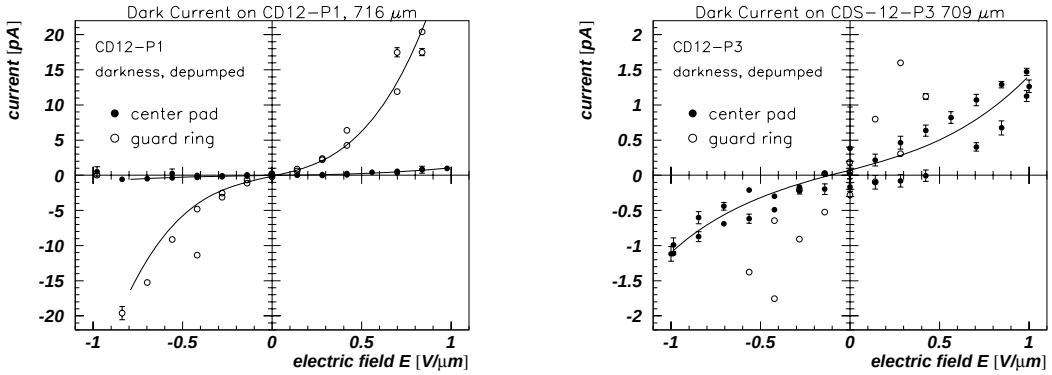

Figure 3.11: Measured current in CVD diamond samples with central contact and guard rings around the central contact. The measurement is shown for two different samples with the full range of the guard current (left) and a magnification on the other sample (right). The polynomial fits are given in order to guide the eye.

4×4 mm^2 and a thickness of 350 μm). A silicon diode is normally operated with a reverse bias voltage which means a positive potential on the n-side relative to the p-side. The current in the reverse biased diode here is 0.5 nA at the depletion voltage of 50 V. The current in this depleted silicon diode is higher than in a CVD diamond sample. It is generally correct to say that CVD diamond samples have a much lower leakage current than silicon samples. More importantly, a CVD diamond does not require a pn-junction like silicon. The junction in a silicon sensor is required in order to raise the resistivity and limit the leakage current at room temperature. A CVD diamond sensor does not need a junction since its resistivity is inherently high and therefore the leakage current is negligibly small at room temperature.

3.2.4 Model of Current Hysteresis

The current-voltage curves from the central contact and from the guard ring generally show hysteresis [Fig. 3.11]. Hysteresis means that the current measured at a given voltage depends on the history of the applied voltage. Hysteresis may be explained by the following model: the contacts on the diamond have a capacitance, C, of the order of the plate capacitance of the contact geometry

$$C \approx \epsilon\,\epsilon_0 \frac{A}{D}. \tag{3.57}$$

A typical capacitance is 0.7 pF for a 500 μm thick CVD diamond sample with A=7 mm^2 contacts. The dielectric constant of CVD diamond is 5.7 [Table 1.1] and ϵ_0 is the permittivity of free space [8]. The current path through the bulk and over the surface can be modelled by a resistor, R_l, in series with the capacitor and a resistor, R_p, in parallel to both, C and R_l, as shown in Fig. 3.12. The relation between the current, I, and the voltage, U, expressed as a differential equation, can be derived from the figure

$$\frac{C \cdot (R_\mathrm{p} + R_\mathrm{l})}{R_\mathrm{p}} \dot{U}(t) + \frac{U(t)}{R_\mathrm{p}} = C\,R_\mathrm{l}\dot{I}(t) + I(t). \tag{3.58}$$

Assuming a linear voltage source, $U(t) = U_0 + mt$, the solution can be found analytically:

[8] The *permittivity of free space* is: $\epsilon_0 = 10^7/(4\pi c^2)$ As/(Vm) = 8.854 pF/m.

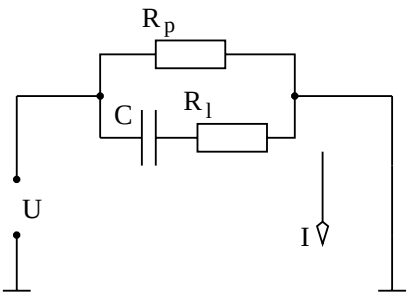

Figure 3.12: Electrical model of a diamond sensor with ohmic contacts on both sides. The contacts have the capacitance C, the current path through the bulk and over the surfaces contains the resistances R_p and R_l.

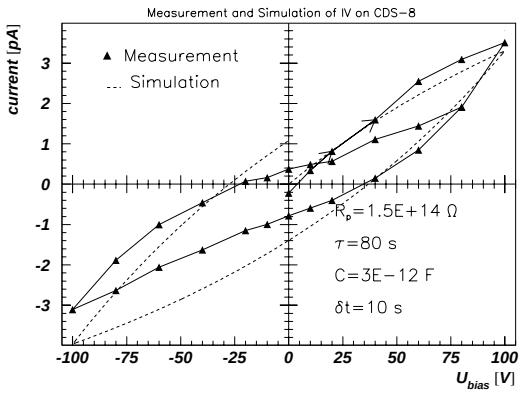

Figure 3.13: Measurement of the current as a function of voltage in diamond sample CDS-8. The measured data is simulated with linear voltage increase of 0.1 V/s using $m = 1/\delta t$ in Eq. 3.59.

$$I(U) = \hat{I}\, e^{-(U-U_0)/(m\,\tau)} + m\,C + \frac{\hat{U}}{R_\mathrm{p}} \qquad ; \qquad \tau \equiv R_\mathrm{l} C. \tag{3.59}$$

The constants $\hat{I}$ and $\hat{U}$ have to be chosen to match the boundary conditions at the turning points of the voltage.

Fig. 3.13 shows a measurement of the current on diamond sample CDS-8 in darkness as a function of voltage. The sample had circular contacts with a size of 20 mm^2 without guard rings. The maximum voltage of ± 100 V corresponds to an electric field strengths of ± 0.16 V/μm. The same figure shows the calculated current from Eq. 3.59 for resistor values $R_\mathrm{p} = 1.5 \times 10^{14}\ \Omega$, $R_\mathrm{l} = 26.6 \times 10^{12}\ \Omega$ and $C = 3$ pF. The expected capacitance [Eq. 3.57] for CDS-8 with a thickness of 645 μm and the contact size of 20 mm^2 is 1.5 pF.

The resistance and the capacitance of the diamond sample determine the *time constant*, τ_RC, on which the current, $I(t)$, equilibrates after changing the external electric field

$$I(t) = I_0\, e^{-t/\tau} + I_\mathrm{inf} \qquad \text{with} \qquad \tau = C R_\mathrm{l}. \tag{3.60}$$

The initial current, I_0, after applying the voltage step $U = U_0 \Theta(t)$ and the current, I_inf, for infinite time can be read from Fig. 3.12

$$I_0 = U_0 \left(\frac{1}{R_\mathrm{p}} + \frac{1}{R_\mathrm{l}} \right) \qquad \text{and} \qquad I_\mathrm{inf} = \frac{U_0}{R_\mathrm{p}}. \tag{3.61}$$

For this diamond sample one finds $\tau^{(\mathrm{di})} \approx 80$ s. This time scale is important to consider when measuring the current in high resistivity CVD diamond samples in general. Silicon has a much shorter time constant: the typical current is 0.5 nA per 16 mm^2 at full depletion of 50 V. The depleted silicon diode [Fig. 3.1], has a capacitance of ≈ 3 pF. With the resistance of 50 V/0.5 nA = 100 GΩ one finds the equilibration time constant $\tau^{(\mathrm{Si})} \approx 0.3$ s which is two orders of magnitude smaller than for diamond. This observation means that for any measurement involving application of a voltage to diamond one has to wait until the current equilibrates before taking the measurement. In order to reduce the error on a current measurement below 10 % one finds

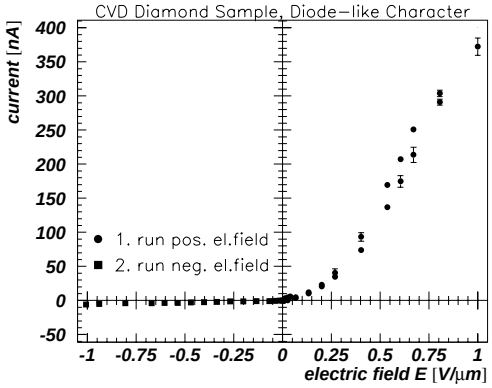

Figure 3.14: Example for a possible current-voltage curve from a CVD diamond sample. This sample deviates from the typical ohmic current-voltage characteristic.

$$\frac{I(t) - I_{\mathrm{inf}}}{I_{\mathrm{inf}}} < 0.1 \qquad \Longrightarrow \qquad t > \tau \, \ln \left[\left(1 + \frac{R_{\mathrm{p}}}{R_{\mathrm{l}}} \right) / 0.1 \right]. \tag{3.62}$$

In order for the measurement to be within 10 % of the final value one must wait 330 s for the case shown here before taking the measurement. In general the term $1 + R_{\mathrm{p}}/R_{\mathrm{l}}$ may vary from 1 to 1000 which corresponds in Eq. 3.62 to a logarithmic factor between 3 and 9. The time, t, to wait is then between 3τ and 9τ which is between 240 s and 720 s for the τ given here.

3.2.5 Results: Diode-like Current-Voltage Curve

Some diamond samples were observed to deviate from the typical and preferred ohmic curve. Fig. 3.14 shows an example of a diode-like current-voltage curve measured in a CVD diamond. The current increases up to 400 nA for positive electric field but remains at a few nanoampere at negative electric field. This is the IV curve of a current rectifier. Several samples had a similar behaviour even after additional re-metallizations which indicates that the rectification is not likely due to the contacts. However, the current-voltage curve always characterizes both the contacts and the diamond sample. Rectifying contacts (Schottky contacts) are possible and can give an asymmetric current-voltage characteristic [36]. It also could be an effect on the surface of the diamond which could not be removed by the cleaning procedure applied before contact preparation. Such samples were not possible to characterize as a particle sensor since their current was too high for the readout amplifier used.

3.2.6 Summary and Discussion

Current-voltage curves were measured for CVD diamond samples with the intention of excluding samples with atypical characteristics. The current-voltage characteristic was normally recorded during charge collection measurements as described in Sec. 3.4. The current measurement described here allows one to quantify the bulk resistivity and the bulk conduction. It was found that a guard ring around a central contact reduces the current in the central contact in comparison to a configuration without guard ring. This effect may be explained by the non-negligible current flow from the contact on one side to the contact on the other side over the diamond surface. A typical current in a CVD diamond sample was of the order of picoamperes using the contact geometry described here. Table 3.1 summarizes results from a typical CVD diamond.

	guarded	not guarded
bulk current at 1 V/μm	≈ 1 pA	(10..30) pA
bulk current density at 1 V/μm	≈ 0.2 pA/mm^2	(1..3) pA/mm^2
current slope at 0 V/μm	≈ 1 pAμm/V	≈ 20 pAμm/V
resistivity, ρ	$\approx 7 \times 10^{14}\Omega$cm	$\approx (0.1..2) \times 10^{14}\Omega$cm

Table 3.1: Typical values of the bulk current from CVD diamond samples tested here. The bulk current is given for a contact size of 7 mm^2 with a biasing field of 1 V/μm. The current slope is given at 0 V/μm and the resistivity, ρ, using Eq. 3.56. The data of the sample with guard ring can be read from Fig. 3.11, the data without guard ring can be read from Fig. 5.36.

The observation that there is a bulk current implies that CVD diamond is not a pure insulator, as might be infered by only considering the large band gap of 5.48 eV. The current can be explained by defects or impurities which act as energy states for de-trapping (DT) and re-trapping (RT) as described in Sec. 3.1.5. The transition rates depend on the defect and impurity concentrations and on the energy level with respect to the VB or to the CB. The measured currents are therefore specific for the class of samples which were available here. Samples from different manufacturers may have different defect and impurity concentration and energy levels and hence different currents. CVD diamond is polycrystalline with columnar crystals from the nucleation to the growth side. Such a structure could suggest current flow preferably along grain boundaries where more defects are likely. Such effects can neither be confirmed nor excluded by the measurement here since the electrodes cover an area much larger than the size of single crystals. The current in the bulk is therefore an average over many crystals and boundaries. Dedicated current measurements on small strip or pad contacts could give more information.

The mechanism of de-trapping depends on the temperature: an increase of the current in diamond is expected from Eq. 3.38. The room temperature currents from the CVD diamond samples here are two orders of magnitude lower than in a silicon diode of similar contact size. The detector leakage current, I_D, of a sensor in a larger detector is important since the power, P, is eventually dissipated as heat

$$P = U\, I_\mathrm{D}. \tag{3.63}$$

A CVD diamond sensor dissipates less heat than a silicon sensor of comparable size. This consideration is particularly important after irradiation with several 10^{14} particles/cm^2 when the leakage current and biasing voltage are much higher for silicon whereas they remain at the same magnitude for a CVD diamond sensor.

3.3 Signal Formation

The signal charge from ionizing particles in solid state detectors depends on the energy deposited along the particle track. The basic description of ionizing particles passing through matter, the energy loss, the energy deposited and the ionization yield are reviewed. Then the signal formation on the electrodes due to moving charges is derived.

3.3.1 Energy Loss of Particles in Matter

When a charged particle traverses a portion of matter, it interacts with the electrons and nuclei of the atoms. Most of these interactions are electromagnetic (quasi-) elastic collisions in which the incoming particle loses energy. One distinguishes between collisions where the energy transferred to the atomic electrons is large enough to extract them from the atom (ionization with production of $\delta-$rays) and collisions where the atomic structure is excited, without complete ionization. The energy transferred to the nuclei is usually negligibly small.

Moderately relativistic charged particles other than electrons lose energy in matter primarily by ionization. Bohr gave the first classical description of such energy loss for heavy charged particles in matter. An approximation, that contains the most important information, for the case of 'slow' moving shell electrons is found as follows [68]: the particle traversing the medium has charge, ze, mass, M, and velocity, βc. The charged particle transfers energy to the shell electrons of atoms in the medium due to the Coulomb interaction. It is assumed that the particle travels sufficiently fast such that the shell electron can be considered to be at rest during the interaction. It is also assumed that the electron mass, m, is much smaller than the particle: $m \ll M$. Then the *transverse momentum transfer* (perpendicular to the motion of the particle) to an electron is

$$\Delta p_{\mathrm{T}} = e\int_{-\infty}^{\infty} |\vec{E}_{\mathrm{T}}(t)|\mathrm{d}t = \frac{2\,e^2\,z}{4\pi\epsilon_0\,b\,c\beta} \qquad \text{with} \qquad |\vec{E}_{\mathrm{T}}| = \frac{ez\gamma b}{4\pi\epsilon_0\,(b^2+\eta^2c^2t^2)^{3/2}}, \tag{3.64}$$

where $|\vec{E_{\mathrm{T}}}|$ is the absolute value of the transverse electric field between the shell electron and the particle at the location of the electron [9]. The transverse electric field contains the longitudinal relativistic distance, ηct, and the transverse distance, b, obtained by Lorentz transformation of the electric field from the moving particle into the coordinate system of the electron. $\gamma \equiv (1+\beta^2)^{-1/2}$ is the relativistic dilatation factor and $\eta \equiv \gamma\beta$. The momentum transfer allows one to calculate the *kinetic energy transfer* to an electron. This only depends on the contribution from transverse momentum transfer since integration over the longitudinal transfer vanishes:

$$-\Delta E = \frac{\Delta p_{\mathrm{T}}^2}{2m}. \tag{3.65}$$

The negative sign indicates that the moving particle loses energy. The *mean differential energy loss* for the charged particle travelling the distance $\mathrm{d}x$ is then

$$-\mathrm{d}\bar{E}_{\text{loss, classic}} = 2\pi\,n\,Z\mathrm{d}x\int \Delta E(b)\,b\,\mathrm{d}b = k\,\varrho\,z^2\,\frac{Z}{A}\frac{1}{\beta^2}\mathrm{d}x\;[\ln B] \tag{3.66}$$

where n is the number of atoms per unit volume which can be expressed using Avogadro's constant, N_A, the atomic mass, A, and the mass density, ϱ, as $n = \varrho\,N_A/A$. The right side of the equation contains the constant

[9] All values in Eq. 3.64 are in MKSA-system units.

$$k \stackrel{\text{def}}{=} 4\pi N_A \frac{e^4}{4\pi\epsilon_0\, mc^2} = 4\pi N_A r_e^2 mc^2 \quad \text{with} \quad r_e = e^2/(4\pi\epsilon_0\, mc^2). \tag{3.67}$$

$r_e = 2.818$ fm is the classical electron radius. For $A = 1$ mol/g : $k/A = 0.307$ MeV g^{-1} cm^2. The value B in Eq. 3.66 only depends on the limits of the integration.

Eq. 3.66 gives the correct dependence of the energy loss on z, Z and ϱ. The $1/\beta^2$ dependence applies for slow moving particles with $\eta < 1$, which actually arises from the Rutherford scattering between two charged, point-like particles. Bohr's classical result included also 'fast' moving shell electrons which adds a second, velocity independent term to Eq. 3.66 and includes the classical evaluation for B in terms of the oscillation frequency of electrons around the nucleus.

The quantum mechanical description of the mean ionizing energy loss by Bethe and Bloch gives B as a function of the energy transfer and the excitation energy, I. If the incident particle velocity, βc, is larger than that of orbital electrons and small enough that radiative effects do not matter then the *mean rate of energy loss in matter* is [9, 69]

$$-\left(\frac{\mathrm{d}\bar{E}}{\mathrm{d}x}\right)_{\text{loss}} = k\,\varrho\, z^2\, \frac{Z}{A}\frac{1}{\beta^2}\left[\frac{1}{2}\ln\left(\frac{2\,m\,c^2\,\eta^2\,T_{\max}}{I^2}\right) - \beta^2 - \frac{\delta}{2}\right], \tag{3.68}$$

which has the same value in front of the brackets as in Eq. 3.66. $T_{\max}$ is the maximum kinetic energy which can be imparted to a free electron in a single collision

$$T_{\max} = \frac{2mc^2\eta^2}{1 + 2\gamma m/M + (m/M)^2}. \tag{3.69}$$

For $\eta > 1$: $T_{\max} \approx \eta^2$ [MeV].

The logarithm in Eq. 3.68 contains the excitation energy, I, of the medium. The excitation energy per Z is $I/Z \approx 10$ eV for most elements with $Z > 35$. For diamond the excitation energy is $I^{(\text{di})} = (78 \pm 6)$ eV [9]. The electric field of very fast charged particles is limited by polarization in the medium which is known as the *density effect*. Eq. 3.68 includes therefore a density correction, δ, which truncates the logarithmic rise at very high energies ($\eta > 10$). The energy loss by electrons and positrons is not described by Eq. 3.68. The dominant source of energy loss for electrons and positrons is bremsstrahlung and requires a different description given by the Bethe-Heitler formula.

The density correction, δ, can be calculated following Sternheimer's parameterization in reference [70, 71]

$$\delta = \begin{cases} 0 & : \quad X \le X_0 \\ 4.6052\,X + C_0 + a(X_1 - X)^m & : \quad X_0 < X < X_1 \\ 4.6052\,X + C_0 & : \quad X \ge X_1 \end{cases} \tag{3.70}$$

with $X = \log_{10}(\eta)$. The quantities X_0, X_1, C_0, a and m depend on the absorbing material. They are listed in Table 3.2 for air, plastic scintillator, silicon, graphite and diamond. The values for diamond could not be found in the literature. The values from graphite were used for the density correction in diamond.

Material	Density [g/cm^3]	I [eV]	C_0	a	m	X_0	X_1
air,(20°C,1atm)	1.29	85.7	-10.6	0.1091	3.40	1.742	4.28
plastic scintillator	1.032	64.7	-3.20	0.1610	3.24	0.1464	2.49
silicon	2.33	173	-4.44	0.1492	3.25	0.2014	2.87
graphite	2.0	78	-2.99	0.2024	3.0	-0.0351	2.486
diamond	3.515	78	assume correction from graphite				

Table 3.2: Constants for the density effect correction. The constants for the materials except diamond are taken from reference [71]. The values for diamond are assumed to be equal to those for graphite.

Division of Eq. 3.68 by the mass density gives the stopping power. Fig. 3.15 shows the stopping power for pions ($M = 140$ MeV/c^2) in diamond, silicon and plastic scintillator derived from Eq. 3.68 as a function of η. The graphs were evaluated without density correction ($\delta = 0$). The energy loss in each medium decreases like $\propto 1/\beta^2$ for $\eta < 1$. At $\eta \approx 3$ the energy loss has a minimum. Particles which lose the minimum amount of energy are called *minimum ionizing particles* (*mip*'s). The energy loss increases logarithmically with η^2 for $\eta > 3$. The stopping power shifts upwards for lower Z material and shifts downwards for high Z material [9]. The stopping power curves are about the same for muons, protons and pions with a minimum at $\eta = 3$.

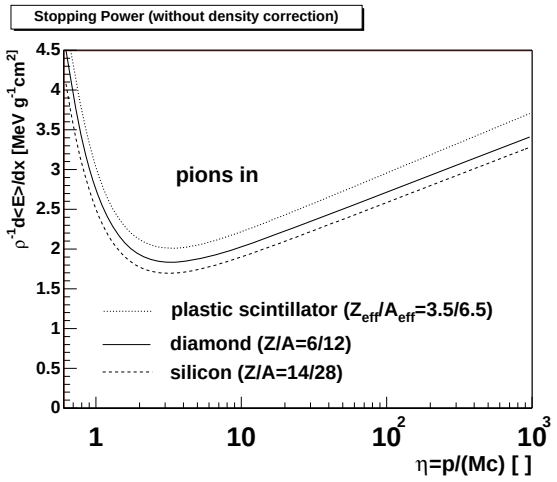

Figure 3.15: Stopping power for pions in diamond, silicon and plastic scintillator as a function of η which is the ratio between the particle momentum, p, and the particle mass, M. The graphs were evaluated for the Bethe-Bloch formula, Eq. 3.68, without density correction.

The energy loss calculated using Eq. 3.68 and the density correction using the values in Table 3.2 for a particle with $\eta = 3$ in silicon is

$$\left(\frac{\mathrm{d}\bar{E}}{\mathrm{d}x}\right)_{\text{loss in si}} = \begin{cases} 1.70\ \text{MeVcm}^2/\text{g} \times 2.33\ \text{g/cm}^3 = 119\ \text{keV}/300\ \mu\text{m} & : \quad \delta = 0 \\ 1.67\ \text{MeVcm}^2/\text{g} \times 2.33\ \text{g/cm}^3 = 117\ \text{keV}/300\ \mu\text{m} & : \quad \text{with } \delta \end{cases} \tag{3.71}$$

and for a particle with $\eta = 3$ in diamond is

$$\left(\frac{\mathrm{d}\bar{E}}{\mathrm{d}x}\right)_{\text{loss in di}} = \begin{cases} 1.84\ \text{MeVcm}^2/\text{g} \times 3.515\ \text{g/cm}^3 = 194\ \text{keV}/300\ \mu\text{m} & : \quad \delta = 0 \\ 1.76\ \text{MeVcm}^2/\text{g} \times 3.515\ \text{g/cm}^3 = 186\ \text{keV}/300\ \mu\text{m} & : \quad \text{with } \delta \end{cases} . \tag{3.72}$$

Using the density correction the calculated energy losses agree with the values given by the Particle Data Group in reference [9]. It should be noted that the density correction for diamond was taken to be the correction as in graphite.

3.3.2 Restricted Energy Loss of Particles

In general the charge signal depends on the energy deposited along the particle track in the detector rather than the energy lost. Some of the energy lost by a fast charged particle is removed from the vicinity of its track by secondary electrons or by Cerenkov radiation (photons). The mean rate of energy deposited along the track in the detector is then described by the *mean restricted energy loss rate*

$$-\left(\frac{\mathrm{d}\bar{E}}{\mathrm{d}x}\right)_{\text{restr.}} = k\,\varrho\,z^2\,\frac{Z}{A}\frac{1}{\beta^2}\left[\frac{1}{2}\ln\left(\frac{2\,m\,c^2\,\eta^2\,T_{\text{upper}}}{I^2}\right) - \frac{\beta^2}{2}\left(1+\frac{T_{\text{upper}}}{T_{\max}}\right) - \frac{\delta}{2}\right] \tag{3.73}$$

where $T_{\text{upper}} = \min(T_{\text{cut}}, T_{\max})$ [9]. The Bethe-Bloch formalism describes the mean energy loss *rate*. The mean energy deposited in the detector by a charged particle travelling the distance, a, is

$$\bar{E}_{\text{dep}}(a) = \int_0^a \left(\frac{\mathrm{d}\bar{E}}{\mathrm{d}x}\right)_{\text{restr.}} \mathrm{d}x \approx a \cdot \left(\frac{\mathrm{d}\bar{E}}{\mathrm{d}x}\right)_{\text{restr.}} . \tag{3.74}$$

The approximation to the right is true if $(\mathrm{d}\bar{E}/\mathrm{d}x)_{\text{restr.}}$ is independent of the travelling distance in the medium. This is correct as long as $\eta > 3$. In case of $\eta < 3$ the particle slows down. As a particle slows down, its rate of energy loss changes as its kinetic energy changes and more energy per unit length is deposited towards larger travelling distance: the particle eventually stops in the medium. The curve E_{dep} as a function of the penetration depth a is called the Bragg curve. α-particles, for example, penetrate only few microns in silicon and diamond. β-particles from ^{90}Sr typically penetrate several hundred microns of silicon or diamond. Beam particles like protons (p), pions (π) or muons (μ) with typically 5 GeV/c to 100 GeV/c traverse several centimeters of matter without significant velocity loss.

Fig. 3.16 shows the mean ionizing energy loss rates in silicon (left) and in diamond (right) for pions. Each figure shows the energy loss according to Eq. 3.68 and the restricted energy loss from Eq. 3.73. Here the restricted energy loss was calculated using $T_{\text{cut}} = 140$ keV in silicon and in diamond for reasons given in Sec. 3.3.5. The restricted energy loss smoothly joins the energy loss from Eq. 3.68 for $T_{\text{cut}} > T_{\max}$. From Fig. 3.16 one can read the restricted energy loss rates of 97 keV/300 μm silicon and 156 keV/300 μm diamond for pions with $\eta = 3$ with density correction.

The Bethe-Bloch formalism does not include energy loss due to radiation. Radiation loss is negligible for heavy particles ($M > m$). When an electron or a photon is incident on matter, it initiates an electromagnetic cascade by pair production and bremsstrahlung. The mean distance over which a high energy electron loses all but $1/e$ of its energy by bremsstrahlung is the *radiation length* [9]

$$X_0 = \frac{716.4\ \text{g/cm}^2\,A}{\varrho\,Z\,(Z+1)\ln(287/\sqrt{Z})}. \tag{3.75}$$

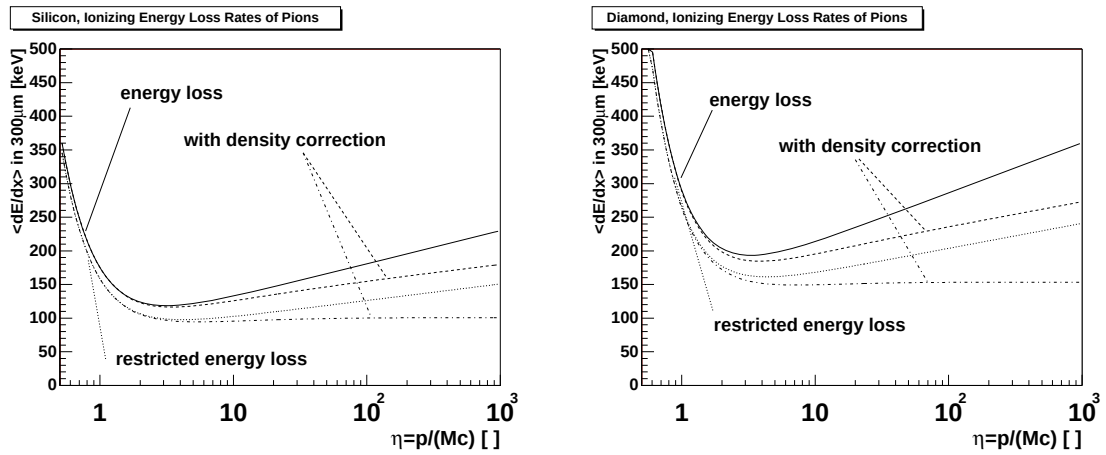

Figure 3.16: Energy loss rate and restricted energy loss rate as a function of η in silicon (left) and in diamond (right). The graphs are given for the cases with density correction and without density correction.

The radiation length in a mixture or a compound may be approximated by [9]

$$\frac{1}{\bar{X}_0} = \sum_j \frac{w_j}{X_0^{(j)}} \quad \text{with} \quad w_j = \frac{D_j}{\sum_j D_j}. \tag{3.76}$$

The radiation length is $X_0^{(\mathrm{di})} = 12.2$ cm for diamond and $X_0^{(\mathrm{si})} = 9.36$ cm for silicon. A typical configuration in particle beam tests, as described in Chapter 4, contains $D_{\mathrm{si}} \approx 2.4$ mm silicon and $D_{\mathrm{di}} \approx 2$ mm diamond which gives a radiation length, $\bar{X}_0 \approx 10.53$ cm. This configuration has a thickness corresponding to $(\sum_j D_j)/\bar{X}_0 = \sum_j (D_j/X_0^{(j)}) \approx 4.2\,\%$ of the radiation length of the setup. The radiation length is important since it is used in the calculation of multiple scattering of high energetic particles from thin layers [Eq. 1.12].

3.3.3 Fluctuations of Energy Loss

The amount of energy loss is subject to two sources of fluctuations. The number of collisions varies as does the energy lost in each collision. For N collisions the number of collisions varies like $\sqrt{N}$. The number of collisions is proportional to the thickness of the absorber and hence the relative variation per path length is $1/\sqrt{N}$. Therefore in the limit of very thick absorbers the fluctuations due to the number of collisions vanishes. The energy loss distribution function is called the *straggling function*. The straggling functions for thick absorbers have a Gaussian form. Thin absorbers have an asymmetric distribution with a mean value higher than the most probable value. A first description of energy straggling for thin absorbers was given by Landau resulting in the Landau energy straggling function which depends only on one parameter [72]. In Landau's derivation three assumptions were made. The most important assumption is that the incoming particle can transfer all its energy to a single shell electron which can be mathematically described by infinite energy transfer. This is the reason why Landau's straggling function has an infinite mean value. The second assumption is that the shell electrons are free. The third assumption is that the traversing particle does not lose velocity. The last assumption is true if the absorber is thin which means

$$\kappa \stackrel{\mathrm{def}}{=} \frac{\xi}{T_{\max}} \ll 1 \quad \text{with} \quad \xi \stackrel{\mathrm{def}}{=} k\,\varrho\,\frac{z^2}{\beta^2}\frac{Z}{A}x, \tag{3.77}$$

where x is the thickness of the absorber. A 500 μm thick diamond sensor illuminated with minimum ionizing particles from a $\beta-$source can be considered as thin since κ is of the order of 10^{-2}. Landau's straggling function can be used to fit measured energy loss spectra. The measured spectrum is always a convolution of the energy loss straggling function with functions due to other processes. A description of energy loss straggling in thin silicon sensors is given in reference [15].

3.3.4 Energy for Charge Carrier Generation

The energy, ϵ_c, to create an electron-hole pair in a semi-conductor is always higher than its band gap energy. This is attributed to the additional excitation of phonon and plasmon states. Phonon excitation transfers energy to the lattice and plasmon excitation transfers energy to the collective excitation of electrons. An attempt to calculate ϵ_c has been made in reference [16]. Measurements of ϵ_c have been summarized in the same article. Fig. 3.17 shows the energy for pair creation as a function of the band gap for various semi-conductors. One can see that, ϵ_c, is proportional to the band gap, E_g. Fitting the data with a linear function gives

$$\epsilon_c(E_g) = 1.76 \text{ eV} + 1.84 \cdot E_g. \qquad (3.78)$$

The energy, $\epsilon_c^{(di)}$, required to create an electron-hole pair in diamond has been measured from the ratio of pulse heights in a natural diamond sensor compared to a silicon sensor in response to ionizing radiation [13, 17]. Such measurement requires that all the generated charge carriers are collected at the electrodes of the silicon and diamond sensor. This assumption is normally true for a fully depleted silicon diode, but not necessarily true for a diamond sensor. The measured energy in diamond is [13, 17]

$$\epsilon_c^{(di)} \approx 13 \text{ eV}. \qquad (3.79)$$

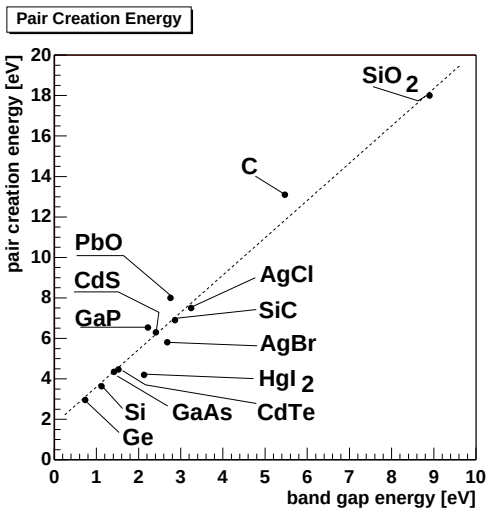

Figure 3.17: The measured energy for electron-hole pair creation as a function of the band gap for various semi-conductors at room temperature. The data is taken from the collection in reference [16].

This value was obtained with α and β-particles. The energy, $\epsilon_c^{(si)}$, required to create an electron-hole pair in silicon is [15, 16]

$$\epsilon_c^{(si)} \approx 3.6 \text{ eV}. \qquad (3.80)$$

3.3.5 Ionization Yield

Fig. 3.18 illustrates the creation of an electron-hole pair by ionizing radiation. The passing particle with charge ze transfers energy to an electron in the valence band (VB). The energy excites the electron into the conduction band (CB). The excited electron is an excess charge carrier. An applied external electric field causes the excess carriers to drift along the field lines which results in an electric current: the particle induced current or excess current.

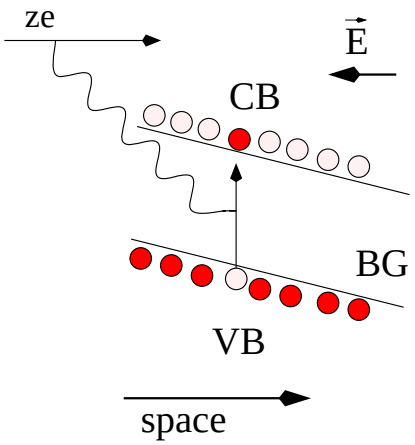

Figure 3.18: Creation of an excess carrier: a passing particle with charge, ze, transfers energy to an electron in the valence band (VB). This energy excites an electron in to the conduction band (CB). The excited electron is an excess charge carrier. The applied external electric field $\vec{E}$ causes the excess carriers to drift along the field lines which results in an electric current (particle induced current or excess current).

The total mean energy deposited, $\bar{E}_{\text{dep}}$ from Eq. 3.74, and the carrier creation energy determine the *number of generated electron-hole pairs*

$$\bar{N}_{\text{gen}} = \frac{\bar{E}_{\text{dep}}(x)}{\epsilon_{\text{c}}} \overset{\text{Eq. 3.74}}{\approx} \frac{x}{\epsilon_{\text{c}}} \left(\frac{\mathrm{d}\bar{E}}{\mathrm{d}x} \right)_{\text{restr.}} \tag{3.81}$$

where the right approximation holds for negligible change of the energy loss rate along the path distance, x, in the material. The *mean ionization yield* is then

$$\bar{Q}_{\text{gen}} \overset{\text{def}}{=} e\, \bar{N}_{\text{gen}}. \tag{3.82}$$

If the particle enters perpendicular to the surface of a planar material, then the path distance, x, equals the thickness, D, and the mean ionization yield is

$$\bar{Q}_{\text{gen}} = \frac{e\, D}{\epsilon_{\text{c}}} \left(\frac{\mathrm{d}\bar{E}}{\mathrm{d}x} \right)_{\text{restr.}}. \tag{3.83}$$

For the following discussion we *assume* the most probable ionization yield in 300 μm silicon

$$\hat{Q}_{\text{gen}}^{(\text{defined})} \overset{\text{def}}{=} 22500\ e \quad \text{from a } \textit{mip} \text{ in 300 } \mu\text{m silicon} \tag{3.84}$$

where the '^' indicates the most probable value. This most probable ionization yield is commonly used in the discussion of the ionization yield of silicon detectors [10]. This value for the most probable ionization yield in silicon as defined in Eq. 3.84 is the basis for further calculations. From Fig. 4.19 in Sec. 4.1.8 one finds the measured ratio of 1.2 between the mean and the most probable ionization yield in 300 μm thick silicon. This implies a mean ionization yield of

$$\bar{Q}_{\text{gen}}^{(\text{derived})} = 27000\ e \quad \text{from a } \textit{mip} \text{ in 300 } \mu\text{m silicon.} \tag{3.85}$$

Using Eq. 3.83 one obtains the mean restricted energy loss of a *mip* in 300 μm thick silicon

$$\left(\frac{\mathrm{d}\bar{E}}{\mathrm{d}x} \right)_{\text{restr. in si}} = 97.2 \text{ keV}/300\ \mu\text{m}. \tag{3.86}$$

This mean restricted energy loss can also be derived from Eq. 3.73 using a cut-off energy of $T_{\text{cut}} = 140$ keV. This is the reason for the cut-off energy chosen in Fig. 3.16. The ratio

[10] This value is based on reference [73]. Another most probable value of 25000 e in 300 μm silicon is proposed in reference [9].

between the mean energy loss [Eq. 3.71] and the mean restricted energy loss [Eq. 3.71] in 300 μm thick silicon is 1.21. If one assumes for diamond the same ratio between the mean energy loss and the mean restricted energy loss one obtains from Eq. 3.72

$$\left(\frac{\mathrm{d}\bar{E}}{\mathrm{d}x}\right)_{\text{restr. in di}} = 154 \text{ keV}/300 \ \mu\text{m}. \tag{3.87}$$

This result is consistent with the mean restricted energy loss of 156 keV/300 μm derived for $T_{\text{cut}} = 140$ keV in Sec. 3.3.2. Using Eq. 3.83 one obtains the mean ionization yield in 300 μm thick diamond

$$\bar{Q}_{\text{gen}}^{(\text{derived})} \approx 11850 \ e \ \text{ from a } \textit{mip} \text{ in 300 } \mu\text{m diamond}. \tag{3.88}$$

If one assumes that the ratio between mean energy loss and mean restricted energy loss is the same for 100 μm thickness then one obtains the *(derived) mean ionization yield in 100* μm *diamond*

$$\bar{Q}_{\text{gen}}^{(\text{derived})} \approx 3950 \ e \ \text{ from a } \textit{mip} \text{ in 100 } \mu\text{m diamond} \tag{3.89}$$

which is within 10 % of the commonly *in-use mean ionization yield in 100* μm *diamond* [11]

$$\bar{Q}_{\text{gen}}^{(\text{in-use})} \approx 3600 \ e \ \text{ from a } \textit{mip} \text{ in 100 } \mu\text{m diamond}. \tag{3.90}$$

We will use the mean ionization yield from Eq. 3.90 in the discussion which follows.

Table 3.3 summarizes the mean energy loss, the mean restricted energy loss, the mean and most probable ionization yield in 300 μm thick silicon (top) and the derived values in 300 μm thick diamond (bottom). The values for the ionization yield in silicon from Eq. 3.84 and diamond from Eq. 3.90 are the basis for further calibration in calculations of the collected charge in diamond.

silicon with $\epsilon_{\text{c}}^{\text{si}} = 3.6$ eV, *mip* ($\eta \approx 3$)		
		$D = 300$ μm
$D \cdot (\mathrm{d}\bar{E}/\mathrm{d}x)_{\text{loss}}^{(\text{derived})}$	[keV]	117
$D \cdot (\mathrm{d}\bar{E}/\mathrm{d}x)_{\text{restr.}}^{(\text{derived})}$	[keV]	97
$\bar{Q}_{\text{gen}}^{(\text{derived})}$	$[e]$	27000
$\hat{Q}_{\text{gen}}^{(\text{defined})}$	$[e]$	22500
diamond with $\epsilon_{\text{c}}^{\text{di}} = 13$ eV, *mip* ($\eta \approx 3$)		
		$D = 300$ μm
$D \cdot (\mathrm{d}\bar{E}/\mathrm{d}x)_{\text{loss}}^{(\text{derived})}$	[keV]	186
$D \cdot (\mathrm{d}\bar{E}/\mathrm{d}x)_{\text{restr.}}^{(\text{derived})}$	[keV]	154
$\bar{Q}_{\text{gen}}^{(\text{derived})}$	$[e]$	11850

Table 3.3: Mean energy loss, the mean restricted energy loss, the mean and most probable ionization yield in 300 μm thick silicon (top) and the derived values in 300 μm thick diamond (bottom). The values were obtained from Eq. 3.68, Eq. 3.73 and Eq. 3.83 using the density correction from Table 3.2.

3.3.6 Charge Collection Mechanism

The ionization yield is the charge which potentially could be collected at the electrodes. However, the actual induced charge may differ depending on material parameters and operating conditions of the sensor. The ratio between the induced charge (that is the measured charge) on the electrodes and the ionization yield is expressed as the *charge collection ratio*

$$\epsilon_{\mathrm{r}} \stackrel{\mathrm{def}}{=} \frac{\bar{Q}_{\mathrm{ind}}}{\bar{Q}_{\mathrm{gen}}}. \tag{3.91}$$

The ratio is between 0 and 1 for the case of no charge carrier multiplication and no photoconductive gain. The charge collection ratio does not yet allow one to extract information about the electrical properties of the sensor material. It is instead necessary to understand the charge collection mechanism.

Any silicon or diamond sensor measures the *induced charge* on its electrodes. A charge is induced on the electrodes by the movement of excess charge carriers in the sensor material. The method of multiple *image charges* is used here to calculate the induced charge at the electrodes.

3.3.6.1 Fixed Single Charge

Fig. 3.19 shows a conductive plate at a position $+D/2$. The plate is kept at a constant electric potential, $+\Phi/2$, where the potential at infinity is defined to be zero. A single charge, q, is *fixed* at the position, a, below a conductive plate. The induced charge on the plate may be calculated using the image charge method. The cylindrical coordinates, ρ and z, are chosen according to the symmetry of this configuration. The boundary condition, $\Phi(\rho, z = D/2; a) = \Phi/2$, defines the position and charge value of the image charge. In order to satisfy the boundary condition it can be shown that the charge at a has a single image charge of opposite sign at $D-a$ where the conductive plate is the mirror plane [68]. The total potential, $\Phi(\rho, z; a)$, is found by superposition of the potentials from the original charge, the image charge and the potential of the plate given by the boundary condition [11]. Once the potential is known one can calculate the derivative of the potential evaluated at $z = D/2$ to obtain the *surface charge density on the plate*

$$\sigma(\rho; a) = -\frac{1}{4\pi}\partial_z \Phi(\rho, z; a)|_{z=D/2}. \tag{3.92}$$

The induced surface charge density is a function of the radial coordinate, ρ, and the position, a, of the original charge [68]. A circular surface region with radius, R, can be chosen in the conductive plate where the region is centered around the axis between charge and image charge. The induced charge, $q_{\mathrm{ind}}(a; R)$, on the plate is then calculated by integration over this surface region

$$q_{\mathrm{ind}}(D/2 - a; R) = \int_0^{2\pi} \mathrm{d}\phi \int_0^R \sigma(\rho; a)\, \rho \, \mathrm{d}\rho = -q + \frac{(D/2 - a)q}{\sqrt{R^2 + (D/2 - a)^2}}. \tag{3.93}$$

The induced charge approaches $-q$ in the limit of large radius:

$$q_{\mathrm{ind}} = -q \qquad \text{for} \qquad (D/2 - a)/R \ll 1. \tag{3.94}$$

[11] It should be noted that the description here assumes vacuum and in particular equal dielectric constants on both sides of the plate.

That means that a single fixed charge below the conductive plate induces the opposite charge on the surface of the conductive plate.

Fig. 3.21 shows a configuration with two conductive plates. The second plate is parallel

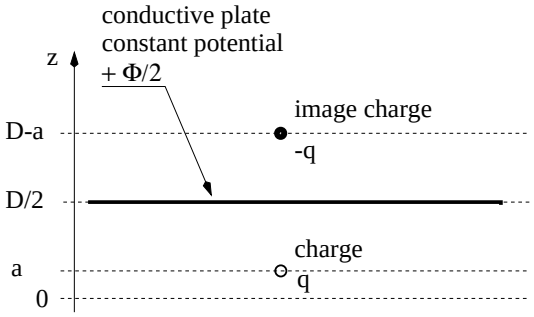

Figure 3.19: A single fixed charge, q, below a conductive plate at position, a. The potential of the plate is constant. The induced charge on the conductive plate can be found using an image charge, $-q$, located at $D - a$.

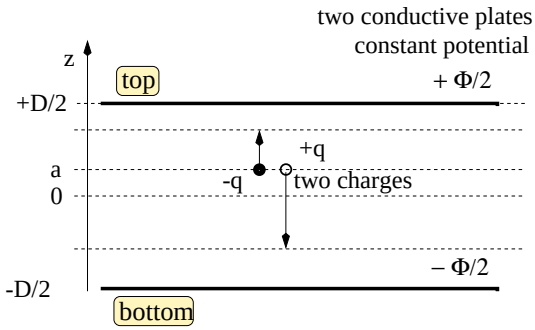

Figure 3.20: Two charges $(q, -q)$ starting at a position a, moving between two conductive plates in opposite directions by distances d_n and d_p respectively.

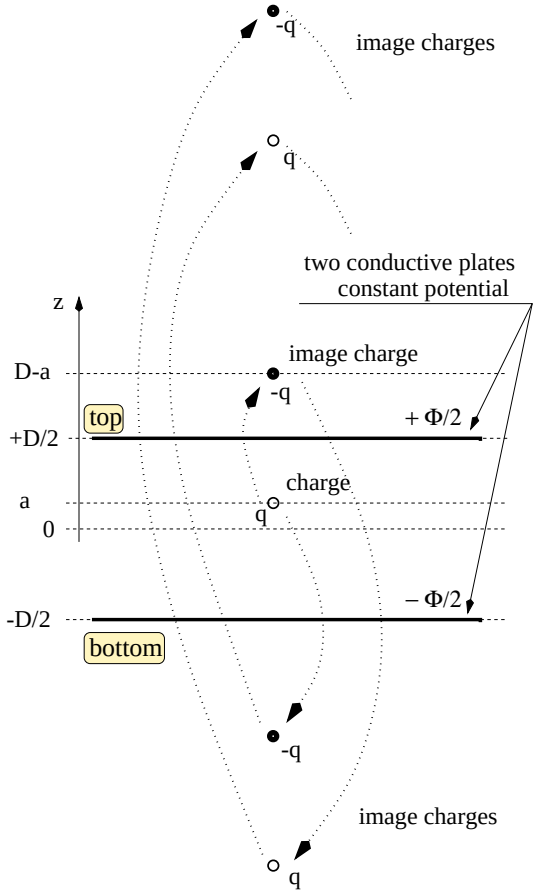

Figure 3.21: Single fixed charge, q, between two conductive plates. The induced charge in a plate can be calculated using the method of multiple image charges.

to the first plate and located at position, $-D/2$. The distance between the plates is D. The second plate is kept on a constant potential, $-\Phi/2$. The charge, q, is fixed between the plates and again located at position, a. In order to calculate the induced charge on the upper plate one can use the method of *multiple image charges*. The image charges are shown in Fig. 3.21. All image charges lie on one axis. Their potentials can be superimposed and the resulting potential is expressed as an infinite sum. Using Eq. 3.92, followed by integration over a surface region with radius R, gives the *total induced charge on the top plate*

$$q_\mathrm{ind}^\mathrm{(top)}(a; D, R) = \frac{q}{2} \sum_{k=-\infty}^{\infty} \left(\frac{2kD - D + a}{\sqrt{R^2 + (2kD - D + a)^2}} + \frac{2kD + a}{\sqrt{R^2 + (2kD + a)^2}} \right). \tag{3.95}$$

Fig. 3.22 shows the induced charge on one plate as a function of the normalized position, a/D, of the original charge between the plates obtained from a numerical summation from Eq. 3.95. A distance, $D = 0.5$ mm, between the plates was chosen for the calculation. The

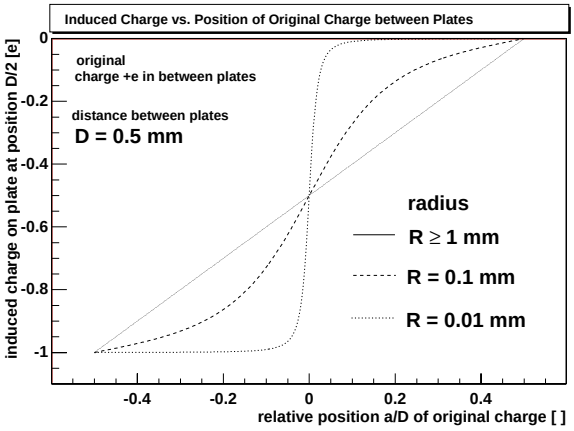

Figure 3.22: Induced charge on one plate as a function of the position of the single charge between the plates, calculated using Eq. 3.95. The distance between the plates was chosen to be 0.5 mm. The radius, R, of the area that measures the induced charge is a parameter. Three graphs are shown for different values of R.

graphs are plotted for different radii, R. The radius, R, represents the area over which the charge is collected. For the case of $R \geq D$ the induced charges on the top and on the bottom plates follow to a very good approximation the linear relations

$$q_{\rm ind}^{\rm (top)} = -\left(\frac{D/2-a}{D}\right) q \quad \text{and} \quad q_{\rm ind}^{\rm (bottom)} = -\left(\frac{D/2+a}{D}\right) q. \tag{3.96}$$

The position, a, may take any value between $-D/2$ and $+D/2$. If the charge is near the top at $a \approx D/2$, one finds $q_{\rm ind}^{\rm (top)} \approx 0$ and $q_{\rm ind}^{\rm (bottom)} \approx -q$. The sum of the charges, $q_{\rm ind}^{\rm (top)}$ and $q_{\rm ind}^{\rm (bottom)}$, induced on the top and on the bottom plate by the *fixed* charge is

$$q_{\rm ind}^{\rm (top)} + q_{\rm ind}^{\rm (bottom)} = -q. \tag{3.97}$$

Charge is conserved.

3.3.6.2 Moving Single Charge

In the derivation of the previous section the charge was fixed. If the charge is moved a distance, $\mathrm{d}z$, between the plates then a change, $\mathrm{d}q_{\rm ind}$, in the induced charge is observed on the plates. Eq. 3.96 gives the *change in the induced charge* as the charge moves by $\mathrm{d}z$:

$$\mathrm{d}q_{\rm ind}^{\rm (top)} = +\frac{q}{D}\mathrm{d}z \quad \text{and} \quad \mathrm{d}q_{\rm ind}^{\rm (bottom)} = -\frac{q}{D}\mathrm{d}z \quad \text{for} \quad \frac{D}{R} < 1. \tag{3.98}$$

The total charge induced on one plate by moving a charge the distance from a to $a+r$ with $r > 0$ is

$$q_{\rm ind}^{\rm (top)} = +\frac{q}{D}\int_a^{a+r} \mathrm{d}z = +\frac{q}{D}\,r \quad \text{and} \quad q_{\rm ind}^{\rm (bottom)} = -\frac{q}{D}\int_a^{a+r} \mathrm{d}z = -\frac{q}{D}\,r. \tag{3.99}$$

The sum of the charges, $q_{\rm ind}^{\rm (top)}$ and $q_{\rm ind}^{\rm (bottom)}$, induced on the top and on the bottom plate by the single *moving* charge is

$$q_{\rm ind}^{\rm (top)} + q_{\rm ind}^{\rm (bottom)} = 0. \tag{3.100}$$

3.3.6.3 Charge Pair Moving in Opposite Directions

Fig. 3.20 shows the configuration of two conductive plates a distance, D, apart with two charges of opposite sign located at a distance, a, from zero. For the case where both charges are fixed one finds that the sum of induced charges on each plate is zero as can be seen by applying Eq. 3.96 to both charges:

$$q_{\text{ind}}^{(\text{top})}\Big|_{\text{by }\bullet} + q_{\text{ind}}^{(\text{top})}\Big|_{\text{by }\circ} = 0 \qquad \text{and} \qquad q_{\text{ind}}^{(\text{bottom})}\Big|_{\text{by }\bullet} + q_{\text{ind}}^{(\text{bottom})}\Big|_{\text{by }\circ} = 0, \tag{3.101}$$

where the '$\circ$' denotes the fixed positive charge and '$\bullet$' denotes the fixed negative charge.

For the case where the plates are kept at different potentials $+\Phi/2$ and $-\Phi/2$ respectively, an electric field, $\vec{E}$, exists between the plates

$$\vec{E} = -\nabla\Phi \overset{\text{here}}{=} -\partial_z\Phi(z). \tag{3.102}$$

The electric field is oriented perpendicular to the plates. The force, $+q\vec{E}$, acts on the charge, $+q$, and the force, $-q\vec{E}$, acts on the charge, $-q$. The force pulls the charges in opposite directions. The negative charge, $-q$, moves to the plate with the positive potential, whereas the positive charge moves to the plate with the negative potential. The moving charges induce a charge on the plates according to Eq. 3.98. Their movement starts from the same position, a. The positive charge is assumed to move the distance, $r_{\text{p}}(a)$, away from the top plate and the negative charge is assumed to move the distance, $r_{\text{n}}(a)$, towards the top plate. The distance each charge moves may depend on the position, a, from where the charges start travelling. The distance travelled are defined to be positive quantities. The induced charge, $q_{\text{ind}}^{(\text{top})}$, on the top plate generated by such movement is

$$q_{\text{ind}}^{(\text{top})}(a) = \int_a^{a+r_{\text{n}}(a)} \frac{-q}{D}\,\mathrm{d}z + \int_a^{a-r_{\text{p}}(a)} \frac{+q}{D}\,\mathrm{d}z = -\frac{q}{D}\left[r_{\text{n}}(a) + r_{\text{p}}(a)\right]. \tag{3.103}$$

and on the bottom plate

$$q_{\text{ind}}^{(\text{bottom})}(a) = +\frac{q}{D}\left[r_{\text{n}}(a) + r_{\text{p}}(a)\right]. \tag{3.104}$$

These expressions suggest that one should define the *charge collection distance*[12]

$$d(z) \overset{\text{def}}{=} r(z) \overset{\text{def}}{=} r_{\text{n}}(z) + r_{\text{p}}(z). \tag{3.105}$$

The charge collection distance is the distance two charges, starting at a common point, move apart under the force of an external applied electric field. The charge collection distance may depend on the position, z, from where the charges start travelling. The sum of charges, $q_{\text{ind}}^{(\text{top})}$ and $q_{\text{ind}}^{(\text{bottom})}$, induced by *two opposite moving* charges is zero as expected.

3.3.6.4 The Role of Contacts

Eq. 3.99 and Eq. 3.103 discribe the induced charge on a plate for the movement of charges between the plates. If a single positive charge is moved from $z = -D/2$ to $z = +D/2$ then the induced charge is $+q$ at $z = +D/2$. One should notice that the charge $+q$ is induced on the plate even if the moving charge only approaches the plate and does not leave the region

[12]The symbols $r(z)$ and $d(z)$ are used synonymously for the charge collection distance.

between the plates. What happens when the charge 'touches' the plate depends on the type of contact. There are two possible types of contacts: blocking contacts and non-blocking contacts [74]. Blocking contacts (Schottky contacts) inhibit the passage of a charge from the region between the plates into the conducting plate. Non-blocking contacts or ohmic contacts allow charge injection from the plate into the region between the plates. If a charge leaves through a non-blocking contact at $+D/2$ then there are two possibilities for what can happen at the opposite plate. If the contact at $-D/2$ is non-blocking then there appears a charge of the same sign at $-D/2$. If the contact is blocking then there is no new charge entering the region between the plates. A contact which blocks the exit of charges and the entrance of opposite charges can cause charge accumulation near the contact.

In the model of charge induction described so far the distances travelled between the plates are limited by the contacts. This limitation is expressed by

$$\begin{aligned} & r_{\mathrm{n}}(a) \leq D/2 - a \qquad \wedge \qquad r_{\mathrm{p}}(a) \leq D/2 + a \qquad \forall \qquad a \in [-D/2, +D/2] \\ \Rightarrow \qquad & r_{\mathrm{n}}(a) + r_{\mathrm{p}}(a) \leq D \qquad \forall \qquad a \in [-D/2, +D/2] \end{aligned} \tag{3.106}$$

hence the absolute charge induced must be smaller than $|q|$

$$r_{\mathrm{n}}(a) + r_{\mathrm{p}}(a) \leq D \qquad \Rightarrow \qquad q_{\mathrm{ind}}^{(\mathrm{top})}(a) \geq -q \qquad \text{and} \qquad q_{\mathrm{ind}}^{(\mathrm{bottom})}(a) \leq q. \tag{3.107}$$

The goal is to identify the distance travelled of a negative charge with the mean drift length of a charge carrier in the CB and to identify the distance travelled of a positive charge with the mean drift length of a charge carrier in the VB [Eq. 3.40]

$$r_{\mathrm{n}}(z) = s_{\mathrm{c}}(z) \qquad \text{and} \qquad r_{\mathrm{p}}(z) = s_{\mathrm{v}}(z) \qquad \text{for} \qquad z \in [z_0, z_1]\,. \tag{3.108}$$

The identification is possible if the mean drift lengths are small compared to the distance between the plates. The width of the interval, $[z_0, z_1]$, on which one can identify the charge collection distance with the drift length depends on the type of contacts.

Fig. 3.23 illustrates the sum of the distances travelled (solid line) of a positive and a negative charge and the carrier drift length (dashed line) as a function of the position between the plates for the case of blocking contacts (left) and non-blocking contacts (right). A comparison with Fig. 3.7 shows that the identification between the distance travelled and the carrier drift length is possible in the region from z_0 to z_1 sufficiently far from the contacts. In the region near the contacts the charge collection distance differs from the carrier drift length. The effect of contacts is illustrated by the arrows in the region from $-D/2$ to z_0 and z_1 to $+D/2$. For the case of blocking contacts the charge collection distance is always smaller than the carrier drift length. For the case of non-blocking contacts the charge collection is smaller than the carrier drift length near one contact and larger near the other contact. For the case on non-blocking contacts it should be noted that the charge collection distance is equal on both sides: $r_0 = r_1$.

A charge which exits the region between the plates may cause another charge to enter from the other side for the case of non-blocking contacts. If in addition the charge collection distance of the material is different from zero on both sides then it is possible that the induced charge on a contact is higher than the amount of initally generated charges. In this case one observes photo-conductive gain. The measurements in Sec. 3.5 indicate small charge collection distance on the nucleation side of an as-grown CVD diamond. In this case photo-conductive gain is not possible.

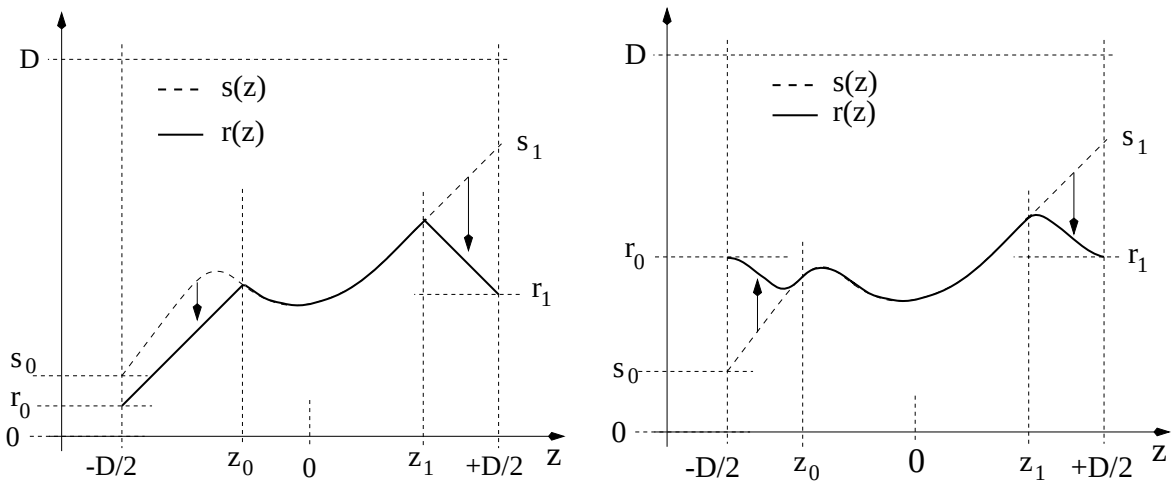

Figure 3.23: Illustration of the charge collection distance with blocking contacts (left) and injecting contacts (right). The dashed line represents the carrier drift length, the solid line represents the charge collection distance. The arrows indicate the difference between the carrier drift length and the charge collection distance.

3.3.6.5 Many Charge Pairs Moving in Opposite Directions

In the model of charge collection considered so far two opposite point charges (a charge pair) travel from a common starting point under the influence of an external electric field. For later applications it is necessary to extend the model to a distribution of N charge pairs along the z-direction as shown in Fig. 3.24. The N charge pairs are assumed to be distributed

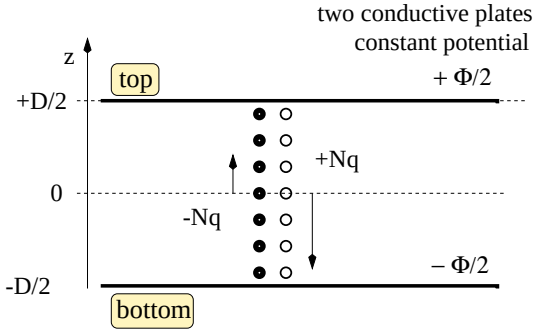

Figure 3.24: Moving charge pairs along a line. The open circles represent N positive charges, the solid circles are N negative charges. The positive charges move towards the plate with the negative potential (bottom), the negative charges move towards the plate with the positive potential (top).

homogeneously along the z-direction perpendicular to the plates:

$$\frac{\mathrm{d}N}{\mathrm{d}z}(z) = \frac{N}{D} = \text{const.} \tag{3.109}$$

Homogeneity means that the distribution is constant as a function of z. The total induced charge on the top plate, for example, is then

$$Q_{\text{ind}}^{(\text{top})} = \int_{-D/2}^{+D/2} \frac{\mathrm{d}N}{\mathrm{d}z}(z)\, q_{\text{ind}}^{(\text{top})}(z)\, \mathrm{d}z = \frac{N}{D} \int_{-D/2}^{+D/2} q_{\text{ind}}^{(\text{top})}(z)\, \mathrm{d}z. \tag{3.110}$$

For any function, $r(z)$, the distribution $\mathrm{d}N(z)/\mathrm{d}z$ can be mapped into the distribution $\mathrm{d}N(r)/\mathrm{d}r$

$$\frac{\mathrm{d}N}{\mathrm{d}z}(z)\, \mathrm{d}z = \frac{\mathrm{d}N}{\mathrm{d}r}(r)\, \frac{\mathrm{d}r}{\mathrm{d}z}\, \mathrm{d}z = \frac{\mathrm{d}N}{\mathrm{d}r}(r)\, \mathrm{d}r. \tag{3.111}$$

Using Eq. 3.103, Eq. 3.110 and Eq. 3.111 one can then rewrite the total induced charge as

$$Q_{\mathrm{ind}}^{(\mathrm{top})} = -\frac{q}{D}\int_{-D/2}^{+D/2} r_{\mathrm{n}}\,\frac{\mathrm{d}N}{\mathrm{d}r_{\mathrm{n}}}(r_{\mathrm{n}})\,\mathrm{d}r_{\mathrm{n}} - \frac{q}{D}\int_{-D/2}^{+D/2} r_{\mathrm{p}}\,\frac{\mathrm{d}N}{\mathrm{d}r_{\mathrm{p}}}(r_{\mathrm{p}})\,\mathrm{d}r_{\mathrm{p}}. \tag{3.112}$$

The integrand in Eq. 3.112 contains the distribution of the distances travelled. The integrals themselves are the mean values of the distances travelled of the charge carriers

$$\bar{r}_{\mathrm{n}} = \frac{1}{N}\int_{-D/2}^{+D/2} r_{\mathrm{n}}\,\frac{\mathrm{d}N}{\mathrm{d}r_{\mathrm{n}}}(r_{\mathrm{n}})\,\mathrm{d}r_{\mathrm{n}} \qquad \text{and} \qquad \bar{r}_{\mathrm{p}} = \frac{1}{N}\int_{-D/2}^{+D/2} r_{\mathrm{p}}\,\frac{\mathrm{d}N}{\mathrm{d}r_{\mathrm{p}}}(r_{\mathrm{p}})\,\mathrm{d}r_{\mathrm{p}} \tag{3.113}$$

and therefore

$$Q_{\mathrm{ind}}^{(\mathrm{top})} = -\frac{q\,N}{D}(\bar{r}_{\mathrm{n}} + \bar{r}_{\mathrm{p}}). \tag{3.114}$$

The charge induced by moving charges along a line between the plates is expressed in terms of the average charge collection distance of positive charges moving towards the negative electrode and negative charges moving towards the positive electrode. This leads one to define the *average charge collection distance sum* [13]

$$\bar{d} \stackrel{\mathrm{def}}{=} \bar{r} \stackrel{\mathrm{def}}{=} \bar{r}_{\mathrm{n}} + \bar{r}_{\mathrm{p}}. \tag{3.115}$$

Finally the induced charges on the top and on the bottom plates are

$$Q_{\mathrm{ind}}^{(\mathrm{top})} = -\frac{q\,N}{D}\,\bar{d} \qquad \text{and} \qquad Q_{\mathrm{ind}}^{(\mathrm{bottom})} = +\frac{q\,N}{D}\,\bar{d}. \tag{3.116}$$

It is important to notice that the derivation of Eq 3.116 does not require any assumption about the form of $r_{\mathrm{n}}(z)$ and $r_{\mathrm{p}}(z)$. The average charge collection distance is

$$\bar{d} = \langle r \rangle = \frac{1}{N}\int_{\infty}^{\infty} r\,\frac{\mathrm{d}N}{\mathrm{d}r}\,\mathrm{d}r. \tag{3.117}$$

Using the mapping of Eq. 3.111 and Eq. 3.111 one finds

$$\bar{d} = \frac{1}{D}\int_{-D/2}^{D/2} r(z)\,\mathrm{d}z. \tag{3.118}$$

3.3.6.6 Fluctuating Charge Pairs Moving in Opposite Directions

The charge pairs described above can be associated with the charges generated by an ionizing particle traversing the region between the plates. The amount of positive and negative charge along the track is

$$Q_{\mathrm{gen,p}} = +q\,N \qquad \text{and} \qquad Q_{\mathrm{gen,n}} = -q\,N \tag{3.119}$$

where N is the number of charges along the path of the ionization. The mechanism of simultaneous charge carrier generation implies $Q_{\mathrm{gen,p}} = -Q_{\mathrm{gen,n}} \stackrel{\mathrm{def}}{=} Q_{\mathrm{gen}}$. The number of generated charges along the track normally fluctuates. For any distribution $\mathrm{d}M/\mathrm{d}Q_{\mathrm{gen}}$ of charges one finds the mean generated charge

[13] The 'average charge collection distance sum' is shortly called the 'average charge collection distance' or 'charge collection distance'. The symbols $\bar{d}$ and $\bar{r}$ are used synonymously.

$$\bar{Q}_{\mathrm{gen}} = \frac{1}{M}\int_{-\infty}^{+\infty} Q_{\mathrm{gen}}\,\frac{\mathrm{d}M}{\mathrm{d}Q_{\mathrm{gen}}}(Q_{\mathrm{gen}})\,\mathrm{d}Q_{\mathrm{gen}}$$
$$\text{with} \tag{3.120}$$
$$M = \int_{-\infty}^{+\infty} \frac{\mathrm{d}M}{\mathrm{d}Q_{\mathrm{gen}}}(Q_{\mathrm{gen}})\,\mathrm{d}Q_{\mathrm{gen}}.$$

The induced charge is a function of the generated charge and therefore

$$\frac{\mathrm{d}M}{\mathrm{d}Q_{\mathrm{gen}}}(Q_{\mathrm{gen}})\,\mathrm{d}Q_{\mathrm{gen}} = \frac{\mathrm{d}M}{\mathrm{d}Q_{\mathrm{ind}}^{(\mathrm{top})}}(Q_{\mathrm{ind}}^{(\mathrm{top})})\,\mathrm{d}Q_{\mathrm{ind}}^{(\mathrm{top})} \tag{3.121}$$

which allows to rewrite Eq. 3.120 using Eq. 3.116

$$\bar{Q}_{\mathrm{gen}} = -\frac{D}{M\,\bar{d}}\int_{-\infty}^{+\infty} Q_{\mathrm{ind}}^{(\mathrm{top})}\,\frac{\mathrm{d}M}{\mathrm{d}Q_{\mathrm{ind}}^{(\mathrm{top})}}(Q_{\mathrm{ind}}^{(\mathrm{top})})\,\mathrm{d}Q_{\mathrm{ind}}^{(\mathrm{top})}. \tag{3.122}$$

The integral is the mean induced charge

$$\bar{Q}_{\mathrm{ind}}^{(\mathrm{top})} = \frac{1}{M}\int_{-\infty}^{+\infty} Q_{\mathrm{ind}}^{(\mathrm{top})}\,\frac{\mathrm{d}M}{\mathrm{d}Q_{\mathrm{ind}}^{(\mathrm{top})}}(Q_{\mathrm{ind}}^{(\mathrm{top})})\,\mathrm{d}Q_{\mathrm{ind}}^{(\mathrm{top})}. \tag{3.123}$$

Hence, the *mean induced charge* on the top plate, and in analogy on the bottom plate, are

$$\bar{Q}_{\mathrm{ind}}^{(\mathrm{top})} = -\frac{\bar{d}}{D}\,\bar{Q}_{\mathrm{gen}} \qquad \text{and} \qquad \bar{Q}_{\mathrm{ind}}^{(\mathrm{bottom})} = +\frac{\bar{d}}{D}\,\bar{Q}_{\mathrm{gen}}. \tag{3.124}$$

This result is important since it relates the mean induced charge on an electrode to the average charge collection distance.

The mean generated charge can be different from the most probable generated charge, $\hat{Q}_{\mathrm{gen}}$. In analogy to Eq. 3.124 one finds the *most probable induced charge*

$$\hat{Q}_{\mathrm{ind}}^{(\mathrm{top})} = -\frac{\bar{d}}{D}\,\hat{Q}_{\mathrm{gen}} \qquad \text{and} \qquad \hat{Q}_{\mathrm{ind}}^{(\mathrm{bottom})} = +\frac{\bar{d}}{D}\,\hat{Q}_{\mathrm{gen}}. \tag{3.125}$$

It should be noted that for the derivation of Eq. 3.124 and Eq. 3.125 no assumption on the shape of the distribution of the (local) charge collection distances between the electrodes has been made and also no assumption about the distribution of generated charge carriers in successive events. Eq. 3.124 and Eq. 3.125 are therefore applicable for the description of induced signal charges in mono-crystalline natural diamond with presumably uniform charge collection distance and for the description of CVD diamond where the charge collection distance depends on the position along the direction of growth. In order to infer the average carrier drift length from Eq. 3.48 with $\bar{d}$ from Eq. 3.124 one has to insure that $s(z) \leq D \;\; \forall \;\; |z| < D/2$. A neccessary condition for this is that the average carrier drift length is smaller than the distance between the contacts.

3.4 Charged Particle Detection

A particle sensor requires both a sensor material and suitable readout electronics. The principle of a CVD diamond sensor is described here. The readout electronics for measuring the charge collection distance is also presented. Finally, results of the typical performance of CVD diamond sensors with a single pair of electrodes on opposite sides of the sensor are given.

3.4.1 Principle of a Diamond Sensor

Fig. 3.25 shows the basic principle of a diamond sensor. The diamond sensor is shown from the side with electrodes on the top and on the bottom. A potential difference, U, is applied to the electrodes. A charged particle traversing the diamond deposits energy along its path due to Coulomb interaction with atomic electrons as described in Sec. 3.3.2. The energy deposited is available to excite electrons from the VB to the CB with subsequent creation of a vacancy (hole) in the VB. The number of generated electron-hole pairs is given by Eq. 3.83. The potential difference applied to the electrodes causes an electric field inside the diamond sensor [Eq. 3.102]. The charge carriers in the CB and the VB move towards the electrodes according to the equation of motion [Eq. 3.14]. The distance travelled can be limited due to defect states in the band gap. The average distance travelled for charge carriers in the CB and the VB is given by the average carrier drift length [Eq. 3.48].

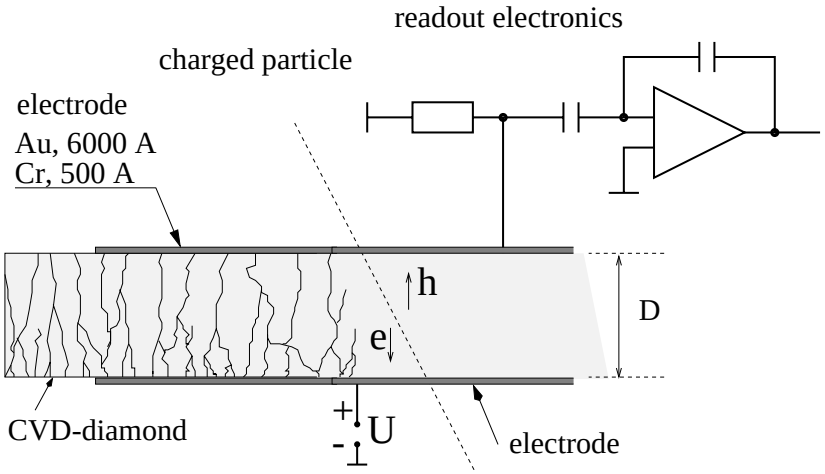

Figure 3.25: Principle of a diamond detector.

By measuring the mean induced charge one finds the average charge collection distance

$$\bar{d} = \frac{\bar{Q}_{\text{ind}}}{\bar{Q}_{\text{gen}}} D. \tag{3.126}$$

The measurement of the average charge collection distance allows one to infer the average carrier drift length

$$\mu\bar{\tau}|\vec{E}| = \frac{\bar{Q}_{\text{ind}}}{\bar{Q}_{\text{gen}}} D \qquad \Leftrightarrow \qquad \mu\tau(z)|\vec{E}| \overset{\text{condition}}{\leq} D \quad \forall\, |z| < \frac{D}{2} \tag{3.127}$$

where the '$\Leftrightarrow$' means 'if and only if'. From this logical statement one infers

$$\mu\bar{\tau}|\vec{E}| = \frac{\bar{Q}_{\text{ind}}}{\bar{Q}_{\text{gen}}} D \qquad \Rightarrow \qquad d(z) \leq D \quad \forall\, |z| < \frac{D}{2} \tag{3.128}$$

which is logically equivalent to

$$\neg \left(d(z) \leq D \quad \forall\, |z| < \frac{D}{2} \right) \qquad \Rightarrow \qquad \mu\bar{\tau}|\vec{E}| \neq \frac{\bar{Q}_{\text{ind}}}{\bar{Q}_{\text{gen}}} D \tag{3.129}$$

which means that if there exists a z with $s(z) \equiv \mu\tau|\vec{E}| > D$ then one can not infer the exact value of the mean carrier drift length from the measurement of the induced charge. However,

if $s(z) < D$ for most z then one can see from Fig. 3.23 that $s(z) = d(z)$ for most z and hence $\bar{s} \approx \bar{d}$. For most CVD diamonds measured here the average charge collection distance was smaller than the thickness by typically a factor of 2 to 5. We assume that for these cases the average carrier drift length can be infered from the average charge collection distance.

The observed charge is typically induced for a time of the order of the mobility weighted lifetime [Eq. 3.43]. The moving charges cause a current between the electrodes which can be described by an exponential decrease

$$i_{\rm ind}(t) = \begin{cases} 0 & : \quad t < 0 \\ \dfrac{Q_{\rm ind}}{\bar{\tau}}\, e^{-t/\bar{\tau}} = \dfrac{Q_{\rm gen}}{D}\dfrac{\bar{d}}{\bar{\tau}}\, e^{-t/\bar{\tau}} & : \quad t \geq 0 \end{cases} . \tag{3.130}$$

The induced current can be approximated by a delta-function[14], $\delta(t)$, if the carrier lifetime is short compared to any time constant of the following readout electronics

$$i_{\rm ind}(t) = Q_{\rm ind}\, \delta(t). \tag{3.131}$$

If the diamond is uniformly illuminated by an electron flux, $f(t)$, from a ^{90}Sr β-source then the induced current at the electrodes of size, A, is

$$I_{\rm ind}(t) = A \int_0^{+\infty} f(t')\, i_{\rm ind}(t - t')\, {\rm d}t' = A\, f(t)\, Q_{\rm ind} = \bar{d}\, \frac{A}{D}\, f(t)\, Q_{\rm gen}. \tag{3.132}$$

For the case of a single excitation, $f(t) = \delta(t)/A$, one obtains the induced current from Eq. 3.130. It can be seen that the induced current is proportional to the average charge collection distance and the particle flux.

The induced charge can be read out on both electrodes by a charge sensitive amplifier (CSA). The readout with one CSA is shown in Fig. 3.25. The CSA is typically a charge integrator and is symbolized as an operational amplifier with a feedback capacitor. The feedback capacitor collects the charge

$$Q_{\rm fp}(t) = \int_0^{t > \bar{\tau}} i_{\rm ind}(t')\, {\rm d}t' \approx Q_{\rm ind}\, \Theta(t). \tag{3.133}$$

The charge on the feedback capacitor is essentially the induced charge multiplied by the step function ($\Theta(t) = 1$ for $t > 0$ and otherwise zero). In practice, the feedback capacitor must be slowly discharged by a feedback resistor since otherwise it would sum the signals from successive events and saturate the output of the amplifier. In Eq. 3.133 the Θ-function needs to be replaced by a slowly decreasing function in order to correctly describe the slow discharge of the feedback capacitor.

3.4.2 Viking/CMOS Charge Sensitive Amplifier (CSA)

A recently developed charge sensitive readout amplifier is the VA2. The VA2 is a successor of the Viking chip and is actually one version of a series of Viking chips [76, 77, 78]. The VA2 is produced in CMOS technology [15] and offers 128 charge sensitive amplifiers (channels) from which one is shown schematically in Fig. 3.26. A single channel contains a charge sensi-

[14] The delta-function, $\delta(x)$, has the property [75]: $\int_{x_0-\epsilon}^{x_0+\epsilon} {\rm d}x \delta(x - x_0)\, f(x) = f(x_0)\ \forall f : x \mapsto f(x) \in R$ with normalization $\int_{x_0-\epsilon}^{x_0+\epsilon} {\rm d}x \delta(x - x_0) = 1$. Where $\epsilon > 0 \to +0$ is a small number compared to the scale chosen for x. From its property one obtains the unit, $[\delta(x)]$, of the delta-function: $[\delta(x)] = 1/[x]$. A general representation of the delta-function is $\delta(x) = g(x/\epsilon)/\left(\epsilon \int {\rm d}x g(x)\right)$ for all 'physically healthy' functions, $g(x)$.

[15] The abbreviation *CMOS*: *C*omplementary *M*etal *O*xide *S*emi-conductor.

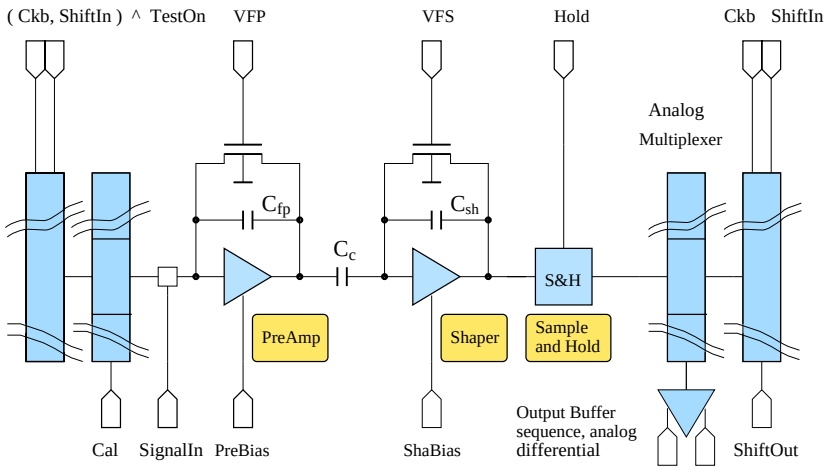

Figure 3.26: Schematic of one channel of the VA2 showing the internal diagram and the external controls necessary for operation.

tive preamplifier (PreAmp) followed by a signal shaper. The shaper differentiates the voltage $Q_{\rm fp}(t)/C_{\rm fp}$, which is approximately $Q_{\rm ind}\Theta(t)/C_{\rm fp}$, and performs 2-pole semi-Gaussian signal shaping (also called CR-RC shaping). The amplitude of the shaped pulse is proportional to the signal charge. The signal peaking time can be adjusted between 1.0 μs and 2.0 μs. For this application the shaping time was chosen to be 2 μs. The shaper is followed by the sample and hold circuit which is adjusted to sample the shaped voltage signal at its peak. The sampled signals from several channels can be multiplexed and read out sequentially through a differential output buffer. Signal multiplexing was used for the readout of up to 256 channels in diamond strip detectors. It is also possible to choose a single channel, bypassing the multiplexer, and directly measure the shaped signal on that channel. This mode was normally used for characterization of sensors with a single electrode. The external controls for the preamplifier and the shaper were adjusted to obtain a desired gain and signal shape. Table 3.4 lists a typical setting for the operation of one chip.

VFS	(400..500) mV
VFP	-350 mV
PreBias	(350..450) mV across 1 kΩ
ShaBias	5 mV across 1 kΩ
BufBias	16 mV across 1 kΩ

Table 3.4: Typical settings for operating a VA2.

VFS and VFP are voltages for the gates of the feedback FETs which adjust the discharging of the feedback capacitors by adjusting the resistance of the drain-source path of the FETs. PreBias, ShaBias and BufBias are the bias currents for the drain source path of the FETs in the preamplifier, the shaper and the buffer. The VA2 was designed for medium sized detectors with a capacitive load up to 10 pF. The VA2 has a linear dynamic range from $-4 \times 22500\ e$ to $+4 \times 22500\ e$. The power consumption is nominally 1.2 mW/channel.

3.4.3 Noise in a CMOS CSA

One important feature of the Viking readout is its low noise. The noise of a sensor readout can be expressed as the equivalent noise charge (ENC). The ENC is the noise charge variation at the input of the CSA. The ENC has units of a charge. The ENC depends on the characteristics of both, the CSA and the pulse shaper. The noise is dominated by the input device of the CSA. In the CMOS process the input device is a field effect transistor (FET). The noise components are commonly separated into the parallel and series noise. Significant series noise components for a device manufactured in the CMOS process are the channel thermal noise at temperature, T, and the frequency dependent flicker noise whose *rms* decreases like $1/f$ with increasing frequency. Both noise sources add in quadrature and give the total series equivalent noise charge, $\langle q^2_{\text{series}} \rangle$. For the CMOS input amplifier followed by a first order CR-RC signal shaping the series equivalent noise charge is proportional to the total capacitance [79]:

$$\left\langle q^2_{\text{series}} \right\rangle = \left\langle u^2_{\text{a}} \right\rangle \cdot C^2_{\text{t}} \quad ; \quad C_{\text{t}} = C_{\text{a}} + C_{\text{e}}. \tag{3.134}$$

The total capacitance, C_{t}, is the sum of the external capacitance, C_{e}, and the preamplifier inherent capacitance, C_{a}. The preamplifier inherent capacitance is the sum of the feedback capacitance of the charge sensitive amplifier, the gate source capacitance and the gate drain capacitance of the input FET. The external capacitance includes the detector capacitance and stray capacitances. The proportionality in Eq. 3.134 is given by the equivalent noise voltage, $\langle u^2_{\text{a}} \rangle$, which can be calculated for the CMOS process

$$\left\langle u^2_{\text{a}} \right\rangle = \left(\frac{8 k_{\text{B}} T}{3 g_{\text{m}}} \cdot \frac{e^2_{\text{E}}}{8 e^2 \tau_{\text{p}}} + \frac{K_{\text{f}}}{C^2_{\text{ox}} W L} \cdot \frac{e^2_{\text{E}}}{e^2} \right) \tag{3.135}$$

where e is the electron charge and e_{E} is Euler's constant (with the subscript 'E' indicating 'Euler' in order not to confuse with the electron charge). C_{ox} is the capacitance of the gate electrode depending on the thickness of the oxide layer and the size of the gate contact on the silicon oxide. The channel thermal noise is white noise and inversely proportional to the channel transconductance, $g_{\text{m}} = e\, I_{\text{bias}}/(k_{\text{B}} T)$. The flicker noise which is the second term of $\langle u^2_{\text{a}} \rangle$ depends on geometrical parameters of the input transistor like the transistor width, W, the effective transistor length, L, and a process dependent constant, K_{f}, which is the $1/f$ frequency dependent noise coefficient. A generalization of Eq. 3.134 for any order of the semi-Gaussian shaped signal is derived in reference [79]. The series noise can be evaluated for a given CMOS process at zero external capacitance which gives the *preamplifier equivalent noise charge*

$$\left\langle q^2_{\text{a}} \right\rangle \stackrel{\text{def}}{=} \left\langle q^2_{\text{series}} \right\rangle \Big|_{C_{\text{e}}=0} = \left\langle u^2_{\text{a}} \right\rangle C^2_{\text{a}}. \tag{3.136}$$

The series equivalent noise charge can therefore be written in terms of the preamplifier equivalent noise charge and a slope term

$$\sqrt{\langle q^2_{\text{series}} \rangle} = \sqrt{\langle q^2_{\text{a}} \rangle} + \sqrt{\langle u^2_{\text{a}} \rangle} \cdot C_{\text{e}}. \tag{3.137}$$

The series equivalent noise charge of a single VA2 amplifier channel, as given by the manufacturer, is at best 60 e + 11.0 e/pF at 2 μs signal peaking time and 80 e + 15.0 e/pF at 1 μs signal peaking time [78].

The parallel equivalent noise charge is due to the detector leakage current, I_{D}, is associated to the bias resistor, R_{B}, and the preamplifier feedback loop resistor, R_{F}. The parallel equivalent noise charge is given by [79]

$$\left\langle q^2_{\rm parallel} \right\rangle = \frac{1}{2} \cdot \left(2\, e\, I_{\rm D} + \frac{4\, k_{\rm B}\, T}{R_{\rm B}} + \frac{4\, k_{\rm B}\, T}{R_{\rm F}} \right) A_{\rm parallel}. \tag{3.138}$$

For the case of first order CR-RC signal shaping with signal peaking time, $\tau_{\rm p}$, the constant $A_{\rm parallel}/2$ is [79]

$$\frac{1}{2} A_{\rm parallel} = \frac{(\pi/2)\, e^2_{\rm E}}{e^2\, 4\pi} \cdot \tau_{\rm p} \tag{3.139}$$

where the constants are left uncancelled to keep the form in reference [79].

The noise due to the detector leakage current is shot noise. This noise contribution, evaluated for the characteristic signal peaking time of 2 μs in the VA-circuit, gives a useful rule of thumb

$$\sqrt{\langle q^2_{\rm D} \rangle}\ [e] \stackrel{\rm def}{=} \sqrt{\frac{1}{2} A_{\rm parallel} \cdot 2\, e\, I_{\rm D}} = \sqrt{\frac{\tau_{\rm p} e^2_{\rm E}}{4e}} \sqrt{I_{\rm D}\ [{\rm A}]} = 150 \sqrt{I_{\rm D}\ [{\rm nA}]}. \tag{3.140}$$

In the last equation the current has to be inserted in nanoampere in order to give the result in *rms* electrons. The noise from the biasing resistor or from the preamplifier feedback resistor is thermal noise. This noise contribution, evaluated for the characteristic signal peaking time of 2 μs in the VA-circuit, gives a useful rule of thumb

$$\sqrt{\langle q^2_{\rm R} \rangle}\ [e] \stackrel{\rm def}{=} \sqrt{\frac{1}{2} A_{\rm parallel} \frac{4\, k_{\rm B} T}{R}} = \sqrt{\frac{\tau_{\rm p} e^2_{\rm E}}{4e}} \sqrt{\frac{2 k_{\rm B} T}{eR}} = 1070 \sqrt{\frac{1}{R\ [{\rm M}\Omega]}}. \tag{3.141}$$

The parallel noise charge is proportional to the square root of the signal peaking time.

The total equivalence noise charge of the readout with the external capacitance, $C_{\rm e}$, is obtained by adding the series noise and the parallel noise components in quadrature:

$$\left\langle q^2_{\rm total} \right\rangle = \left(\sqrt{\langle q^2_{\rm a} \rangle} + \sqrt{\langle u^2_{\rm a} \rangle} \cdot C_{\rm e} \right)^2 + \left\langle q^2_{\rm parallel} \right\rangle. \tag{3.142}$$

3.4.4 Experimental Method: Sample Preparation

The preparation of CVD diamond samples for charge collection measurements is the same as described for the current measurements in Sec. 3.2.1. CVD diamond samples with electrical contacts on both sides are shown in Fig. 3.1.

3.4.5 Experimental Method: Charge Collection Distance

Fig. 3.27 shows a possible setup for measuring the charge signal response and the charge collection distance from a diamond. The bias voltage was applied via the resistor, R_1, to one electrode of the diamond sensor. The combination of the capacitor, $C_1 = 4.7$ nF (with a small resistor, R_3, to ground, small is $R_3/R_1 \ll 1$) and the resistor, $R_1 = 100$ MΩ, served as a low-pass filter in order to reject ripple on the bias voltage. The 3 dB attenuation frequency of this low-pass filter is at $f = 1/(2\pi R_1 C_1) \approx 0.3$ Hz. If one would chose $R_1 = 1$ MΩ and the same C_1 the 3 dB attenuation frequency would be at 300 Hz. Hence a 50 Hz ripple on the DC bias voltage would pass the filter [16]. The electrode on the other side of the diamond

[16] The unit *dezibel*: unit of attenuation, a. If a voltage, $u_{\rm i}$, is attenuated to a voltage, $u_{\rm o}$, then $a = 20 \log_{10} (u_{\rm o}/u_{\rm i})$. For the case $u_{\rm o}/u_{\rm i} = 0.707$ one finds $a = -3$ dB [80].

was AC coupled to the preamplifier of a VA2 readout channel. Care was taken to choose the coupling capacitance, C_2, sufficiently large ($C_2 \gg$ detector capacitance) in order to transmit all of the induced charge. The readout electrode was at virtual ground via the resistor R_4. A collimated ^{90}Sr source was located above the diamond sensor. ^{90}Sr emits 100 % electrons (e^-) and anti-neutrinos ($\bar{\nu}_e$) from successive β^--decays:

$$^{90}_{38}\mathrm{Sr} \overset{(e^-,\bar{\nu}_e)}{\longrightarrow} {}^{90}_{39}\mathrm{Y} \overset{(e^-,\bar{\nu}_e)}{\longrightarrow} {}^{90}_{40}\mathrm{Zr}. \tag{3.143}$$

No photons are emitted. The first transition has a physical half-life of $\tau_{1/2} = 28.5$ y and an electron endpoint kinetic energy of 0.546 MeV, the second transition has a half-life of 64 h and an endpoint kinetic energy of $T_{\max} = 2.283$ MeV [9]. The endpoint kinetic energy of the second transition corresponds to $\eta \equiv \sqrt{T^2_{\max}/m^2 + 2T/m} = 5.37$. The endpoint kinetic energy is above minimum ionizing as can be seen in Fig. 3.16. The mean energy deposited from electrons of the yttrium decay is close to the energy deposited from a minimum ionizing particle. It was shown in reference [11] that the mean energy deposited from the source using a similar configuration was 8 % higher than that deposited by a minimum ionizing particle in a 500 μm thick CVD diamond

$$\bar{Q}^{(\mathrm{source})}_{\mathrm{gen}} = 1.08\,\bar{Q}^{(\mathrm{mip})}_{\mathrm{gen}} \qquad \Longrightarrow \qquad \bar{Q}^{(\mathrm{source})}_{\mathrm{ind}} = 1.08\,\bar{Q}^{(\mathrm{mip})}_{\mathrm{ind}}. \tag{3.144}$$

The signal readout of the diamond was triggered by a silicon diode behind the diamond. The trigger therefore selects only events from electrons which traverse the diamond. The exact value for the energy deposited from the ^{90}Sr source depends on the amount of material between the diamond sample and the trigger. If there is more material one selects events which are closer to minimum ionizing. However, additional material also lowers the event rate.

Fig. 3.5 lists the sources which were used together with their calculated activity at different dates [17,18]. The original activity and date were imprinted on the source. The activities were then calculated from the exponential law for radioactive decays using the given half-life of ^{90}Sr. It can be seen that the change in activity was below 10 % for the period of time shown.

source name	original activity [MBq]	[mCi]	date	activity [MBq]	date	activity [MBq]	date	activity [MBq]	date
3513RP	37.0	1.0	08/94	35.1	10/96	34.3	10/97	33.5	10/98
3595RP	37.0	1.0	07/95	35.9	10/96	35.0	10/97	34.2	10/98
3752RP	3.7	0.1	10/96	3.6	10/96	3.5	10/97	3.4	10/98

Table 3.5: List of ^{90}Sr sources in use for measuring the charge collection distance. The calculated activities are given for different dates.

The waveform of the shaped pulse was recorded by a digitizing oscilloscope (LeCroy 9310A [81]). The amplitude was read from the scope via GPIB into a PC using software written in Labview [67]. The average charge collection distance was found from the measurement of the induced charge by re-arranging Eq. 3.124 and using Eq. 3.90

$$\bar{d} = \frac{\bar{Q}_{\mathrm{ind}}\,[e]}{36\ e/\mu\mathrm{m}}. \tag{3.145}$$

[17]The unit *becquerel*: 1 Bq = 1 disintegration per second, unit of activity.
[18]The unit *curie* : 1 Ci = 3.7×10^{10} Bq, unit of activity.

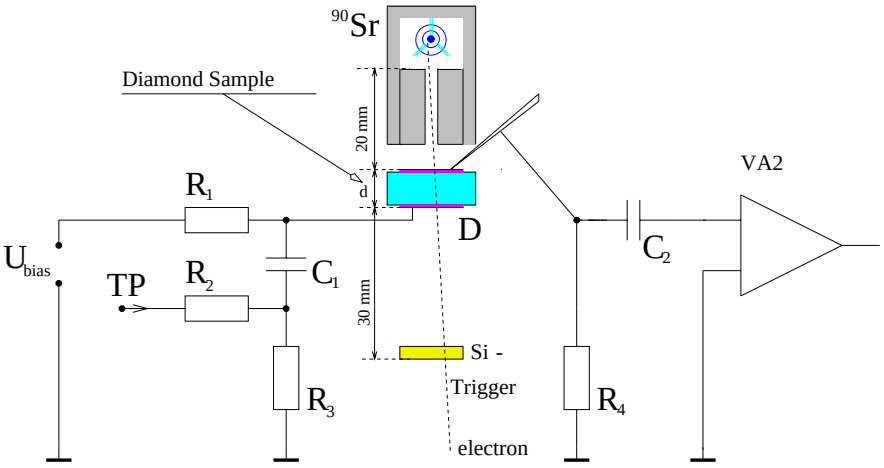

R_1 R_4 =100 M Ω C_1 = 4.7 nF U_{bias} = 0..1 kV
R_2 = 47 Ω C_2 = 0.1 nF
R_3 =10 Ω d = 100 µm .... 800 µm

Figure 3.27: Schematic of the setup for measuring the charge collection distance in a diamond detector using a radioactive β-source.

A typical mean induced charge of 6000 e at 1 V/μm in a CVD diamond therefore corresponds to a mean charge collection distance of 167 μm. The typical equivalent noise charge of the electronics was 210 e without a sample connected.

3.4.6 Experimental Method: Gain Calibration

The induced signal charge was measured as the voltage amplitude of the shaped pulse. A calibration was required in order to obtain the gain constant that converts the voltage amplitude into a charge. Various methods were used in order to find the gain constant, two of them were the photo-absorption method and the test-pulser method. The photo-absorption method measured the photo yield in a fully depleted silicon photo-diode from a radioactive γ-source. The source used was ^{57}Co that emits photons at two distinct energies of $E_1 = 0.122$ MeV and $E_2 = 0.136$ MeV. A silicon diode was mounted at the location of the diamond in the setup shown in Fig. 3.27 with the cobalt source illuminating the diode. The voltage separation, ΔU, of the photo-absorption peaks in the recorded spectrum is proportional to the energy difference between the peaks. Using the energy, $\epsilon_c^{(si)}$, for carrier generation in silicon one obtains the gain constant

$$g_\gamma = \frac{E_1 - E_2}{\epsilon_c^{(si)}\,\Delta U}. \tag{3.146}$$

This method was used as a cross check. In the test-pulser method a pulser supplied a voltage step into a capacitance, C, that was connected to the preamplifier input. The cable which transmited the voltage step was terminated by a resistor, R. Typical values were $R = 50\ \Omega$, $C = 1.8$ pF, and the step magnitude of the order of several millivolt. The voltage step injects a charge $Q(t) = C\,U(t) = C\,U_0\,\Theta(t)$. The current that charges the preamplifier feedback capacitor is given by Eq. 3.131 by replacing the induced charge with the injected charge. The charge injection causes a voltage amplitude, $\hat{U}_{\rm out}$, of the shaped pulse. Then the gain constant is

$$g_{\mathrm{tp}} = \frac{C\,U_0}{\hat{U}_{\mathrm{out}}}. \tag{3.147}$$

Fig. 3.28 shows a measurement of $\hat{U}_{\mathrm{out}}$ as function of the input charge, $C\,U_0$, from one channel of a VA2. The input charge was generated using a constant capacitance of 1.8 pF and voltages U_0 ranging from -5.4 mV to +5.4 mV. The gain can be read from the slope of the measured curve: $g_{\mathrm{tp}} \approx 25\ e/\mathrm{mV}$. The measurement in Fig. 3.28 also demonstrates the linearity of the VA2 for positive and negative charge injection. It should be noted that no direct current flows into the preamplifier during this measurement. For the case that a detector is connected to the preamplifier with a leakage current flowing into the gate of the preamplifier the response could be different since the conductivity of the drain-source path of the feedback FET depends on the direction of the current in the drain-source path. For applications with a diamond detector or with AC coupled detectors one can assume a negligible feedback current and hence linearity of the VA2 for positive and negative charge injection.

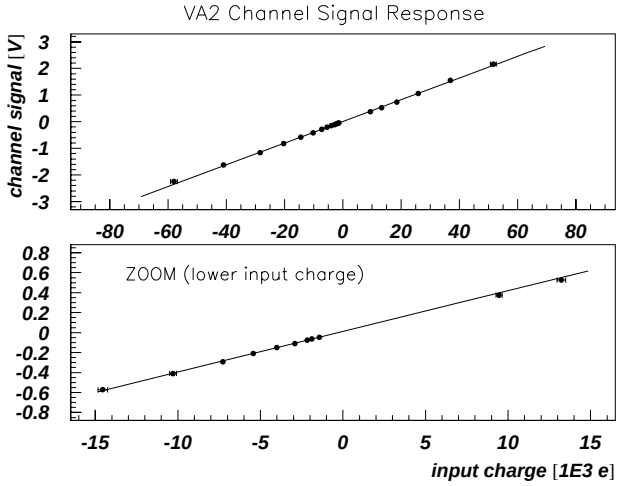

Figure 3.28: Voltage amplitude of the shaped signal as a function of the injected charge into the preamplifier of a channel of a VA2 at negligibly small direct current flowing into the preamplifier. The upper graph shows a range from -60000 e to +60000 e. The lower graph shows a magnification in the interval from -15000 e to +15000 e. The solid line is a linear fit to the measured data points.

The statistical error on the gain constant, g_γ, is determined by the statistical error of the line position in the recorded histogram. The relative statistical error, $1/\sqrt{N}$, decreases as the number of entries, N, in a photo-absorption peak of the histogram increases. The relative statistical error was estimated to be below 1 % for a histogram with about 4000 entries in the photo-peak at E_1. The statistical error on the gain constant, g_{tp}, depends on the statistical error of $\hat{U}_{\mathrm{out}}$ and U_0, where both decrease like $1/\sqrt{N}$ for increasing number, N, of test pulses. In practice the error is determined by the measurement of the capacitance. The capacitance was measured for a series of capacitors with a relative deviation below 4 % compared to the printed value. Stray capacitances may contribute as well depending on the geometry. The reproducibility of the gain constant had a 1 σ standard deviation of about 5 % of the gain constant.

3.4.7 Observation: The Pumping Effect

Fig. 3.29 shows a measurement of the charge collection distance as a function of time in the setup. The bias voltage for the diamond was constant at 1 V/μm. The electron flux from the 37 MBq ^{90}Sr source was constant as well and therefore the time shown in the figure is proportional to the absorbed dose from the source. The charge collection distance was derived from the induced charge using Eq. 3.145. It can be seen that the charge collection distance increased in time from a value of (50 ± 5) μm to (87 ± 3) μm. The increase in charge collection distance at relatively low dose is called *pumping*. It is attributed to trap filling which then allows charge carriers to travel longer distances before being trapped. The measured data is fitted by an exponential function

$$\bar{d}(t) = \bar{d}_{\mathrm{p}} \cdot (1 - r\, e^{-t/\tau}) \qquad \text{with} \qquad r \stackrel{\mathrm{def}}{=} \frac{\bar{d}_{\mathrm{p}} - \bar{d}_0}{\bar{d}_{\mathrm{p}}}. \tag{3.148}$$

The time constant, $\tau = 64$ min, was obtained from the fit to the data. Pumping was seen on CVD diamond samples from other manufacturers and also on a natural diamond and therefore seems to be characteristic for diamond.

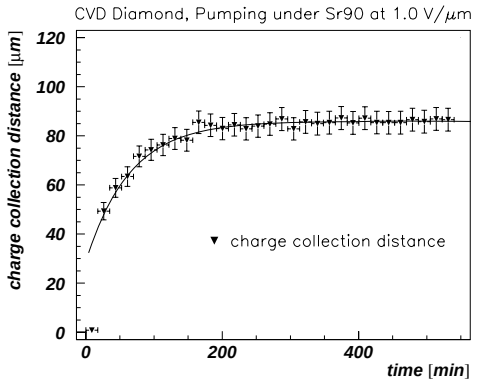

Figure 3.29: Charge collection distance as a function of time in the measuring setup under the ^{90}Sr source. The source used for this measurement had an activity of 37 MBq.

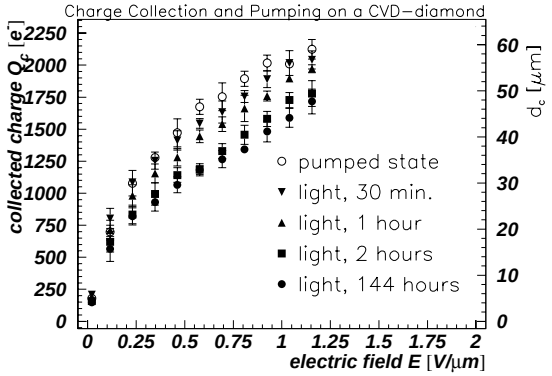

Figure 3.30: Charge collection distance as a function of voltage after several exposures to fluorescent light.

Fig. 3.30 demonstrates the effect of fluorescent light: the charge collection distance was measured several times as a function of the applied electric field with intermediate exposures to fluorescent light. The time of exposure to the light was doubled between the first two measurements. The time of the last exposure was 144 hours. The absolute spectral intensity of the fluorescent light and the absorbed photon dose is unknown. The time of exposure gives the frequency integrated relative dose of light. The charge collection distance decreased with increasing exposure time to fluorescent light. The decrease of charge collection distance is called *depumping*. Depumping is explained by releasing filled traps. The effects of pumping and depumping were reproducible. The charge collection distance ratio between the pumped and the depumped state was typically between 1.5 and 2.

The effect of pumping and depumping has been tested by measuring temperature stimulated currents using the setup described in reference [82] and by measuring the thermoluminescence light during linear heating in a thermoluminescence reader [83]. Fig. 3.31 shows the current from a CVD diamond (CDS-9) at 100 V as a function of the temperature after exposure to β-radiation from a ^{90}Sr source. The temperature is given as a function of time

in the lower graph. The current in the diamond increases from a few picoamperes at room temperature to several 100 μA during heating. The current peaks at about 230 °C. Once heated, charge carriers are flushed and the current peak is missing during cooling or repeated heating.

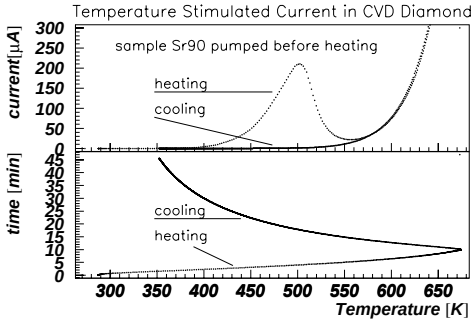

Figure 3.31: Temperature stimulated current as a function of temperature after exposure to β-radiation from a ^{90}Sr source.

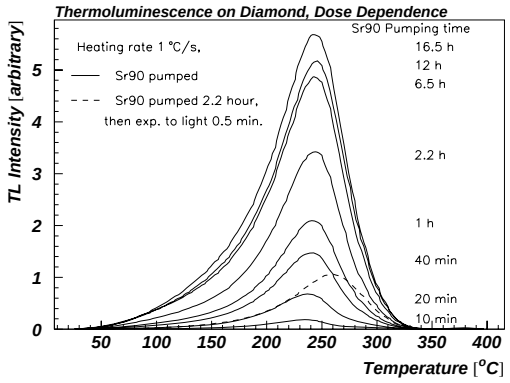

Figure 3.32: Thermoluminescence signal as a function of temperature at different doses of β-radiation from a ^{90}Sr source. The dashed graph shows the thermoluminescence response after 2.2 hours pumping with ^{90}Sr followed by an exposure to a fluorescent light lamp.

Fig. 3.32 shows the intensity of light emission during heating from a CVD diamond (CDS-12-P4). The observation of luminescence light emission from a CVD diamond after exposure to β-radiation from a ^{90}Sr source was described in Sec. 1.1.2. The curves here are given for different time of exposure to radiation. The time of exposure is proportional to the fluence from the source. It was found that the integral under the luminescence curve is proportional to the time of exposure up to an accumulated dose of about 1 Gy. The intensity of the luminescence peaks at 240 °C. It is also shown that the thermoluminescence after 2.2 hours pumping with ^{90}Sr followed by an exposure to a fluorescent light lamp decreases the luminescence response (dashed graph). The comparison between the temperature stimulated current and the thermoluminescence response shows that the peaks occur at about the same temperature which indicates that both effects originate from the same trap levels. It can be concluded that exposure to light decreases luminescence and thermally stimulated current as well as charge collection distance. It was confirmed that the pumping state remains stable over at least one month for the case that the diamond is kept in darkness and at room temperature.

3.4.8 Results: Charge Collection Distance

Fig. 3.33 shows the mean induced charge measured from two CVD diamond samples, CDS-28 (left) and UTS-5 (right), as a function of the electric field. The charge collection distance was derived using Eq. 3.145 and is given on the right axis. The charge collection distance increases with increasing electric field as expected from Eq. 3.48. At about 0.5 V/μm the charge collection distance saturates as explained by velocity saturation due to electron phonon scattering in Sec. 3.1.4. Initially an offset from zero between -200 e and +200 e at 0 V was observed. The data was then corrected such that the graph intersects with the origin of the coordinate system. The charge collection distance from CDS-28 is shown in the

partially pumped and in the fully pumped state. The sample was relatively thick (1098 μm) which lowered the acquisition rate since less electrons could penetrate the sample compared to thinner samples. Hence, the time for acquiring 800 events was longer on a thick sample than on a thinner sample. A thick diamond therefore pumps during the measurement and the graph is therefore labeled as 'partially pumped'. The fully pumped curve reaches a signal charge of (8700 ± 100) e corresponding to (242 ± 3) μm charge collection distance at 1 V/μm. The charge collection distance of the sample UTS-5 in the pumped state is shown for positive and negative electric field to the right. The measurement for positive and negative signals is possible since the amplifier gain is symmetric for positive and negative input charge as shown in Fig. 3.28. The charge induced at an electrode changes polarity for the reversed field as expected by the reversed movement of charges. The mean induced charge was (8350 ± 100) e at +1 V/μm corresponding to a charge collection distance of (232 ± 3) μm. The induced charge at -1 V/μm was about -6700 e. The absolute induced charge was lower for negative polarity than for positive polarity. This observation has been made for several samples. As a convention the charge collection distance is almost always given for a positive voltage applied to the nucleation side with the charge read out on the growth side. This convention applies to all measurements with diamond strip sensors in the beam in Chapter 4 and to the characterization of irradiated diamonds in Chapter 5.

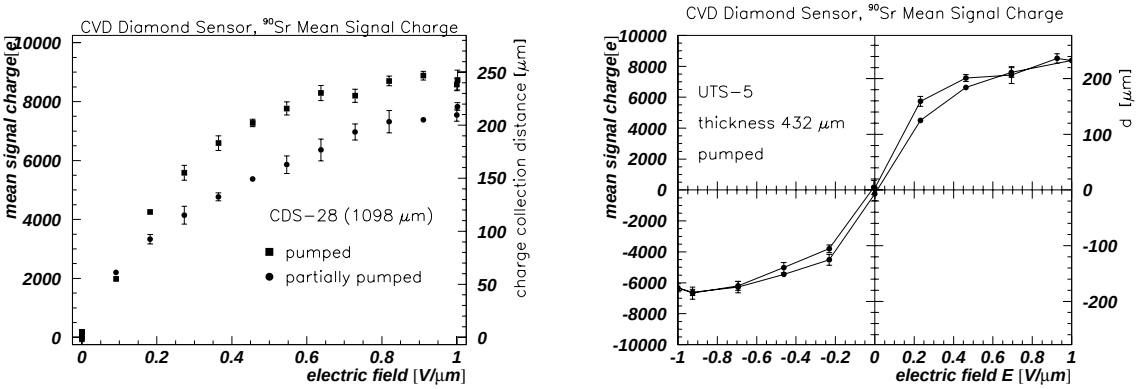

Figure 3.33: Charge collected and charge collection distances from two CVD diamond samples, CDS-28 and UTS-5, as a function of the electric field.

Fig. 3.34 shows the charge collected and the charge collection distance from a 285 μm thick natural diamond. The diamond was classified by the vendor as a class IIa single crystal, natural diamond [19]. In the depumped state the mean induced charge reached 470 e corresponding to 13 μm charge collection distance at 1 V/μm. The sample remained under the ^{90}Sr source for 17 hours. The measurement after 17 hours showed a mean induced charge of 860 e corresponding to a charge collection distance of 24 μm at 1 V/μm. The natural diamond sample pumped similarly to the CVD diamonds. The pumping factor, the ratio between the charge collection distance in the pumped and the depumped state, was 1.8 which is comparable to what was seen on CVD diamonds. A charge collection distance of about 20 μm at 1 V/μm is confirmed on other type-IIa natural diamonds [85, 11]. The maximum charge collection distance on this natural diamond is lower than what was measured on CVD

[19] Natural diamonds are classified according to their optical transmission for wavelengths between 225 nm and 2.5 μm in the types Ia, Ib, IIa, IIb [84, 2]. Diamonds of type Ia and Ib transmit light with wavelengths longer than 340 nm whereas IIa transmits starting from 225 nm. The different transmission is due to impurities, where common impurities in diamond are nitrogen and boron.

diamonds which indicates that the electrical quality of CVD diamonds has exceeded that of natural diamond. It can also be seen that the charge collection distance in the natural diamond does not saturate in the electric field range measured (up to 1.25 V/μm). This observation is confirmed on another natural diamond in reference [11]. In CVD diamond saturation of the charge collection distance was always observed below 1 V/μm. Hence, the carrier velocity in natural diamond saturates at a higher electric field strength than in CVD diamond.

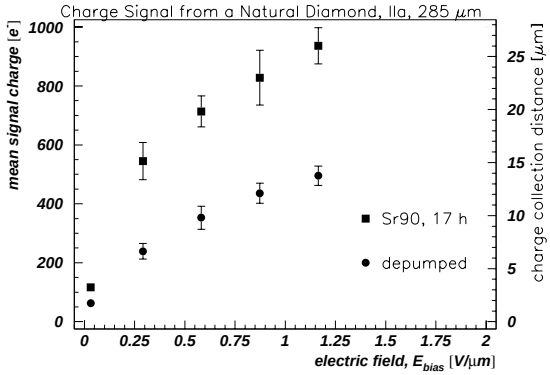

Figure 3.34: Charge collected and charge collection distance measured from a natural diamond (type IIa). The charge collection distance is shown in the depumped state and in the pumped state after 17 hours under the ^{90}Sr source.

Table 3.6 on page 107 lists the mean signal charge and the charge collection distance for a series of diamond samples in the pumped state. The samples are ordered according to their delivery from the manufacturer. The applied electric field was normally 1 V/μm. A maximum voltage of 1100 V was applied if a sample was thicker than 1100 μm. For the samples shown the charge collection distance ranges from 40 μm to 347 μm. Three samples of this set had a diode-like current-voltage curve as described in Sec. 3.2.5 and the signal charge could not be measured.

Fig. 3.35 (left) shows the charge collection as a function of the sample thickness. The graph contains unprocessed samples (as-grown) and processed samples. One can see that the charge collection distance increases with the thickness of the as-grown samples. Assuming similar growth conditions one may conclude that the local charge collection distance increases along the direction of growth. An increase along the direction of growth indicates an increase in the carrier drift length and therefore an increase of the electrical quality.

The slope of the bulk averaged charge collection distance versus thickness is

$$\frac{\bar{d}}{D} \overset{\text{Eq. } 3.124}{=} \frac{\bar{Q}_{\text{ind}}}{\bar{Q}_{\text{gen}}} \overset{\text{Eq. } 3.91}{=} \epsilon_{\text{r}} \tag{3.149}$$

where the right side was defined as the charge collection ratio in Eq. 3.91. For unprocessed samples the charge collection ratio can be read from Fig. 3.35 ranging between 0.1 and 0.2. The graph also shows samples which were lapped on the nucleation side. The charge collection distance was typically higher on samples which were lapped than on the as-grown sample. The charge collection ratio reached 0.5 for lapped samples.

3.4.9 Results: Signal Charge Distribution

Fig. 3.36 shows signal charge distributions from two CVD diamond samples in the pumped state: CDS-36 with a thickness of 1202 μm (left) and UTS-5 with a thickness of 432 μm (right). Both distributions have a pedestal at 0 e due to false triggers. The mean of the pedestal verifies that the overall distribution has no offset from zero. The standard

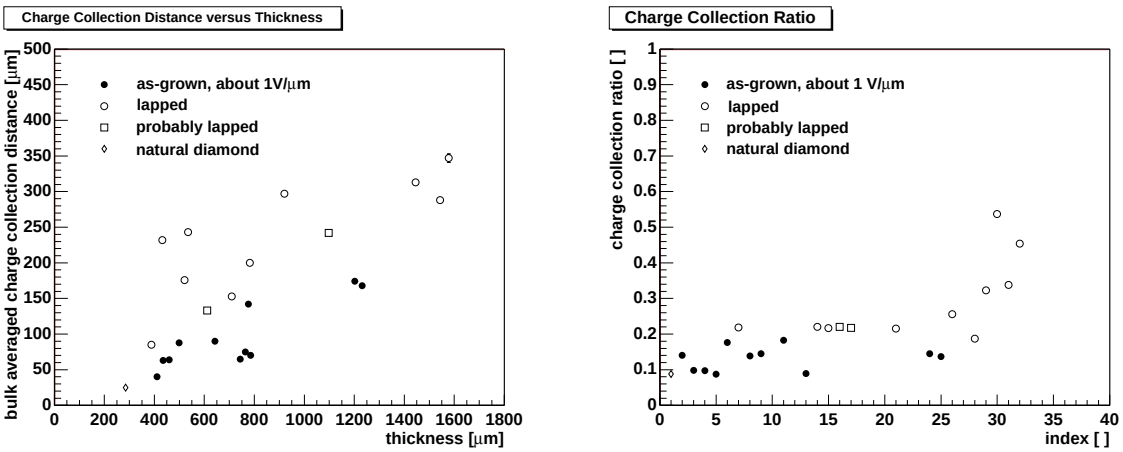

Figure 3.35: The charge collection distance versus sample thickness (left) and the charge collection ratio (right) for samples from Table 3.6. The graphs show unprocessed samples (as-grown) and processed samples (lapped). The biasing electric field was normally 1 V/μm.

deviation of the pedestal corresponds to the readout noise. The pedestal distributions in both samples have a standard deviation of $\sqrt{\left\langle q_{\mathrm{ped}}^2 \right\rangle} \approx 350\ e$. The leakage current in the station under the source is about 100 pA at 1 V/μm which contributes to the parallel equivalent noise charge with $\approx 50\ e$ [Eq. 3.140]. The biasing resistor, $R_{\mathrm{B}} = 100$ MΩ, and the feedback resistor, $R_{\mathrm{F}} = 100$ MΩ, contribute to the parallel noise with 107 e each [Eq. 3.141]. Hence the calculated parallel noise is $\sqrt{\langle q_{\mathrm{a}}^2 \rangle} \approx 160\ e$. The series noise can be calculated using $\sqrt{\langle q_{\mathrm{a}}^2 \rangle} \approx (70 \pm 10)\ e$ and $\sqrt{\langle u_{\mathrm{a}}^2 \rangle} = 11\ e/\mathrm{pF}$. If one assumes an external capacitance, $C_{\mathrm{e}} = 20$ pF, one obtains a total noise $\sqrt{\langle q_{\mathrm{total}}^2 \rangle} \approx (330 \pm 10)\ e$. The external capacitance is the sum of the detector capacitance, C_{d}, and the stray capacitance, C_{stray}. Since the diamond sample had a capacitance of $C_{\mathrm{d}} \approx 3$ pF according to Eq. 3.57 one inferes a stray capacitance of about 17 pF. Such high stray capacitance may be possible, since the mechanics that contacts the diamond is all metal and much larger than the electrode on one side of the diamond. The readout noise is therefore dominated by the noise of the setup which is mainly due to the stray capacitance.

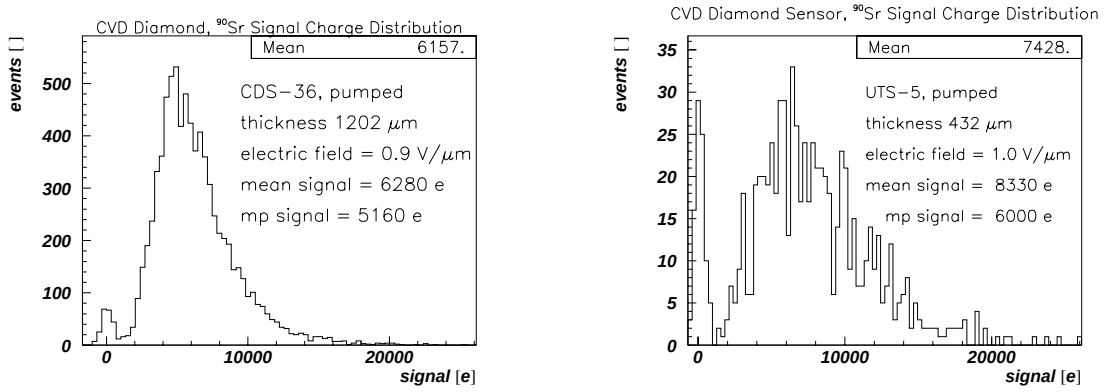

Figure 3.36: Charge signal distribution from two CVD diamond samples, CDS-36 (left) and UTS-5 (right), in the pumped state.

Fig. 3.36 shows the signal distributions for CDS-36 and UTS-5. The mean, $\bar{Q}_{\rm ind}$, of the induced signal charge distribution (without entries from the pedestal) is (6280 ± 24) e for CDS-36 and (8330 ± 100) e for UTS-5. The signal charge distributions are separated from zero. The signal distribution starts at about $Q_{\rm min} = (1500 \pm 500)$ e for CDS-36 and $Q_{\rm min}(1200 \pm 400)$ e for UTS-5. This corresponds to a separation to most probable ratio of 1/4 in CDS-36 and 1/5 in UTS-5. The separation in silicon can be read from the measurement of the signal distributions in Fig. 4.50: the separation between the rise of the distribution from zero is about 3/4 of the most probable signal. The separation from silicon is about 3 times larger than from these diamonds.

A technique to find the mean of the signal distribution is to calculate the *background corrected mean value of the histogram with pedestal*

$$\bar{Q}_{\rm ind} = \left(1 + \frac{N_{\rm p}}{N_{\rm s}}\right) \bar{H} \tag{3.150}$$

where $\bar{H}$ is the mean value of the whole histogram (including entries from the pedestal) and $N_{\rm p}$ is the number of entries in the pedestal and $N_{\rm s}$ is the number of entries in the signal distribution. For the measurements of the charge collection distances in Table 3.6 a background correction was made if the measurement had a pedestal distribution. The histogram of CDS-36 includes 8000 entries while the histogram of UTS-5 (right) only includes 800 entries. The number of entries in the signal distribution determines the *statistical error of the mean of the signal distribution*

$$\Delta Q_{\rm ind} \approx \frac{\rm FWHM}{2.35\sqrt{N_{\rm s}}}. \tag{3.151}$$

The FWHM is the full width of the distribution at half the maximum. Eq. 3.151 is an approximation which assumes a Gaussian signal distribution. The statistical error of the mean is 24 e for CDS-36 and 100 e for UTS-5. The statistical error of the mean charge directly corresponds to the error in the charge collection distance measurement. The error of 100 e corresponds to an error of 3 μm for the charge collection distance. The statistical error can be reduced by recording more events.

The shape of the signal charge distribution is determined by fluctuations of the energy loss process. The Landau distribution can be used as a description of the energy loss distribution [Sec. 3.3.3] assuming a characteristic width $\sigma_{{\rm d}E/{\rm d}x}$ [20]. The energy necessary for the creation of an electron-hole pair straggles as well and may contribute with a width σ_{eh}. The width of a distribution due to straggling is then

$$\sigma_{\rm straggling} = \sqrt{\sigma^2_{{\rm d}E/{\rm d}x} + \sigma^2_{eh}}. \tag{3.152}$$

The electronics noise, $\sigma_{\rm noise} = \sqrt{\left\langle q^2_{\rm ped} \right\rangle}$, also contributes to the width of the induced charge distribution. In addition there are variations in signal charge laterally across the sample as shown in Sec. 4.4. These variations may contribute with a width $\sigma_{\rm LV}$. The FWHM of the signal charge distribution is then approximated by

$$\rm FWHM \approx 2.35\sqrt{\sigma^2_{straggling} + \sigma^2_{noise} + \sigma^2_{LV}}. \tag{3.153}$$

[20] The mean and the *rms* of the Landau distribution are infinite. The characterization of the widths may be done by the FWHM which could be used to define $\sigma_{{\rm d}E/{\rm d}x}$. Alternatively one could define a cut-off energy for the Landau distribution and calculate the standard deviation for values below the cut-off energy.

The FWHM was chosen to characterize the width of measured signal charge distributions. Table 3.7 on page 108 lists results from a series of CVD diamond samples. The thickness, D, ranges from 600 μm up to 2253 μm. The mean charge signal ranges from 2000 e to 12500 e. The values were measured on samples in the pumped state and if possible at 1 V/μm. Eq. 3.151 was used to calculate the error on the most probable signal charge. Fig. 3.37 compares the most probable value of the distributions with their FWHM value. It can be seen, that the FWHM increases as the signal charge increases. For some samples the ratio of FWHM and the most probable value is less than one and for some samples bigger than one. The solid line in the figure has a slope of one. Two points (open circles) are shown from a measurement on silicon detectors (the distribution from silicon are shown in Fig. 4.50 in Sec. 4.3.4.). Also in silicon the FWHM increases as the most probable signal increases. The silicon points are near to a line with slope 0.5 (dashed line).

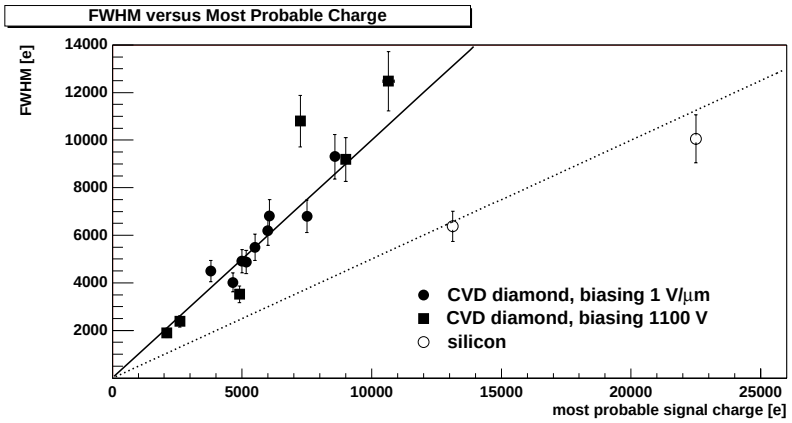

Figure 3.37: FWHM as a function of the most probable value in CVD diamond samples (solid circles) and in silicon (open circles).

3.4.10 Summary and Discussion

The method of characterizing a diamond sample by its charge collection distance has been described in this section. The characterizations were made using VA2 readout electronics. The linearity, noise performance and gain were studied in order to obtain reliable data from measurements in diamond.

Charge collection measurements were made using a ^{90}Sr β-source. The energy deposited from ^{90}Sr in this setup is assumed to be 8 % higher than from a minimum ionizing particle. One effect observed was pumping: the charge collection distances increased with absorbed dose from the β-source. The pumping and depumping of the charge collection distance was found on all diamond samples that were measured. The increase was typically a factor 1.5 to 2.0 from the unpumped value to the pumped value. Pumping is explained by filling traps with electrons, depumping by releasing electrons from traps. This model is supported by measurements of the temperature stimulated current and the thermoluminescence signal: both methods confirm release of electrons from trapped energy states during heating. Depumping with fluorescent light was observed to lower the charge collection distance and the luminescence response. The characterization of CVD diamond using the method of temperature stimulated currents and luminescence seems natural for characterizing the energy of trap levels and their concentration and eventually quantify their influence on the charge collection distance. In particular thermally stimulated current methods are a useful tool in identifying trap levels in other semi-conductor devices. This is also interesting for characterizations of

irradiated samples. Finally, it may be noted that a diamond sensor in a high luminosity experiment would quickly pump due to the high radiation background.

For recent samples the mean collected charge in the pumped state was above 6000 e at 1 V/μm corresponding to 166 μm charge collection distance. Samples with higher charge signal exceeding 8000 e (220 μm charge collection distance) were also available. The signal charge distribution from most diamonds was separated from zero by about 1200 e which is 1/5 of the most probable value. The separation in silicon was normally 3/4. Separation from zero is important for the determination of the particle hits in strip or pixel sensors. Hit finding relies on the threshold chosen for discriminating signal from noise. The threshold has to be sufficiently high in order to exclude noise hits. A separation above 3 times the noise charge variation prevents loss of signal due to a threshold cut. The noise charge variation was between 660 e and 850 e using fast (25 ns) LHC type readout electronics with a 1 pF load capacitance [Sec. 4.5]. Therefore one would desire a separation of about 3×660 e to 3×850 e. A separation of 1200 e is near the lower end of the desired separation. The separation has to improve to not loose signal charge. It was found that the width of the signal charge distribution increases with the most probable charge signal. The ratio of the FWHM to the most probable value was near 1.0 in CVD diamond and near 0.5 in silicon. The width from silicon sensors was lower than what was observed in CVD diamond sensors. A possible explanation for the FWHM in CVD diamond is a lateral variation in the charge collection distance.

As a result of the measurements on about 100 CVD diamond samples, often from different growths, the charge collection distance from one manufacturer has been improved from originally 30 μm to now typically between 170 μm and 200 μm and sometimes above 200 μm. It is likely that chemistry and control of impurities have improved during the last years of collaboration with the manufacturer. These years were mainly used to gain experience and understanding in research growth reactors. It is now time to transfer the growth to production reactors, this means the process should become a defined recipe which can be reproduced in other growth reactors and by different personal. This work has been started and samples from production growths have been delivered. For example the large trackers in Sec. 4.3 originate from production growths.

3.5 Material Removal Study

CVD diamond typically grows in a polycrystalline columnar structure along the growth direction. The substrate side begins with small grains (≈ 1 μm) which grow with material thickness. As the material grows it develops the texture of the fastest growing crystal orientation. It has previously been shown [11, 86, 87] that the electrical properties of CVD diamond vary with the thickness of the material: the carrier lifetimes are small on the substrate side and large on the growth side. As a result, the raw diamond material can be "improved" by removing material (lapping) from the substrate side. This procedure has been used to increase the signal size by 35% over the as-grown sample. This section presents measurements of the charge collection distance after material removal from the nucleation and growth side and explains the results with the linearly increasing charge collection distance in the material.

3.5.1 Successive Lapping on the Nucleation Side

Fig. 3.38 shows the charge collection distance versus electric field measured in a diamond sample (CDS-14) before and after material removal from the nucleation side. The charge collection distance was measured using the technique described in Sec. 3.4. The sample had a thickness of 624 μm as-grown. The charge collection distance at that thickness was (43 ± 4) μm at 1 V/μm in the depumped state. After lapping by 175 μm from the nucleation side, which is 28 % of the original thickness, the charge collection distance was (57 ± 4) μm at 1 V/μm in the depumped state which is higher than before lapping. The increase in charge collection distance is therefore (25 ± 4) % compared to the as-grown sample. This measurement shows that the average charge collection distance can be improved by material removal from the nucleation side. Successive lapping has been performed on CDS-14 and the charge collection distance was measured after each removal step. Fig. 3.39 shows the average charge collection distance, $\bar{d}$, normalized to the average charge collection distance, $\bar{d}_0$, before material removal as a function of the material removed from the nucleation side where D is the thickness before material removal. The measurements were performed by two groups (A

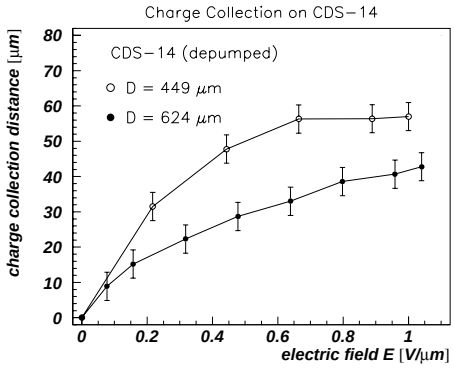

Figure 3.38: Charge collection distance as a function of the electric field in a diamond sample (CDS-14) before and after material removal from the nucleation side. The sample was measured in the depumped state for this measurement.

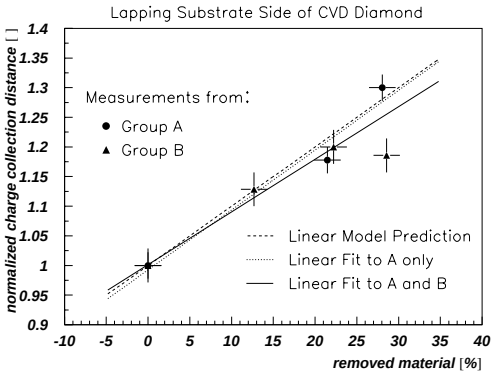

Figure 3.39: Measured charge collection distance as a function of the material removed from the substrate side. The sample was lapped three times by about 60 μm at each step. The charge collection increases after each step which is explained by the linear increase of charge collection from the substrate side in the diamond.

at CERN in the pumped state and B at OSU [85] in the depumped state). The normalized charge collection distance increases linearly with Δ_n/D after each step of material removal with a slope of $m = 1.0$ using the A data only and $m = 0.89$ using A and B data. The measurements from A and B agree except for the point after 28 % material removal. The measured increase is described by a linear function

$$\bar{d}(\Delta_n) = \bar{d}_0 + m\,\bar{d}_0\,\frac{\Delta_n}{D}. \tag{3.154}$$

The measurement can be explained with the following model. The charge collection distance depends on the position in the material along the direction of growth and can be described with a function, $d(z)$, which increases monotonically along the direction of growth on the interval from 0 to D with $0 \le d(z) \le D$ for all z in this interval. The mean value, $\bar{d}$, of the charge collection distance is then

$$\bar{d} = \frac{1}{D}\int_0^D d(z)\,\mathrm{d}z. \tag{3.155}$$

The average charge collection distance, $\bar{d}$, after material removal Δ_n from the nucleation side leaving the sample of thickness $D - \Delta_\mathrm{n}$ is then given by

$$\bar{d}(\Delta_\mathrm{n}) = \frac{1}{D-\Delta_\mathrm{n}}\int_{\Delta_\mathrm{n}}^D d(z)\mathrm{d}z. \tag{3.156}$$

For $\Delta_\mathrm{n} = 0$ one obtains the charge collection distance $\bar{d}_0 \stackrel{\mathrm{def}}{=} \bar{d}(0)$ before material removal. Calculation of the derivative $\partial\bar{d}/\partial\Delta_\mathrm{n}$ from Eq. 3.156 gives the charge collection distance as a function of the position z in the material

$$d(z) = \bar{d}(z) - (D-z)\cdot\frac{\partial\bar{d}}{\partial z}(z) \tag{3.157}$$

where the argument z is used instead of Δ_n to stress that Eq. 3.157 can be used for any position. Eq. 3.157 is useful since it relates the bulk averaged charge collection distance to the local charge collection distance. It allows one to deduce the local charge collection distance for any change of the measured bulk charge collection distance after several steps of lapping. The linear increase of the bulk charge collection distance as measured and described with Eq. 3.154 can be inserted in Eq. 3.157 and one obtains a *linear increase of the local charge collection distance from the nucleation to the growth side*

$$d(z) = (1-m)\,\bar{d}_0 + 2\,m\,\bar{d}_0\,\frac{z}{D}. \tag{3.158}$$

Using Eq. 3.158 it is possible to calculate the local charge collection distance at any position z in the bulk. In particular one finds the charge collection distance, d_0, on the nucleation side for $z = 0$ from the measured slope of $m \approx 1$ from Fig. 3.39

$$d_0 \equiv d(0) = (1-m)\;\bar{d}_0 \approx 0 \tag{3.159}$$

and the charge collection distance on the growth side from the measured slope

$$d(D) = (1+m)\;\bar{d}_0 \approx 2\,\bar{d}_0. \tag{3.160}$$

The slope, n, of the charge collection distance inside the bulk can be read from Eq. 3.158

$$n = \frac{2\,m\,\bar{d}_0}{D} \approx \frac{2\,\bar{d}_0}{D}. \tag{3.161}$$

The approximations in each of the previous equations have been made from the observation that $m \approx 1$ and therefore $d_0 \approx 0$.

3.5.2 Linear Model of the Carrier Drift Length

The observation above started with the measurement of the bulk averaged charge collection distance and deduced the local charge collection distance. It was shown that the measured linear increase of the bulk averaged charge collection after successive material removals implies the linear increase of charge collection distance in the material. The charge collection distance, d, can be identified with the carrier drift length, s, for the case of $0 \le s(z) \le D$ for all z along the direction of growth. For that case one can start with the assumption of a linearly increasing carrier drift length. This assumption, known as the linear model [11, 86, 87] starts with a *linear Ansatz for the carrier drift length*

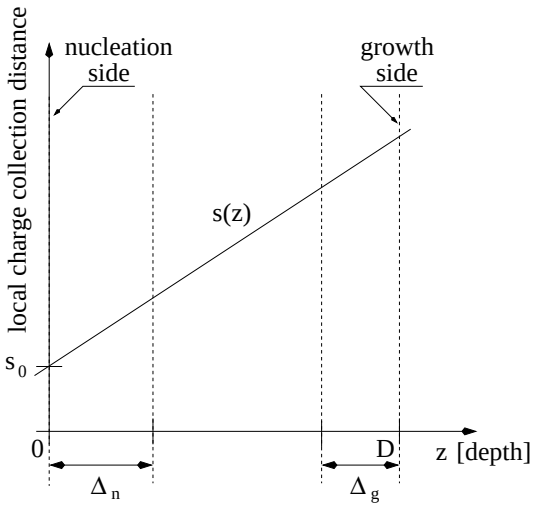

Figure 3.40: *Linear model* of the drift length, $s(z)$, as a function of the depth, z, in the diamond bulk. The nucleation side of the diamond is at $z = 0$ the growth side is at $z = D$ which gives the as-grown thickness D. Lapping on the nucleation side or growth side reduces the thickness by the amount Δ_n or Δ_g.

$$s(z) = s_0 + n\,z. \tag{3.162}$$

Fig. 3.40 illustrates the carrier drift length from the nucleation side to the growth side. The nucleation side at $z = 0$ has the carrier drift length, d_0, which can be different from zero. The carrier drift length is assumed to increase in direction of growth with the slope n. One can identify the carrier drift length with the charge collection distance if $s(z) \leq D$ for all z along the direction of growth

$$\text{if} \quad s(z) \leq D \quad \text{then} \quad d(z) = s(z) \quad \text{and} \quad d_0 = s_0. \tag{3.163}$$

Integration of Eq. 3.162 as in Eq. 3.48 gives the bulk averaged charge collection distance

$$\bar{d}(\Delta_n) = \bar{d}_0 + \frac{n}{2}\,\Delta_n \qquad ; \qquad \bar{d}_0 = \left(d_0 + \frac{n}{2}\,D\right) \tag{3.164}$$

where Δ_n denotes again the amount of material removed from the nucleation side. In particular one obtains the bulk averaged charge collection distance after *lapping on the nucleation side*

$$\frac{\bar{d}}{\bar{d}_0} = 1 + \left(1 - \frac{d_0}{\bar{d}_0}\right)\,\frac{\Delta_n}{D}, \tag{3.165}$$

which is overlayed to the measured data in Fig. 3.39. In other words, the change in the carrier drift length after lapping is proportional to the change in thickness. One can conclude that the linear model of carrier drift length is consistent with the measurement of linearly increasing charge collection distance. The measured slope, m, from Eq. 3.154, is then related to the charge collection distance (= carrier drift length) on the nucleation side and the initial bulk averaged charge collection distance

$$m = 1 - \frac{d_0}{\bar{d}_0}. \tag{3.166}$$

The measured slope, $m \approx 1$, is consistent with zero charge collection distance and carrier drift length on the nucleation side ($d_0 = s_0 = 0$).

3.5.3 Lapping on the Growth Side

For tracker preparation with strips on the growth side it was necessary to remove material from the growth side in order to obtain a smooth surface. Lapping on the growth side is expected to decrease the averaged carrier drift length and hence the averaged charge collection distance since according to the linear model regions with comparable high carrier drift length are removed. The bulk averaged charge collection distance for lapping on the growth side by the amount Δ_g is given in analogy to Eq. 3.156 by

$$\bar{d}(\Delta_g) = \frac{1}{D-\Delta_g}\int_0^{D-\Delta_g} d(z)\mathrm{d}z. \tag{3.167}$$

One can use the model of linearly increasing carrier drift length [Eq. 3.162] and assume that one can identify the carrier drift length with the charge collection distance. Then one obtains the bulk averaged charge collection distance after *lapping on the growth side*

$$\frac{\bar{d}}{\bar{d}_0} = 1 - \left(1 - \frac{d_0}{\bar{d}_0}\right)\frac{\Delta_g}{D} \tag{3.168}$$

which differs from Eq. 3.165 by the sign in front of the brackets, only. For the general case of lapping on both sides of one obtains

$$\frac{\bar{d}}{\bar{d}_0} = 1 + \left(1 - \frac{d_0}{\bar{d}_0}\right)\left(\frac{\Delta_n}{D} - \frac{\Delta_g}{D}\right). \tag{3.169}$$

Fig. 3.41 shows the measured charge collection distance before and after lapping on the growth side of a CVD diamond sample (CDS-38) as a function of the electric field. The

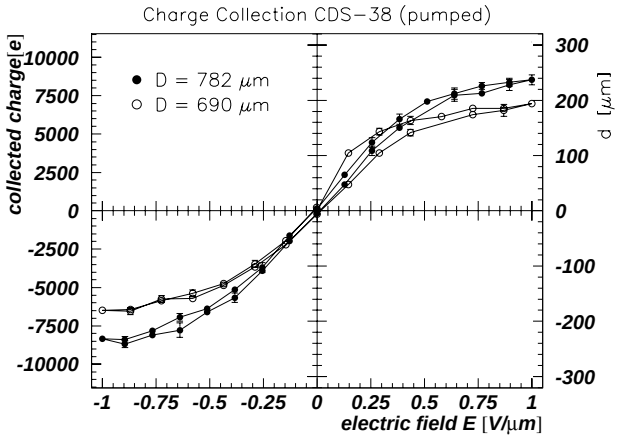

Figure 3.41: Collected charge signal and charge collection distance as a function of the electric field in a diamond sample (CDS-38) before and after material removal from the growth side. In both measurements the sample is in the pumped state.

sample had a thickness as-grown of 782 μm and a charge collection distance of (238 ± 10) μm at +1 V/μm. After lapping of 92 μm from the growth side to a thickness of 690 μm the charge collection distance is (193 ± 10) μm at +1 V/μm. The measured ratio $\bar{d}/\bar{d}_0$ is therefore 0.811 ± 0.07. The expected ratio from Eq. 3.168 assuming $d_0 = 0$ μm is 0.88 which is slightly higher than the measured ratio.

3.5.4 Summary and Discussion

CVD diamond samples have been thinned by successive lapping on the nucleation side. The charge collection distance has been measured after each removal step. The charge collection distance is observed to increase after each lapping step. Taking the measured increase

it was shown that the local charge collection distance increases linearly from the nucleation side to the growth side. The measurement indicates that the carrier drift length is nearly zero on the nucleation side and twice the bulk carrier drift length on the growth side. It was also demonstrated by one measurement that lapping on the growth side leads to a decrease of the average charge collection distance. These observations agree with previous work on CVD diamonds produced by other manufacturers [11, 86, 87]. It has been shown in Sec. 2.2 that the grain size increases linearly from the nucleation side to the growth side. It could therefore be that in the region of larger grains the carrier drift length is higher than in regions with smaller grains. A possible reason for a lower carrier drift length on the nucleation side could be a high concentration of grain boundaries or a high concentration of defects in general. It could also be that the orientation of growth is important for the carrier drift length and hence for the charge collection distance.

The carrier drift length was measured on the surface of a diamond as described in reference [11, 86] using carrier excitation by a laser. The carrier drift length was measured between two contacts on the surface of CVD diamonds and natural diamond. It was found that the carrier drift length is near zero on the nucleation side of CVD diamond and twice the bulk average carrier drift length on the growth side. In natural diamond the carrier drift lengths are equal on both sides. The carrier drift length was infered from the charge collection distance. The linear model implies a thickness above which the carrier drift length exceeds the thickness of the sensor. For this case the carrier drift length can no longer be infered from the charge collection distance. The measurement of the surface charge collection distance allows one to infer the surface carrier drift length at any thickness. The identification is only limited by the distance of the contacts on the surface. In order to infer the carrier drift length the measurement of the surface charge collection distance is therefore favorable if the charge carrier drift length approaches or exceeds the detector thickness. Finally it should be noted that for the case that the carrier drift length exceeds the detector thickness and for the case of injecting contacts one should be able to observe photo-conductive gain which means that the signal charge on the electrodes exceeds the generated charge.

sample index	sample name	delivery number	D [μm] $\pm 5\mu$m	N_s	$\bar{Q}_{ind}$ [e]	$\bar{d}$ [μm]	comment
1	DRDS-1	-	285	800	900 ± 14	25 ± 1	natural
2	CDS-14	(42)	642	800	3240 ± 50	90 ± 1	as-grown
3	CDS-15	(43)	764	800	2700 ± 41	75 ± 1	as-grown
4	CDS-16	(44)	411	800	1440 ± 22	40 ± 1	as-grown
5	CDS-17	(47)	743	800	2340 ± 35	65 ± 1	as-grown
6	CDS-18	(58)	499	800	3168 ± 48	88 ± 1	as-grown
7	CDS-19	(61)	388	800	3060 ± 46	85 ± 1	lapped
8	CDS-20	(63)	460	800	2304 ± 81	64 ± 2	as-grown
9	CDS-21	(64)	435	800	2268 ± 34	63 ± 1	as-grown
10	CDS-22	(67)	2620	800	8028 ± 110	223 ± 3	as-grown
11	CDS-23	(68)	776	800	5112 ± 78	142 ± 2	as-grown
12	CDS-24	(69)	765	not measured			as-grown
13	CDS-25	(70)	785	800	2520 ± 38	70 ± 1	as-grown
14	CDS-26	(71)	1578	580	12500 ± 220	347 ± 6	lapped
15	CDS-27	(72)	1445	4400	11270 ± 70	313 ± 2	lapped
16	CDS-28	(73)	1098	800	8700 ± 100	242 ± 3	prob. lapped
17	CDS-29	(74)	611	800	4800 ± 70	133 ± 2	prob. lapped
18	CDS-30	(75)	2253	1260	2900 ± 30	81 ± 1	as-grown
19	CDS-31	(76)	2242	3164	2350 ± 14	65 ± 1	as-grown
20	CDS-32	(77)	2000	1168	6100 ± 44	169 ± 1	as-grown
21	CDS-33	(78)	710	790	5482 ± 61	153 ± 2	lapped
22	CDS-34	(79)	diode-like				
23	CDS-35	(80)	diode-like				
24	CDS-36	(81)	1202	7760	6280 ± 24	174 ± 1	as-grown
25	CDS-37	(82)	1232	6870	6050 ± 25	168 ± 1	as-grown
26	CDS-38	(83)	782	700	7200 ± 110	200 ± 3	lapped
27	CDS-41	(84)	diode-like				
28	CDS-39	(85)	1543	9000	10400 ± 41	288 ± 1	lapped
29	CDS-42	(86)	920	7200	10700 ± 47	297 ± 1	lapped
30	UTS-5	-	432	700	8330 ± 100	232 ± 3	lapped
31	CDS-61	-	521	4000	6340 ± 37	176 ± 1	lapped
32	CDS-62	-	535	4000	8750 ± 46	243 ± 1	lapped

Table 3.6: Results from a series of diamond samples measured in the pumped state: the thickness, D, the number, N_s, of events taken for calculating the mean signal charge, the mean signal charge, $\bar{Q}_{ind}$, and the charge collection distance, $\bar{d}$. The samples are listed in the order of delivery by the the manufacturer (number in brackets). The index in the very left column is assigned in order to display the results Fig. 3.35.

sample name	delivery no.	D [μm] ± 5	$\lvert\vec{E}\rvert$ [V/μm]	N_s	$\bar{Q}_{ind}$ [e]	$\hat{Q}_{ind}$ [e]	FWHM [e] $< \pm 10\%$	FWHM/$\hat{Q}_{ind}$ $< \pm 12\%$
CDS-26	(71)	1578	0.70	580	12500 ± 220	10650 ± 220	12477	1.17
CDS-27	(72)	1445	0.77	4400	11270 ± 70	7250 ± 70	10800	1.48
CDS-28	(73)	1098	no histogram					
CDS-29	(74)	611	1.00	800	4800 ± 70	3800 ± 70	4500	1.18
CDS-30	(75)	2253	0.50	1260	2900 ± 30	2600 ± 30	2380	0.90
CDS-31	(76)	2242	0.50	3164	2350 ± 14	2100 ± 14	1900	0.90
CDS-32	(77)	2000	0.55	1168	6100 ± 44	4900 ± 44	3520	0.72
CDS-33	(78)	710	1.00	790	5482 ± 61	4650 ± 61	4020	0.86
CDS-34	(79)	diode-like						
CDS-35	(80)	diode-like						
CDS-36	(81)	1202	0.90	7760	6280 ± 24	5160 ± 24	4880	0.94
CDS-37	(82)	1232	0.90	6870	6050 ± 25	5000 ± 25	4906	0.98
CDS-38	(83)	782	1.00	700	7200 ± 110	6064 ± 110	6820	1.13
CDS-41	(84)	diode-like						
CDS-39	(85)	1543	0.70	9000	10400 ± 41	9000 ± 41	9186	1.02
CDS-42	(86)	920	1.00	7200	10700 ± 47	8580 ± 47	9300	1.08
UTS-5	-	432	1.00	700	8330 ± 100	6000 ± 100	6200	1.03
CDS-61	-	521	1.00	4000	6340 ± 37	5500 ± 37	5500	1.00
CDS-62	-	535	1.00	4000	8750 ± 46	7500 ± 46	6800	0.91

Table 3.7: Results from a series of diamond samples measured in the pumped state: The thickness (D), the magnitude of the electric field, $\lvert\vec{E}\rvert$, the number of signal entries, N_s, the mean induced charge ($\bar{Q}_{ind}$), the most probable induced charge ($\hat{Q}_{ind}$), the full width at half maximum (FWHM) and the ratio FWHM/$\hat{Q}_{ind}$ are listed. The statistical errors on the mean and most probable value were calculated using Eq. 3.151. The samples are listed in the order as they were delivered by the the manufacturer (number in brackets).

Chapter 4

Particle Tracking

Position sensitive CVD diamond detectors were studied in particle beams to understand the mechanisms involved in charge collection and to measure their intrinsic spatial resolution and hit recognition efficiency. A silicon beam reference telescope was used to predict the incident angle of particle tracks into the diamond and the intersection point of the track with the diamond. The response of the diamond sensor to the incident particle was studied. The methods used to analyse beam data are presented. Wherever possible the results from silicon sensors are presented in order to verify the methods. A photograph of a CVD diamond strip sensor and its readout is shown in Fig. 4.1. This diamond sensor is an example of a large diamond strip detector which was read out by low noise electronics and studied in a particle beam.

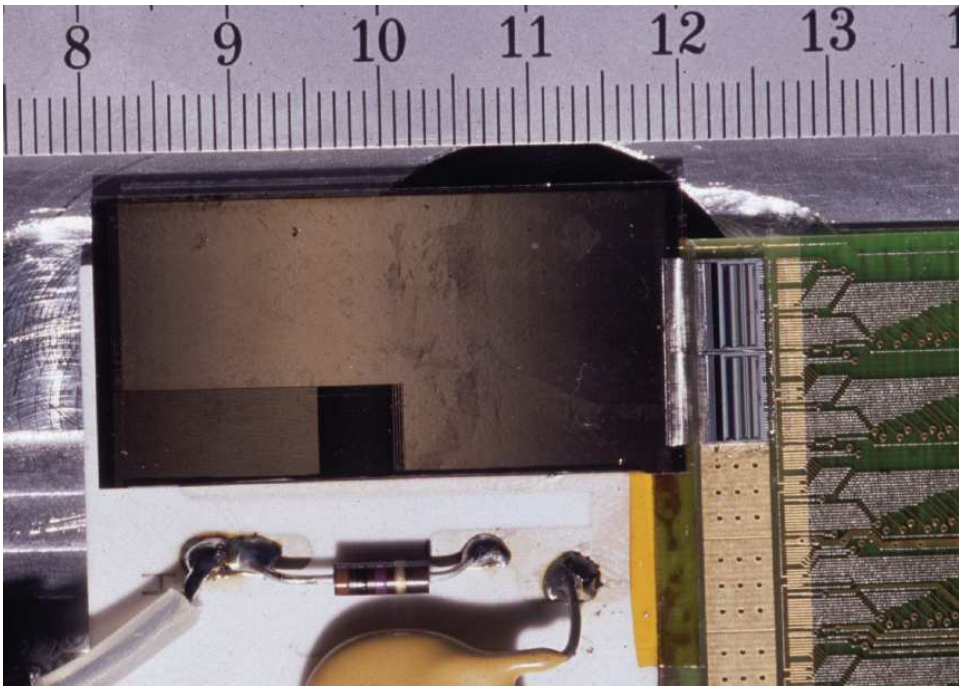

Figure 4.1: Photograph of a 2×4 cm^2 CVD diamond strip detector. The diamond had a thickness of 650 μm. The strips on the diamond surface were 25 μm wide and had a pitch of 50 μm. In total 256 strips of the detector were read out by two low noise CMOS chips (VA2).

Contents

4.1 The Silicon Beam Reference Telescope

This section describes the silicon beam reference telescope, its performance in terms of signal-to-noise ratio, spatial resolution and track prediction. The analysis methods of determining the pedestal, common mode shift and signal, hit finding, track finding and detector alignment are also discussed.

4.1.1 The Beam

The beam tests described were performed at CERN using pions in the X5 west area of the SPS and in beam areas of the PS. A good description of the SPS beam transport to X5, its conditions and layout may be obtained from reference [88]. The pion momentum in X5 was chosen to be 100 GeV/c at a flux of below 10^6 particles/spill. The beam was brought to a focus at the region of the silicon beam reference telescope. The beam had an oval shape with a width of about 1 cm at the center of the telescope.

4.1.2 Telescope Setup in the Beam Area and Data Acquisition

A schematic diagram of the silicon beam reference telescope used here is shown in Fig. 4.2. The beam telescope had eight silicon detector planes, each with a size of (length × width ×

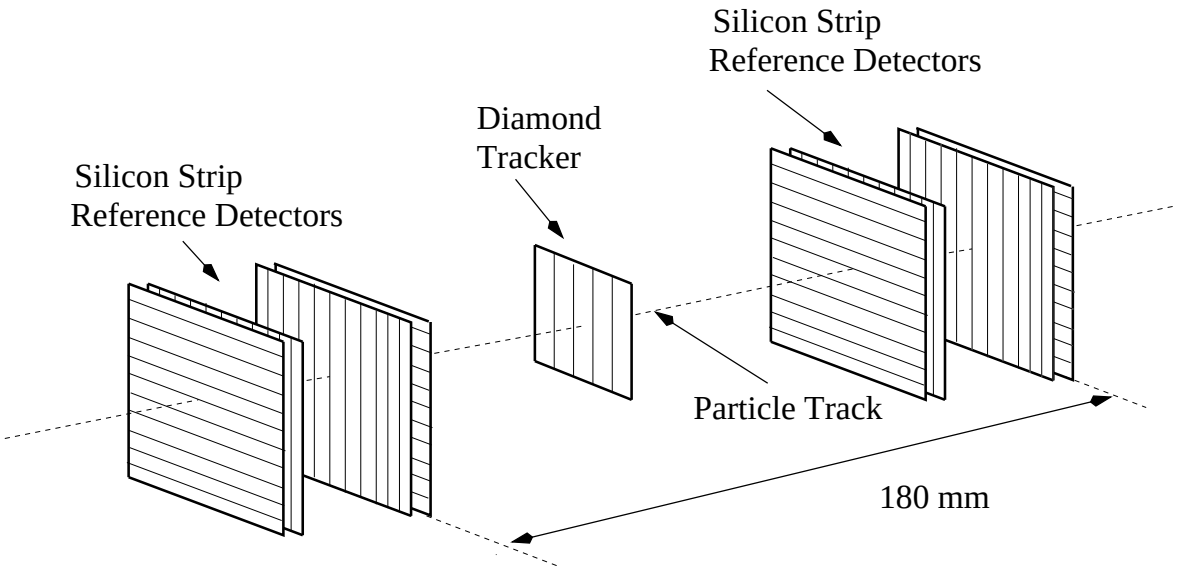

Figure 4.2: Schematic of the silicon beam telescope. The telescope had two sets of modules containing four silicon planes each. The modules were 180 mm apart. The diamond detectors under test were placed between the two sets of planes.

thickness) = (12.8 mm × 12.8 mm × 300 μm) arranged in two modules of four planes 180 mm apart. The silicon detectors were single sided p-on-n strip detectors with a strip pitch of 50 μm [89]. The silicon strip detectors in one module had one intermediate strip between two readout strips, the other module had detectors with two intermediate strips between readout strips. The strips of a plane were oriented vertically (V) or horizontally (H) in the order HVVH per module. Diamond detectors under test were placed between the two sets of silicon reference planes. A fast plastic scintillator trigger (not shown) with a size of 7×7 mm^2 was centered in the beam in front of the telescope. The scintillation light was detected by two photomultiplier tubes: their coincident signal in response to a traversing charged particle defined a trigger event (beam event).

A total of 256 strips per plane were read out with low noise VA2 (CMOS) electronics [78]. The channel acquisition rate was 1 MHz; reading 128 channels from the multiplexer of a VA2 required 128 μs as illustrated in Fig. 4.3. The analogue voltage levels of each channel in the sequence were digitized by sirocco VME analogue-to-digital-converters (ADC) [90]. The sirocco ADC for the silicon beam reference telescope digitized the analogue signal with a precision of 8 bits. The data acquisition system, based on VME bus with ELTEC E-16 processor running OS/9, had a typical acquisition rate of 300 to 400 trigger events per spill with simultaneous data recording on 8 mm EXABYTE magnetic tapes during spill breaks. One event, containing data from a maximum of 16×256 strips, had a size of 8 kByte in memory which allowed 250000 events to fit on one 2 GByte tape. In practice a full tape with 250000 beam trigger events could be recorded in 3 to 4 hours of good beam performance. The off-line analysis used 'DiamondTracking' object oriented C++ code [91] linked to classes of the ROOT framework [92]. Small analysis jobs with an execution time of less than 60 minutes ran on an interactive node of the ATLAS HP-Unix work group server. Large analysis jobs with an execution time of more than 60 minutes (for data 'production') were submitted as a batch job to the SHIFT-ATLAS computers.

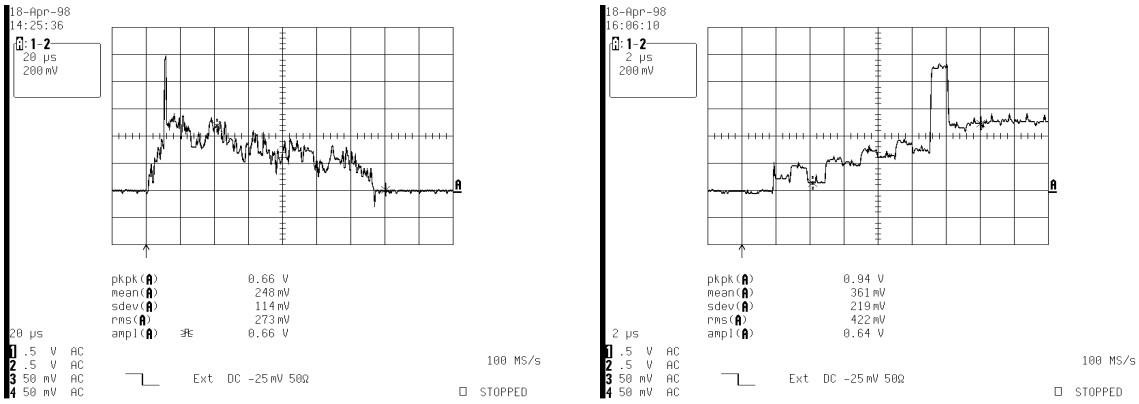

Figure 4.3: Left: raw data sequence from 128 channels at the output of the multiplexer from a VA2 readout chip. Right: raw data sequence from 16 channels in another event. A silicon diode was bonded to the 10^{th} channel. In both events the 10^{th} channel has a higher value due to a signal in the diode.

4.1.3 Pedestal, Common Mode, Signal and Noise Determination

The *raw signal*, $r_k(n)$, on the strip k in the event n from a detector measured by the sirocco analogue-to-digital converter [Fig. 4.3] can be expressed in terms of the physical charge signal, $q_k^{\text{phy}}(n)$, the random charge signal, $q_k^{\text{rnd}}(n)$, the pedestal, $p_k(n)$, and the common mode shift, $c(n)$:

$$r_k(n) = q_k^{\text{phy}}(n) + q_k^{\text{rnd}}(n) + p_k(n) + c(n). \tag{4.1}$$

These quantities have dimensions of a charge measured in ADC units [1]. The physical signal charge, $q_k^{\text{phy}}(n)$, is due to a particle interaction in the detector and is to be distinguished from the noise signal charge, $q_k^{\text{rnd}}(n)$, which occurs randomly. After acquiring N beam events the *'true' initial pedestal* value is

[1] The unit *ADC*: 1 ADC $\stackrel{\text{def}}{=}$ 1 value from the analogue to digital converter.

$$p_k(N) = \frac{1}{N}\sum_{n=1}^{N}\left[r_k(n) - q_k^{\mathrm{phy}}(n)\right] \tag{4.2}$$

where the summation goes over *signal suppressed raw values*

$$r'_k(n) \stackrel{\mathrm{def}}{=} r_k(n) - q_k^{\mathrm{phy}}(n). \tag{4.3}$$

In practice it is not obvious how to extract signal suppressed raw values. A possible *estimator for the pedestal* is

$$p_k^{(\mathrm{est})}(N) = \frac{1}{N}\sum_{n=1}^{N} r_k(n). \tag{4.4}$$

On a strip k a total of N beam events contains N_p events with no physical signal charge and $N_\mathrm{s} = N - N_\mathrm{p}$ events with physical signal charge. The pedestal estimator Eq. 4.4 can therefore be rewritten in terms of a true pedestal and a contribution from raw values with signal

$$\begin{aligned} p_k^{(\mathrm{est})}(N) &= \frac{1}{N}\sum_{n:\ r_k(n)\ \text{in pedestal}}^{N} r_k(n) + \frac{1}{N}\sum_{n:\ r_k(n)\ \text{in signal}}^{N} r_k(n) \\ &= p_k(N) + \frac{1}{N}\sum_{n:\ r_k(n)\ \text{in signal}}^{N_\mathrm{s}} r_k(n) \\ \Longrightarrow \qquad & \frac{p_k^{(\mathrm{est})}(N) - p_k(N)}{\langle Q_\mathrm{s}\rangle} = 1 - \frac{N_\mathrm{p}}{N} \\ \text{with} \qquad & \langle Q_\mathrm{s}\rangle = \frac{1}{N_\mathrm{s}}\sum_{n:\ r_k(n)\ \text{in signal}}^{N} r_k(n). \end{aligned} \tag{4.5}$$

It can be seen that the pedestal estimator and the true pedestal are different. The difference depends on the fraction, N_p/N. The goal is to find a pedestal estimator which is as close as possible to the true pedestal.

In this analysis the pedestal estimator for each channel was calculated as follows. A buffer was filled with $M = 5$ raw values from M successive beam events. Any arbitrary value in this buffer unequal to the extremum of the buffer is an estimator for a signal suppressed raw value. After M events the buffer was cleared and filled with the next M events. The difference $p_k^{(\mathrm{est})}(N) - p_k(N)$ between the pedestal estimator and the true pedestal can be quantified for this method and for the method using Eq. 4.4. In a simplified model one may assume a point like true pedestal distribution with N_p entries at zero and a point like signal distribution with $N_\mathrm{s} = N - N_\mathrm{p}$ entries at $\langle Q_\mathrm{s}\rangle = 1$. The pedestal estimator according to Eq. 4.4 is then a linear function of N_p/N as illustrated by the solid line in Fig. 4.4. The pedestal estimator which uses signal suppressed values from the buffer by excluding the extremum is superimposed in the same figure (dashed line). The function is $(N - N_\mathrm{p})^2/N^2$ since this is the probability of having two physical signals in the buffer. The method which uses signal suppressed values from the buffer gives a pedestal estimator closer to the true pedestal at zero. Under the test beam condition here, the mean signal charge is $\langle Q_\mathrm{s}\rangle \approx 50$ ADC and with $K_\mathrm{chip} = 256$ strips one obtains the ratio $N_\mathrm{p}/N \approx 1 - 1/K_\mathrm{chip} = 0.996$. Using the pedestal estimator from Eq. 4.4 one obtains the difference of ≈ 0.2 ADC between the true pedestal and the pedestal estimator. Using the pedestal estimator with signal suppressed values one obtains the difference of ≈ 0.00076 ADC between the true pedestal and the pedestal estimator. In

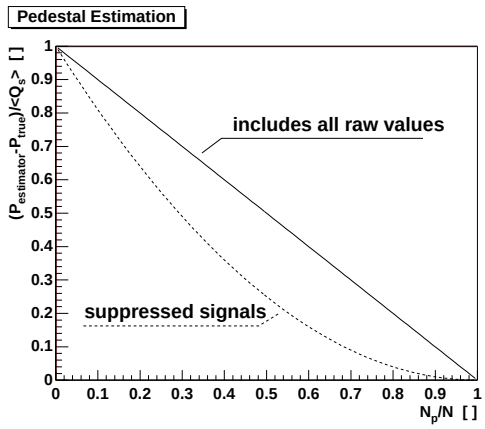

Figure 4.4: Difference between the pedestal estimator, $P_{\text{estimator}} \hat{=} p_k^{(\text{est})}$, and the true pedestal, $P_{\text{true}} \hat{=} p_k$, normalized to the mean, $\langle Q_{\text{s}} \rangle$, of the signal distribution as a function of the ratio between the number, N_{p}, of beam events in the pedestal and all beam events, N.

this analysis the buffer for the signal suppressed pedestal calculation was chosen to have a size of $M = 5$. $N = 100$ events were chosen for calculating the initial pedestal.

After acquiring the first N events the *initial noise*, $\Delta q_k^{\text{rnd}}(N)$, on single strips was calculated

$$\Delta q_k^{\text{rnd}}(N) \equiv \sqrt{\langle (q_k^{\text{rnd}})^2 \rangle} = \frac{1}{\sqrt{N-1}} \sqrt{\left[\left(\sum_{n=1}^{N} r'_k(n)^2 \right) - N \cdot p_k(N)^2 \right]} \tag{4.6}$$

where $r'_k(n)$ denotes signal suppressed raw values which were taken from the buffer $\{r_k(n)$, $..,r_k(n+M-1)\}$ by excluding the extremum. If one would not suppress raw values with signal one would find an increased noise on strips which were illuminated by the beam.

For events $n > N$ the *common mode shift* was calculated on K strips where K was normally the number of channels of a readout chip:

$$c(n) = \frac{1}{K} \sum_{k=1}^{K} \left[r_k(n) - p_k(n) \right]. \tag{4.7}$$

The common mode calculation included only channels with $[r_k(n) - p_k(n)] < 3 \cdot \Delta q_k^{\text{rnd}}(n)$ in order to exclude signals related to a particle hit. The *current pedestal* for events $n > N$ was found by using the *recursive pedestal-follower-method*

$$p_k(n)|_{n>N} = \frac{1}{A} \left[(A-1) \cdot p_k(n-1) + r'_k(n) - c(n) \right] \tag{4.8}$$

where $p_k(n-1)$ was the pedestal value from the previous event and $r'_k(n)$ is a signal suppressed raw value. A weight, $A = 10$, was chosen to be sufficiently robust against fluctuations and sensitive enough to follow modest changes in the pedestal. Weights $A \geq 10$ could be chosen to give slower response to changes in the pedestal. The *signal charge* was then extracted from Eq. 4.1

$$q_k(n) \stackrel{\text{def}}{=} q_k^{\text{phy}}(n) + q_k^{\text{rnd}}(n) = r_k(n) - p_k(n) - c(n). \tag{4.9}$$

The hit cluster finding required a signal-to-noise threshold cut on the seed strip and threshold cuts on adjacent strips in the cluster. The *single strip noise*, $\Delta q_k^{\text{rnd}}(n)$, is the statistical error on the measurement of the single strip signal; it was calculated from the strip noise in the previous event and the noise charge of the actual event:

$$\Delta q_k^{\text{rnd}}(n) = \sqrt{\frac{1}{B} \left[(B-1) \cdot \left[\Delta q_k^{\text{rnd}}(n-1) \right]^2 + q_k^{\text{rnd}}(n)^2 \right]} \tag{4.10}$$

where $q_k^{\rm rnd}(n)$ is given by Eq. 4.9. The signal suppressed raw value, $r_k(n) - q_k^{\rm phy}$, was taken from the buffer with M values with the requirement to be different from the buffer's extremum. The value B is a weight which was chosen as $B = 10$. It could be different from the weight A. A similar method to calculate the pedestal, common mode and signal can be found in [93, 94].

Fig. 4.5 shows the distribution of the pedestal subtracted, common mode corrected and signal suppressed values, $q_k(n) = r_k(n) - p_k(n) - c(n)$, measured on 128 strips which were not in a hit cluster. Each entry in the upper histogram was taken from one strip chosen randomly with equal probability from the 128 strips. The distribution of $q_k(n)$ is non-Gaussian but

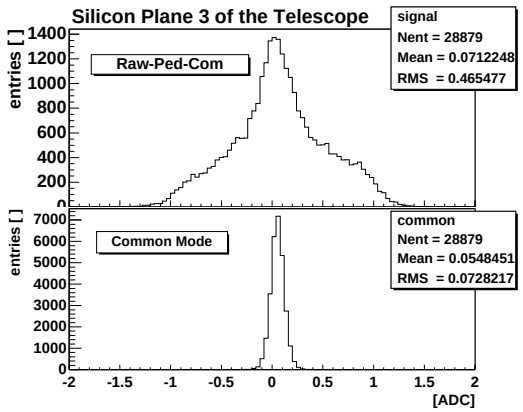

Figure 4.5: Distribution of the pedestal subtracted and common mode corrected signals $q_k^{\rm rnd}(n) = r_k(n) - p_k(n) - c(n)$ (above) and the common mode shifts $c(n)$ (below).

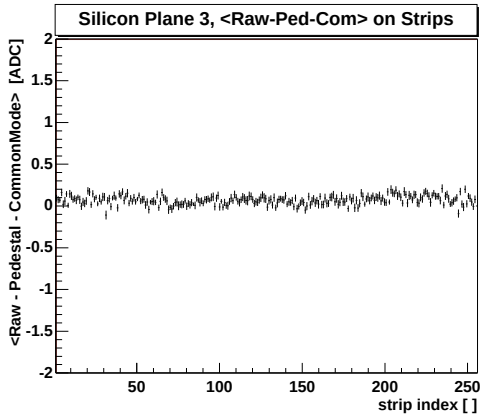

Figure 4.6: Mean value of the pedestal subtracted and common mode corrected raw values as a function of the strip index for 256 strips.

symmetric around the mean value of 0.07 ADC. The *mean noise* is the average over strips

$$\Delta q^{\rm rnd}(N) = \frac{1}{K}\sum_{k=1}^{K} \Delta q_k^{\rm rnd}(N) \quad ; \quad \Delta q_k^{\rm rnd}(N) \overset{\text{Fig. 4.5}}{=} \sqrt{\frac{1}{N-1}\sum_{n=1}^{N} q_k^2(n)\Big|_{|q_k(n)|<2 \text{ ADC}}}. \quad (4.11)$$

The mean noise can be read from the histogram as $rms = 0.465$ ADC. The averaging was done over $K = 128$ strips and the *rms* was calculated for $N \approx 30000$ events.

The raw values were digitized by the 8-bit analogue to digital converter producing integers. The signal charge, $q_k(n)$, is a floating type since the pedestal and the common mode are floating types. The reason for the non-Gaussian shape of the distribution is the quantization by the ADC. The underlying distribution in Fig. 4.5 (top) are three peaks at $-1, 0$ and 1 which have an $rms = \sqrt{100 \cdot (-1)^2 + 1350 \cdot 0^2 + 200 \cdot 1^2}/\sqrt{1650} \approx 0.43$ ADC. The precision due to the quantization is $1/\sqrt{12}$ ADC ≈ 0.3 ADC. The measured distribution is a convolution of the quantized raw values and the floating type pedestal and common mode. The later smear out the quantized distribution. The measured *rms* is of the order of the precision of the sirocco ADC.

The measurement of the signal in the beam [as it will be described in Sec. 4.1.4] and the expected most probable number of 22500 electrons collected in 300 μm thick silicon gives the gain of the detector-readout from which one obtains the single strip noise in electrons as listed in Table. 4.1 for the planes 3,4,7 and 8 of the telescope. The equivalent noise charge averaged over four planes with one intermediate strip was measured to be ≈ 210 e. The planes with two intermediate strips had, within error, the same single strip noise. Fig. 4.5 also shows the

distribution of the common mode shifts. The common mode shifts are Gaussian distributed around 0.05 ADC. The common mode standard deviation, $\Delta c = 0.073$ ADC $\hat{=}$ 36 e, can be read from the histogram *rms*. The measured common mode variation is 15 % of the total variation of the pedestal subtracted raw values and therefore small compared to the single strip noise. Such small variations of the common mode noise as measured here suggest that one may dispense with the common mode correction. The common mode shift and single strip noise signal are independent quantities and their standard deviations add in quadrature to give the *variation of the pedestal subtracted and signal suppressed raw values*:

$$\left\langle (r' - p)^2 \right\rangle = \left(\Delta q^{\mathrm{rnd}} \right)^2 + (\Delta c)^2 \tag{4.12}$$

where $r' - p = \frac{1}{K} \sum_{k=1}^{K} (r'_k - p_k)$. Eq. 4.12 results in $\langle (r' - p)^2 \rangle \approx \sqrt{0.4655^2 + 0.0728^2}$ ADC = 0.4708 ADC where the values were taken from Fig. 4.5. A measurement of the pedestal corrected raw data without common mode correction (not shown) gives $\sqrt{\langle (r' - p)^2 \rangle}$ = 0.4708 ADC in agreement with the result from Eq. 4.12. The statistical error in the mean of the common mode measurement is $\Delta c / \sqrt{K} \approx 0.006$ ADC where $K \approx 128$ is the number of channels without hits. It is also found that the common mode on strips read out by one chip is correlated to the common mode on strips which are read out by the other chip of the detector. This effect is understood since common mode shifts are caused by variations of the detector bias voltage or variations in the supply voltage of the readout which affects both chips.

Fig 4.6 shows the *mean value of the pedestal subtracted and common mode corrected raw values*

$$\left\langle q_k^{\mathrm{rnd}} \right\rangle \equiv \langle r'_k - p_k - c \rangle \overset{\text{Fig. 4.6}}{=} \frac{1}{N} \sum_{n=1}^{N} q_k(n) \Big|_{|q_k(n)| < 2 \text{ ADC}} \tag{4.13}$$

as a function of the strip index, k, where N denotes the number of entries acquired for the strip k. The figure shows that the individual strip noise mean values vary by a fraction of an ADC value which is negligibly small compared to the physical signal charge which is of the order of 50 ADC.

4.1.4 Hit Cluster Charge

A charged particle from the beam which traverses the detector causes a *hit* in the detector plane. The first hit (*principal hit*) was found by searching for the strip, k_{s}, that had the highest signal charge, $q_{k_{\mathrm{s}}}$, and whose strip signal-to-noise ratio exceeded the seed strip signal-to-noise threshold, t_{s}

$$\frac{q_{k_{\mathrm{s}}}}{\Delta q^{\mathrm{rnd}}_{k_{\mathrm{s}}}} \geq t_{\mathrm{s}} \quad \wedge \quad q_{k_{\mathrm{s}}} > q_{k_{\mathrm{n}}} \tag{4.14}$$

where $q_{k_{\mathrm{n}}}$ is a signal charge on a strip, k_{n}, in the neighbourhood of the seed strip. The strip with the index k_{s} becomes the seed of the hit cluster [2]. A hit cluster contains the seed strip and eventually contiguous neighbour strips. Contiguous neighbour strips, k_{n}, were included in the cluster if their signal-to-noise ratio exceeded the neighbour strip signal-to-noise threshold, t_{n},

$$\frac{q_{k_{\mathrm{n}}}}{\Delta q^{\mathrm{rnd}}_{k_{\mathrm{n}}}} \geq t_{\mathrm{n}} \tag{4.15}$$

[2] An alternative method could be to go sequentially through the channels and process the value that exceeds the threshold.

where $t_n \leq t_s$. Once the neighbour strip signal-to-noise ratio was below t_n then that strip and others which were further away from the seed were not included in this cluster. A maximum number of 4 strips could be included on either side of the seed strip. A hit cluster is the set of contiguous strips

$$\mathcal{K} = \{k_1, .., k_K\} \quad ; \quad K = |\mathcal{K}| \overset{\text{here}}{<} 9 \tag{4.16}$$

where the signal charge on the strips satisfies Eq. 4.14 and Eq. 4.15.

A hit cluster with K strips has a total *hit cluster charge* of

$$Q_K \overset{\text{def}}{=} \sum_{k \in \mathcal{K}} q_k \tag{4.17}$$

where the measured charge, q_k, on each strip is a sum of the random charge, q_k^{rnd}, and the physical signal charge, q_k^{phy}. Additional hits can be found by finding a new seed with neighbours which are not included in a previous hit cluster.

Alternatively the hit cluster charge can be required to include K contiguous strips, independent of the signal-to-noise ratio on the neighbour strips

$$Q_K = q_{k_s} + \sum_{k_n=1}^{K-1} q_{k_n} \quad ; \quad q_{k_s} > q_1 > q_2 > ... > q_{K-1}. \tag{4.18}$$

Fig. 4.7 show distributions of measured 1-, 2-, 3-, and 4-strip cluster charges $\{Q_1, Q_2, Q_3, Q_4\}$ in one of the silicon strip detector planes of the reference telescope. The number of strips in the cluster was required to be $K = 1, 2, 3, 4$ independent of the neighbour strip signal-to-noise ratio. Only the seed strip had to satisfy the condition Eq. 4.14. Cluster charges with 2

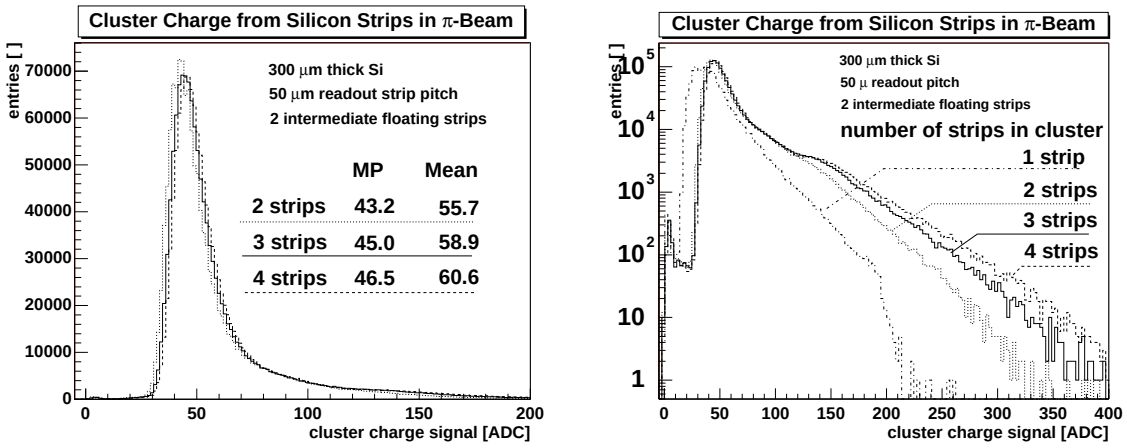

Figure 4.7: Distribution of cluster charges in a silicon strip detector plane of the telescope. The distributions are shown for 1-, 2-, 3-, and 4-strip clusters of principal hits with a linear ordinate (left) and a logarithmic ordinate (right).

or more strips are Landau distributed as can be seen in the linear representation (left). The same data is shown in a logarithmic representation (right). The 1-strip charge distribution is shown in the logarithmic representation only. The 1-strip charge is not Landau distributed and peaks at lower signal. Only a fraction of the total charge can be collected on a single strip in silicon detectors with intermediate strips since the charge is capacitively shared to the adjacent neighbour strip [94]. The mean and most probable values of clusters with 2 and more strips are shown in the left figure. The charge collected in 3- and 4-strip clusters

is slightly higher than for 2-strips. In the logarithmic representation one can see differences among the distributions. The distributions differ at higher charge signals. The 2-,3- and 4-strip cluster charge distributions deviate above 70 ADC from an exponential decrease. This deviation may be attributed to events with multiplicity two. Multiplicity 2 events may be due to secondary electrons (δ-electrons). *Delta*-electrons would release energies depending on their distance travelled. Hence the spectrum added to the single particle spectrum is wider than the single particle Landau distribution from a *mip*. The 3-strip and 4-strip cluster charges show a 'bump' at 135 ADC in the spectrum. This bump is at $\approx 3\times$ most probable value and may be attributed to events of multiplicity 3. Multiplicity 3 events may be due to nuclear interaction in the detector plane. The multiplicity 3 events do not cause a bump in the spectrum of two strip clusters.

The most probable value of 3-strip cluster charges is 45 ADC. This value was taken to be 22500 e (see also Sec. 3.3.5). The mean-to-most-probable ratio as read from the 3-strip charge distribution is 1.3 which corresponds to a mean collected charge in this detector plane of 29450 e. Using the measured single strip noise from Sec. 4.1.3 one finds the most-probable signal-to-noise ratio of 110-to-1. Similar results were obtained for the other seven silicon planes in the telescope.

Table 4.1 shows a summary of measurements of 3-strip most probable signals, single strip equivalent noise charge and signal-to-noise ratios from four planes of the silicon beam telescope. The most probable signal-to-noise ratio averaged over all 8 reference planes was $\approx$ 110-to-1.

plane	3-strip signal (most probable) [ADC]	gain [e/ADC]	single strip noise (ENC) [*rms* ADC]	[*rms* e]	most probable signal / noise [ ]
7	44.8	502.2	0.420	211	107
8	51.4	437.7	0.411	180	125
3	52.5	428.6	0.465	200	113
4	50.8	442.9	0.483	214	105

Table 4.1: Measurement of 3-strip most probable signal in ADC and single strip equivalent noise charge in *rms* ADC in four planes of the silicon beam telescope. The gain was calculated using the definition of 22500 e for the most probable collected charge on three strips of the 300 μm thick silicon sensor. The gain allows one to convert from ADC units to charge units. The ratio of the most probable collected charge to single strip noise is also shown.

4.1.5 Hit Position

A position sensitive detector is able to measure the hit position, the impact point of the particle in the detector plane. The measured position has an error which is a composition of the systematic and statistical error. The statistical error is due to charge fluctuations on strips (*i.e.* electronics noise, common mode noise). The systematic error is introduced by the hit finding method. Detectors which are designed to measure the position of a particle are characterized by their intrinsic spatial resolution which is equivalent to the error on the hit position. The collected charge on strips in a hit allows the determination of the position, u_{h}, of the hit perpendicular to the direction of the strips. Various methods are available to find the position of the hit. The goal is to apply a position finding method which has the smallest measurement error, Δu_{h}, and to attain the highest precision. A prediction for the position, u_{t}, of the hit was made by measuring the parameters of the particle track (offset, inclination,

curvature) using the beam reference telescope. This section describes the hit finding method used and the residual to the predicted hit position [3]. The method of how to predict the hit position is shown later in Sec. 4.1.6. In what follows one assumes that the beam illuminates the sensor uniformly. However, the methods can be generalized for any beam illumination.

4.1.5.1 Digital Hit Position

The digital hit finding method returns the center position, u_0, of the hit cluster seed strip. The *digital hit position* is

$$u_{\mathrm{h}}^{(\mathrm{dig})} \stackrel{\mathrm{def}}{=} u_0. \tag{4.19}$$

A measured distribution of residuals, $r = u_0 - u_{\mathrm{t}}$, is shown in Fig. 4.8 (left). The digital residual distribution is centered around zero and roughly constant in the interval from $-P/2$ to $+P/2$ where P is the readout strip pitch of 50 μm. The distribution has an $rms_{\,\mathrm{unrestr.}} =$ 15.01 μm as can be seen from the statistic box of the histogram. This *rms*-value is valid for the interval from -60 μm to +60 μm chosen for the presentation of this data. This *rms*-value is refered to as the unrestricted spatial resolution. The limits of the interval may be chosen differently. The choice may depend on the shape of the distribution. The shape of the distribution is described by a rectangular density function

$$\frac{\mathrm{d}N}{\mathrm{d}r}(r)\Big|_{r=u_{\mathrm{h}}^{(\mathrm{dig})}-u_{\mathrm{t}}} = K_{\mathrm{all}} \cdot \frac{N}{U_{\mathrm{f}}} \cdot \Theta\left(\frac{P}{2} - |r|\right) \qquad ; \qquad N = \int_{-\infty}^{+\infty} \frac{\mathrm{d}N}{\mathrm{d}r}(r)\mathrm{d}r \tag{4.20}$$

where $\Theta(x) = 1$ for $x > 0$ and $\Theta(x) = 0$ for $x \leq 0$ and N is the number of events which uniformly illuminate the fiducial region of length $U_{\mathrm{f}} = P \cdot K_{\mathrm{all}}$ perpendicular to the strips and $K_{\mathrm{all}} = 256$ is the number of strips in the detector. The full width at half maximum of this rectangular residual distribution is 50 μm. The measured full width at half maximum value is 50 μm, consistent with the rectangular distribution Eq. 4.20. The calculation of the standard deviation (the root mean square, *rms*) of the rectangular distribution gives the spatial resolution of the digital method

$$\Delta u_{\mathrm{h}}^{(\mathrm{dig})} \stackrel{\mathrm{def}}{=} \sqrt{\langle r^2 \rangle} \equiv \sqrt{\frac{1}{N}\int_{-\infty}^{+\infty} r^2 \frac{\mathrm{d}N}{\mathrm{d}r}\,\mathrm{d}r} \stackrel{\text{Eq. 4.20}}{=} \frac{P}{\sqrt{12}}. \tag{4.21}$$

The theoretical spatial resolution using the digital method (the digital resolution) is $rms_{\,\mathrm{theory}} = \Delta u_{\mathrm{h}}^{(\mathrm{dig})} = 14.43$ μm for a detector with $P = 50$ μm strip readout pitch and $rms_{\,\mathrm{theory}} = \Delta u_{\mathrm{h}}^{(\mathrm{dig})} = 28.87$ μm for a detector with $P = 100$ μm strip readout pitch. The unrestricted spatial resolution is larger than the theoretical value. If the limits of the interval chosen are lowered one finds that the *rms* slightly decreases until the limits fall below 30 μm corresponding to about twice the unrestricted spatial resolution. The restricted spatial resolution for the limits from -30 μm to +30 μm, was measured to be $rms_{\,\mathrm{restr.}} = 14.45$ μm. The restricted spatial resolution is about equal to the theoretical spatial resolution expected for the digital method.

It can be seen that the measured residual distribution has a few entries in the tails for $|r| > 25$ μm. The *rms* spatial resolution is sensitive to these entries. Events in the tails of

[3] The *residual* (engl.): here the difference between the predicted and the measured hit position, plural *residuals*. The latin word *residuum* (plural residua) can be found in chemistry as a difference of quantities. The graphs here are often labeled with residuum instead of residual. Both words are used with the same meaning here.

the residual distribution occur from multiple scattering or from track prediction errors. The angle deviation from a straight line due to multiple scattering in one silicon plane of 300 μm thickness has an *rms* of $\Delta\Theta = 24$ μrad for 100 GeV/c pions [Eq. 1.12]. The distance between the third and the fourth silicon plane is 6 mm. Using this distance the angle deviation causes a position uncertainty of 0.14 μm for the track prediction into the fourth silicon plane. An error in the track prediction may have two causes: firstly the intrinsic spatial resolution of each plane which gives a precision of the track prediction at the location of the fourth plane of about 1.4 μm (as shown below). Secondly the possibility to identify false hits and to associate false hits to a track causes events in the tails of residul distribution. False association of hits to tracks may occur in the detector under test or in tracking planes. Multiple hits may cause false association of hits to a track. The tracking code used was not optimized for multiple hits. The beam intensity is such that as few as possible multiple tracks were recorded. The calculation of the digital resolution, rms_{theory} from Eq. 4.20, does not account for multiple scattering or for errors in the track prediction. Hence the theoretical digital resolution is the smallest resolution which one could hope to attain. It is therefore not surprising to observe a small difference between the measured *rms* of the residual distribution and the theoretical spatial resolution. We conclude that the measured residual distribution is consistent with the expected shape of the residual distribution of the digital method. The entries in the tails are understood from a few misidentified hits and false association of hits to a track. Only if the measured residual distribution would have significantly more entries in the tails and only if the *rms* would be much larger than $P/\sqrt{12}$ one would need to investigate further. This is not the case here.

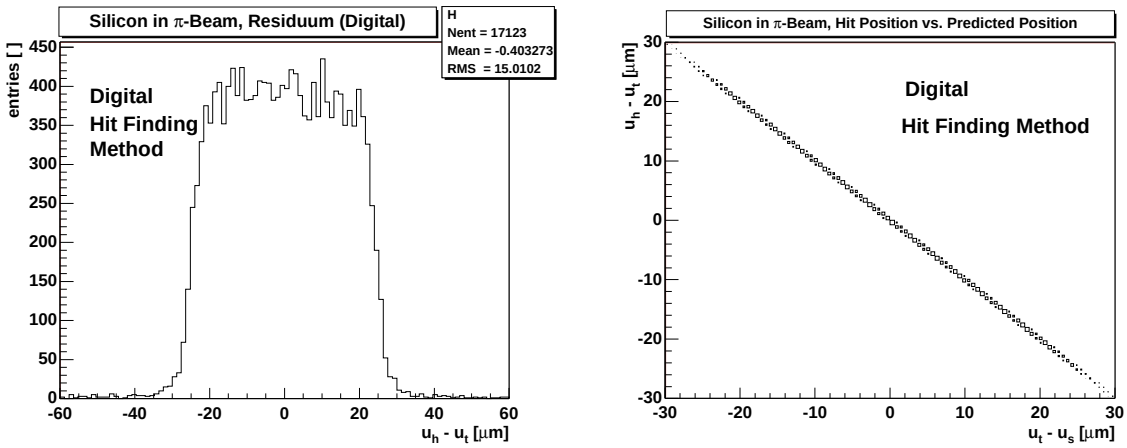

Figure 4.8: Digital residual distribution (left) and the residuals as a function of the hit position relative to strip positions centered at zero (right). The readout strip pitch is 50 μm. The slope of the 'line' ($u_{\text{h}} - u_{\text{t}}$ versus $u_{\text{t}} - u_{\text{s}}$) is -1.

Fig. 4.8 (right) shows a measurement of the residuals as a function of the difference, $u_{\text{t}} - u_{\text{s}}$, between the true hit position, u_{t}, and the position, u_{s}, of a strip. u_{s} is the position of a strip chosen for each beam event relative to the track. The position of the strip chosen is defined to be zero in this representation. It should be noted that one can chose strips which are either in an interval from $-P/2$ to $+P/2$ or further away than $\pm P/2$. It should also be noted that the difference, $u_{\text{t}} - u_{\text{s}}$, only relies on the hit prediction by the tracking system. The figure therefore shows the quantity, $u_{\text{h}} - u_{\text{t}}$, which involves a measurement from the detector under test as a function of a quantity, $u_{\text{t}} - u_{\text{s}}$, which is determined by the reference telescope only. It can be seen that the residuals depend on $u_{\text{t}} - u_{\text{s}}$. The measurement shows that the residuals follow a function

$$\begin{aligned} & r(t) = t \qquad \text{with} \qquad t \stackrel{\text{def}}{=} u_{\text{s}} - u_{\text{t}} \\ \Rightarrow \qquad & \frac{\mathrm{d}r}{\mathrm{d}t} = 1. \end{aligned} \tag{4.22}$$

The variable, t, is equally distributed for the case of *uniform illumination by the beam*

$$\frac{\mathrm{d}N}{\mathrm{d}t}(t) = \frac{N}{P}. \tag{4.23}$$

The digital method maps t into equally distributed residuals

$$\frac{\mathrm{d}N}{\mathrm{d}r}(r) \equiv \frac{\mathrm{d}N}{\mathrm{d}t}\frac{\mathrm{d}t}{\mathrm{d}r} \stackrel{\text{Eq. 4.23}}{=} \frac{N}{P}\frac{\mathrm{d}t}{\mathrm{d}r} \stackrel{\text{Eq. 4.22}}{=} \frac{N}{P}. \tag{4.24}$$

This expression is consistent with Eq. 4.20 for residuals $|r| < P/2$. The 'line', r as a function of t, has a slope of one. The slope represents the *systematic error* of the digital method. It is important to notice that, in general, the slope of $r(t)$ represents a systematic error of the hit finding method.

4.1.5.2 Center of Gravity Hit Position

The impact point of the particle in the detector can be measured using the center of gravity method. The center of gravity method gives the hit position, $u_{\text{h}}^{(\text{cog})}$, in terms of the charge fractions, η_{kK}, in the cluster:

$$\begin{aligned} u_{\text{h}}^{(\text{cog})} \quad & \stackrel{\text{def}}{=} \quad \frac{1}{Q_K}\sum_{k\in\mathcal{K}} u_k \cdot q_k \qquad ; \quad Q_K \stackrel{\text{Eq. 4.17}}{=} \sum_{k\in\mathcal{K}} q_k \\ & = \quad u_0 - \sum_{k\in\mathcal{K}} (u_0 - u_k)\cdot \eta_{kK} \qquad ; \quad \eta_{kK} \stackrel{\text{def}}{=} \frac{q_k}{Q_K} \\ \Longrightarrow \qquad & = \quad u_0 - P \cdot \sum_{k=k_1}^{k=k_{|\mathcal{K}|}} k \cdot \eta_{kK} \qquad ; \quad P = |u_k - u_{k-1}|\,. \end{aligned} \tag{4.25}$$

The last expression is true if $\mathcal{K}$ is ordered such that the seed strip has index 0 and neighbours to the left (right) have negative (positive) indices. The sum includes charge fractions from all strips whose signal-to-noise ratio exceeds the threshold t_{n}. The center of gravity method assumes that charge fractions have equal probability for a given cluster size. This assumption is *not true* for silicon strip detectors as will be seen by looking at charge fraction distributions in Sec. 4.1.5.3.

Fig. 4.9 shows the measured residual distribution for one of the silicon planes of the reference telescope using the center of gravity method. The residuals are Gaussian distributed and centered around zero. The *rms* of the residual distribution is 5.8 μm as can be seen in the statistic box of the histogram. The limits of the interval chosen are -30 μm and +30 μm. The distribution is described by a Gaussian function with a standard deviation of $\sqrt{\langle r^2\rangle} = \sigma = 4.6$ μm in the restricted interval from -12 μm to $+12$ μm. These limits were chosen to be about twice the *rms* of the resdual distribution. The measured standard deviation is to first order the error of the hit measurement [4]. Fig. 4.9 (right) shows the residuals versus the position of tracks relative to the position, u_{s}, of strips. It can be seen

[4] The measured residual is in fact a convolution of the intrinsic residual and the residual of the hit prediction [see Sec. 4.1.8.1] such that $\sigma^2 = (\Delta u_{\text{h}})^2 + (\Delta u_{\text{t}})^2$.

that the mean residual (superimposed by dark cross markers) depends on the true (predicted) hit position:

$$\bar{r}(t) \stackrel{\text{def}}{=} \frac{1}{N} \int_{-\infty}^{+\infty} r \frac{\mathrm{d}N}{\mathrm{d}r\mathrm{d}t}(r,t)\,\mathrm{d}r \qquad \text{with} \qquad N = \int_{-\infty}^{+\infty} \mathrm{d}t \int_{-\infty}^{+\infty} \mathrm{d}r\, \frac{\mathrm{d}N}{\mathrm{d}r\mathrm{d}t}(r,t). \tag{4.26}$$

In the interval $|r| < 25$ μm the mean residual, $\bar{r}(t)$, may be approximated by a 'line' with a slope of $\mathrm{d}\bar{r}/\mathrm{d}t = 0.25$. The slope contributes systematically to the measured hit position and hence to the spatial resolution. The slope observed using the center of gravity method is smaller than the slope observed using the digital method (see Fig. 4.8). The slope contributes to the spatial resolution. The spatial resolution may be approximated by

$$\sqrt{\langle r^2 \rangle} = \sqrt{\left(\frac{\mathrm{d}\bar{r}}{\mathrm{d}t}\frac{P}{\sqrt{12}}\right)^2 + \sigma_\mathrm{a}^2}. \tag{4.27}$$

There are variations around $\bar{r}$ which represent the inherent variation of the hit position. The variation, σ_a, around $\bar{r}$ denotes the spatial resolution without systematic errors from the method used. It is important to note that Eq. 4.27 is an approximation since it combines a systematic error and a statistical error. Combining the errors depends on the relative size of the errors. For the case of small systematic error Eq. 4.27 is correct. For the case of large systematic error Eq. 4.27 underestimates the contribution from the statistical error. Using the measured spatial resolution from Fig. 4.9 (left) one obtains $\sigma_\mathrm{a} = 2.85$ μm. This value includes contributions due to multiple scattering, the error of the track prediction and the intrinsic spatial resolution of the device. It may be noted that Eq. 4.27 is consistent with the digital resolution using the slope, $\mathrm{d}\bar{r}/\mathrm{d}t = 1$. The center of gravity method would give a smaller error (better spatial resolution) if the charge fractions would be equally distributed.

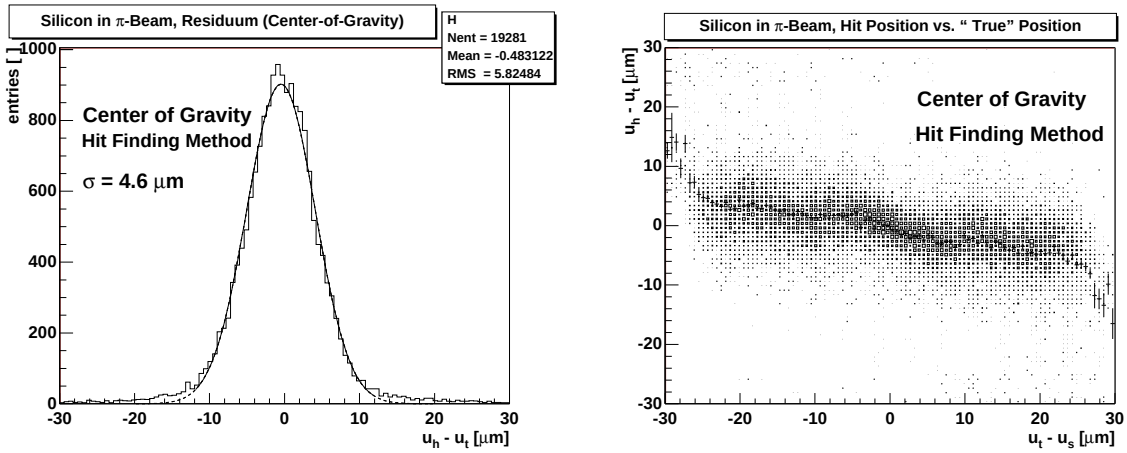

Figure 4.9: Center of gravity residual distribution (left) and residuals as a function of the position of the predicted hit around strips centered at zero (right). The mean residuals are shown by dark cross markers. The slope of the mean residuals is about -0.25.

The cluster charge distribution in Fig. 4.7 shows that the 2-strip cluster charge is only slightly smaller than the 3-strip cluster charge. The rising edge of the 2-strip cluster charge distribution is 2 ADC smaller than the rising edge of the 3-strip distribution and the most probable is 1.8 ADC smaller which means that 2 strips collect 4 % less charge than 3 strips. Therefore one may use the charge from two strips in order to obtain the measured hit position. The 2-strip cluster charge is $Q_2 = q_\mathrm{l} + q_\mathrm{r}$ with the charges q_l and q_r collected on the left and

on the right strips. The charge fractions are defined as $\eta_\mathrm{l} \stackrel{\mathrm{def}}{=} q_\mathrm{l}/Q_2$ for the left strip and $\eta_\mathrm{r} \stackrel{\mathrm{def}}{=} q_\mathrm{r}/Q_2$ for the right strip. The 2-strip center of gravity method gives the position of the hit

$$\begin{aligned} u_\mathrm{h}^{(\mathrm{cog})}\Big|_{K=2} &= \frac{1}{Q_2}\sum_{k=\mathrm{l,r}} u_k \cdot q_k \qquad \text{with} \;\; Q_2 = q_\mathrm{l} + q_\mathrm{r} \\ &= u_\mathrm{l} - u_\mathrm{l}\cdot(\eta_\mathrm{l}+\eta_\mathrm{r}) + \eta_\mathrm{l}\cdot u_\mathrm{l} + \eta_r \cdot u_\mathrm{r} = u_\mathrm{l} + \eta_\mathrm{r}\cdot(u_\mathrm{r}-u_\mathrm{l}) \\ &= u_\mathrm{l} + \eta_\mathrm{r}\cdot P \\ &= u_\mathrm{r} - \eta_\mathrm{l}\cdot P \qquad \text{with} \;\; P = |u_\mathrm{r} - u_\mathrm{l}|\,. \end{aligned} \tag{4.28}$$

The center of gravity method for 2-strip clusters is linear in η_r or η_l and sometimes called the linear eta method [95]. The two strip center of gravity method is generalized in the following to the non-linear eta method.

4.1.5.3 'Eta' Hit Position

Fig. 4.10 shows the charge signals measured on the left strip versus the charge signals on the right strip for two strip clusters for two different silicon detectors. In both detectors

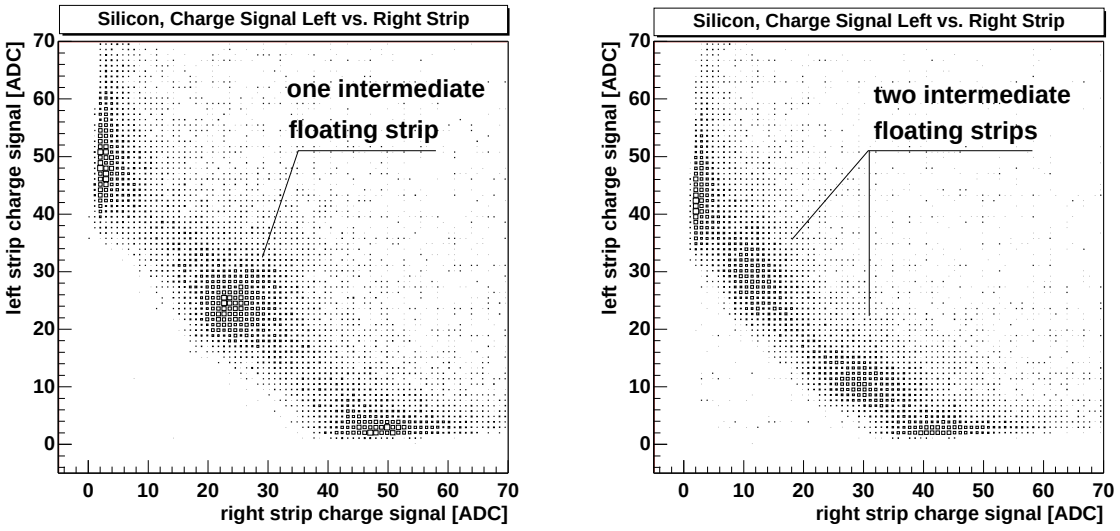

Figure 4.10: Distribution of the signal charge on the left strip versus the signal charge on the right strip. Left: a detector with one intermediate strip. Right: a detector with two intermediate strips.

the charge is anti-correlated since the charge sum from the left and right strip is on average a constant for every event. The silicon planes have either one or two intermediate strips between the readout strips. The number of entries is abundant near the strips. For planes with two intermediate floating strips, entries are more abundant at $\eta = 0.75$ and $\eta = 0.25$, where η denotes either η_r or η_l. The projection of the correlation plot on the abscissa and division by the total charge gives the distributions $\mathrm{d}N/\mathrm{d}\eta$ as a function of η as shown for both types of planes in Fig. 4.11. It can be seen that the distributions are non-uniform. As seen in the scatter plot the number of entries peaks at $\eta = 0.5$ for one intermediate strip and at $\eta = 0.75$ and $\eta = 0.25$ for two intermediate strips. The peaks occur due

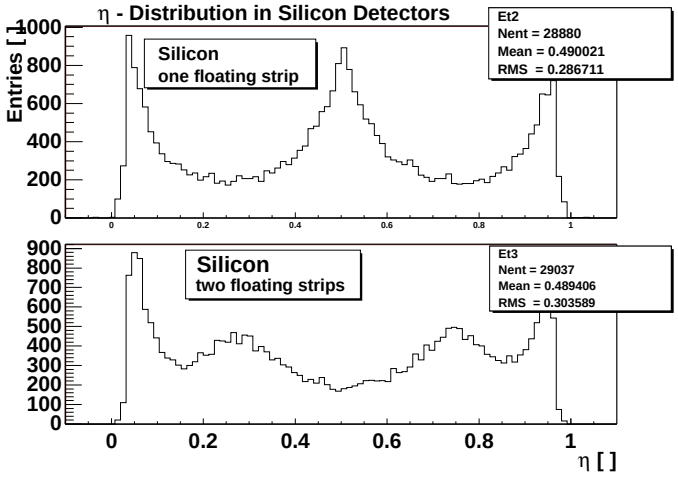

Figure 4.11: Distribution of the variable η in silicon strip detectors of the beam telescope (the distributions of η_l and η_r are the same hence the axis is labeled with η only). The upper figure shows the distribution for one intermediate strip, the lower for two intermediate strips. The distributions have a peak corresponding to the position of the readout strips at 0 and 1 and at the position(s) corresponding to the intermediate strip(s).

to capacitive charge coupling from the intermediate strip(s) to the readout strips [95, 96]. Intermediate strips are introduced to equally increase the number of events with η between 0 and 1. The distributions show that the charge fractions have non-equal probability although any interval in the detector is illuminated uniformly (with equal probability). The center of gravity method assumes equally probable charge fractions which is not the case for the silicon strip detectors used here. Therefore using a center of gravity method in the silicon planes introduces a systematic error in the hit measurement as shown in Fig. 4.9.

In Eq. 4.28 one can see that the hit position, $u_\mathrm{h}^{(\mathrm{cog})}$, is linear in

$$f(\eta) = \eta = \int_0^\eta \mathrm{d}\eta \tag{4.29}$$

where η denotes either η_r or η_l. The distribution of f is then

$$\frac{\mathrm{d}N}{\mathrm{d}f}(f) = \frac{\mathrm{d}N}{\mathrm{d}\eta}(\eta). \tag{4.30}$$

This distribution is not constant (η is not equally distributed) as shown in Fig. 4.11. In order to account for the non-uniform charge collection on two strips one re-defines

$$f(\eta_\mathrm{r}) \stackrel{\mathrm{def}}{=} \frac{1}{N}\int_0^{\eta_\mathrm{r}} \frac{\mathrm{d}N}{\mathrm{d}\eta_\mathrm{r}}(\eta_\mathrm{r})\mathrm{d}\eta_\mathrm{r} \qquad \text{with} \qquad N = \int_0^1 \frac{\mathrm{d}N}{\mathrm{d}\eta_\mathrm{r}}(\eta_\mathrm{r})\,\mathrm{d}\eta_\mathrm{r}. \tag{4.31}$$

The distribution of f is then

$$\frac{\mathrm{d}N}{\mathrm{d}f}(f) = \frac{\mathrm{d}N}{\mathrm{d}\eta_\mathrm{r}}(\eta_\mathrm{r}) \cdot \left(\frac{\mathrm{d}f}{\mathrm{d}\eta_\mathrm{r}}\right)^{-1} \stackrel{\text{Eq. 4.31}}{=} N = \mathrm{const} \tag{4.32}$$

which implies that f is equally distributed. The function, f, is a mapping

$$f: \quad \eta_\mathrm{r} \quad \longmapsto \quad \frac{1}{N}\int_0^{\eta_\mathrm{r}} \frac{\mathrm{d}N}{\mathrm{d}\eta_\mathrm{r}}(\eta_\mathrm{r})\mathrm{d}\eta_\mathrm{r}. \tag{4.33}$$

The mapping, f, transforms the non-uniform η_r into equally distributed values, $f(\eta_\mathrm{r})$. This leads to the definition of the *non-linear eta corrected hit position* for 2-strip clusters

$$u_\mathrm{h}^{(\mathrm{eta})} \stackrel{\mathrm{def}}{=} u_\mathrm{l} + P \cdot f(\eta_\mathrm{r}) \stackrel{\mathrm{Eq.\ 4.31}}{=} u_\mathrm{l} + \frac{P}{N} \cdot \int_0^{\eta_\mathrm{r}} \frac{\mathrm{d}N}{\mathrm{d}\eta_\mathrm{r}}(\eta_\mathrm{r})\mathrm{d}\eta_\mathrm{r}. \tag{4.34}$$

Fig. 4.12 shows the residual distribution using the 2-strip non-linear eta method. The *rms* of the distribution is 4.5 μm using the interval from -30 μm to $+30$ μm. The measurement is fitted by a Gaussian function in the interval from -4 μm to $+4$ μm. The Gaussian fit has a standard deviation of 1.93 μm. This corresponds to an intrinsic spatial resolution of 1.35 μm as discussed below. The limits were chosen to exclude the entries in the non-Gaussian tails of the residual distribution.

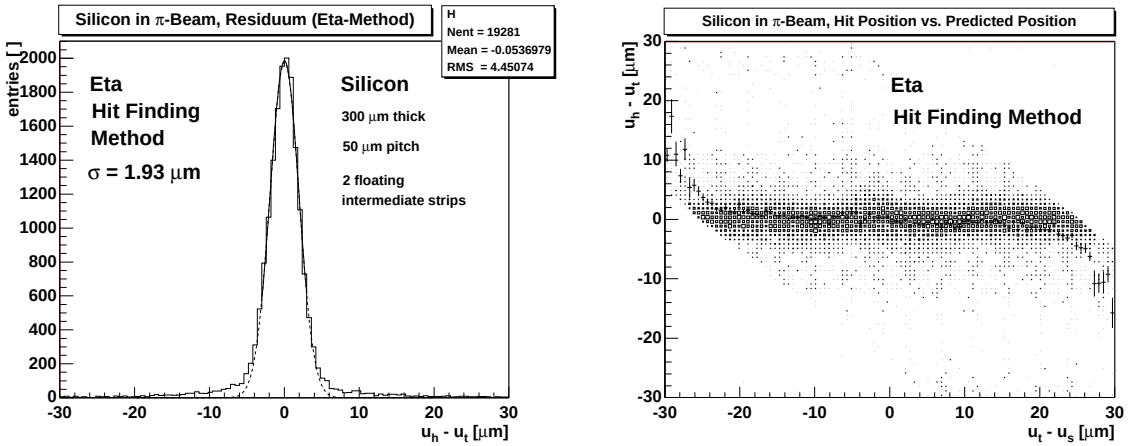

Figure 4.12: Left: residual distribution determined using the non-linear eta method. The measured distribution is fitted by a Gaussian function (solid line). Right: residuals as a function of the position of the predicted hit relative to strips centered at zero.

Fig. 4.12 (right) shows the residual as a function of the true (predicted) hit position around strips. It can be seen that the residuals are nearly independent of the true hit position. The mean residual, $\bar{r}(t)$, as a function of $t = u_\mathrm{s} - u_\mathrm{t}$ is slightly inclined. There are no entries in the triangular regions to the lower left, $r < (t - P/2)$, and the upper right, $r > (t + P/2)$, of the figure which implies that $|u_\mathrm{h} - u_\mathrm{s}| \leq P/2$ for most entries in the figure. The most probable residual, as seen by the size of the rectangular boxes, is parallel to the abscissa. The systematic error of the eta method is smaller than the systematic error of the center of gravity method and smaller than the systematic error of the digital method:

$$0 \approx \frac{\mathrm{d}\bar{r}}{\mathrm{d}t}(t)\Big|_\mathrm{eta} < \frac{\mathrm{d}\bar{r}}{\mathrm{d}t}(t)\Big|_\mathrm{cog} < \frac{\mathrm{d}\bar{r}}{\mathrm{d}t}(t)\Big|_\mathrm{dig} = 1 \qquad \forall \ \ |t| < \frac{P}{2}. \tag{4.35}$$

The remaining spread around $\bar{r}$ is due to statistical fluctuations (noise charge on strips). It should be noted that the residuals obtained from the eta and from the center of gravity method have a spread around $\bar{r}$. The digital method has no spread around $\bar{r}$ (the distribution in Eq. 4.26 is a delta-function) which allows one to use $\bar{r} = r(t)$ for the digital method.

The 2-strip non-linear eta method was used as the 'default' hit position finding method of the reference telescope. In practice an initialization was performed once for each silicon detector plane in order to obtain the integral of the η distribution as a function of η for all $\eta \in (0..1)$ which was later used to quickly look-up the associated hit position. Fig. 4.13 shows the integrated η distribution from an initialization with 8000 events. The function, $f(\eta)$ from Eq. 4.31, is shown on the ordinate. The non-linear mapping of η into $f(\eta)$ can be seen. It

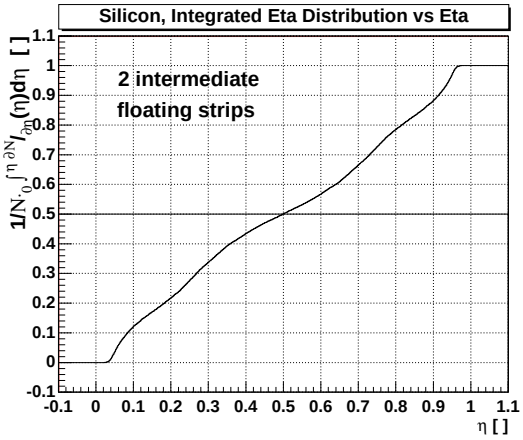

Figure 4.13: Integrated η-distribution as a function of the upper limit η. The integration was obtained from the measured η-distribution of a silicon strip detector with two intermediate floating strips.

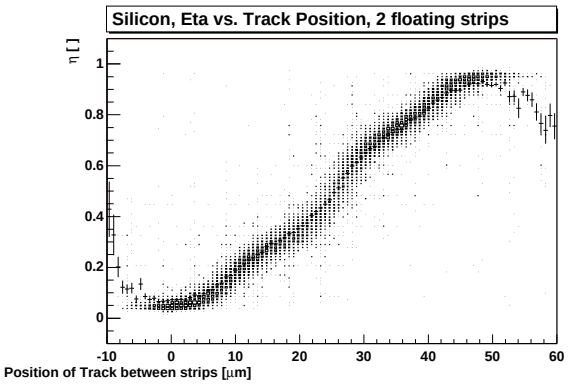

Figure 4.14: The charge fraction η as a function of the position of the true hit position between two strips in silicon. The true hit position was measured with three other silicon strip detector planes and predicted for this plane.

can also be seen that $f(\eta) \approx 0$ for $\eta < 0.04$ and $f(\eta) \approx 1$ for $\eta > 0.96$. The reason is that η is very seldom measured to be close to 0 or close to 1 (see Fig. 4.11) because of the noise charge, q^{rnd}, on the second strip. If the noise would go to zero then η would be closer to 0 and closer to 1. Near the limits $\eta < 0.04$ and $\eta > 0.96$ it would be favourable to use the strip position as the hit position. For very high signal-to-noise ratios it may be correct to use the non-linear eta method over the entire interval from $\eta = 0$ to $\eta = 1$. In the analysis here the non-linear eta method was used over the whole interval from $\eta = 0$ to $\eta = 1$. Fig. 4.14 shows the measured correlation of η with the predicted position of the hit between two strips. One should turn the figure such that η becomes the abscissa in order to compare with Fig. 4.13. The mean values of the correlation are superimposed. One could also use these mean values as a look-up table for the track position.

An optimal hit position method should give for any change $\mathrm{d}u_{\mathrm{t}}$ an equal change in $\mathrm{d}u_{\mathrm{h}}$. The following shows that the non-linear eta method for two strips optimizes the spatial resolution. It is assumed that the charge which is relevant for measuring the hit position is collected on two strips which is almost the case for the silicon strip sensors used. Using $t = u_{\mathrm{s}} - u_{\mathrm{t}}$ one obtains

$$\begin{aligned} \frac{\mathrm{d}(u_{\mathrm{h}}^{(\mathrm{eta})} - u_{\mathrm{l}})}{\mathrm{d}t} &\overset{\text{Eq. 4.34}}{=} \frac{P}{N} \cdot \frac{\mathrm{d}N}{\mathrm{d}\eta_{\mathrm{r}}}(\eta_{\mathrm{r}}) \cdot \frac{\mathrm{d}\eta_{\mathrm{r}}}{\mathrm{d}t} \equiv \frac{P}{N} \frac{\mathrm{d}N}{\mathrm{d}t}(t) \overset{\text{Eq. 4.23}}{=} 1 \\ \Rightarrow \\ \mathrm{d}u_{\mathrm{h}}^{(\mathrm{eta})} &= \mathrm{d}u_{\mathrm{t}}. \end{aligned} \tag{4.36}$$

The calculation assumes uniform illumination, $\mathrm{d}N/\mathrm{d}t = N/P$. Any change of the true hit position u_{t} gives an equal change in the measured hit position $u_{\mathrm{h}}^{(\mathrm{eta})}$ which shows that the non-linear eta method indeed optimizes the spatial resolution.

4.1.6 The Particle Track

Fig. 4.15 shows the coordinate systems which are defined by the unit vectors $(\vec{e}_1, \vec{e}_2, \vec{e}_3)$ for the reference telescope and the unit vectors $\left(\vec{f}_1, \vec{f}_2, \vec{f}_3\right)$ for a detector plane. The origin

(zero) of a plane is located in the center of the plane. The coordinate system of the telescope is defined by four primary silicon reference planes which have orthogonal directions of strips: the direction $\vec{f}_1$ is parallel to horizontal strips, the direction $\vec{f}_2$ is parallel to the vertical strips. The direction $\vec{f}_3$ is perpendicular to the planes and points along the axis of the particle beam. *An orthogonal and parallel mounting of these four planes is assumed.* The origin of the telescope is located half way between both silicon modules on an imaginary line which connects the central points of the primary silicon reference planes. The individual plane coordinate systems can have an offset perpendicular to the strips by u_{off}. Each plane is rotated by an angle, $\varphi = \varphi_0 + \varphi_{\text{off}}$, ($\varphi$ is called the view angle) such that $\vec{e}_3$ remains parallel to $\vec{f}_3$. The view angle is given in terms of an initial angle, φ_0, and an offset, φ_{off}. The initial angle is zero for planes with horizontal strips and 90 ° for planes with vertical strips. The angle offset is a correction of the view angle which is used in the alignment procedure described in Sec. 4.1.7. The components of a vector u_i given in the coordinate system of plane, p, transform into components of a vector, x_i, given in coordinates of the telescope as follows:

$$\begin{aligned} x_i &= (\vec{e}_i \circ \vec{f}_j) \cdot (u_j - u_{\text{off},j}) \quad ; \quad i,j = 1,2,3 \\ \text{here} \quad (\vec{e}_i \circ \vec{f}_j) &= \begin{pmatrix} \cos\varphi & \sin\varphi & 0 \\ -\sin\varphi & \cos\varphi & 0 \\ 0 & 0 & 1 \end{pmatrix} \quad \text{and} \quad \vec{u}_{\text{off}} = \begin{pmatrix} u_{\text{off},1} \\ 0 \\ 0 \end{pmatrix}. \end{aligned} \tag{4.37}$$

The measurement of the hit position in each plane returns the vector, $\vec{u}_{\text{h}}^{(p)} = \left(u_{\text{h}}^{(p)}, 0, 0\right)$, which can be transformed by Eq. 4.37 into the hit position, $\vec{x}_{\text{h}}^{(p)}$, in the telescope coordinates.

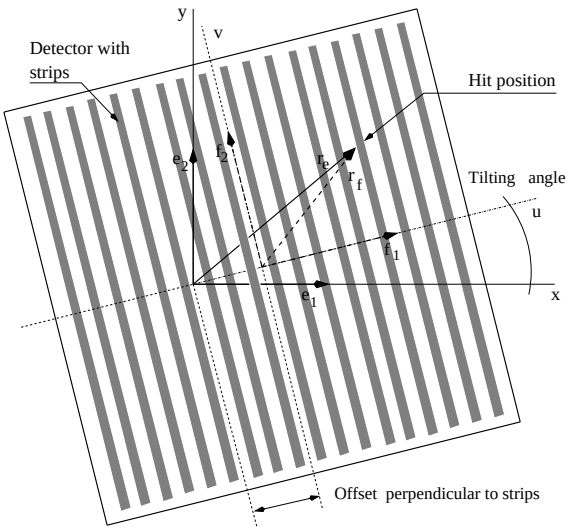

Figure 4.15: Coordinate systems defined by the unit vectors $(\vec{e}_1, \vec{e}_2, \vec{e}_3)$ of the telescope and $\left(\vec{f}_1, \vec{f}_2, \vec{f}_3\right)$ of a detector plane. The detector coordinate system may be offset and rotated with respect to the telescope coordinate system.

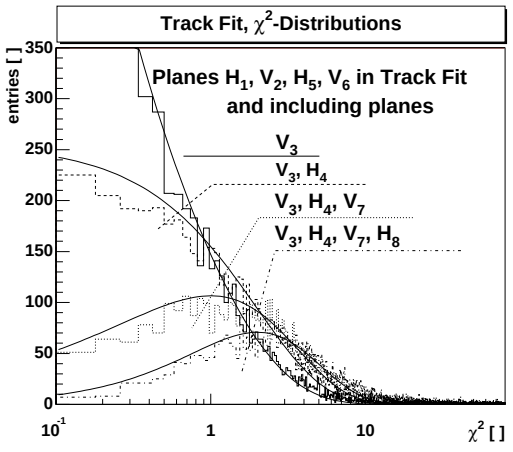

Figure 4.16: Distribution of χ^2 of the track fit to the measured hits using 5,6,7 and 8 silicon planes. The solid lines are the expected χ^2-distributions for 1,2,3 and 4 degrees of freedom.

The trajectory of any particle is assumed to be a straight line. No electromagnetic field is present which could bend the particle track. The angle deviation from a straight line due

to multiple scattering in one silicon plane of 300 μm thickness has an *rms* of $\Delta\Theta = 24$ μrad for 100 GeV/c pions [Eq. 1.12] causing deviations with an *rms* of 4.3 μm in a distance of 180 mm. For all practical cases the deviation is smaller: firstly scattering in a plane of the first module alone still provides a straight track to the rest of the tracking system. Only for the case of multiple scattering in several detectors does the track deviate from a straight line. Secondly the lever arm into a detector under test is always smaller than the length of the reference telescope. As a result the deviation due to multiple scattering is below 1 μm at positions inside the telescope. Secondary particles which produce additional hits in the silicon are not considered.

A linear fit to the $\vec{x}_{\mathrm{h}}^{(p)}$ returns the vector components a_i of the origin and vector components Δx_i of the inclination of the track. The method of finding the origin and the inclination is shown below. The predicted hit position in a plane in coordinates of the telescope is obtained as the intersection point of the trajectory with the plane at $x_3^{(p)}$

$$x_{\mathrm{t},i}^{(p)} = a_i + x_3^{(p)} \cdot \Delta x_i \qquad ; \quad i = 1,2,3. \tag{4.38}$$

Transformation in the plane coordinate system gives the position, $\vec{u}_{\mathrm{t}}^{(p)}$, of the predicted hit in the plane coordinate system

$$u_{\mathrm{t},j}^{(p)} = (\vec{f}_i \circ \vec{e}_j) \cdot x_{\mathrm{t},i}^{(p)} - u_{\mathrm{off},j}^{(p)}. \tag{4.39}$$

The assumption that the trajectory is a straight line can be tested with the χ^2-test. The variable χ^2 is defined as usual [97]

$$\chi^2 = \sum_{p=1}^{p_{\max}} \frac{\left(u_{\mathrm{h},1}^{(p)} - u_{\mathrm{t},1}^{(p)}\right)^2}{\left(\Delta u_{\mathrm{h}}^{(p)}\right)^2}. \tag{4.40}$$

The intrinsic error $\Delta u_{\mathrm{h}}^{(p)} = 1.35$ μm is found from a measurement in Sec. 4.1.8.1 and is assumed to be the same for all silicon planes. By forming the χ^2 a measure of the 'reasonableness' of the fluctuations in the measured data about the predicted values can be obtained. Fig. 4.16 shows the measured χ^2-distributions for track fits using in total 5,6,7 or 8 planes of the telescope. The measured distributions are fitted with the theoretically expected probability functions $p(\chi^2) = (\chi^2/2)^{(\nu/2)-1} \cdot e^{(-\chi^2/2)} / (2\Gamma(\nu/2))$ for ν = 1,2,3 and 4 degrees of freedom where Γ is the gamma function [71]. It can be seen that the measured distributions are consistent with the theoretical distribution of χ^2 indicating that multiple scattering is small.

The track fit was derived using a matrix formalism [98]. The *vector of measured values* is

$$\vec{U}_{\mathrm{h}} \stackrel{\mathrm{def}}{=} \left(u_{\mathrm{h},1}^{(1)}, .., u_{\mathrm{h},1}^{(P)}\right). \tag{4.41}$$

The measurements $u_{\mathrm{h},1}^{(p)}$ are the positions of the hits in the planes $p = 1, .., P$. The measured values have the covariance matrix

$$V_{\vec{U}_{\mathrm{h}}} \stackrel{\mathrm{def}}{=} \begin{pmatrix} (\Delta u_{\mathrm{h}}^{(1)})^2 & & . \\ . & & . \\ . & & (\Delta u_{\mathrm{h}}^{(P)})^2 \end{pmatrix}. \tag{4.42}$$

The diagonal elements of this matrix are the intrinsic resolutions of the planes. The off-diagonal elements are zero under the assumption of no correlations between planes. The

straight line fit Eq. 4.38 is defined by the point (a_1, a_2, a_3) and the inclination $(\Delta x_1, \Delta x_2, \Delta x_3)$. The values a_3 and Δx_3 are redundant and were chosen to be

$$a_3 = 0 \qquad \wedge \qquad \Delta x_3 = 1. \tag{4.43}$$

The remaining values can be written as the *vector of the unknown values*

$$\vec{R} \stackrel{\text{def}}{=} (a_1, \Delta x_1, a_2, \Delta x_2)\,. \tag{4.44}$$

The *vector of the predicted hit positions* in the planes is

$$\vec{U}_\text{t} \stackrel{\text{def}}{=} \left(u_{\text{t},1}^{(1)}, .., u_{\text{t},1}^{(P)}\right) = H\vec{R}^\text{T} - \vec{U}_\text{off} \tag{4.45}$$

where the $u_{\text{t},1}^{(p)}$ are given by Eq. 4.39 and the matrix is

$$H \stackrel{\text{def}}{=} \begin{pmatrix} \cos\varphi^{(1)} & x_3^{(1)}\cos\varphi^{(1)} & \sin\varphi^{(1)} & x_3^{(1)}\sin\varphi^{(1)} \\ \cos\varphi^{(2)} & x_3^{(2)}\cos\varphi^{(2)} & \sin\varphi^{(2)} & x_3^{(2)}\sin\varphi^{(2)} \\ . & . & . & . \\ \cos\varphi^{(P)} & x_3^{(P)}\cos\varphi^{(P)} & \sin\varphi^{(P)} & x_3^{(P)}\sin\varphi^{(P)} \end{pmatrix} \tag{4.46}$$

and the offset is

$$\vec{U}_\text{off} \stackrel{\text{def}}{=} \left(u_\text{off}^{(1)}, .., u_\text{off}^{(P)}\right). \tag{4.47}$$

The generalization of Eq. 4.40 for χ^2 is given by

$$\chi^2 = \left(\vec{U}_\text{h} - \vec{U}_\text{t}\right) W \left(\vec{U}_\text{h} - \vec{U}_\text{t}\right)^\text{T} \qquad \text{with} \qquad W \stackrel{\text{def}}{=} V_{\vec{U}_\text{h}}^{-1}. \tag{4.48}$$

The fit imposes the *condition of least squares*

$$\frac{\partial\chi^2}{\partial\vec{R}} = \vec{0} \tag{4.49}$$

from which follows the *solution for the vector of the unknown values*

$$\vec{R} = \left(H\,W\,H^\text{T}\right)^{-1} H\,W\,\left(\vec{U}_\text{h} + \vec{U}_\text{off}\right)^\text{T} \tag{4.50}$$

and the covariance matrix of $\vec{R}$

$$V_{\vec{R}} \stackrel{\text{def}}{=} \left(\frac{\partial\vec{R}}{\partial\vec{U}_\text{h}}\right) V_{\vec{U}_\text{h}} \left(\frac{\partial\vec{R}}{\partial\vec{U}_\text{h}}\right)^\text{T} \stackrel{\text{Eq. 4.50}}{=} \left(H\,W\,H^\text{T}\right)^{-1}. \tag{4.51}$$

The solution $\vec{R}$ given by Eq. 4.50 contains the origin and the inclination of the particle track.

4.1.7 Alignment Procedure

Four primary silicon reference planes were used to define the coordinate system of the telescope. The four remaining silicon planes were aligned with respect to the telescope coordinate system. Alignment means to correct the offsets, $\varphi_\text{off}^{(p)}$, for the view angles and the offsets, $u_\text{off}^{(p)}$, perpendicular to the strips. These offsets were found by plotting the residuals $r^{(p)} = u_\text{h}^{(p)} - u_\text{t}^{(p)}$ versus the predicted hit position $v_\text{t}^{(p)} \equiv u_{\text{t},2}^{(p)}$.

Fig. 4.17 illustrates the four basic cases of misaligned detector planes: a.) $u_\text{off} \neq 0$, b.) $\varphi \neq 0$, c.) both previous cases, d.) wrong location of the plane along the beam. The scatter

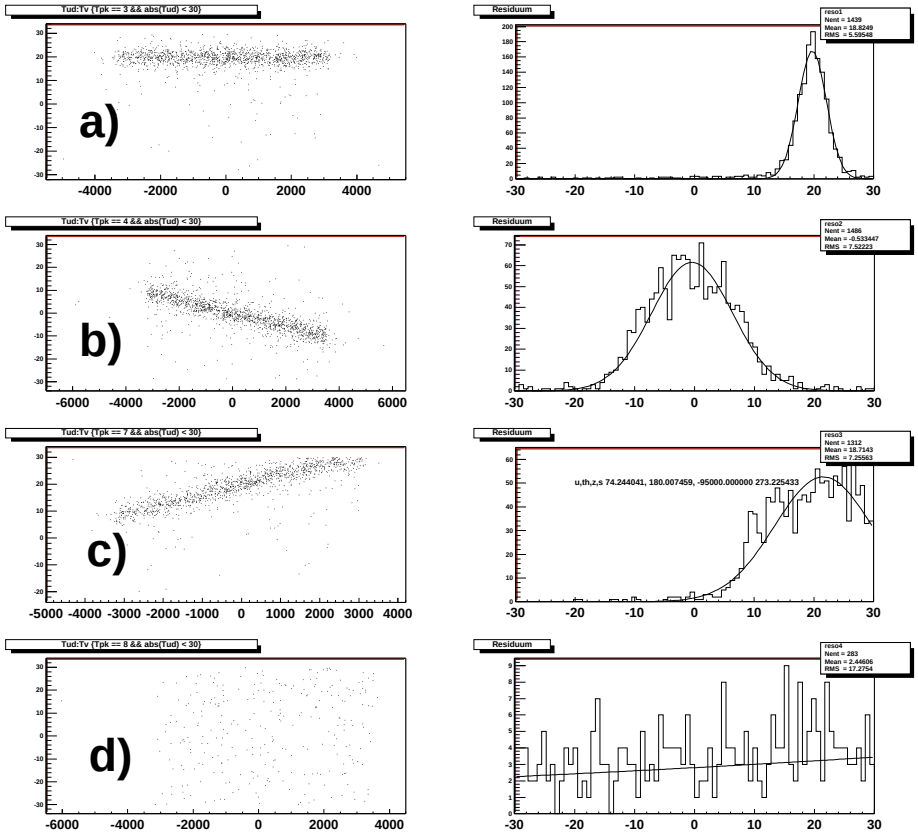

Figure 4.17: Examples of four misaligned silicon reference planes in the silicon telescope. Left: residuals as a function of the position, v_t, of the hit along the strip. Right: distributions of the residuals.

plot for each plane, p, in Fig. 4.17 (left) is a graph of $N^{(p)}$ measurements $(r^{(p)}(n), v_\mathrm{t}^{(p)}(n))$ where n denotes the event number. The measurements can be fitted by a linear function

$$r^{(p)} = u_\mathrm{off}^{(p)} + m^{(p)} \cdot v_\mathrm{t}^{(p)} \qquad \text{with} \qquad m^{(p)} = \tan\varphi_\mathrm{off}^{(p)}. \tag{4.52}$$

The coefficients $u_\mathrm{off}^{(p)}$ and $m^{(p)}$ are the offset and the slope of the linear fit function. Using the method of least squares [97] one finds that the coefficients satisfy two linear equations

$$\begin{aligned} N\, u_\mathrm{off} + [v]\; m &= [r] \\ \text{and} \qquad\qquad & \\ [v]\; u_\mathrm{off} + [v^2]\; m &= [vr]\,. \end{aligned} \tag{4.53}$$

Gauß brief notation for the summation applies here [5]. The index p labeling the plane is omitted for clarity. Cramers rule [97] allows to solve Eq. 4.53 for the coefficients and one obtains the offset of a plane perpendicular to the strips

$$u_\mathrm{off} = \frac{[r]\;[v^2] - [vr]\;[v]}{N\;[v^2] - [v]\;[v]} \tag{4.54}$$

[5] Gauß notation for summation: $[f(x)] = \sum_{n=1}^{N} f(x(n))$ where f is a function of x and n is the index of summation.

and the rotation in the view angle

$$\varphi_{\text{off}} = \arctan(m) = \arctan\left(\frac{N\ [vr] - [r]\ [v]}{N\ [v^2] - [v]\ [v]}\right). \tag{4.55}$$

Hits were considered in the interval $|v_{\text{t}}^{(p)}| < L_{\text{v}}$ and $|r^{(p)}| < L_{\text{r}}$ (initial interval). The interval had to be large enough to include hits from the entire region of the detector. Eq. 4.54 and Eq. 4.55 are linear and independent. In principle one can obtain the offset and inclination from a unique set of N data points in the initial interval. However, the interval chosen contains hits from good signals and also background hits. The signal to background ratio can be increased by lowering the limits of the intervals. Therefore the alignment was usually performed in several iterations. Initially the offsets, $u_{\text{off}}^{(p)}$ and $\varphi_{\text{off}}^{(p)}$, were assumed to be zero. The first iteration, based on about 200 events, gave an offset according to Eq. 4.54 and and an angle offset according to Eq. 4.55. The measured offset and rotation angle were subtracted from the initial values. The following iteration was based on the next 200 events and gave new values for the offset and rotation angle. Each iteration considered hits in the interval, $|r^{(p)}| < L_{\text{r}}$, perpendicular to the strips and centered around the predicted hit position. From one iteration to the next the length of the interval, L_{r}, was decreased which excluded background hits and increased the signal to background ratio for the alignment fit. The number of iterations depends on the hit signal to background ratio in the detector. The lowest interval length depends on the spatial resolution. At a spatial resolution of $\sigma = \sqrt{\langle r^2 \rangle} = 2$ μm one may lower the interval to a length of $L_{\text{r}} = 8$ μm (corresponding to a $\pm 2\sigma$ cut) which then excludes 4.6 % of good hits. Alignment of the secondary silicon reference planes required in practice 5 iterations using a total of 5×200 events.

Fig. 4.18 shows the residuals of the four secondary reference planes of the telescope after alignment. The residuals are centered around zero and have zero inclination versus v_{t}. The positions, $x_3^{(p)}$, of the secondary reference planes were adjusted along the beam (direction of $\vec{f}_3$) by measuring the spatial resolution as a function of $x_3^{(p)}$ (not shown here). The position along the beam is correct when the spatial resolution is at a minimum.

The secondary reference planes were aligned for each new run where a new run was always started after any changes to the telescope (for example after mounting new detectors). Diamond detectors were aligned later with respect to tracks which were found by the aligned telescope.

4.1.8 Transparent Charge Signal

The charge collection on strips in a detector plane can be studied at the predicted hit position. The prediction is independent of any parameter of the detector plane under test. Hence the charge on strips in the detector plane under test can be studied without using a threshold cut for the signal charge. Since no threshold cut is applied this method may also include noise charge in the measurement. Fig. 4.19 shows the transparent 3-strip charge signal distribution, $\mathrm{d}N/\mathrm{d}Q_3$, as a function of the 3-strip charge, Q_3. The transparent signal charge is the sum of charge signals from strips which are closest to the predicted hit position. The ratio of the transparent mean to most probable signal is 1.206 which is smaller than the ratio obtained from the cluster charge distribution in Sec. 4.1.4. For comparison the distribution of 3-strip hit cluster charges from Fig. 4.7 is superimposed on the transparent signal distribution with equal number of entries in both distributions. Both distributions are essentially equal except for high charge signals and very low charge signals. In the logarithmic presentation, Fig. 4.7 (right), it can be seen that the cluster charge distribution has more entries at higher signal charge which leads to a larger mean to most probable ratio for the cluster charge

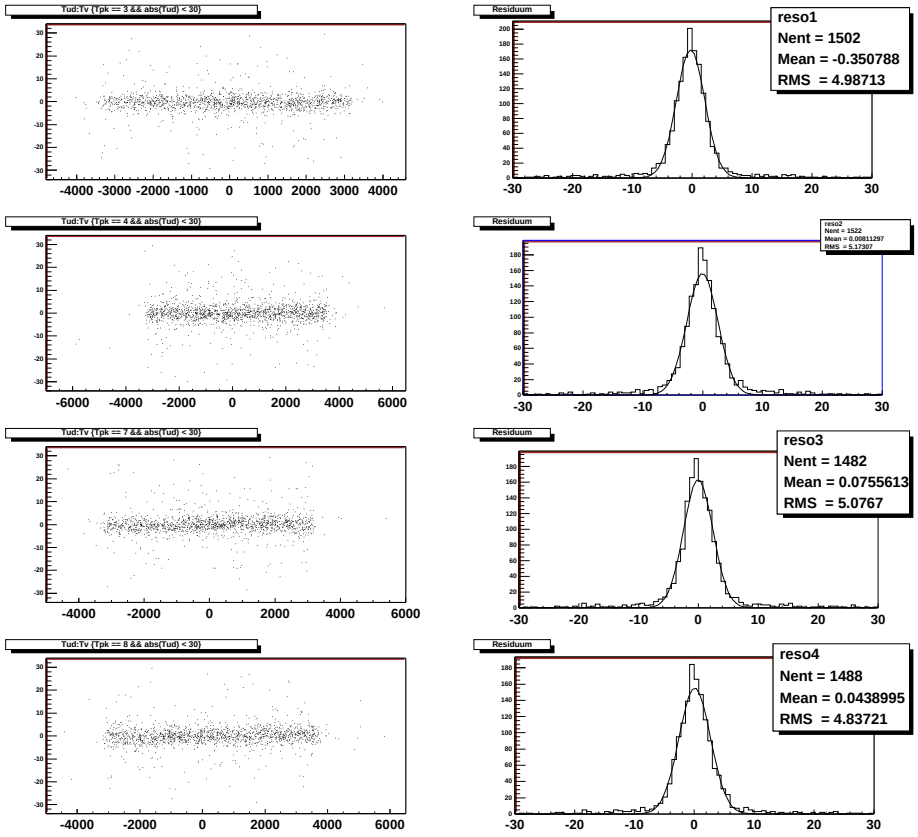

Figure 4.18: Residuals in silicon planes after alignment. Left: residuals as a function of the position, v_t, of the hit along the strip. Right: distributions of the residuals.

distribution compared to the transparent charge distribution. The large number of entries with higher signal charge is explained by the threshold which is applied for selecting events in the cluster analysis. The cluster analysis is biased towards higher signal charge whereas the transparent analysis is unbiased with respect to a threshold cut [6]. The transparent signal distribution has a few events, 0.1 % of all entries, between zero and the most probable value. These events are real and appear on good tracks with good χ^2. The transparent charge signal for these events is distributed over more than 3 strips which can be shown by summing the charge up to 6 strips. The distribution of charges from 6 strips for these 0.1 % events peaks at the most probable value of the 3-strip distribution. The distribution of the charge over 6 strips is possible for particles which scatter perpendicular to the track and do not leave the detector.

In a transparent analysis one can measure the *hit recognition efficiency of a plane* which is defined for K strips as a function of the cluster threshold, t_c, as follows

$$\epsilon_K(t_c) \stackrel{\text{def}}{=} \frac{1}{N}\int_{t_c}^{+\infty} \frac{\mathrm{d}N}{\mathrm{d}Q_K}(Q_K)\mathrm{d}Q_K \qquad ; \qquad N = \int_{-\infty}^{+\infty} \frac{\mathrm{d}N}{\mathrm{d}Q_K}(Q_K)\mathrm{d}Q_K. \tag{4.56}$$

The hit recognition efficiency quantifies the number of hits which can be found in a cluster analysis for the given cluster threshold t_c. The 2-strip and 3-strip cluster hit recognition

[6] In addition one should note that the transparent analysis is biased with respect to the position of the track whereas the cluster analysis is unbiased with respect to the track position.

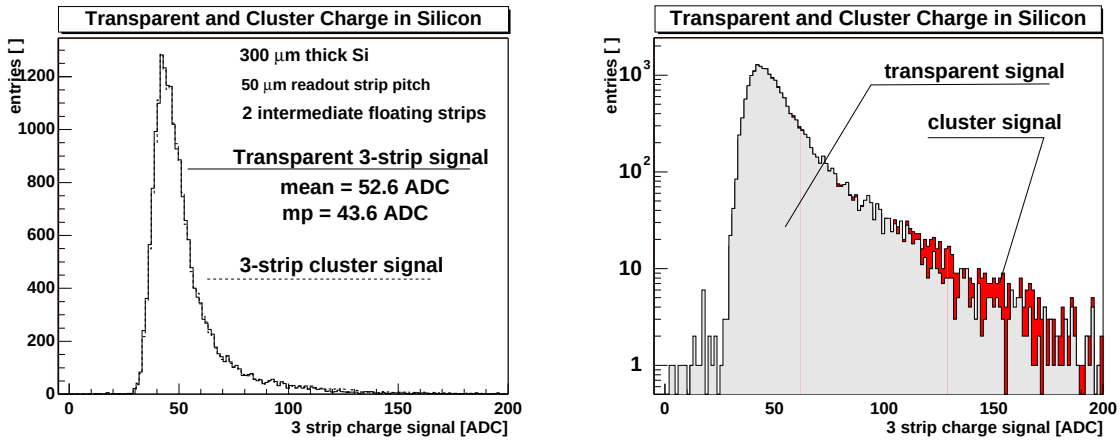

Figure 4.19: Distribution of 3-strip charge signals from a silicon plane of the telescope. The figure overlays the measured cluster signal distribution and the transparent signal distribution. Both distributions contain the same number of entries. The distributions are shown with a linear ordinate (left) and the same distributions with a logarithmic ordinate (right). The entries between 0 and the rise of the distribution is the signal charge from real particles. The total charge of these events is spread out over more than 3 strips.

efficiency for the silicon planes of the telescope was found to be above 98 % for thresholds below $0.6 \times MP_{\mathrm{mip}}$. The hit recognition efficiency is discussed more in Sec. 4.2.8.

4.1.8.1 Telescope Precision

The distribution, $\mathrm{d}N(r)/\mathrm{d}r$, of residuals, r, allows one to measure the standard deviation $\Delta r = \sqrt{\langle r^2 \rangle}$ of the distribution. This standard deviation is a convolution of the intrinsic spatial resolution, Δu_{h}, in the detector under test and the precision, Δu_{t}, of the hit prediction in the detector under test

$$(\Delta r)^2 = (\Delta u_{\mathrm{h}})^2 + (\Delta u_{\mathrm{t}})^2 \,. \tag{4.57}$$

This assumes no correlation between the positions, u_{t} and u_{h}.
The hit position error can be derived for positions, z, along the beam. Two reference planes may be located at z_1 and at z_2 a distance $L = z_2 - z_1$ apart. Under the assumption that the planes have the same intrinsic spatial resolution, Δu_{h}, one obtains the error on the hit prediction at the position, z

$$\Delta u_{\mathrm{t}}(z) = \frac{\Delta u_{\mathrm{h}}}{L} \sqrt{(z - z_1)^2 + (z_2 - z)^2} \tag{4.58}$$

where z may be the position of a third plane. One can see that the precision of the prediction has a minimum at $z = (z_1 + z_2)/2$ where $\Delta u_{\mathrm{t}}(0) = \Delta u_{\mathrm{h}}/\sqrt{2}$. For the case that the third plane has the same intrinsic resolution as the reference planes one obtains the measured spatial resolution of the plane at z under the assumption that z near z_1 or near z_2

$$\Delta r \overset{\text{Eq. 4.58}}{=} \Delta u_{\mathrm{h}} \sqrt{2}. \tag{4.59}$$

For the case of z near z_1 or near z_2 one finds $u_{\mathrm{h}} \approx u_{\mathrm{t}}$ and using Eq. 4.57 one also obtains the expression in Eq. 4.59. Therefore the measurement of $\Delta r = 1.93$ μm in Fig. 4.12 gives the intrinsic resolution of the plane: $\Delta u_{\mathrm{h}} = 1.35$ μm.

The prediction error from four planes is found as follows: under the assumption that the planes have equal intrinsic spatial resolution one first calculates the prediction errors from two adjacent planes for the positions between them which gives the error for two virtual planes. The position of these virtual planes is chosen to minimize the prediction error. Then one calculates the prediction error from the virtual planes at the position z. One obtains the *error of the predicted hit position from four planes*

$$\Delta u_{\mathrm{t}}(z) = \frac{\Delta u_{\mathrm{h}}}{\sqrt{2} \cdot |(z_1 + z_2)/2 - (z_3 + z_4)/2|} \sqrt{\left[\left(z - \frac{z_1 + z_2}{2} \right)^2 + \left(\frac{z_3 + z_4}{2} - z \right)^2 \right]}. \quad (4.60)$$

Fig. 4.20 shows the error of the predicted hit position as a function of the position, z, along the beam. The error was calculated for two intrinsic resolutions of 1.5 μm and 1.35 μm. The hit position prediction error has a minimum in the middle between both silicon modules. For an intrinsic resolution of 1.35 μm per plane the hit position error is 0.7 μm at the minimum. The prediction error increases at positions outside the telescope.

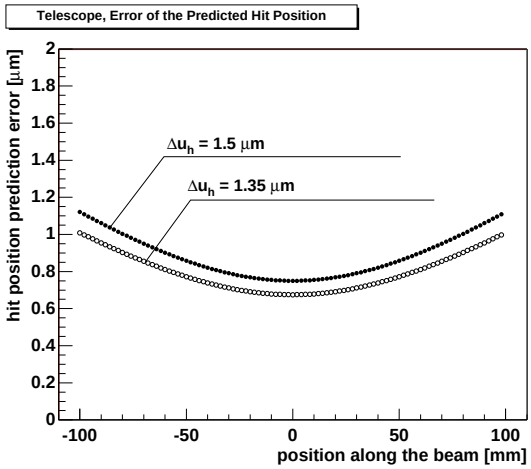

Figure 4.20: Error of the predicted hit position in horizontal and vertical direction. The graphs were calculated for four planes using Eq. 4.60. The planes were located at $(z_1, z_2, z_3, z_4) = (-93, -87, +87, +93)$ mm. Two graphs are shown: one graph was calculated for an intrinsic spatial resolution $\Delta u_{\mathrm{h}} = 1.35$ μm the other for $\Delta u_{\mathrm{h}} = 1.5$ μm.

4.1.9 Summary

The silicon beam reference telescope has been described in this section. Each plane had a single strip noise of about 210 e and a most probable signal-to-noise ratio of around 110-to-1. The intrinsic spatial resolution of a plane was measured to be 1.35 μm by using the non-linear 2-strip eta method. The hit recognition efficiency of each plane was above 98 % for thresholds below 0.6 times the most probable signal charge. The reference telescope allowed the prediction of the particle hit position in detectors under test to a precision of below 2 μm for all positions inside the telescope. This is of great importance in the study of diamond detectors in the following sections.

4.2 CVD Diamond Strip Detectors

The silicon beam telescope described in the previous chapter has been used to study CVD diamond strip detectors. Here the preparation method of diamond strip sensors and the tests in the the beam are reported. A typical behaviour of a strip sensor is shown with respect to signal charge, spatial resolution and hit recognition efficiency.

4.2.1 Introduction to CVD Diamond Microstrip Sensors

Free-standing CVD diamond can be grown in the form of planar disks, several centimeters in diameter and up to several millimeters thickness [33, 34] with the material characteristics reported in Chapter 2. Fig. 4.21 shows a photograph of a transparent CVD diamond disk produced for an optical application [34]. The disk has a diameter of 100 mm. CVD diamond samples for particle sensors were cut from similar disks.

The first diamond strip detector was tested in 1993 at CERN [99]. The detector had a charge collection distance of 50 μm. The strip pitch was 100 μm and the spatial resolution attained was 26 μm. Since then a variety of diamond strip detectors have been tested in the beam. The goal of these tests was mainly to characterize the diamond material from different growth processes in terms of charge collection distance and spatial resolution in order to improve the production process.

Figure 4.21: Free-standing, 100 mm diameter CVD diamond window, (courtesy of De Beers Industrial Diamond Division (UK) Ltd.) [53].

4.2.2 Principle of Operation

Fig. 4.22 shows the schematic representation of a diamond strip detector with strips on one side, typically the growth side, and a solid back plane electrode on the opposite side. A charged particle that traverses the diamond bulk in the direction perpendicular to the surface uniformly creates charge pairs along the track as illustrated by solid circles (electrons) and open circles (holes). A positive voltage is applied to the backplane causing an electric field inside the bulk with field lines from the backplane to the strips. The electric field is assumed to be constant and homogeneous over most of the bulk and only bends towards the strips in the region near the strips. The assumption of a homogeneous electric field, although seemingly reasonable, has not been confirmed for the polycrystalline bulk of CVD diamond. The electron-hole pairs separate in the electric field as discussed in Sec. 3.3 and travel a certain distance until they get trapped. The motion induces a charge proportional to the charge collection distance as shown for large electrodes in Eq. 3.124. However, here the moving charges induce charge on several strips. In order to deduce the charge induced on strips one needs to calculate the field distribution for the strip geometry. Discussions about charge induction on strips can be found in the references [100, 101, 102, 103].

Fig. 4.23 shows a schematic of a diamond strip detector from the top view. Typical detectors had a size of 1×1 cm^2. The strips where surrounded by a guard contact which was connected to ground potential.

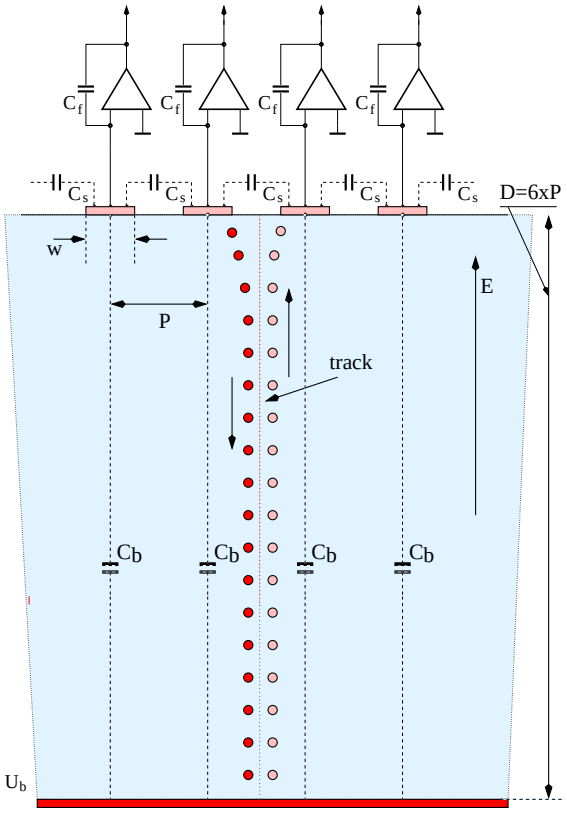

Figure 4.22: Schematic representation of a diamond microstrip sensor (side view) with electronic readout of each strip. The strips have a width, w, and a pitch, P. The thickness, D, has been chosen to be six times the pitch in order to illustrate the relation of the pitch to thickness.

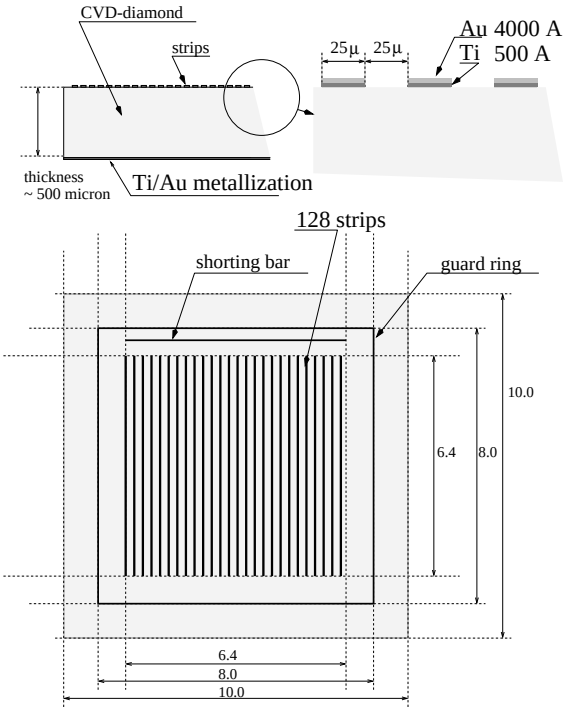

Figure 4.23: Schematic of a diamond strip sensor seen from the top. The dimensions are in millimeters and are correct for most of the trackers tested.

Estimates of the equivalent noise charge in the detector readout require an estimate of the capacitance, $C_{\rm e}$, at the input of an amplification channel:

$$C_{\rm e} = C_{\rm d} + C_{\rm stray} \tag{4.61}$$

where $C_{\rm stray}$ is a stray capacitance and $C_{\rm d}$ is the detector capacitance. The detector capacitance is given in terms of the interstrip capacitance, $C_{\rm s}$, and the strip to backplane capacitance, $C_{\rm b}$

$$C_{\rm d} \approx 2\,C_{\rm s} + C_{\rm b}. \tag{4.62}$$

This expression is an approximation since the capacitance to strips further away then the strip pitch is neglected. The interstrip capacitance per unit length, L, in a medium of dielectric constant, ϵ_r, is [68]

$$\frac{C_{\rm s}}{L} = \frac{2\pi\,\epsilon_0\,\epsilon_r}{\ln\left[2\,(P-w)^2/w^2 - \sqrt{2\,\left(P-w\right)^2/w^2 - 1}\right]}, \tag{4.63}$$

where w is the width of the strips and P is the pitch of the strips. The equation was derived for round wires with a diameter w and is used here as an approximation for the flat strips on the diamond surface. The expression is only correct if the wires are embedded in the material. A comparison with the potential of a line charge at the interface of two dielectrics with dielectric constants 1 and ϵ, as discussed in reference [95], gives $\epsilon_r = a\epsilon + 1 - a$ where a is determined by the electric field at the interface. The geometry here has $a = 1/2$ and hence $\epsilon_{\rm r} = (\epsilon + 1)/2$. The relative dielectric constant of diamond is $\epsilon = 5.6$ [Table 1.1]. Eq. 4.63 was used to calculate the capacitance between two strips on the surface of the diamond as a function of the distance between the strips with the result shown in Fig. 4.24. One finds the interstrip capacitance $C_{\rm s} = 0.54$ pF for two 6.4 mm long and 25 μm wide strips at a pitch of 50 μm.

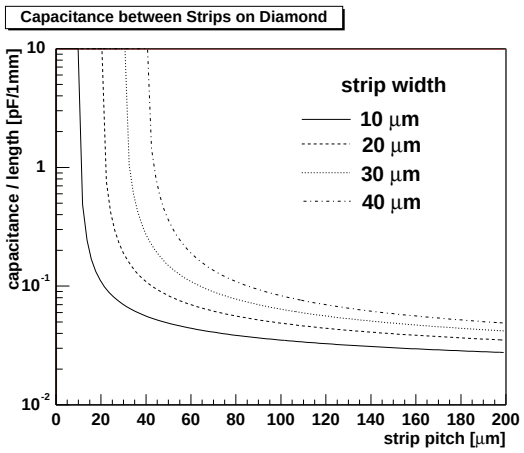

Figure 4.24: Calculated capacitance between two strips on the diamond surface as a function of the strip pitch. The calculation is based on Eq. 4.63. The capacitance is given for different strip widths and is normalized to 1 mm strip length.

The capacitance to the backplane is

$$\frac{C_{\rm b}}{L} = \epsilon_0 \epsilon \frac{P}{D}. \tag{4.64}$$

It should be noted that the area which determines the capacitance to the backplane is $P\,L$. One obtains $C_{\rm b} = 0.032$ pF for a 500 μm thick diamond. The interstrip capacitance is larger by a factor 17 than the capacitance to the backplane. The detector capacitance at the input of an amplification channel is therefore $C_{\rm d} \approx 1.1$ pF for 6.4 mm long and 25 μm wide strips at a pitch of 50 μm.

4.2.3 Experimental Method: CVD Diamond Microstrip Preparation

Fig. 4.25 shows four regions of the strip side of a CVD diamond strip detector. The strip pattern on the diamond surface was prepared by reference [104]: the diamond surface was completely covered with either Cr/Au by evaporation or Ti/Au by sputtering. The gold prevents the chromium from oxidizing. Gold is a good conductor and later allows wire bonding to the readout chip. The strips were prepared as follows: a thin layer of UV-light sensitive photoresist was spun on the gold surface. Then a glass mask with a positive image of the strips was positioned on top of the photoresist and the surface was exposed to UV-light through the glass mask. The positive image of the glass mask prevented illumination at the positions of the strips. Then the sensor was put in developer solution and the photoresist

was dissolved where exposed (between the strips). The metal layers were then etched (in the sequence first gold then chromium) in those regions which were not covered with photoresist. After etching no metal remained between the strips. The remaining photoresist (covering the strips) was removed with acetone. The detector was annealed for 5 minutes at 400 °C in an N_2 atmosphere in order to form a carbide interface between the strips and the diamond. The carbide gives the ohmic contact between the metal and the diamond. The strips were prepared on one side of the diamond, the other side had a solid electrode which reached close to the edges of the diamond.

The sensor shown in Fig. 4.25 had strips of a width of 25 μm and a pitch of 50 μm. The chromium layer had a thickness of 500 Å before annealing and the gold layer had a thickness of 2000 Å. The strips were staggered and had bond pads on both sides in order to facilitate wire bonding to the readout electronics. The total sensitive area was therefore 128 × 50 μm × 6400 μm. The strips were surrounded by one rectangular guard contact. The guard contact, properly connected to the same potential as the strips, prevented leakage current from the backplane over the edges of the diamond to the strips. The photograph of the sensor shows dark spots on the surface. These are voids in the diamond surface which remained after lapping. A visual inspection showed that the strip metallization was not broken at most of the voids. The majority of strips had no breaks or shorts.

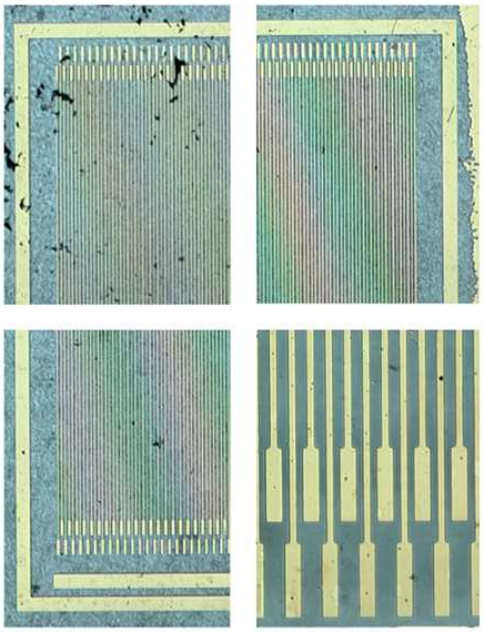

Figure 4.25: Photographs from four regions of a CVD diamond strip detector. The strips on the diamond can be seen. The strips have a width of 25 μm and a pitch of 50 μm. The magnification to the right at the bottom shows bond pads for wire bonding to the readout electronics [104].

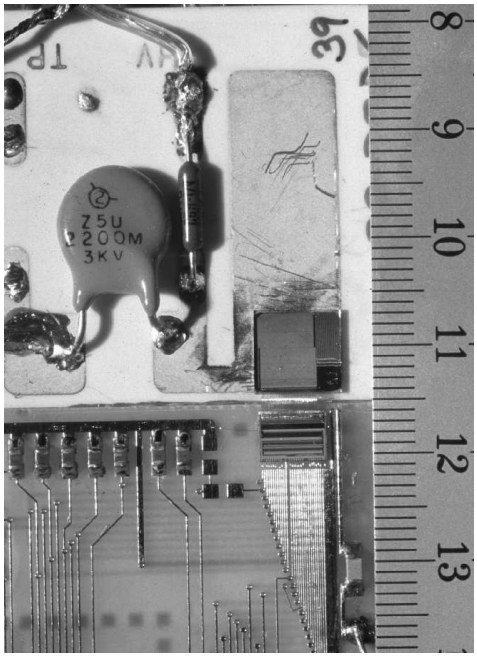

Figure 4.26: Photograph of a CVD diamond strip sensor mounted on a ceramic board and bonded to the VA2 readout chip.

Fig. 4.26 shows a picture of a diamond sensor mounted on a ceramic printed circuit board and bonded to the VA2 readout electronics. The sensor was glued with conductive epoxy to the ceramic board and mounted next to a G10 printed circuit board with a VA2 readout chip. The readout electronics was directly wire bonded to the strips on the diamond. After selection of a diamond sample using the β-source setup described in Sec. 3.4.5 the VA2 readout electronics [Sec. 3.4.2] was always used for the first tests with new diamond strip sensors. The VA2 electronics had low noise and could easily be operated in the testbeam. The diamond sensors were normally biased with 1 V/μm via a 100 MΩ resistor with a positive voltage applied to the detector backplane. A capacitor of 4.7 nF/3.3 kV from the backplane to ground was used to smoothen ripples on the DC bias voltage to ground. The strips were at virtual ground potential via the input amplifier. The diamond sensor and its readout chip were then mounted inside a light tight and electrically shielded aluminium frame in the beam reference telescope.

4.2.4 Experimental Method: Setup in the Beam

The frames containing the diamond sensors were mounted in the silicon beam telescope shown in Fig. 4.2 in Sec. 4.1. The diamond planes were parallel to the silicon reference planes. The whole telescope was adjusted in the beam such that the pion tracks were normally incident to each plane. The signal acquisition from diamond detectors was accomplished using 12 bit sirocco ADCs in the VME create described in Sec. 4.1.2. The offline analysis for diamond detectors was the same as for the silicon reference detectors: pedestal, common mode, signal and noise were found using the same algorithms and analysis code as described for silicon detectors in Sec. 4.1.3.

4.2.5 Results: Noise on Strips

The noise charge gives important information about the performance of a sensor. Suppression of the physical signal charge, $q_k^{\mathrm{phy}}(n)$, in Eq. 4.3 gives the noise charge

$$q_k^{\mathrm{rnd}} = r'_k(n) - p_k(n) - c(n) \tag{4.65}$$

where k is the strip index and n is the event number. The noise charge is the pedestal subtracted, common mode corrected and hit suppressed charge on a strip.

Fig. 4.27 shows the noise charge measured on a CVD diamond strip sensor as a function of the strip index. One can see that most values scatter around zero as expected. There are three strip regions at the strips 58/59, at the strips 67/68 and at the strip 98 which have higher noise charge. The noise was higher on a pair of strips if two preamplifier channels were electrically connected. A connection between strips on the sensor or a connection between the bond wires could account for this. Higher noise on a single channel could be due to a broken amplifier channel. Strips which were noisier than other strips were excluded from the analysis by a software selection rule in the analysis code.

Fig. 4.28 (upper graph) shows the distribution of the noise charge superimposed from all channels. The superposition was performed since the mean noise charge from individual strips varied by fractions of ADC values which is negligibly small. The standard deviation of the noise charge from all channels is 4.5 ADC. The common mode distribution is shown as well. The common mode has a standard deviation of 2.3 ADC and is centered at 3 ADC. The distribution is not centered at zero since a few strips with a signal charge related to a hit may be included in the common mode calculation. This effect should be studied further

using a more effective method of signal suppression. Using the calibration of 22 e/ADC one finds a noise charge variation of 100 e and a common mode variation of 51 e.

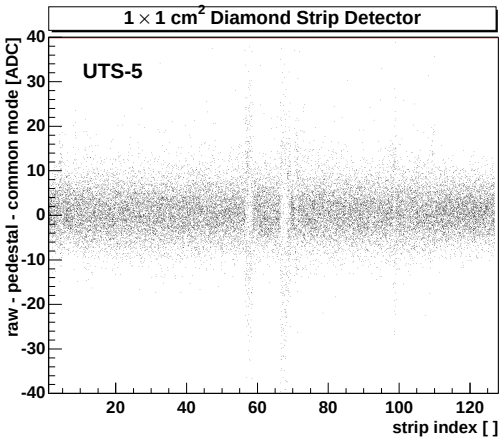

Figure 4.27: Pedestal subtracted, common mode corrected and hit suppressed raw values as a function of the readout channel index for 128 channels (one chip).

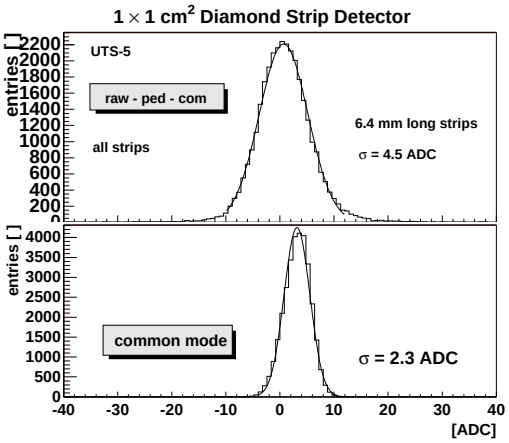

Figure 4.28: Distribution of the pedestal subtracted, common mode corrected and hit suppressed raw values (above) and the distribution of common mode shifts (below).

The noise charge has a series noise term described by Eq. 3.137 and parallel noise term described by Eq. 3.138. Fig. 4.29 shows a model of a strip detector with the equivalent noise voltage, u_k, for the strip number k in series with the input of the preamplifier. The series equivalent noise charge of a single readout amplifier as described by Eq. 3.137 is here

$$\sqrt{\langle q^2_{\text{series}}\rangle} = \sqrt{\langle u^2_{\text{a}}\rangle}\, C_{\text{a}} + \sqrt{\langle u^2_{\text{a}}\rangle}\, C_{\text{e}} \equiv \sqrt{\langle q^2_{\text{a}}\rangle} + \sqrt{\langle u^2_{\text{a}}\rangle}\, C_{\text{e}}. \tag{4.66}$$

where $C_{\text{a}} = C_{\text{i}} + C_{\text{f}}$ the sum of the feedback capacitor, C_{f}, and the internal capacitance, C_{i}, of the preamplifier. The external capacitance, C_{e}, of a strip connected to a channel of the charge sensitive amplifier is given by Eq. 4.62. The capacitance from the detector is $C_{\text{d}} \approx 1.1$ pF as calculated in Sec. 4.2.2. This calculation neglects the capacitance from strips farther than one pitch away. Assuming a stray capacitance of about $C_{\text{stray}} = 1$ pF per bond wire from the bond pad of the preamplifier to the strip on the sensor one obtains $C_{\text{e}} \approx 2$ pF. Using Eq. 4.66 and the preamplifier equivalent noise charge variation of $\sqrt{\langle q^2_{\text{a}}\rangle} = 81$ e and the preamplifier equivalent noise voltage $\sqrt{\langle u^2_{\text{a}}\rangle} = 11$ e/pF one obtains the series equivalent noise of 103 e on a single strip. In reality each noise source couples to every strip. A calculation which takes this coupling and its correlation into account is proposed in reference [105]. This calculation predicts a 10 % higher noise. The parallel noise is neglected here because of the small detector leakage current and the large feedback resistor of the preamplifier. The estimate of the total noise is therefore 103 e in a single readout channel. This is in good agreement with the noise measurement of 100 e.

The noise charge shown so far was taken from a single strip. The noise charge from K strips in a cluster is

$$Q^{\text{rnd}}_K = \sum_k^K q^{\text{rnd}}_k. \tag{4.67}$$

Assuming that there are no noise correlations between strips one obtains the *cluster noise charge variation*

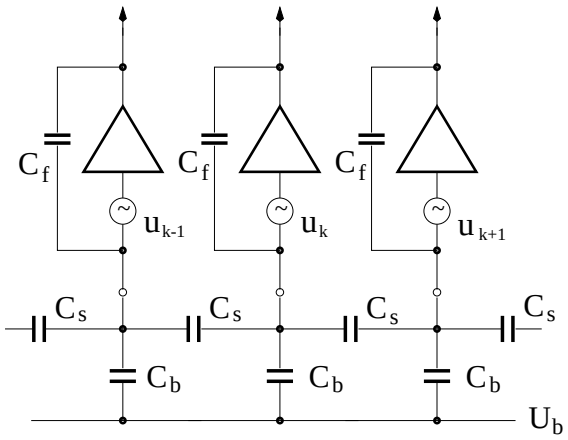

Figure 4.29: Schematic of a strip detector with interstrip capacitance, C_s, backplane capacitance, C_b, and charge integrating readout electronics with feedback capacitor, C_f. The series noise voltage, u_k, models the internal noise voltage of the amplifier [105].

$$\sqrt{\langle (Q_K^{\mathrm{rnd}})^2 \rangle} = \sqrt{\sum_k^K \langle (q_k^{\mathrm{rnd}})^2 \rangle} \tag{4.68}$$

where $\sqrt{\langle (q_k^{\mathrm{rnd}})^2 \rangle}$ is the equivalent noise charge variation measured on adjacent strips in a cluster. Fig. 4.30 shows the distribution of the cluster noise charge for $K = 2, 3, 5$ and 7 strips included in the cluster. The noise distributions are Gaussian shaped and centered at a value close to zero. The unit chosen for the presentation of the cluster noise charge is the standard deviation of the single strip noise charge from Fig. 4.28. Under the assumption that the noise charge variation is the same on all strips in the cluster one obtains a prediction on the cluster noise charge variation as a function of the number of strips included in the cluster

$$\sqrt{\langle (Q_K^{\mathrm{rnd}})^2 \rangle} = \sqrt{K} \cdot \sqrt{\langle (q^{\mathrm{rnd}})^2 \rangle} \tag{4.69}$$

where $\left\langle (q^{\mathrm{rnd}})^2 \right\rangle \stackrel{\mathrm{def}}{=} \left\langle (q_k^{\mathrm{rnd}})^2 \right\rangle$ is the same equivalent noise charge variation of a single strip for all k in the cluster. Fig. 4.31 shows a measurement of the cluster noise charge variation as a function of the number of strips included in the cluster. The data were measured on three CVD diamond strip sensors and a silicon strip sensor. Overlayed to the measured data is the expected noise charge variation from Eq. 4.69. The measured cluster noise charge variation in silicon and diamond are in good agreement with the expectation of uncorrelated noise on strips.

4.2.6 Experimental Method: Alignment in the Beam

Alignment of diamond detectors in the beam was performed by the procedure described for silicon detectors in Sec. 4.1.7. The silicon beam telescope predicts the position, $(u_\mathrm{t}, v_\mathrm{t})$, in the diamond sensor and the diamond sensor measures the position, u_h. Fig. 4.32 shows the residuals, $u_\mathrm{h} - u_\mathrm{t}$, as a function of the position of the track, v_t, in CVD diamond sensor UTS-5 after alignment. One can see that the mean residual has zero offset and zero rotation with respect to the position v_t. This demonstrates good alignment. The sensors were also aligned along the beam by optimizing the resolution as a function of z (not shown here).

Fig. 4.33 shows the residual of the same strip detector as a function of the position u_t. The graph shows regions where the residuals are centered around zero and regions where the residuals form a 'line' with inclination -1. The lines appear at strips which are electrically shorted since in this case the measured hit position, u_h, is independent of the predicted hit position. Lines also appear at the rim of the detector (at the left end and at the right end in

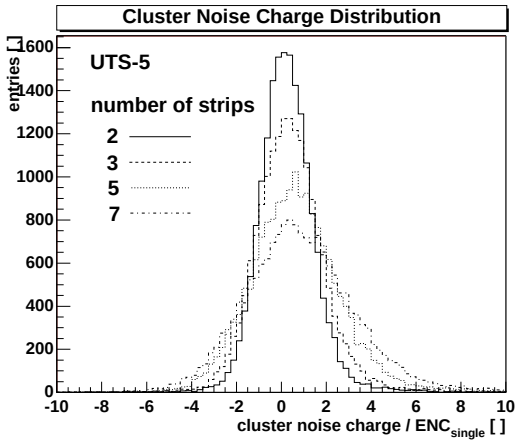

Figure 4.30: Distribution of the cluster noise charge from the diamond detector UTS-5 including 2, 3, 5 and 7 strips in the cluster. The cluster noise charge is normalized by the single strip noise charge variation $ENC_{\rm single} \equiv \sqrt{\langle (q^{\rm rnd})^2 \rangle}$.

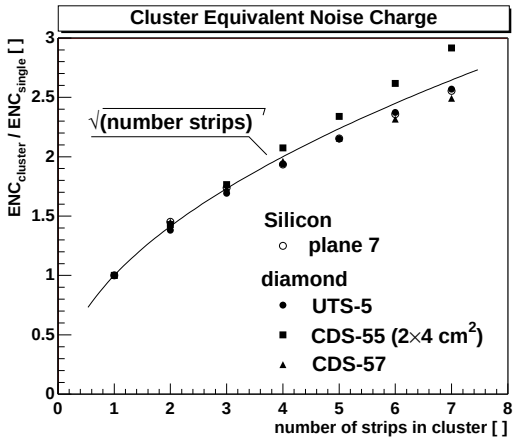

Figure 4.31: Normalized cluster equivalent noise charge variation in one of the silicon planes and in three diamond sensors. The cluster charge variation is labeled as $ENC_{\rm cluster} \equiv \sqrt{\langle (Q_K^{\rm rnd})^2 \rangle}$.

the figure) where the true hit was outside the sensitive area of the diamond and the position was determined as the last strip of the diamond detector and hence again independent of $u_{\rm t}$. Fig. 4.33 shows that the position of hits are properly measured in most of the sensitive area. The fiducial regions chosen for characterizing the diamond sensor are drawn in the figure and exclude the shorted and noisy strips and the rim. The choice of fiducial regions allows one to focus the analysis on the inherent properties of the diamond. The alignment was always performed and fiducial regions were always chosen before analyzing signal charges and residuals.

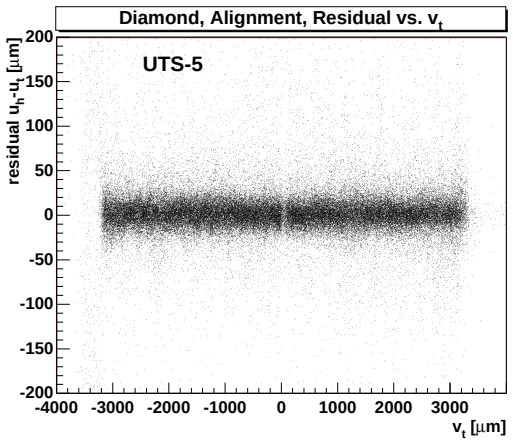

Figure 4.32: Residuals, $u_{\rm h} - u_{\rm t}$, versus $v_{\rm t}$ in diamond sensor UTS-5 after alignment.

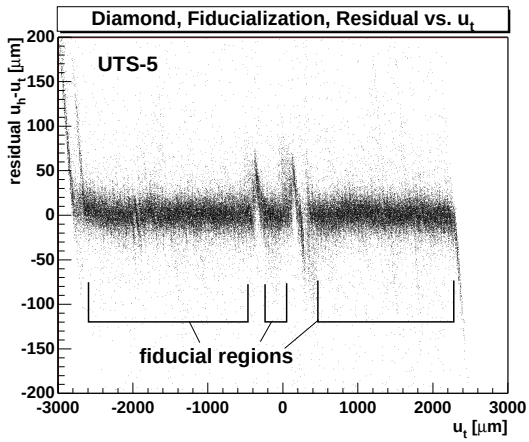

Figure 4.33: Residuals, $u_{\rm h} - u_{\rm t}$, versus $u_{\rm t}$. Three possible fiducial regions are shown.

4.2.7 Results: Signal Charge

Fig. 4.34 shows distributions of measured 1-, 2-, 3-, and 4-strip cluster charges in UTS-5. The cluster charge was measured according to Eq. 4.17 as described in Sec. 4.1.4. The cluster

charge distributions are asymmetric and Landau-like. It can be seen that the distribution for 2-,3- and 4-strip cluster charges starts at about 50 ADC. The start of the distribution is higher than the seed strip threshold of 8-to-1 chosen (corresponding here to a seed strip threshold of $\approx$ 36 ADC). The charge collected on one strip is smaller than the cluster charges including more than one strip. This observation has been made in silicon as well. The most probable two and three strip cluster charge are 204 ADC and 230 ADC. Using the single strip noise of 4.5 ADC one finds a most probable signal-to-noise ratio of 45-to-1 and 51-to-1 for two and three strips respectively. The mean two and three strip cluster charges are 341 ADC and 383 ADC corresponding to a mean signal-to-noise ratio of 76-to-1 and 85-to-1. Using the calibration of 22 e/ADC one finds a mean two and three strip hit cluster charge of 7500 e and 8426 e corresponding to a charge collection distance of 208 μm and 234 μm. It can be seen that the amount of charge collected depends on the number of strips included in the cluster. Using the most probable two strip charge as a normalization one finds 13 % and 19 % more charge on three and four strips than on two strips. It should be noted that the amount of charge collected in silicon also depends on the number of strips in the cluster. From Fig. 4.7 it can be seen that the cluster charge in silicon is 4 % and 8 % higher on three and four strips than the most probable two strip signal. In Fig. 4.5 and Fig. 4.28 it was shown that the noise charge is centered at 0.07 ADC in silicon and about 0.5 ADC in diamond. This value is small compared to the difference between the strip cluster charges. We infer that the increase in cluster charge is real and is not an artifact of the method used. A reason could be $\delta-$rays and particles from nuclear interaction which release energy in the vicinity of the track. These particles create electron-hole pairs in the vicinity of the track which may appear on neighbour strips. One should expect a cluster charge saturation if one includes more and more strips. It should be noted that the increase of the cluster charge in diamond is about twice as high as the increase in silicon. Based on this observation one can infer that the induced charge in diamond extends over a larger area than in silicon. In silicon the carrier drift length is longer than the thickness of the sensor. A charge travels along the field line and induces a charge on several strips. The sign of the induced charge is determined by the direction of motion of the charge carrier relative to the strip. When the charge carrier approaches the strip where the field line ends it moves away from other strips and induces there a negative charge which cancels the charge initially induced on these strips. In diamond the carrier drift length is shorter than the thickness of the sensor. A moving charge induces a charge on several strips as in silicon and the sign is also determined by the direction of motion. In diamond the charge may not always reach the strip since it may be trapped. In this case there is no cancellation of charge on adjacent strips. This may explain the excess of charge on neighbour strips compared to silicon. One should note that the diamond shown here is 432 μm thick which is 44 % thicker than the silicon sensors used for comparison. In order to compare the extension of induced charge in silicon and diamond one should use both sensors of the same thickness.

The logarithmic distribution in Fig. 4.34 to the right has been prepared in analogy to Fig. 4.7. It can be seen that one strip collects less charge than two or more strips. The distributions for two or more strip clusters have similar shape. The three and four strip cluster charge distributions have slightly more entries at higher ADC values. This observation has been made in silicon and may be explained by $\delta-$rays and particles produced from nuclear interactions. It has to be noted that the data here are from UTS-5 measured with strips widths of 30 μm and 40 μm as discussed below.

The transparent analysis (see Sec. 4.1.8) allows one to measure the signal charge at the intersection of the particle track with the diamond sensor. The charge on strips around the track in the diamond can be studied without applying a threshold cut on the diamond signal

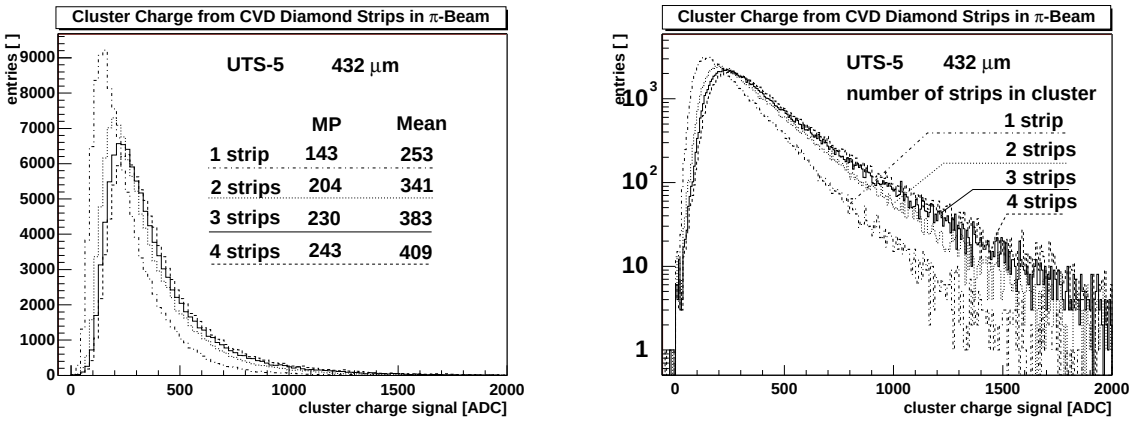

Figure 4.34: Hit cluster charge distributions in CVD diamond sensor UTS-5 for 1, 2, 3 and 4 strips included in the hit cluster. The data are presented on a linear ordinate (left) and a logarithmic ordinate (right).

charge. Fig. 4.35 shows the transparent 3-strip charge in diamond sensor UTS-5 overlayed to the 3-strip hit cluster charge. The distributions have the same number of entries. Most of the events are common to both distributions. The 3-strip cluster charge was chosen to compare with the transparent 3-strip charge in silicon. However, one could also compare the 2-strip cluster and transparent charges. The transparent 3-strip charge distribution shown has a most probable of 215 ADC and a mean charge of 328 ADC. These values are smaller than the 3-strip most probable cluster charge of 230 ADC and the 3-strip mean cluster charge of 383 ADC. The cluster charge distribution has an excess of entries in the high end and a deficiency of entries at the low end. The cluster analysis uses the three largest charges on strips whereas the transparent analysis uses the charges of the three strips closest to the track. The cluster charge is biased towards higher signal charge and the higher cluster most probable and mean values are therefore inherent to the cluster method.

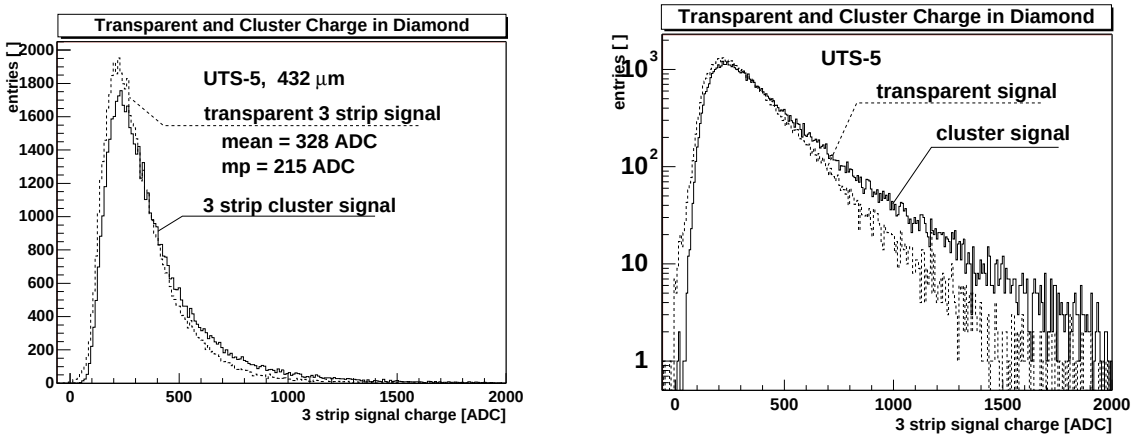

Figure 4.35: Transparent 3-strip signal charge distribution (solid line) and the 3-strip cluster charge distribution (dashed line) in CVD diamond sensor UTS-5. The distributions are shown with a linear ordinate (left) and with a logarithmic ordinate (right).

From the signal charge distributions shown we infer that the principles of charge induction on strips in diamond and silicon are similar. The most significant amount of charge is

collected on two strips. Using more strips the signal charge in silicon and diamond increases by a few percent. The charge induced in diamond may extend over a larger region than in silicon. However, this observation requires confirmation using a 300 μm thick diamond to directly compare with silicon.

Table 4.2 summarizes the performance for a variety of CVD diamond sensors in terms of the transparent 3-strip charge signal-to-noise ratio. These results are discussed in the summary.

4.2.8 Result: Hit Recognition Efficiency

The transparent analysis allows one to study the hit recognition efficiency, ϵ_K, of the detector. Using the transparent signal charge distribution, $\mathrm{d}N/\mathrm{d}Q_K$, of the transparent signal charge a possible definition of the *hit recognition efficiency* is given by Eq. 4.56. The efficiency depends on the number, K, of strips which are included in the transparent signal charge, $Q_K = \sum_{k=1}^{K} q_k$, where $q_k = q_k^{\mathrm{rnd}} + q_k^{\mathrm{phy}}$. By definition ϵ_K takes values between 0 and 1 depending on the cluster threshold, t_{c}, in Eq. 4.56. Fig. 4.36 shows a measurement of the hit recognition efficiency in silicon (left) and in diamond (right) as a function of the threshold and for $K = 1$ to $K = 5$. One can see that for sufficiently low threshold the hit recognition efficiency is one corresponding to 100 %. The efficiency is still close to 100 % as the threshold increases. However, at a certain threshold the efficiency decreases. A decrease in efficiency for single strip signal charge sets in at a threshold lower than for two or more strips. In silicon the efficiency is above 98 % for thresholds below 30 ADC corresponding to 0.6 times the two strip most probable charge. In diamond the efficiency is above 98 % for thresholds below 80 ADC corresponding to 0.4 times the most probable two strip charge. The efficiency drops to 90 % for thresholds of 0.8 times the two strip most probable value in silicon and 0.9 times the two strip most probable value in diamond. The definition of the hit finding efficiency implies that $\epsilon_K = 0.5$ for thresholds equal to the mean value of the K-strip signal charge distribution.

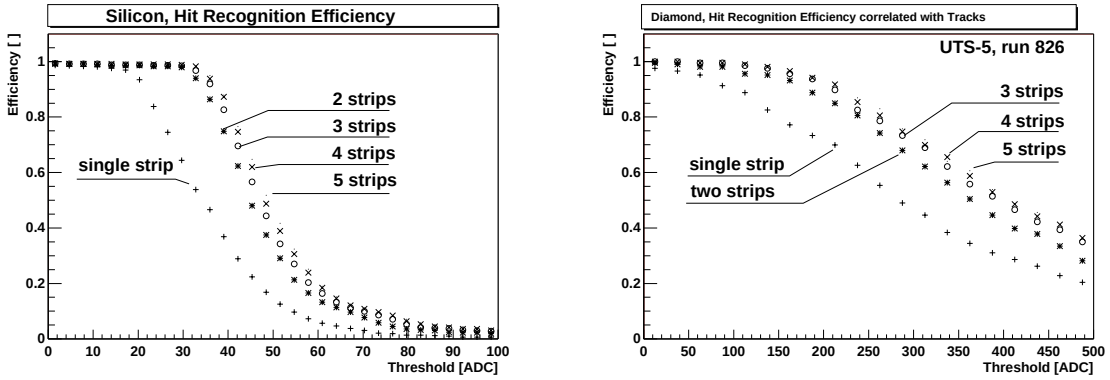

Figure 4.36: Hit recognition efficiency in silicon (left) and in a CVD diamond sensor (right) as a function of the threshold. The efficiency is given for different numbers of strips included in the transparent charge.

In silicon or diamond one can always determine the threshold where the efficiency is close to 100 %. However, if the threshold is chosen too low one acquires noise hits which spoil the spatial resolution. One method of judging the lower limit of the threshold is counting the number, N, of strips with a signal above threshold as a function of the threshold. Fig. 4.37 shows $1/N$ as a function of the threshold in one of the silicon planes (left) and in the diamond sensor UTS-5 (right). The graphs were prepared as a scatter plot with a profiling histogram

of the entries in each threshold bin overlayed (cross markers). One can see that the number of strips with a signal charge above threshold increases with lower threshold. This corresponds to a decrease of $1/N$ with lower threshold. This is expected because noise signals exceed low thresholds. It was shown that two strips collect most of the charge in silicon and diamond strip detectors. In silicon it was also shown that two strips give a good spatial resolution. From Fig. 4.37 one can read the threshold for two strips hit on average. One finds 4 ADC in silicon and 80 ADC in diamond (using three strips one finds about 2 ADC in silicon and 55 ADC in diamond). From this and Fig. 4.36 one infers the range for choosing a threshold with a hit finding efficiency of above 98 %. Using two strips one obtains the range from 4 ADC to 30 ADC in silicon and 80 ADC as the lower and upper limit in diamond. This corresponds to a cluster signal-to-noise cut between 9-to-1 and 64-to-1 in silicon and 18-to-1 in diamond. One may certainly lower the thresholds in order to allow more strips to be on average included in the hit cluster. If one applies the same thresholds below 18-to-1 to diamond and silicon one finds a hit recognition efficiency above 98 % in both devices.

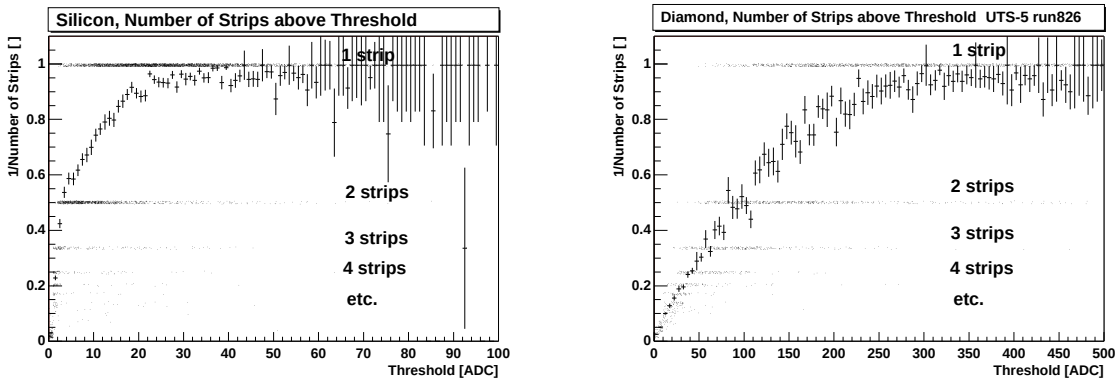

Figure 4.37: The inverse of the number of strips in a silicon detector (left) and the CVD diamond sensor UTS-5 (right) as a function of charge threshold. The case of zero number of strips is excluded.

4.2.9 Results: Charge Collection and Strip Width

The charge collection has been studied on strips with variable widths and constant pitch. Fig. 4.38 (left) shows the schematic of a strip with variable widths. Each strip had four regions, a, b, c, d, with the widths 10 μm, 20 μm, 30 μm and 40 μm. The strips were read out on the wide end. This strip geometry allows one to study the charge collection as a function of the strip width. In Fig. 4.38 (center and right) one can see the mean charge collected on a strip as a function of the particle position, $(u_t - u_0, v_t)$, with respect to the center of the strip in the interval from -50 μm to $+50$ μm. The measurements from all strips in the fiducial region are mapped into a single strip centered at zero. One can recognize a region with high collected charge near the bonding pads and a region with lower collected charge at the end opposite to the bonding pads. The bonding pads are in region e. The bonding pads also collect charge. The start of the region d is at -2250 μm in UTS-5 and at -2000 μm in CDS-57. Each region had a length of 1500 μm as illustrated in the figure. Region a was partially outside of the area defined by the beam trigger counter. One can see that for the widths below 30 μm the mean single strip charge decreases with decreasing strip width. This effect was seen in two diamond sensors CDS-57 and UTS-5.

Fig. 4.39 and Fig. 4.40 facilitates the representation of the contents from UTS-5 in the previous figure [Fig. 4.38]. The single strip charge is shown versus the distance between

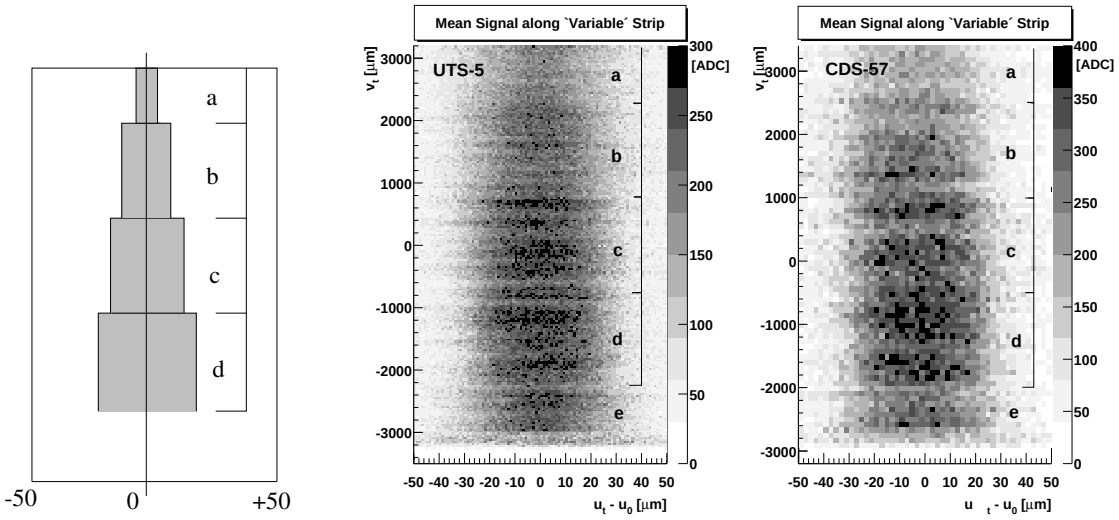

Figure 4.38: Schematic of a strip on the diamond sensor (left): the strip has four regions a, b, c, d with widths of 10 μm, 20 μm, 30 μm and 40 μm. Center and right: mean signal charge on a single strip at zero in the diamond sensors UTS-5 and CDS-57. The mean signal charge is gray scale coded and plotted along the strip direction, v_t, and versus the distance, $u_\mathrm{t} - u_0$, from the center of the strip at zero. The region e corresponds to four rows of bonding pads.

the track and the center of a strip at zero. The number of entries is logarithmically gray scale coded. Three important features can be observed in these figures: first the shape of the distribution is trapezoidal with a flat top corresponding to the width of the strip and a linear decrease from the edge of the strip. The slope of the linear decrease depends on the width of the strip. It can be shown that the slope is proportional to the strip width. The second observation is that if a track passes through a strip then there are no entries which induce a signal charge of less than 50 ADC counts corresponding to about 1100 e. The third observation is that the signal charge is larger on wide strips than on narrow strips. For example in Fig. 4.39 and Fig. 4.40 the histogram in region a has a top of 220 ADC whereas in region d the flat top is at 280 ADC.

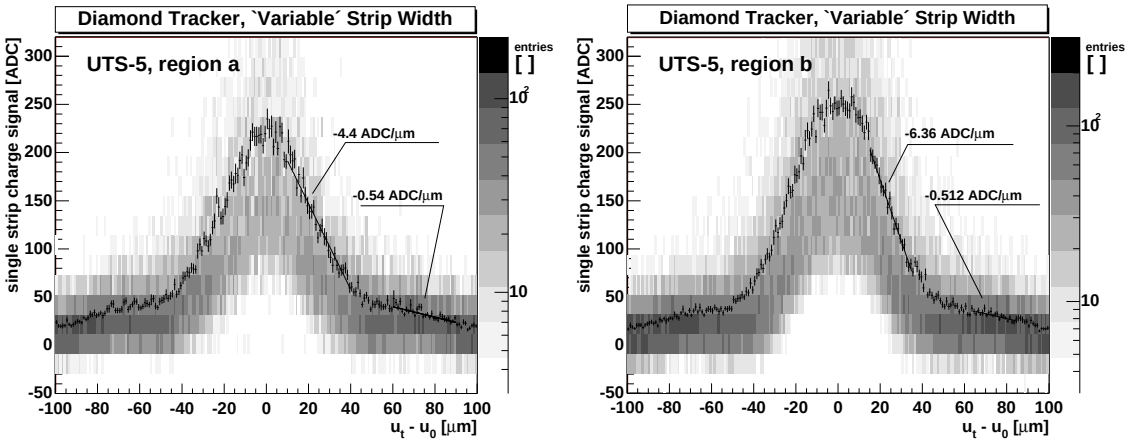

Figure 4.39: Charge collected on the single strip versus the distance $u_\mathrm{t} - u_0$ in the diamond detectors UTS-5. The signal is shown for the regions, a and b, with different strip width.

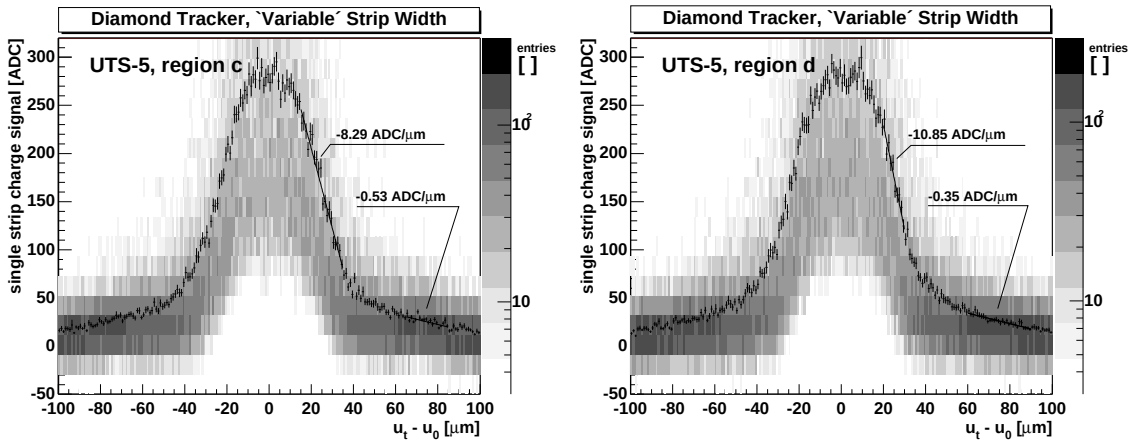

Figure 4.40: Charge collected on the single strip versus the distance $u_t - u_0$ in the diamond detectors UTS-5. The signal is shown for the regions, c and d, with different strip width.

Fig. 4.41 shows the signal charge from two strips as a function of the position of the track between two strips. One can see that the measured charge is independent of the position of the track. In other words, there is no loss of induced charge for tracks which pass between two strips. The comparison of the charge on two strips in region a with region d shows that there is less charge induced on two strips for the narrow strip width.

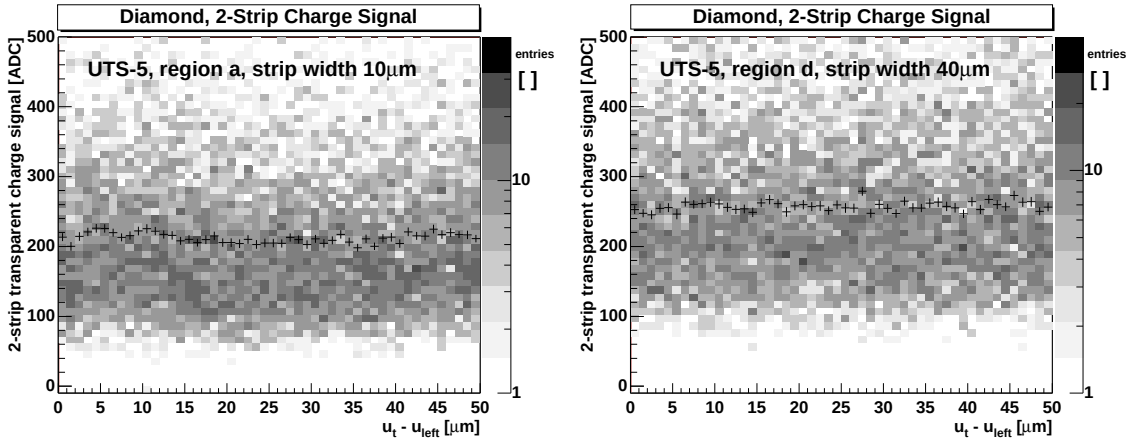

Figure 4.41: The sum of the signal charge from the left and the right strip as a function of the position of the track between the strips for 10 μm wide strips (left) and for 40 μm wide strips (right).

Fig. 4.42 shows the mean signal-to-noise ratio for three strips as a function of the strip width measured from UTS-5 and CDS-57. One can see that the signal is larger on wider strips. The signal appears to plateau above 30 μm strip width.

For comparison Fig. 4.43 shows the induced charge on a strip in a silicon detector as a function of the position of the track relative to the strip. The strip measures the highest charge if the track passes through the strip. For distances away from the strip the induced charge decreases non-linearly and reaches a value close to zero at the position of the adjacent strip. The sum of the charges from two adjacent strips in silicon is shown as a function of the track position between the strips in Fig. 4.44. One can see that the charge sum depends on the position of the track. There are relative minima at the position of intermediate strips.

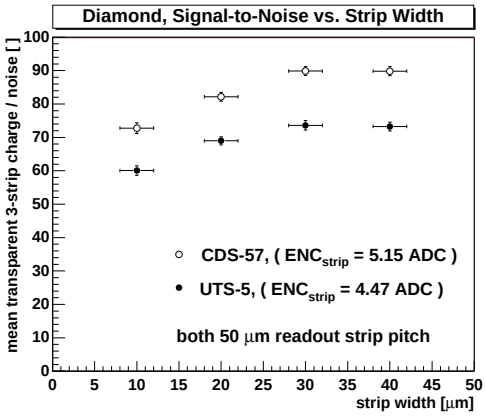

Figure 4.42: Mean transparent 3-strip charge signal-to-noise ratio measured on two diamond strip detectors with variable strip widths ranging from 10 μm to 40 μm along the strip.

The charge loss at the position of the intermediate strips is understood by the capacitive coupling from the intermediate strips to the backplane of the silicon detector as described in reference [94].

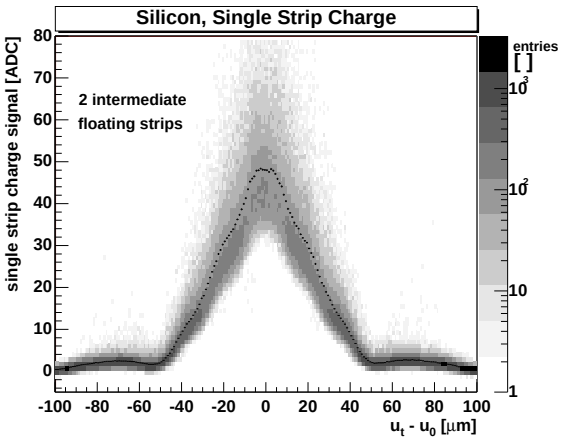

Figure 4.43: Signal charge on a single strip as a function of the position of the track relative to the position of the track in a silicon strip detector. The silicon detector has two intermediate strips.

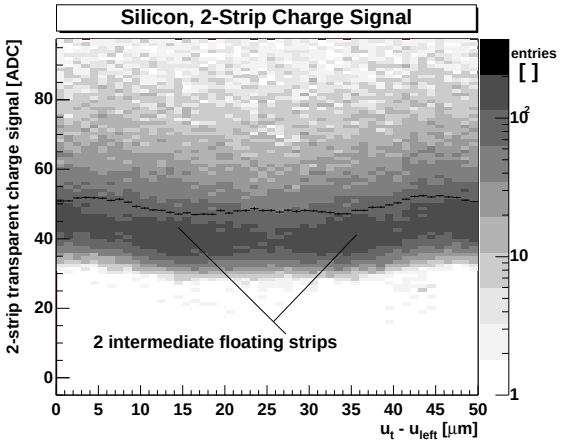

Figure 4.44: The sum of the signal charge from the left and the right strip as a function of the position of the track between the strips in silicon.

Fig. 4.45 shows the relation between the signal charge on the left strip versus the right strip in hits in the diamond UTS-5. The distributions show anti-correlation similar to what was observed in silicon sensors in Fig. 4.10 in Sec. 4.1.5.3. The entries are accumulated in two 'islands' corresponding to a complete charge collected on either one strip or on the other strip. For region d (wide strips) the separation between the islands is more pronounced than it is the case for region a (narrow strips). This indicates that on narrow strips there is more charge sharing between the strips. A single wide strip more often collects all the charge.

4.2.10 Results: Spatial Resolution

The spatial resolution in diamond strip detectors was found using the K-strip center of gravity (c.o.g.) method as described in Eq. 4.25 in Sec. 4.1.5.2. Fig. 4.46 shows the residual distribution for UTS-5 in the region a and in region d. The hit position found by the diamond was measured here using the digital hit position, the 2-strip c.o.g. position and the 3-strip

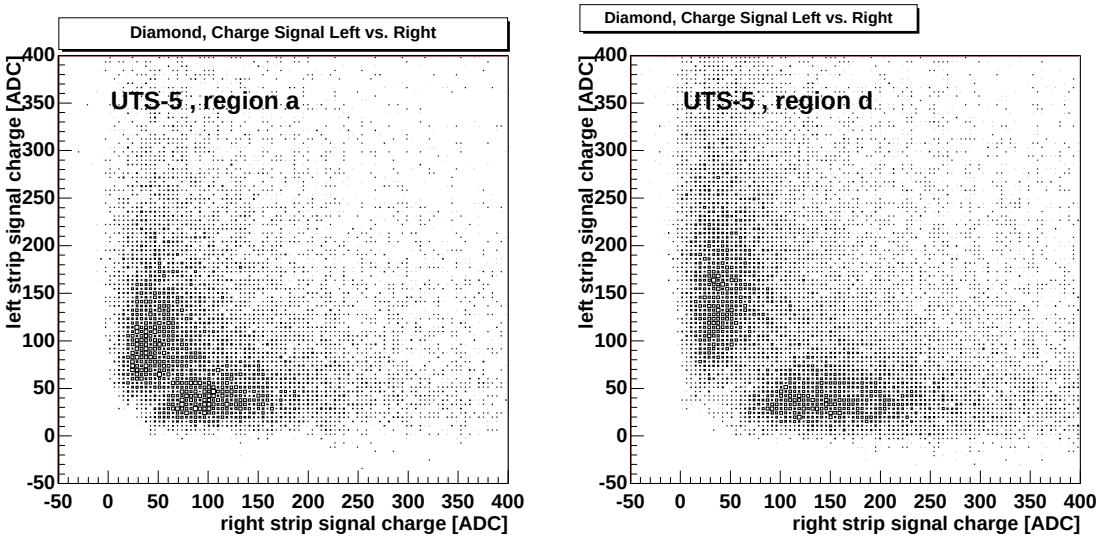

Figure 4.45: Relation between the signal charge on the left strip and the signal charge on the right strip for the region a with 10 μm wide strips (left) and for region d with 40 μm wide strips (right).

c.o.g position. One can see that the residuals are symmetrically distributed around zero. The digital residual distribution is a flat-top distribution. The digital residual distribution is more rectangular for wider strips than for narrower strips. The spatial resolution using the digital method is 18.5 μm in region a and 16.9 μm in region d as obtained from the *rms* in the interval for $|u_{\rm h} - u_{\rm t}| < 50$ μm. A Gaussian fit to the digital residual distribution in the interval $|u_{\rm h} - u_{\rm t}| < 50$ μm gives the same spatial resolution as the *rms*. If one extends the interval to $|u_{\rm h} - u_{\rm t}| < 60$ μm the digital spatial resolution increases by about 0.1 μm. The measured digital resolution is larger than $P/\sqrt{12} = 14.43$ μm. It can be seen that the measured digital residual distributions have entries in the tails for $|u_{\rm h} - u_{\rm t}| > 25$ μm. The measured spatial resolution, the *rms*, is sensitive to these entries. The measured FWHM is 50 μm for both distributions as expected for the digital method. The shape of the single strip residual distributions in this diamond are trapezoidal. For comparison the digital residual distribution in silicon has a rectangular shape [Fig. 4.8]. The 3-strip c.o.g. residual distribution has a Gaussian-like shape and is narrower than the digital residual distribution. The shape of the distribution in region a has a flat top whereas the shape in region d has a 'round' top. The spatial resolution using the 3-strip c.o.g. method is 14.5 μm in region a and 13.9 μm in region d obtained from the standard deviation of a Gaussian fit to the residual distribution for $|u_{\rm h} - u_{\rm t}| < 25$ μm. The 2-strip c.o.g. residual distribution has a Gaussian-like shape and is narrower than the 3-strip c.o.g. residual distribution. The shape of the distribution in region a might have a flat top whereas the shape in region d is point like. The spatial resolution using the 2-strip c.o.g. method is 12.1 μm in region a and 12.4 μm in region d obtained from the standard deviation of a Gaussian fit to the residual distribution for $|u_{\rm h} - u_{\rm t}| < 25$ μm.

4.2.11 Summary and Discussion

The method of analyzing the noise and signal charge in CVD diamond strip sensors has been described. A typical noise on 6 mm to 7 mm long strips has been measured to be 100 e in agreement with the expected equivalent noise charge. Two analysis methods, a cluster and a transparent analysis, were used. The signal charge from a cluster analysis is slightly higher than the transparent charge which is inherent to the method used. Table 4.2 shows a summary

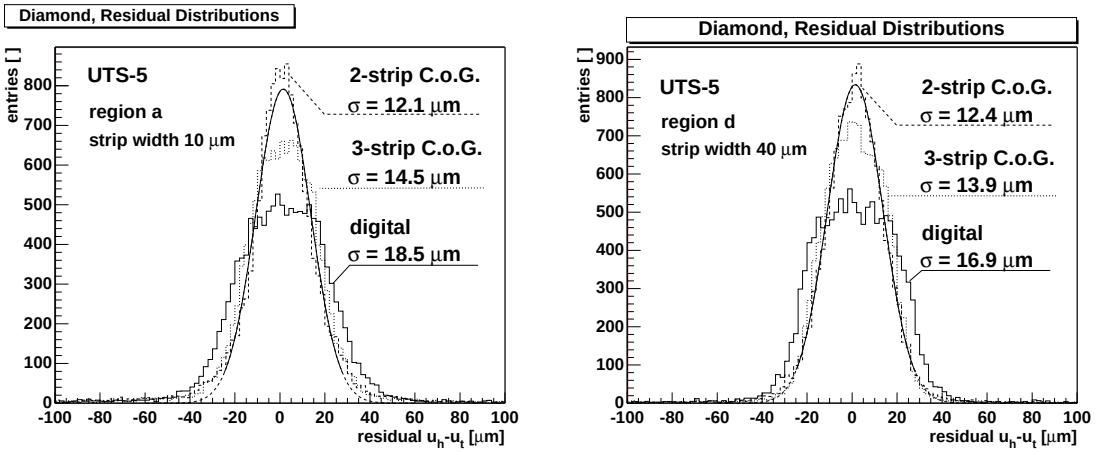

Figure 4.46: Residual distributions of the diamond detector with 10 μm wide strips in region a (left) and 40 μm wide strips in region d (right). The distributions for the 2-strip center of gravity, the 3-strip center of gravity and the digital hit finding methods are shown.

of results obtained on recent CVD diamond sensors in the beam. The thickness ranges from 432 μm to 1570 μm. The electrical field was normally 1 V/μm. For some diamonds larger leakage current of the order of several hundred nanoamperes made it necessary to operate at lower field. The values for signal-to-noise and K-strip c.o.g. spatial resolution are shown for the diamond sensors in the pumped state (except for CDS-51). The pumped state was reached by several hours exposure of the sensor to electrons from a 37 MBq ^{90}Sr source. The mean signal-to-noise ratios were obtained in the transparent analysis. All pumped sensors listed had a mean signal-to-noise ratio above 30-to-1. UTS-5 and CDS-57 had the largest ratio of 73-to-1 and 89-to-1. Using the K-strip c.o.g. method the spatial resolution was typically between 13.5 μm and 16 μm. There were sensors with spatial resolution above 20 μm. The reason for the relatively poor spatial resolution in CDS-57 despite its high signal-to-noise ratio is not clear. Different hit finding methods have been used from which the 2-strip c.o.g. method was the most promising so far. The spatial resolution could be improved by using the 2-strip c.o.g. method as demonstrated in UTS-5 reaching a spatial resolution between 12.1 μm and 12.4 μm which is better than digital resolution.

The influence of the strip width on the charge collection and on the spatial resolution has been investigated. Given that the residual distributions for different strip widths were measured on the same detector there can be no differences due to gain or noise variations as they could occur using two different sensors. Using the strip geometry with variable strips on one diamond one is sensitive to the strip width only. Therefore differences in the charge collection on different strip width are due to the strip width only. It was shown that 30 μm and 40 μm wide strips collect about 20 % more charge than 10 μm wide strips. The signal charge appears to plateau above 30 μm strip width. Strips with a width of 25 μm at a strip pitch of 50 μm are therefore a reasonably good choice from the point of charge collection. Using the hit finding methods described here it was shown that there are differences in the shape of the residual distributions for 10 μm wide strips and 40 μm wide strips. The important observation is that the 2-strip c.o.g. method gives a better spatial resolution than the 3-strip c.o.g. method. Normally the K-strip c.o.g. method has been used for hit position finding where K was variable depending on how many strips were exceeding the neighbour strip threshold. As a result of the observation made here and on other diamond strip sensors analysed one should consider using the 2-strip c.o.g. method rather than the 3-strip or K-

CVD diamond sensor	thickness [μm]	$\lvert\vec{E}\rvert$ [V/μm]	state	mean transp. 3-strip S/N	c.o.g. spatial resolution (K strips) [μm]
CDS-83	690	0.86	p	37	13.7
CDS-51	557	0.45	dp	22	15.6
UTS-5	432	1.0	p	73	15.0
CDS-57	480	1.04	p	89	26.5
CDS-26	1570	0.7	p	38	21.0
CDS-22	690	0.8	p	35	22.0
CDS-44	650	0.3	p	35	14.0
CDS-55	452	0.66	p	51	15.9

Table 4.2: Overview of the performance of recent CVD diamond sensors in the beam. The sensor thickness, the biasing electric field and the pumping state (dp=depumped, p=pumped) are shown. The mean signal-to-noise ratio from three strips measured in the transparent analysis and the spatial resolution obtained using the K-strip center of gravity method (c.o.g.) are given. CDS-55 and CDS-44 are 2×4 cm^2 sensors and their results are reported in detail in Sec. 4.3.

strip c.o.g. methods. Preliminary work using the 2-strip non-linear eta method in diamond has begun.

4.3 Large Area Diamond Strip Detectors

The typical size of a sensor module for particle tracking in high energy physics experiments ranges from one square centimeter to several tens of square centimeters. Sensors can be arranged next to each other to build a module and to cover larger areas. Many modules may then be grouped in wheel or barrel structures to meet the physics requirements. This structure may cover several hundred square centimeters, for example 1300 cm^2 in the Delphi Silicon Tracker [1]. In an application using diamond detectors one would also group several diamond sensors in the required structure. CVD diamond strip detectors with a size of 2 cm × 4 cm *were tested in pion beams. Their charge collection properties and spatial resolution are reported below.*

4.3.1 Introduction

The first 2×4 cm^2 CVD diamond sample was delivered in 1996 together with a 1 cm^2 sample from the same diamond disk. The charge collection distance of the 1 cm^2 sample was considered too low for use in a beam test with the large sample. This large sample was therefore returned to the manufacturer. After feedback on how to improve the charge collection distance large diamond samples from a second growth where delivered in 1997. The second delivery contained four 2×4 cm^2 samples and three 1 cm^2 samples from the same disk.

4.3.2 Experimental Method

Fig 4.47 shows the drawing of a diamond disk. The disk has a size of 120 mm in diameter. Inside the disk one can see the locations of the four 2×4 cm^2 samples and three 1×1 cm^2 samples, CDS-23,24,25. CDS-23 was cut from the center, CDS-24 was cut from a position between the center and the rim and CDS-25 was cut from the rim. The 1 cm^2 samples had a thickness of 770 μm as-grown. The 2×4 cm^2 samples were cut as shown. The surfaces of the 2×4 cm^2 diamonds were lapped and then optically polished on both sides. After lapping the diamond CDS-44 had a thickness of 650 μm. The thickness variation was measured from five uniformly distributed points over the area of 2 cm × 4 cm. The thickness variation was 2.6 μm on this sample. Another sample, UTS-1, had a thickness of 660 μm after lapping and a thickness variation of 7.6 μm. The diamond growth side of CDS-44 was then metallized with Cr/Au and patterned with 384 strips using the method described in Sec. 4.2.3. Fig. 4.1 shows a photograph of the diamond detector, CDS-44, after metallization and bonding to the readout electronics. The strips on the diamond growth side were 25 μm wide with a strip pitch of 50 μm. 256 strips had a length of 3.8 cm, 128 strip a length of 1.9 cm. In total 256 strips of the detector were read out by two low noise CMOS VA2 chips [78]. A rectangular contact was metallized at the end of the 1.9 cm strips for charge collection measurements with ^{90}Sr in the lab. Other strips of 100 μm pitch behind the rectangular contact remained unused in these tests. The backside of the diamond had one solid Cr/Au electrode with a size of 3.8 cm × 1.9 cm. The sensor was mounted on a 650 μm thick ceramic printed circuit board which also contained a 100 MΩ biasing resistor to the diamond backplane and one 4.7 nF/3.3 kV capacitor to ground in order to reject ripples on the DC bias voltage. The sensor and readout chips were fixed inside a light tight and electrically shielded aluminium frame. The Al-frame had thin Al-foil windows above and below the sensor for the pion beam to pass through.

Table 4.3 gives an overview of the detectors prepared for testing. It contains the $2 \times$

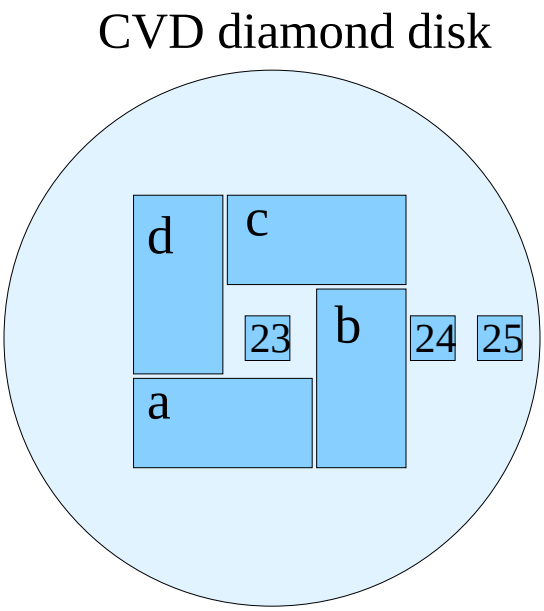

Figure 4.47: Schematic view of the diamond disk showing the locations of the various diamond samples. The diamond disk shown has a diameter of 120 mm. The sample CDS-44 and the other 3 large samples have a size of 2×4 cm^2, the smaller pieces are 1×1 cm^2.

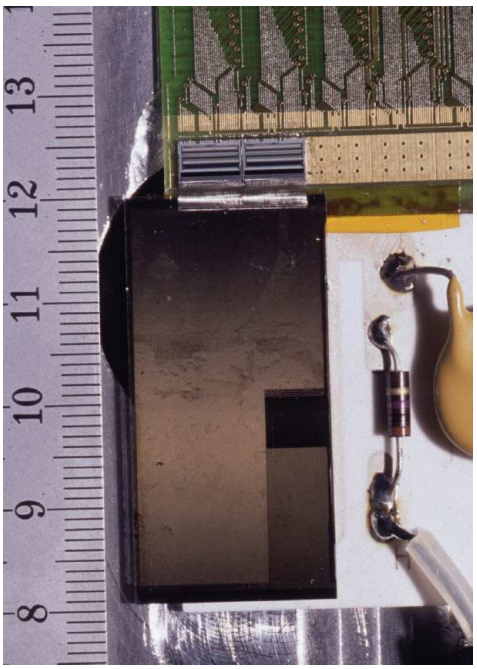

Figure 4.48: Photograph of a 2×4 cm^2 large diamond strip detector. The diamond substrate had a thickness of 650 μm. The strips on the diamond surface were 25 μm wide and had a pitch of 50 μm. In total 256 strips were read out by two low noise CMOS chips (VA2).

4 cm^2 samples and the three 1×1 cm^2 samples from the same disk. The beam tests were carried out using the silicon beam reference telescope and data acquisition system described in Sec. 4.1.2. The same analysis program was used to analyze the data: the algorithms for pedestal, common mode, signal and noise calculations from the raw data were the same as for the silicon reference planes. Only the thresholds for seed strip signal-to-noise and neighbour strip signal-to-noise for the hit finding were chosen lower than in silicon.

4.3.3 Results: Charge Signal versus Location on the Diamond Disk

Fig. 4.49 shows the charge collection distance as a function of the applied electric field measured on CDS-23 and CDS-25. CDS-23 was cut from the center of the diamond disk and CDS-25 was cut from the rim of the disk. The charge collection distance is shown for the depumped and for the pumped state. In the pumped state and at 1 V/μm the charge collection distance was 142 μm in CDS-23 and 106 μm in CDS-25. In the depumped state and at 1 V/μm the charge collection distance was 70 μm in CDS-23 and 29 μm in CDS-25. Two observations can be made: first the charge collection distance, pumped and depumped, for the center sample is higher than for the rim sample. Second the sample from the rim pumps by a factor of 3.6 whereas the center sample pumps by a factor of 2.0. Table 4.4 summarizes the measured charge collection distances at an electric field of 1 V/μm. The table also lists the measurements from another group (group A) [85]. The measurements from group A are given in the depumped state. It can be seen that the depumped values for CDS-23 and CDS-25 from group A agree with the depumped values measured here (group B). The charge collection distance of CDS-24 from group A is also given. The charge collection distance is 51 μm for CDS-24 which is slightly larger than the average of 47 μm obtained from CDS-23

sample	thickness [μm]	size [cm $\times$ cm]	mask	measurement
CDS-23	775	1×1	dot	*ccd* with ^{90}Sr
CDS-24	765	1×1	dot	*ccd* with ^{90}Sr
CDS-25	785	1×1	dot	*ccd* with ^{90}Sr
UTS-1	660	2×4	none	thickness variation
CDS-44	650	2×4	strips	in beam and *ccd* with ^{90}Sr
CDS-55	452	2×4	strips	in beam and *ccd* with ^{90}Sr
CDS-56	435	2×4	strips	failed

Table 4.3: Overview of samples and the measurements performed (*ccd* abbreviates charge collection distance).

and CDS-25. The charge collection distance appears to increase from the rim of the diamond disk to the center.

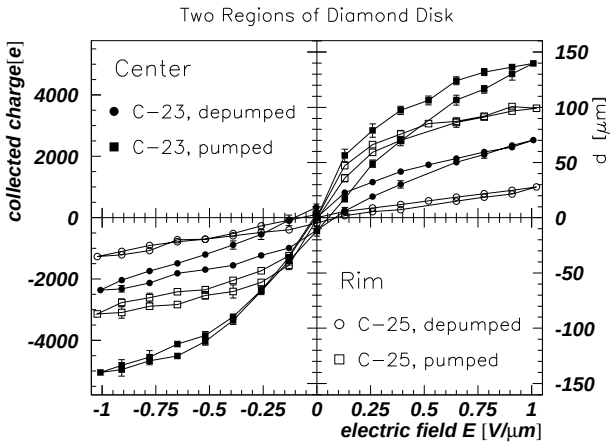

Figure 4.49: Charge collection distance as a function of the applied electric field in two samples from different regions of the diamond disk measured in the depumped and pumped state. Sample CDS-23 was cut from the center, sample CDS-25 was cut from the rim.

The leakage current was measured as well. The 1 cm^2 samples had equal leakage currents of 0.2 nA at 1 V/μm measured on round contacts with a size of 20 mm^2 corresponding to a current density of 10 pA/mm^2.

4.3.4 Results: Charge Signal of CDS-44 in Beam

CDS-44 was operated at an electric field of 0.3 V/μm in the beam. The total leakage current was 500 nA. At higher electric field the leakage current went above several microamperes. High leakage current was observed later on other 2×4 cm^2 strip detectors as well (on CDS-55 and CDS-56). The leakage current was high because the metallization partially covered the corners of the diamond which provided a conductive path to the backplane. This effect was cured later by leaving sufficient margin between the guard ring and the corner, and on the other side between the back plane and the diamond corner.

Fig. 4.50 shows the transparent signal charge distribution of CDS-44 in the beam and the 3-strip cluster charge distribution from CDS-44 measured with a ^{90}Sr source. The figure also shows the 3-strip cluster charge distributions from two silicon strip detectors measured with a ^{90}Sr source. The transparent signal of CDS-44 has a mean value of 209 ADC. It has

sample	thickness [μm]	charge collection distance [μm] at 1 V/μm		location on disk
		group A	group B	
CDS-23	775	62	70..142	center
CDS-24	765	51	-	between center and rim
CDS-25	785	32	29..106	rim

Table 4.4: Charge collection distance measured on three 1 cm^2 samples with a ^{90}Sr source from different locations on the diamond disk. The measurements of group A are shown for the depumped state only. The measurements of group B are shown for the depumped and pumped state. The measurement on CDS-24 from group B is missing.

a few pedestal entries around 0 ADC due to broken or shorted strips or shorted bonds in the fiducial region. The equivalent noise charge was measured between 6 ADC and 7 ADC. Hence the mean signal-to-noise ratio was between 30-to-1 and 35-to-1. The 3-strip cluster signal from the ^{90}Sr measurement, at the same electronic gain and bias voltage, has a distribution of similar shape as the transparent signal. The mean 3-strip cluster charge is 198 ADC as read from the figure.

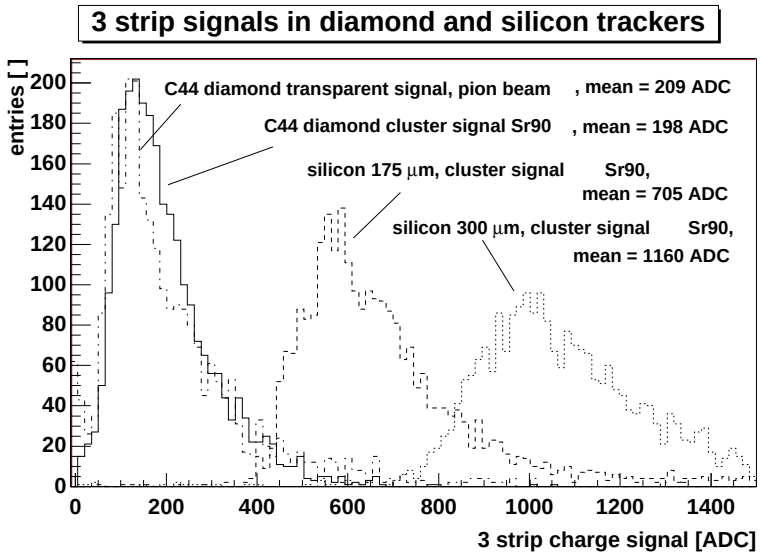

Figure 4.50: Distribution of the transparent 3-strip signal charge in CDS-44 measured in the pion beam and the 3-strip cluster signal measured with a ^{90}Sr source. The 3-strip cluster signal distributions measured with ^{90}Sr on 175 μm and 300 μm thick silicon strip detectors at the same gain are overlayed.

The 3-strip cluster charge distributions from two silicon detectors with a thickness of 175 μm and 300 μm were measured later with a ^{90}Sr β-source at the same electronic gain using the same sirocco ADC. The most probable charge of the distributions is (1000$\pm$40) ADC for 300 μm and (575 ± 30) ADC for 175 μm thick silicon read from Fig. 4.50. Using the 'in-use' most probable charge collected of 22500 e in 300 μm thick silicon (see Sec. 3.3.5) one obtains the gain of (22.7 ± 1) e/ADC. One therefore infers the mean transparent charge of the diamond detector to be 4730 e corresponding to a bulk average charge collection distance of 132 μm at 0.3 V/μm. From the measured equivalent noise charge in ADC units one infers the equivalent noise charge to be between 136 e and 159 e. This noise measurement includes strips from both length, 1.9 cm and 3.8 cm.

4.3.5 Results: Charge Signal of CDS-55 in Beam

The second large area strip detector, CDS-55, was tested half a year later in the pion beam. CDS-55 was from a different disk than CDS-44. CDS-55 had the same strip pattern as CDS-44. CDS-55 was lapped and polished on both sides and had a thickness of 452 μm. CDS-55 was operated at 300 V corresponding to an electric field strength of 0.66 V/μm. It should be noted that the electric field for CDS-55 is higher than the electric field for CDS-44 in the previous test.

Fig. 4.51 shows the transparent 3-strip charge distribution measured from CDS-55 in two different regions of the detector. The second region was offset to the first region by 1 cm. The offset was realized by moving the detector vertically along the direction of the strips and mounting it 1 cm higher than the first position. The fiducialization area analyzed in both positions had a rectangular area size of 19 mm^2. It can be seen that both distributions have the same shape and approximately the same mean value. This indicates that the detector has the same signal response under lateral translation by 1 cm. It should be noted that the area averaged over has a size of 19 mm^2 for both positions. The size is relevant since for small areas the mean signal charge can change as a function of the size of the area as described in Sec. 4.4. Fig. 4.51 shows the mean charge collected of 193 ADC in region 1 and of 212 ADC in region 2. The average charge collected from both regions is 203 ADC. The most probable charge collected is 122 ADC in region 1 and 140 ADC in region 2 giving an average most probable charge of 131 ADC. The single strip equivalent noise charge was measured to be 4.0 ADC on 1.9 cm long strips and 5.1 ADC on 3.8 cm long strips (see below). Using the noise measurement of 4.0 ADC for 1.9 cm long strips one obtains the most probable signal to noise ratio of 33-to-1 and the mean signal to noise ratio of 51-to-1. Using the noise measurement of 5.1 ADC for 3.8 cm long strips one obtains the most probable signal to noise ratio of 26-to-1 and mean signal-to-noise ratio of 40-to-1.

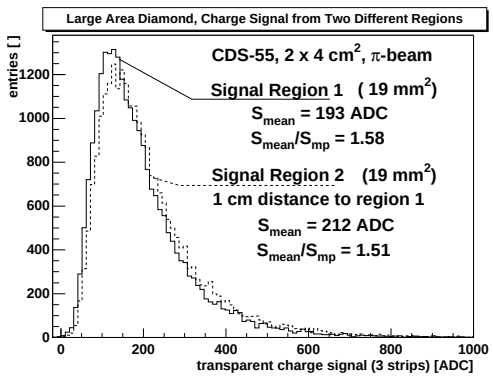

Figure 4.51: Distribution of the transparent signal charge from 3-strips in the 2×4 cm^2 diamond strip detector CDS-55 measured in two regions 1 cm apart.

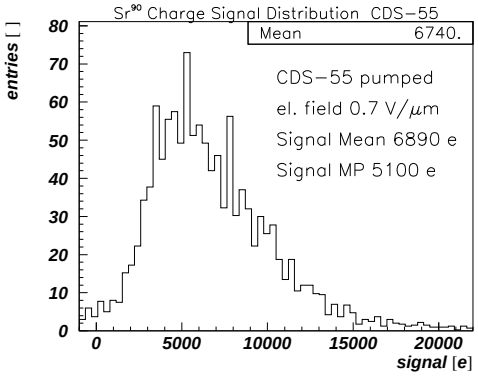

Figure 4.52: Signal charge distribution measured with a ^{90}Sr β-source on a rectangular contact on the large diamond strip detector CDS-55.

Fig. 4.52 shows the signal charge distribution from CDS-55 at 0.7 V/μm measured using a ^{90}Sr $\beta-$source. The signal was measured on the rectangular electrode in the characterization station described in Sec. 3.4.5. The distribution was measured before wire bonding the detector to the readout electronics and installation in the beam. The distribution has a most probable charge of about 5100 e and a mean signal charge of 6890 e. The mean signal charge corresponds to a charge collection distance of 191 μm. Based on the agreement between

the signal obtained in CDS-44 using the beam and using the ^{90}Sr source we infer the mean of CDS-55 in the beam to be at 6890 e. Based on the experience with other sensors the reliability (error) is approximately 15 %. Using the average measured mean of 203 ADC from Fig. 4.51 one derives the gain of (34 ± 5) e/ADC for CDS-55 in the beam.

4.3.6 Results: Comparison between CDS-44 and CDS-55

The electrical quality of CDS-44 and CDS-55 can be compared. One must consider that CDS-44 and CDS-55 were operated at different electric fields. The electric field was 0.3 V/μm for CDS-44 and 0.66 V/μm for CDS-55. In order to compare the signal charge from CDS-44 with CDS-55 one has to scale the signal charge of CDS-44 to the electric field of CDS-55. Scaling of CDS-44 is possible by using the measured mean signal charge from CDS-23 and CDS-25 as a function of the electric field. CDS-23 to CDS-25 where from the same disk as CDS-44. Therefore one can assume the same shape of the mean signal charge as a function of the electric field for CDS-44 and CDS-23 to CDS-25. Using the shape of the mean signal charge as a function of the electric field from CDS-23 to CDS-25 one can derive the scaling factor between the signal charge at 0.66 V/μm and 0.3 V/μm.

sample	thickness [μm]	charge collection distance [μm] at 0.3 V/μm	[μm] at 0.66 V/μm	ratio
CDS-23	775	77	115	1.49
CDS-24	765	-	-	-
CDS-25	785	66	90	1.36
CDS-44	650	132	-	1.45
CDS-55	452	-	191	

Table 4.5: Comparison of CDS-44 and CDS-55 based on the measurements on CDS-23 and CDS-25.

Table 4.5 shows the charge collection distance from CDS-23, CDS-25, CDS-44 and CDS-55 at an electric field of 0.3 V/μm and 0.66 V/μm. The values for CDS-23 and CDS-25 were obtained from the measurement shown in Fig. 4.49. The values for CDS-44 and CDS-55 were obtained from the measurements shown above. The scaling factor is the ratio between the charge collection distance at 0.66 V/μm and 0.3 V/μm. The scaling factor is 1.49 for CDS-23 and 1.36 for CDS-25. The average scaling factor for these two samples is 1.4. The charge collection distance measured for CDS-44 was 132 μm at 0.3 V/μm. Using the scaling factor of 1.4 obtained from CDS-23 and CDS-25 one derives the scaled charge collection distance of 185 μm for CDS-44 at 0.66 V/μm. The scaled charge collection distance for CDS-44 at 0.66 V/μm is approximately equal to the charge collection distance of 191 μm for CDS-55 at 0.66 V/μm. We conclude that CDS-44 has comparable electrical quality to CDS-55. It should be noted that CDS-55 had less leakage current than CDS-44. The lower leakage current of CDS-55 is likely due to a more accurate metallization which allowed to operate CDS-55 at higher electric field than CDS-44.

4.3.7 Results: Noise

Fig. 4.53 shows the single strip noise measured in fiducial regions on $L_1 = 3.8$ cm long strips and $L_2 = 1.9$ cm long strips. The distributions are Gaussian and centered around zero with a standard deviation of 4.0 ADC on short strips and 5.1 ADC on the longer strips. Using the gain calibration of (34 ± 5) e/ADC for CDS-55 one obtains an equivalent noise charge of (136 ± 20) e for 1.9 cm long strips and (173 ± 25) e for 3.8 cm long strips. This noise

is consistent with the noise measured on CDS-44 in the previous beam test. The leakage current density 10 pA/mm^2 at 1 V/μm was measured on CDS-23 and CDS-25. The DC leakage current of ≈ 4.7 pA per 1.9 cm long and 25 μm wide strip was derived from the these measurements. Using Eq. 3.140 one obtains a equivalent noise charge of 10 e at 2 μs signal peaking time due to the leakage current of 4.7 pA into the amplifier. This noise adds in quadrature to the total equivalent noise charge. One finds that the noise due to the diamond detector leakage current can be neglected.

It can be seen that the noise charge is 1.1 ADC larger on 3.8 cm long strips than on 1.9 cm long strips. The excess noise charge of 1.1 ADC must be attributed to the extra length of 1.9 cm. Using the gain calibration of (34 ± 5) e/ADC for CDS-55 one obtains an excess noise charge of $\Delta\sqrt{\langle q^2_{\rm total}\rangle} = (37 \pm 6)$ e. The parallel noise in the readout can be neglected since the channel leakage current is of the order of picoampere and the feedback resistor is of the order of hundred megohm. The excess equivalent noise charge can therefore be approximated by the excess series equivalent noise charge

$$\Delta\sqrt{\langle q^2_{\rm total}\rangle} \approx \Delta\sqrt{\langle q^2_{\rm series}\rangle} = \left[C_{\rm e}(L_1) - C_{\rm e}(L_2)\right]\sqrt{\langle u^2_{\rm a}\rangle} \tag{4.70}$$

where the series noise is given by Eq. 4.66. The equivalent noise voltage for the VA2 is $\sqrt{\langle u^2_{\rm a}\rangle} = 11$ e/pF. Using Eq. 4.61 and Eq. 4.62 one finds the external capacitance

$$C_{\rm e}(L) = 2\,C_{\rm s}(L) + C_{\rm b}(L) + C_{\rm stray} \tag{4.71}$$

where the interstrip capacitance, $C_{\rm s}(L)$, is given by Eq. 4.63 and the strip-to-backplane capacitance, $C_{\rm b}(L)$, given by Eq. 4.64. It should be noted that $C_{\rm s}$ and $C_{\rm b}$ are linear in the strip length, L, such that the external capacitance can be written

$$C_{\rm e} = C_{\rm stray} + \frac{\Delta C_{\rm d}}{\Delta L}\,L \tag{4.72}$$

where $\Delta C_{\rm d}$ denotes the change of the detector capacitance when changing the length by ΔL. Inserting Eq. 4.71 in Eq. 4.70 and rearranging gives the *specific capacitance per unit length for strips on diamond*

$$\frac{\Delta C_{\rm d}}{\Delta L} = \frac{\Delta\sqrt{\langle q^2_{\rm series}\rangle}}{\sqrt{\langle u^2_{\rm a}\rangle}\,(L_1 - L_2)}. \tag{4.73}$$

Using the measured excess noise charge one obtains

$$\frac{\Delta C_{\rm d}}{\Delta L} = (1.77 \pm 0.3)\ \text{pF/cm}. \tag{4.74}$$

It should be noted that this measurement is valid for diamond sensors with 50 μm pitch, 25 μm strip width and 452 μm thickness. The dependence of the noise on the thickness is less than on the pitch and on the strip width. One also should note that the measurement is independent of the stray capacitance, $C_{\rm stray}$.

The measured specific noise allows one to derive the equivalent noise charge for 6.4 mm long strips: $C_{\rm d}(L = 6.4\ \text{mm}) = (1.13 \pm 0.2)$ pF. This measured capacitance is consistent with the calculated capacitance in Sec. 4.2.2.

The calculation from Fig. 4.24 shows that the detector capacitance is $C_{\rm d} = 3.1$ pF for 1.9 cm long strips and $C_{\rm d} = 6.1$ pF for 3.8 cm long strips. The strip to backplane capacitance is negligibly small compared to the interstrip capacitance as shown in Sec. 4.2.5. Using the measured specific capacitance one finds $C_{\rm d} = (3.4 \pm 0.6)$ pF for 1.9 cm long strips and $C_{\rm d} = (6.7 \pm 1.1)$ pF. The calculation is consistent with the measured specific capacitance.

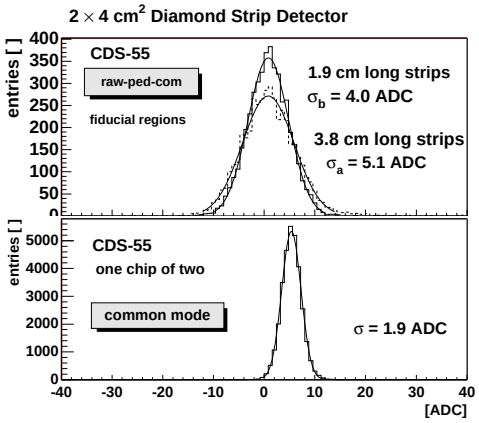

Figure 4.53: Distribution of the pedestal subtracted, common mode corrected and hit suppressed raw values (above) in the region with 3.8 cm long strips and 1.9 cm long strips and the distribution of common mode shifts in one readout chip (below).

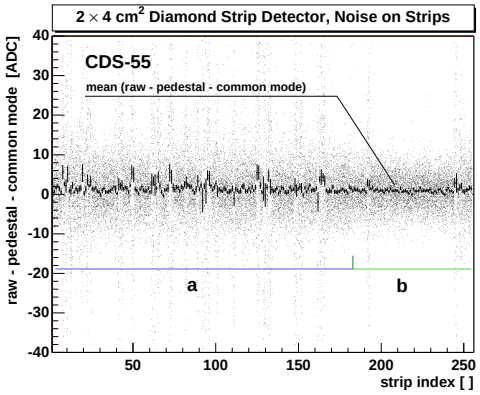

Figure 4.54: Pedestal subtracted, common mode corrected and hit suppressed raw values as a function of the readout channel index for 256 channels (two chips). The strips in region a have a length of 3.8 cm and in region b a length of 1.9 cm.

Fig. 4.53 also shows the distribution of the common mode shifts. It can be seen that the common mode variation (or common mode noise) is 1.9 ADC corresponding to a variation of 65 e. The common mode correction was applied to correct the pedestal subtracted charge raw values.

Fig. 4.54 shows noise charge values (the pedestal subtracted, common mode corrected and hit suppressed raw values) versus the strip number. It can be seen that the mean noise charge values are centered around zero. The figure should be compared with the same measurement of the noise charge values from UTS-5 in Fig. 4.27. One can see that CDS-55 has more channels with larger noise charge than UTS-5. The channels with larger noise charge are channels with bond wire shorts or shorts between two adjacent strips on the strip mask.

4.3.8 Results: Spatial Resolution

The digital method and the K-strip center of gravity method (c.o.g.) were used to measure the position of hit clusters. The K-strip c.o.g. method uses K strips where K depends on the seed strip and neighbour strip thresholds chosen. The signal-to-noise threshold was 8-to-1 for seed strips and 4-to-1 for neighbour strips. The thresholds determine the distribution of K. The distribution of K was (28 %, 30 %, 18 %, 13 %, 7 %) for $K = (1, 2, 3, 4, 5)$. One can see that the mean number of strips in a cluster is approximately two: $\langle K \rangle = 1.96$.

Fig. 4.55 shows the K-strip c.o.g. residual distribution (solid histogram) and the digital residual distribution (dotted histogram). The K-strip c.o.g. residual distribution is fitted by a Gaussian function in the interval of residuals smaller than 30 μm. The standard deviation gives the spatial resolution of 15.9 μm for the K-strip c.o.g. method. This result is comparable with the spatial resolution observed in 1×1 cm^2 strip sensors using the K-strip c.o.g. method. The distribution of the residuals obtained using the digital method is shown for comparison. The digital residual distribution has a flat top as observed in UTS-5 using the digital method. The digital residual distribution has approximately the same width as the residual distribution obtained with the K-strip c.o.g. method.

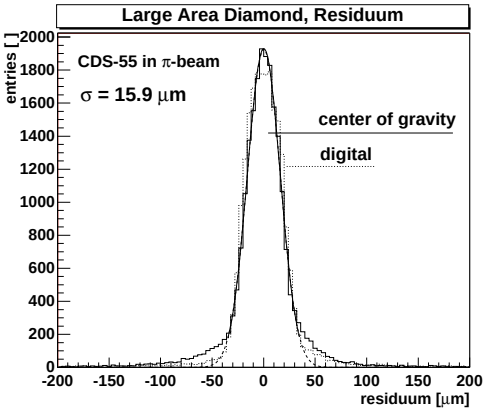

Figure 4.55: Residual distribution in CDS-55. The Gaussian fit (solid line) has a standard deviation of $\sigma = 15.9$ μm and represents the spatial resolution of the K-strip center of gravity method.

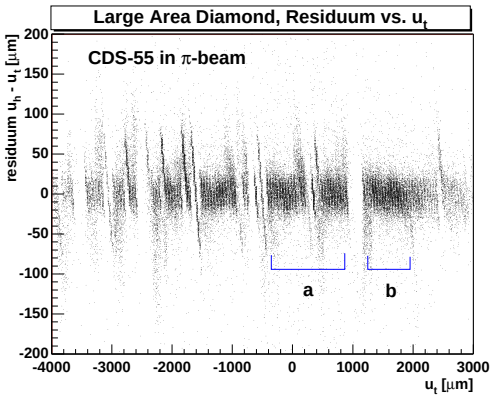

Figure 4.56: Residuals, $u_\mathrm{h} - u_\mathrm{t}$, as a function of the predicted hit position, u_t, perpendicular to the strips. Two regions, a and b, were chosen for the residual distribution in Fig. 4.55.

Fig. 4.56 shows the residuals versus the position u_t. In some regions there are contiguous strips where the residuals are centered around zero. In other regions the residuals extend over two or three strips along a 'line' with inclination -1. This 'line'-effect was observed in UTS-5 [Fig. 4.33] and is explained by electrically shorted or missing strips (see Sec. 4.2.6). The fiducial regions chosen for the residual distribution are drawn in the figure (region a and b). Region a contains a few strips which have residuals on a line. These events cause the tails in the residual distribution in Fig. 4.55.

4.3.9 Summary on Large Area Diamond Strip Sensors

Results from two 2×4 cm^2 diamond strip detectors (CDS-44 and CDS-55) with low noise VA2 readout electronics have been presented. The charge collection of 191 μm at 0.66 V/μm was measured on CDS-55. The same charge collection distance was measured in two regions one centimeter apart averaged over a rectangular area of 19 mm^2. This indicates that CDS-55 is uniform on a length scale comparable to a rectangular area of 19 mm^2. The charge collection distance of 132 μm at 0.3 V/μm was measured on CDS-44 using the pion beam and a ^{90}Sr β-source. Using two samples (CDS-23 and CDS-25) the charge collection distance of CDS-44 was scaled to 185 μm at 0.66 V/μm and compared with CDS-55. CDS-44 and CDS-55 have the same charge collection distance at the same electric field. This implies that both samples have comparable electrical quality. CDS-44 was cut from a disk together with 1×1 cm^2 samples, CDS-23 (center), CDS-24 (middle) and CDS-25 (rim). The charge collection measurement of the 1×1 cm^2 samples showed increasing charge collection distance from 106 μm at the rim to 142 μm at the center. Using the 3-strip transparent analysis the mean signal-to-noise ratio between 30-to-1 and 35-to-1 were measured on CDS-44 at 0.3 V/μm. The analysis on CDS-44 did not distinguish between 1.9 cm long strips and 3.8 cm long strips. The distinction between long and short strips was made in the analysis of CDS-55 (operated at 0.66 V/μm). A mean signal to noise ratio of 51-to-1 was measured on CDS-55 in the region of 1.9 cm long strips and a mean signal-to-noise ratio of 40-to-1 was measured in the region of 3.8 cm long strips due to higher noise.

The noise was measured on the strips in CDS-55. The additional noise on longer strips allowed an estimate of the specific detector capacitance, ΔC_d, per strip length, ΔL, on the dia-

mond surface. For 25 μm wide with 50 μm pitch the result was $\Delta C_{\rm d}/\Delta L = (1.77\pm0.3)$ pF/cm. This measurement is consistent with the calculated detector capacitance [Sec. 4.2.2].

The spatial resolution was measured on CDS-55 and CDS-44. The results of CDS-55 were reported here. The analysis of CDS-55 used a K-strip c.o.g. method and attained a spatial resolution of 15.9 μm. The residual distribution using the digital method was comparable to the residual distribution using the K-strip c.o.g. method. This result is consistent with the spatial resolution obtained in other CVD diamonds. In the analysis of UTS-5 reported in Sec. 4.2.10 it was shown that the 2-strip center of gravity method gives smaller residuals than the K-strip c.o.g. method. Preliminary work on CDS-55 confirms that the spatial resolution can be improved by using the 2-strip center of gravity method.

Finally it should be noted that other large diamond samples with a size of 3×3 cm^2 were delivered in the past for a diamond-tungsten calorimeter [106] and to collaborators in RD42 for heavy ion experiments where they were used as trigger counters (as in the HADES/GSI experiment) and for beam diagnostics [107]. This shows that the production of large detector grade CVD diamond is becoming routine.

4.4 Study of Signal Uniformity

CVD diamond is inherently polycrystalline in nature. Silicon in comparison is mono-crystalline. One may ask whether this morphological difference influences the charge collection properties laterally across the sensor. Pictures of mean charge collected laterally across the sensor can be taken by illumination in particle beams. Regions of high mean signal and valleys of low mean signal were observed in diamond detectors using this method. The level of signal uniformity in a CVD diamond sensor and a silicon sensor were studied. It was discovered that in the CVD diamond the level of uniformity changes with length scale. The signal charge distribution from macroscopic regions of several millimeters were found to be a convolution of signal distributions with high and low signal charge from microscopic regions on a scale of several 100 micrometers. In diamond detectors which have macroscopic signal separation from zero all microscopic regions give charge. Therefore macroscopic signal separation from zero appears to be an important characteristic for a CVD diamond detector.

4.4.1 Uniformity Maps

The lateral signal uniformity of a sensor can be studied by means of a signal map which is prepared as follows: a rectangular fiducial region may be chosen with width, U, in direction u perpendicular to the strips and the length, V, in direction v along the strips. The area is then divided into bins, with a size of $\delta_u\times\delta_v$ each, which defines the number of bins $B_u = U/\delta_u$ in direction of u and $B_v = V/\delta_v$ in direction of v and the total number of bins $B = B_u \cdot B_v$. The fiducial region is uniformly illuminated by $N = \sum_{b=1}^{B} n_b$ beam particles such that the number of entries in any bin is estimated by the *mean number of entries* which is $\bar{n} = N/B$. The mean charge $\bar{Q}_b$ in bin b with n_b entries of measured charges Q_j is then $\bar{Q}_b = \frac{1}{n_b}\sum_{j=1}^{n_b} Q_j$.

Fig. 4.57 shows the the mean collected 3-strip charge signal, $\bar{Q}_b$, in one silicon plane of the beam reference telescope and in the diamond strip detector UTS-5 as a function of the position of the particle track measured in run 911. The regions of both detectors are divided into rectangular bins with a size of $\delta_u \times \delta_v = 100$ μm $\times$ 100 μm. The bins have a mean number of $\bar{n} = 52.3$ entries for silicon and diamond. The mean charge signals are gray scale

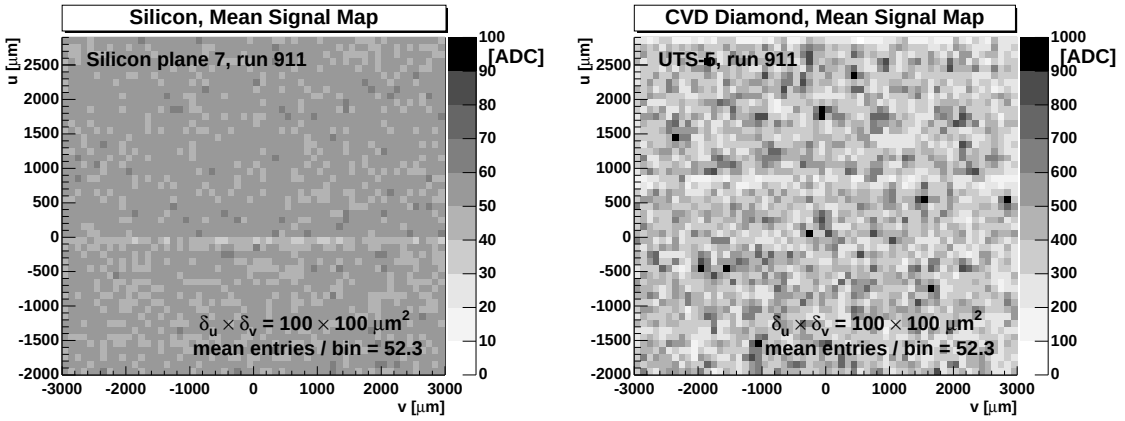

Figure 4.57: Mean collected charge in a silicon (left) and diamond (right) detector as a function of the position of the particle track. The mean charge is gray scale coded and measured in bins of 100 μm $\times$ 100 μm. The charge was measured on three strip in the transparent analysis.

coded and given in ADC units. It can be seen that the mean signal charge in individual bins of the silicon detector and in the diamond detector differ from one bin to the other. It should be noted that the ADC range controls the contrast of the mean signal map. To make a qualitative visual comparison between the silicon and the diamond it is necessary to chose the ADC range (a combination of contrast and brightness) properly. The following limits, $Q_{\rm min}$ and $Q_{\rm max}$, of the ADC range are proposed

$$Q_{\rm min} = 0 \qquad \text{and} \qquad Q_{\rm max} = \hat{Q} + 3 \times \text{FWHM}. \tag{4.75}$$

Using the 3-strip most probable signal of $\hat{Q}^{(\rm si)} = 44$ ADC and FWHM$^{(\rm si)}$=20 ADC in silicon read from Fig. 4.19 one obtains $Q^{(\rm si)}_{\rm max} = 104$ ADC. Using the 3-strip most probable signal of $\hat{Q}^{(\rm di)} = 215$ ADC and FWHM$^{(\rm di)}$=270 ADC in UTS-5 read from Fig. 4.35 one obtains $Q^{(\rm di)}_{\rm max} = 1025$ ADC. One can see that the ADC range chosen in Fig. 4.57 is close to the proposed ADC range. With the ADC range chosen here there appear to be stronger variations in CVD diamond than in silicon.

It is possible to prepare signal maps with finer bin scales by using more beam events. Fig. 4.58 shows the illumination of the diamond detector UTS-5 by the particle beam. This histogram has been prepared by counting the number of tracks traversing in each bin where the bins had a size of 25 $\times$ 25 μm^2 using data from runs 945, 954, 955, 961 and 962. From this figure one can infer that the detector was illuminated uniformly with pions. The line at $v \approx 0$ μm is due to a missing bond in one of the silicon planes. The missing bond is the reason that only a few tracks were reconstructed when passing this strip. There is a small triangular region in the upper left corner of UTS-5 where no tracks where predicted. The 'line' and the 'triangular region' should not be considered in the following pictures since the number of tracks is too low. From the uniform illumination of UTS-5 it can be concluded that the silicon detectors of the beam reference telescope were illuminated uniformly as well. The mean signal response of a silicon strip detector of the reference telescope to uniform illumination is shown in Fig. 4.59. For this presentation the range is chosen according to Eq. 4.75. No systematic variations in mean signal are observed in silicon on the bin scale of 25 μm $\times$ 25 μm.

Fig 4.60 shows the mean signal map of the diamond detector UTS-5 on a bin scale of $\delta_u \times \delta_v = 25$ μm $\times$ 25 μm. Each bin contains on average 11.5 entries. The data is shown

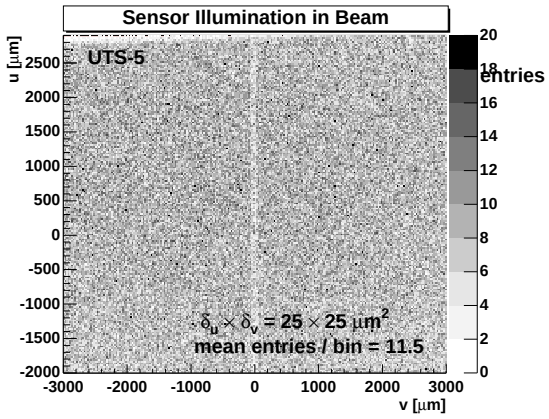

Figure 4.58: Illumination of diamond UTS-5 in the beam. The number of particles in 25 μm $\times$ 25 μm bins which traverse the detector is shown gray scale coded as a function of the position of the particle track. The histogram contains 17 bins with 0 entries randomly distributed over the area shown.

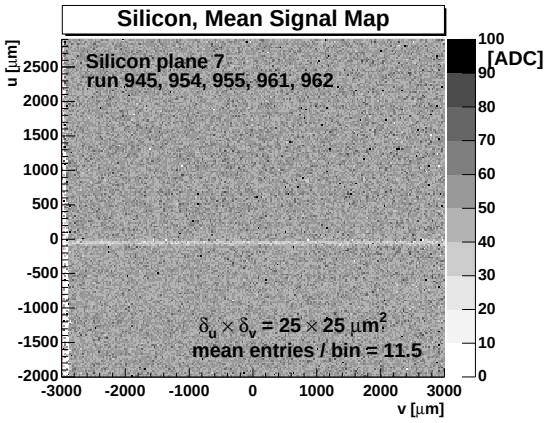

Figure 4.59: Mean collected charge in a silicon detector as a function of the position of the particle track. The mean charge is measured in bins of 25 μm $\times$ 25 μm.

for four ADC ranges where the lower limit is always 0 ADC. The upper limits were chosen to be, $Q_{\max} = 1200$ ADC (upper left), which is higher than proposed by Eq. 4.75, and $Q_{\max} = 160$ ADC (lower right), which is lower than the most probable signal value of UTS-5. Also maps for $Q_{\max} = 800$ ADC and $Q_{\max} = 400$ ADC are shown. One can see that the contrast changes depending on the range chosen. In the upper maps one observes regions of higher and lower mean signal. It can be seen that the mean signal fluctuates from bin to bin. It can also be seen that there are contiguous regions where the bins have the same gray-scale-code. There are dark regions (spots) and light regions. The dark regions have a typical size of the order of 100 μm for $Q_{\max} = 800$ ADC. The lower maps were prepared in order to emphasize regions with mean signals at the lower end of the charge distribution (around the most probable signal and below the most probable signal charge). The map with $Q_{\max} = 160$ ADC is mainly dark and shows very few bins which have a mean signal below 100 ADC. It should be noted that bins with zero entries are coded white. It should also be noted that with $\bar{n} = 11.5$ entries per bin on average one does expect a few bins with $n = 0$ entries. The number of bins with zero entries in the figure is about 17.

The maps were prepared using data from runs 945, 954, 955, 961 and 962. Run 911 (used in Fig. 4.57) was recorded a few hours earlier. The map from run 911 should be overlayed to Fig. 4.60 (upper right) in order to compare the positions of dark spots and light regions in both maps. It can be seen that many dark spots from one map correspond to dark spots in the other map. This observation is an indication for systematic signal variations in the diamond.

The variations from bin to bin may have various reasons. There are statistical variations and systematic variations. The statistical variations are due to noise and fluctuations of the energy loss (Landau fluctuations). The systematic variations may be due to variations of the signal response laterally across the sample. These variations are due to fluctuations in the local properties of the detector.

Signal maps from CVD diamond detectors have been prepared in the past [108, 3] with 100 μm $\times$ 100 μm bin size from particle beam tests with diamond strip detectors. Quantification of the level of uniformity and the length scale of variations were preliminary and not yet

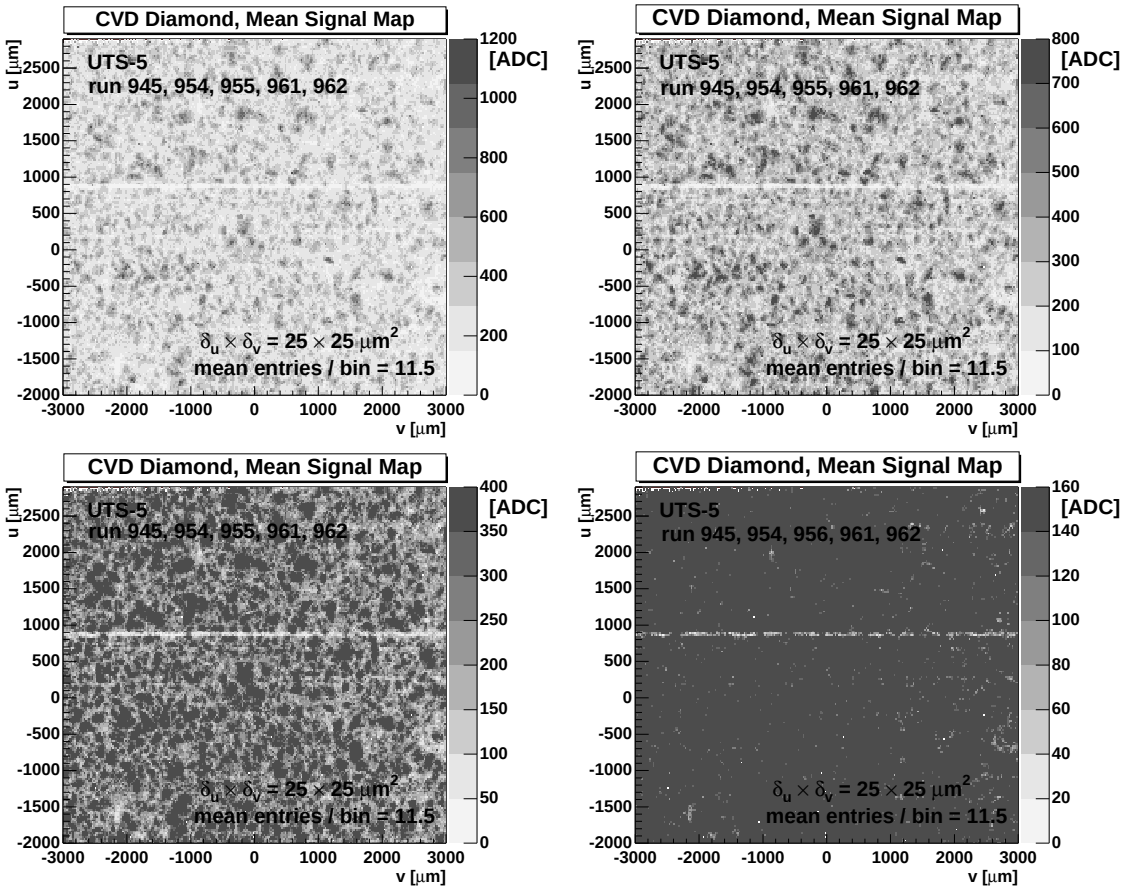

Figure 4.60: Mean collected charge in diamond detector UTS-5 as a function of the position of the particle track. The mean charge is gray scale coded and measured in bins of 25 μm $\times$ 25 μm. Four maps are shown. The maps are based on the same data. The maps differ in the ADC range chosen.

presented. This was mainly due to limited statistics. It should be noted that it is not obvious to extract 'uniformity results' based on images only. In the section below a possibility to quantify uniformity is proposed.

In other work the beam induced current from 2 MeV He^+ in 250 μm thick polycrystalline diamond films was measured [109] and "high resolution images of single grains in films" having peaks in locally distinct regions of the sample were observed. In again other work the induced current from a proton micro-beam was measured [110] and a few "hot spots" under a solid electrode were observed. The measurements of induced currents are difficult to perform and not obvious to compare with the measurements of the induced charge as they were shown here.

4.4.2 Signals from Selected Regions

Fig. 4.61 shows a magnification of the mean signal map of the diamond detector UTS-5. The bin size is 25 μm $\times$ 25 μm. The rectangular region was chosen from -500 μm to $+500$ μm in both the u and v direction. The figure identifies several spots of relatively high mean signal and relatively low mean signal. Three regions were selected with graphical cuts in order to analyze the signal distributions for predicted particle hits in these regions. The regions are surrounded by solid lines and labeled a, b, c. The signal distributions for hits which were

predicted in these regions are shown in Fig. 4.62. Region a contains bins with relatively low

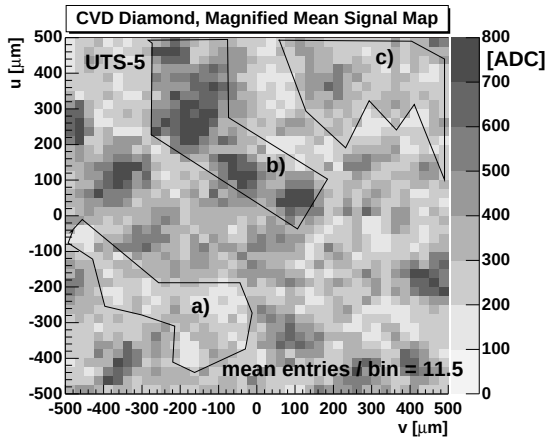

Figure 4.61: Magnification from Fig. 4.60 into the rectangular region from -500 μm to $+500$ μm in direction of v and u centered around 0 at a bin size of 25 μm $\times$ 25 μm. Regions a, b and c are selected with graphical cuts for further inspection.

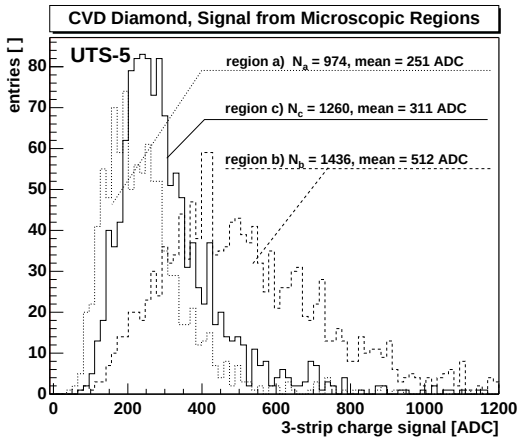

Figure 4.62: Charge signal distributions in selected regions of UTS-5 from Fig. 4.61: a low signal, b high signal and c medium signal. The number N of entries and the mean value is given for each histogram.

mean values in the signal map. The distribution of signals in this region has a mean value of 251 ADC which is smaller by a factor 2 compared to the mean value from signals in the highest region b. The ratio of mean-to-most probable value in region a is 1.19 ± 0.16. The smallest signal in the distribution from a is still separated from 0. Region b was chosen from the signal map because it shows bins with relative high mean values. The signal distribution has a mean of 512 ADC. The measured mean-to-most probable value is 1.14 ± 0.13. Region c has bins with medium mean signals. The signal distribution from this region has a mean of 311 ADC which is slightly lower than the arithmetic mean from the highest and the lowest signal regions. The mean-to-most probable value in region c is 1.24 ± 0.15. Therefore a signal distribution measured on a macroscopic scale appears as a convolution of signal distributions from microscopic regions. The signal distributions from regions have mean-to-most probable ratios of on average 1.19 ± 0.15 which is smaller than the mean-to-most probable ratio of the convoluted distribution from the macroscopic scale.

4.4.3 The Level of Uniformity

Fig. 4.63 shows a histogram of the normalized mean values from signal maps of a silicon and a CVD diamond strip detector. The mean values were measured using a bin size of 100 μm $\times$ 100 μm. The mean value of each distribution is normalized to the *average mean over all bins*, $\bar{Q} = \frac{1}{B}\sum_{b=1}^{B} \bar{Q}_b$. The measured distribution is a convolution of two distributions: firstly statistical variations of the inherent Landau fluctuations and the noise fluctuations which have the variance $\mathrm{VAR}(Q_b)$. Secondly there is a systematic variation from bin to bin whose distribution is unknown. The systematic variation of the mean signal has the variance $\mathrm{VAR}(\bar{Q}_b)$. The normalized mean signal variation, $\hat{\sigma}_\mathrm{m}$, measured from the histogram *rms* of Fig.4.63 is then expressed in terms of the statistical variation and the bin-to-bin variation:

$$\hat{\sigma}_\mathrm{m}^2 = \frac{1}{\bar{n}} \cdot \frac{\mathrm{VAR}(Q_b)}{\bar{Q}^2} + \frac{\mathrm{VAR}(\bar{Q}_b)}{\bar{Q}^2}. \tag{4.76}$$

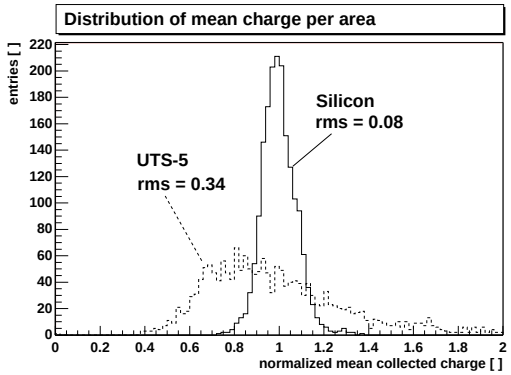

Figure 4.63: Distribution of mean charge signal in silicon and diamond (UTS-5) taken from a signal map with bin size of 100 μm $\times$ 100 μm and about 46 events per bin.

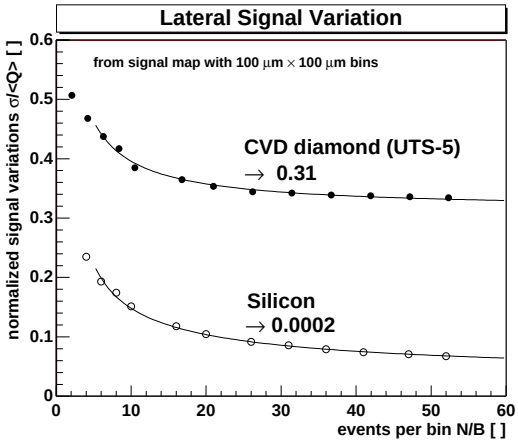

Figure 4.64: Normalized variation, $\hat{\sigma}_{\mathrm{m}}$, of mean signals from silicon and diamond (UTS-5) as a function of the mean number of entries in bins. The bin size is 100 μm $\times$ 100 μm. The points are measurements, the solid line is a fit from the model [Eq. 4.76].

The term containing statistical variations decreases asymptotically as $1/\bar{n}$, since for any quantity X with $\mathrm{VAR}(X) < \infty$ its mean $\bar{X}$ is asymptotically Gaussian distributed such that in n measurements $\mathrm{VAR}(\bar{X}) = \mathrm{VAR}(X)/n$ [97]. No information about the actual distribution of Q_b in a bin is necessary for Eq. 4.76 to hold. The systematic variation does not decrease as $1/\bar{n}$ and is independent of the number of entries per bin.

A measurement of the normalized variation as a function of the mean number of entries per bin is shown in Fig. 4.64. The variation in diamond and silicon decrease as expected asymptotically with increasing number of entries per bin. At entries $\bar{n} \geq 5$ the measured variation is well approximated by Eq. 4.76 which is shown as a fit to the data. At the given scale of 100 μm $\times$ 100 μm the value for infinite number of entries per bin is 0.31 in diamond and close to zero in silicon. The value for infinite number of entries was found from the fit to the data. We associate in the fit the asymptotic value with the systematic variation. The systematic variation allows one to define the *signal uniformity of the detector*

$$\mu \stackrel{\mathrm{def}}{=} 1 - \frac{1}{\bar{Q}} \cdot \sqrt{\mathrm{VAR}(\bar{Q}_b)} \stackrel{\mathrm{Eq.\,4.76}}{=} \lim_{\bar{n}\to\infty} (1 - \hat{\sigma}_{\mathrm{m}}). \tag{4.77}$$

where μ takes values between 0 to 1 or 0 % to 100 %. On the chosen scale of 100 μm $\times$ 100 μm the uniformity of silicon is close to 100 % and the uniformity of the diamond UTS-5 is $\approx$69 %.

4.4.4 The Scale of Uniformity

In Sec. 4.3.5 CDS-55 was analysed in the beam. Two different regions of 19 mm^2 and 1 cm apart were studied. On a macroscopic length scale CDS-55 appeared to be uniform. The previous analysis on uniformity of UTS-5 was performed with a bin size of 100×100 μm^2 and 25×25 μm^2. It is of interest to investigate the uniformity (that means the systematic term of signal variations) as a function of the length scale.

It was observed that the mean signal variations change with the bin size chosen. This means that the uniformity is a function of a length scale. This observation was verified by measuring the uniformity using relatively large bin size. Fig. 4.65 shows the mean signal map with bins of 500×500 μm^2. The upper limit of the ADC range was chosen to satisfy Eq. 4.75.

UTS-5 appears more uniform than on the signal maps shown previously. It can also be seen that the mean charge is on average bigger on the left side ($v_t \leq 1000$ μm) of the detector than on the right side. The reason for this observation is the strip width which is narrower on the right side than on the left side. The strip width of UTS-5 used here was described in Sec. 4.2.9. On the larger bin scale shown in Fig. 4.65 it is important to remember that the strip width changes along the direction of the strips. In order to exclude the effect of the variable strip width one should either restrict oneself to consider the left or the right side separately or perform tests with continuous strips.

The length scale chosen here is $\sqrt{\delta_u \cdot \delta_v}$. The uniformity was studied as a function of $\sqrt{\delta_u \cdot \delta_v}$ by measuring $\hat{\sigma}_{\rm m}$ either at constant $\bar{n}$ which means a constant offset to the measured mean signal variation (Eq. 4.76) or at any $\bar{n}$ which then requires correction for the statistical variations. The uniformity, μ, for any $\bar{n}$ is obtained from Eq. 4.76

$$\mu = 1 - \sqrt{\hat{\sigma}_{\rm m}^2 - \frac{\hat{s}^2}{\bar{n}}} \tag{4.78}$$

where $\hat{s}^2 = {\rm VAR}(Q_b)/\bar{Q}^2$ was obtained from the fit to the data in Fig. 4.64.

Fig. 4.66 shows a measurement of the uniformity according to Eq. 4.78 as a function of the length scale, $\sqrt{\delta_u \cdot \delta_v}$. At the 100 μm scale the uniformity is 69 % as shown in the previous section. The uniformity decreases to 61 % at a length scale of 23 μm. It can be seen that on a scale of 1 mm the method used here gives a uniformity of 90 %. This underestimates the actual uniformity since the strip width varies along the direction of the strips. From Fig. 4.65 it can be seen that the uniformity is close to 100 % at a length scale of 500 μm in regions with the same strip width. Generally it is found that the uniformity decreases with decreasing length scale.

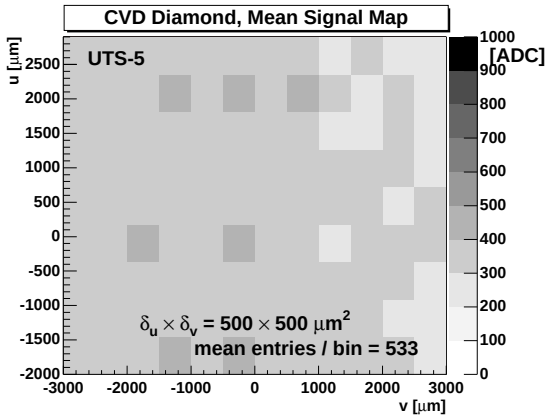

Figure 4.65: Mean collected charge in diamond detector UTS-5 as a function of the position of the particle track in the beam. The mean signal is measured in bins of 500 μm $\times$ 500 μm.

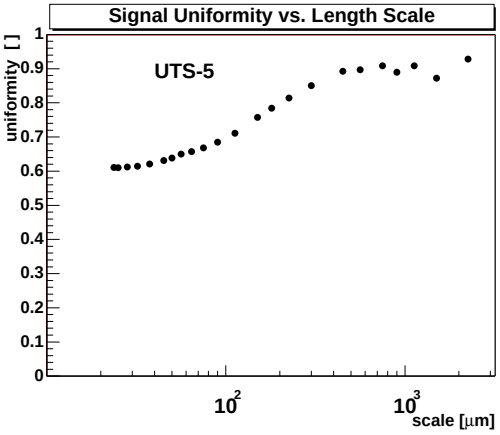

Figure 4.66: Uniformity in diamond (UTS-5) as a function of the length scale $\sqrt{\delta_u \cdot \delta_v}$.

4.4.5 Summary on Uniformity

A signal map was measured from a CVD diamond sensor in a pion beam. The map shows regions of higher and lower signal response. Signal fluctuations (variations) laterally across the sample were observed. The variations have a statistical term and a systematic

term. The statistical term was found to decrease with the number of entries per bin. The signal variations due to statistical fluctuations was calculated and then subtracted from the measured fluctuations. The remaining systematic term is due to systematic variations of properties in the sensor. The term *signal uniformity* was defined in order to quantify the systematic variations: the signal uniformity is one minus the normalized variation of the mean signal charge for on average infinite number of entries per bin.

It was found that the uniformity depends on the lateral scale (the binning). The uniformity in the first diamond measured was between 60 % and 80 % on the length scale from 23 μm to 200 μm. The uniformity was between 80 % and 100 % on the length scale above 200 μm. For comparison silicon detectors had a signal uniformity of 100 % at 2 mm length scale. Regions with higher and lower mean signal have individual signal distributions which are Landau-like distributed. The mean-to-most probable value of distributions from individual regions was on average 1.19 ± 0.15. This ratio comes close to what is seen in silicon detectors. Charge signal distributions measured on a macroscopic scale (several millimeters) are convolutions of signal distributions from microscopic regions (below several 100 μm) with shifted mean values. The convolution could account for the wider signal distribution observed on macroscopic diamond detector regions. Regions with smallest mean signal show signal distributions which are still separated from zero.

The signal variations may be due to grain boundaries or lattice orientations in grains. The grain size on the growth side reaches up to 300 μm as observed visually from diamonds of similar growth. Contamination of the diamond surface or in the bulk may also cause signal variation. The uniformity should be measured on other CVD diamond samples and eventually on samples from different manufacturers in order to find out whether systematic variations are specific to certain growths or a general property of CVD diamonds.

4.5 Diamond Sensor with Analogue SCT/DMILL Readout

Diamond sensors with good results on VA2 electronics were tested with fast front end electronics (SCT/DMILL) in the beam. The SCT/DMILL chips were manufactured in a radiation hard DMILL technology. Each amplifier has a bipolar input transistor followed by a shaper with 25 ns signal peaking time. The charge signals of diamond strip detectors with SCT readout and their spatial resolution have been measured in pion beams and results are shown in this section.

4.5.1 Introduction to the Analogue SCT/DMILL Readout

The high radiation level in the inner regions of LHC detectors requires radiation hardened electronics. Research on radiation hard electronics was performed in the RD29 collaboration. Its goal was to develop and industrialize Durci Mixte sur Isolant Logico-Lineaire (DMILL), a new radiation hard analogue-digital technology especially designed to meet the High Energy Physics requirements [111]. DMILL uses a silicon on insulator (SOI) substrate and integrates monolithically [7] radiation hard anolog-digital CMOS, JFET and bipolar transistors. In 1993 a first multi-project wafer run was organized to allow the development of prototype circuits [112, 113]. In 1997 the Matra MHS company transfered the DMILL technology to its 6" silicon foundry. Prototype chips for the analogue readout of silicon strip detectors in the ATLAS semiconductor tracker (SCT) have been designed and manufactured, in 32 channel and 128 channel versions using the radiation hard BiCMOS DMILL process [114]. Combined neutron and gamma irradiation tests have been performed for the manufactured bipolar devices which show acceptable values of the current gain, β, of bipolar transistors after 10^{14} n/cm^2 and 12 Mrad of ionizing radiation [115].

Fig. 4.67 shows a block diagram of the analogue SCT chip. This diagram shows the components which are of importance for the description here. A more detailed diagram can be found in reference [116]. The front-end circuit contains a fast transimpedance amplifier with a bipolar *npn*-transistor at the input. It is followed by an integrator, providing a semi-Gaussian shaping with a peaking time of ≈25 ns. The shaped signal peak values are sampled at 40 MHz rate and stored in the analogue pipeline. The pipeline is a chain of capacitors which store signal charges from successive samplings. The depth of the pipeline is 128 cells for the SCTA128 and 112 cells at the SCTA32. This means that a signal is available in the pipeline for 128/(40 MHz) = 3.2 μs. The pipeline is an analogue delay buffer (ADB). Upon arrival of the trigger the voltage from a cell in the ADB is sampled in the sample and hold buffer and sent out through the analogue multiplexer (MUX). The multiplexer sends the analogue sequence of signals from all channels with 40 MHz into the output buffer. Fig. 4.68 shows a simulated readout sequence from the multiplexer. It is important to notice the header and trailer sequence with the channel data in between. The header was used here to recognize the correct start of the data sequence and effectively allowed one to correct jitters between the MUX clock and the recording sampling clock.

Analogue SCT chips are under development and are available as 32 channel (SCTA32) and 128 channel (SCTA128) versions. The SCTA128 exists in a high capacitance version (SCTA128HC), optimized for 15 pF to 20 pF, and a low capacitance version (SCTA128LC), optimized for 2 pF to 5 pF. The LC version is a very attractive readout for diamond sensors but was not available for the beam tests reported here.

[7] monolithic [*greek*: *mónos* = single, *líthos* = stone]: small electronic components on a single device substrate.

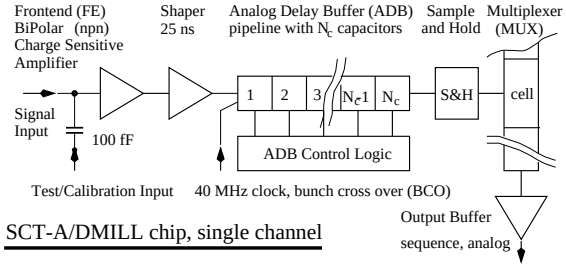

Figure 4.67: Block diagram of one channel of the analogue SCTA/DMILL chip.

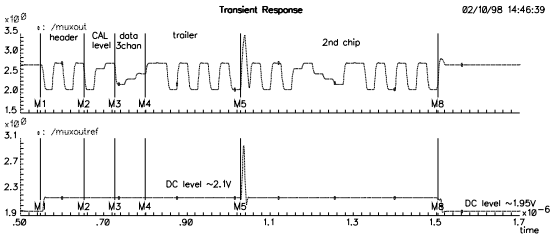

Figure 4.68: Readout sequence from the multiplexer of the SCTA128HC/LC chip [117].

4.5.2 Signal Formation in the BJT Transresistance Amplifier

The principle of charge control in a bipolar transistor is illustrated on an idealized *npn* structure in Fig. 4.69. The emitter is an n doped implant in an n doped bulk. The bulk is the collector. The base is a thin p doped implant that separates the emitter from the collector. The base-emitter is a *pn*-junction and electrons have to pass the potential energy barrier $eU_{\rm BE}$. In a normal operating condition the collector-base junction is reversed biased and the emitter-base junction is forward biased. At the temperature, T, and base-emitter voltage, $U_{\rm BE}$, the Boltzmann distribution of electron energies determines the *current across the junction (channel current)* [118]

$$I_{\rm c} = I_{\rm c0}\, e^{+eU_{\rm BE}/k_{\rm B}T} \tag{4.79}$$

where $I_{\rm c0}$ is the thermally generated current. Electrons which are injected from the emitter into the base diffuse across the base and are swept away by the field between the base and the positively biased collector. In the equilibrium state (without any charge signal from the detector) the *trans-conductance* is obtained from Eq. 4.79

$$g_{\rm m} \stackrel{\rm def}{=} \frac{{\rm d}I_{\rm c}}{{\rm d}U_{\rm BE}} \stackrel{\text{Eq. 4.79}}{=} \frac{I_{\rm c}e}{k_{\rm B}T} \stackrel{\text{see text}}{=} \frac{I_{\rm c}}{25\ {\rm mV}}. \tag{4.80}$$

The last equation is true at room temperature where $k_{\rm B}T = (1/40)\ eV$. The base is normally connected to a collecting electrode of the detector. After the passage of a charged particle, the signal charge, $Q_{\rm ind}$, injects the *signal current into the base*

$$i_{\rm ind}(t) = Q_{\rm ind}\, \delta(t) \tag{4.81}$$

which is amplified with the DC current gain, β, of the input transistor.

Fig. 4.70 shows the schematic diagram of the input transistor of a channel in the SCT/DMILL chip [114]. The *npn* transistor, T1, is connected as a common-emitter amplifier: the emitter potential is the common reference potential for both, the detector at the base input and the output which leads to the shaper. An electrode from a detector was directly coupled to the 'CHARGE in' connection at the basis of the transistor. The signal charge is collected on the feedback capacitor $C_{\rm fp} \approx 30$ fF. The capacitor and the resistors, R, form are a feedback loop from the signal output at the emitter of T2 back to the base of T1. The chain of feedback resistors has 80 kΩ in the SCTA128HC. The capacitor discharges theoretically in 6 ns to the fraction $1/e$. In practice this time is about 20 ns due to additional stray capacitances. The voltage output signal, $u_{\rm out}$, appears at the emitter of T2 in order to be feed into the signal shaper (which is not shown). The circuit is called a trans-resistance amplifier since it amplifies the signal input current, $i_{\rm ind}$, and converts to the output voltage, $u_{\rm out}$. The ratio $u_{\rm out}/i_{\rm ind}$ is called the trans-resistance since it has the units of a resistance.

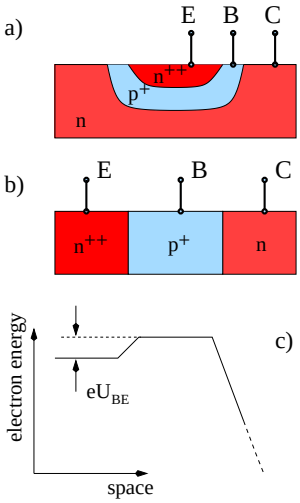

Figure 4.69: Schematic of a bipolar transistor: a) cross section of a typical *npn* bipolar transistor with doped regions for the emitter, E, base, B, and the collector, C. b) Idealized transistor, c) relative potential electron energy (energy band) under normal operating conditions (forward biased emitter-base junction and reversed biased collector-base junction). The potential difference for electrons from the emitter to the base is eU_{BE} [119].

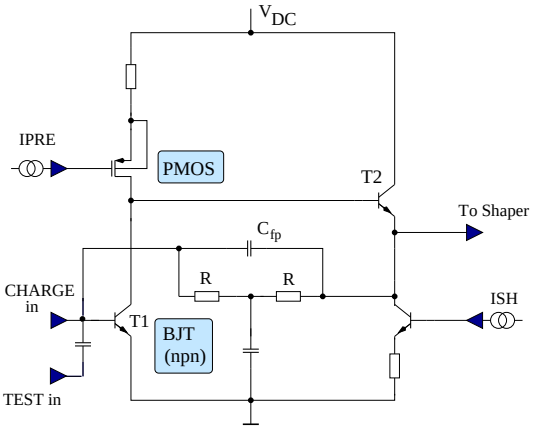

Figure 4.70: Schematic diagram of the front of the front-end circuit in each amplifier channel of the SCTA128HC chip [114].

4.5.3 Noise in the BJT Transresistance Amplifier

The *equivalent noise charge*, $\sqrt{\langle q^2_{\mathrm{total}}\rangle}$, in a charge sensitive detector with bipolar junction transistor is given by [119, 114]

$$\begin{aligned}\langle q^2_{\mathrm{total}}\rangle &= \frac{1}{2}\cdot 4\,k_{\mathrm{B}}T\left(r_{\mathrm{bb'}}+\frac{1}{2\,g_{\mathrm{m}}}\right)(C_{\mathrm{a}}+C_{\mathrm{D}})^2\,A_{\mathrm{series}}\\ &+ \frac{1}{2}\cdot\left(\frac{2\,e\,I_{\mathrm{c}}}{\beta}+2\,e\,I_{\mathrm{D}}+\frac{4k_{\mathrm{B}}T}{R_{\mathrm{B}}}+\frac{4k_{\mathrm{B}}T}{R_{\mathrm{F}}}\right)A_{\mathrm{parallel}}.\end{aligned} \tag{4.82}$$

The first term is the *series noise* and contains the thermal noise in the base spreading resistance, $r_{\mathrm{bb'}}$, between the base contact and the active region of the base and the shot noise from the collector current, I_{c}, because carriers are randomly injected from the emitter into the base. The constants are the electron charge, $e = 1.602\times10^{-19}$ C, and at room temperature the factor $k_{\mathrm{B}}T = (1/40)$ eV. The series noise is linear in the sum of capacitances which are the detector capacitance, C_{D}, and the amplifier input capacitance, C_{a}. The second term is the *parallel noise* and contains the shot noise due to the base current, I_{c}/β, the shot noise from the detector leakage current, I_{D}, and the thermal noise from the feedback resistor, R_{F}, and the detector biasing resistor, R_{B}. The factors, A_{series} and A_{parallel}, depend on the signal shape at the output of the shaper. They can be calculated by integrations in the time or frequency domain as described in [79, 119]. The calculation for the 'cusp' signal shape, $e^{-|t|/\tau_{\mathrm{P}}}$, gives $A_{\mathrm{series}} = 1/\tau_p$ and $A_{\mathrm{parallel}} = \tau_{\mathrm{p}}$ where τ_{p} is the signal peaking time. Hence, the series noise decreases with increasing signal peaking time whereas the parallel noise increases. Eq. 4.82 also shows that the noise decreases with increasing detector biasing and feedback resistor. The factors for the series and the parallel noise in Eq. 4.82 are given by the transfer function, $h(t)$, of the shaper in the time domain [119]

$$A_{\text{series}} = \int_{-\infty}^{+\infty} \left(\frac{\mathrm{d}h(t)}{\mathrm{d}t} \right)^2 \mathrm{d}t \tag{4.83}$$

and the factor for the parallel noise

$$A_{\text{parallel}} = \int_{-\infty}^{+\infty} h^2(t)\mathrm{d}t. \tag{4.84}$$

The integrals can be calculated analytically for semi Gaussian signals as described in [79] in the time or frequency domain or numerically by integration of the measured signal pulseshape.

4.5.4 Experimental Method

Three sensors were studied in the beam: a silicon pad detector, a CVD diamond sensor CDS-40 (alias D39) with SCTA32 readout and the CVD diamond sensor UTS-5 with SCTA128HC readout. The detectors were prepared for testing in the 100 GeV/c pion beam as described in Sec. 4.2.3. The measurement setup with the beam telescope and data acquisition were described in Sec. 4.1. The tracking analysis was done similar to the analysis used for VA2 readout.

During the experiment, the charge signal from the shaper was continuously clocked with a frequency of 40 MHz into the ADB. The signal readout from the chips was triggered by a beam particle using a scintillator. The beam trigger was asynchronous with the 40 MHz clock. The time between the trigger and the clock phase was recorded using a timer (LeCroy model 1176, 16 bit VME multi-hit TDC with 1 ns time resolution [81]). The time was recorded on tape, together with the charge signal data from the strips. The TDC time information was used in the analysis to select signals which were sampled at the maximum of the shaped signal.

4.5.5 Results: Noise in the SCTA128HC Frontend

Noise measurements were performed on the SCTA128HC using channels with open inputs and channels which were bonded first to silicon pads and later to the diamond strip detector UTS-5. The measurements were performed in the beam setup to ensure the same gain as for the signal measurements.

Fig. 4.71 shows the measurement of the equivalence noise charge from the SCTA128HC as a function of the collector bias current, I_{c}. It can be seen that the equivalent noise charge on open channels is (580±50) e at $I_{\text{c}} = 50\ \mu$A and increases to (700±50) e at $I_{\text{c}} = 250\ \mu$A. The increase with collector bias current is mainly due to the increase in base current, $I_{\text{b}} = I_{\text{c}}/\beta$, were β is the current gain of the bipolar input transistor. The noise on channels which were bonded to silicon pads is higher than on open channels. The noise on the silicon pads can be understood from the geometry and size of the pads. The silicon pad detector had a thickness of 300 μm and pads with a size of 1×1 mm^2. The pads were surrounded by neighbour pads which were at virtual ground potential via the amplifier inputs and hence had a defined pad capacitance. For the noise measurement the pads were fully depleted with a biasing voltage of 150 V. The capacitance of a single pad seen by the amplifier was about 2.0 pF calculated from the sum of the pad-to-backplane capacitance of 0.36 pF and about 1.5 pF of the pad-to-neighbour capacitance. The measured equivalent noise charge was (740 ± 50) e at $I_{\text{c}} = 50\ \mu$A and increased to (900 ± 50) e at $I_{\text{c}} = 250\ \mu$A. The reason for higher noise on bonded channels is mainly due to the detector capacitance which is an additional load capacitance at the input amplifier in addition to the 'open' amplifier capacitance. The detector leakage current and

the feedback resistor contribute to the noise as well. The noise increase with silicon pads is about 110 e independent of the collector bias current. The noise in the diamond strip detector (UTS-5) at a collector bias current of 100 μA was (620 ± 50) e in the same setup using the gain factor obtained from the measurement on silicon. The noise on diamond was slightly smaller than the noise with the silicon pads.

Fig 4.72 shows a measurement of the signal gain as a function of the preamplifier bias current. The measurement was performed using the silicon pad detector in the beam. The gain was obtained under the following assumptions: the pad detector was fully depleted at the bias voltage of 150 V. All created charges were collected within the signal peaking time of 25 ns. The most probable charge collected from a pion in the beam was taken to be 22500 e. Then the gain is the most probable collected charge in ADC units per most probable number of electrons. The measurement in the beam showed an increase of the charge signal with increasing collector bias current. Since the collected charge at the input of the pre-amplifier is the same for all collector current settings one infers that the gain increases with collector current. The increase of the gain can be seen in Fig. 4.72. The gain was used to convert the measured noise from ADC units to electron units.

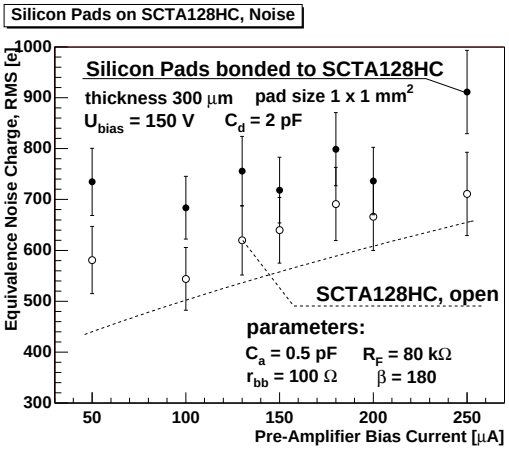

Figure 4.71: Equivalent noise charge in rms ADC as a function of the collector bias current in the input transistor measured from single channels of the SCTA128HC with and without detector. The dashed line is from calculating Eq. 4.82 using the parameters given.

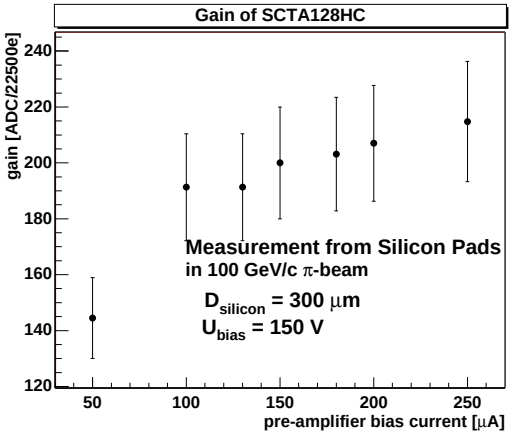

Figure 4.72: Measurement of the gain from SCTA128HC as a function of the collector bias current in the pre-amplifier.

The equivalence noise charge was calculated using Eq. 4.82. Fig. 4.71 shows the result of the calculation for open channels of the SCTA128HC. For the noise calculation the parameters shown in the figure were used: the SCTA128HC has a feedback resistor of $R_{\mathrm{F}} = 80$ kΩ as can be seen from the design layout [117], the value $\beta = 180$ is slightly higher than given in [114] but correct for this chip, the amplifier capacitance, $C_{\mathrm{a}} = 0.5$ pF, and the base spreading resistance, $r_{\mathrm{bb'}} = 100\ \Omega$, are the usual values for this design. Using Eq. 4.82 the calculated noise is 100 e lower than the noise measured. The difference between the calculated and the measured noise may be due to deviations from the assumed parameters used for the calculation (listed in Fig. 4.71) or missing noise contributions. It may be that the ADB contributes to noise which is not considered in the calculation.

4.5.6 Results: Silicon Pad Detector with SCTA128HC

Fig. 4.73 shows the mean single pad charge measured in the silicon pads as a function of the TDC value. A single pad hit cluster charge contains the charge from the seed pad where the seed is the pad with the largest signal charge. The number of events with charge sharing to to neighbour pads is negligibly small in this geometry. The measurement is shown for the time interval from 0 ns to 75 ns corresponding to 3 cells of the ADB. It can be seen that the mean signal increases steeply at 0 ns, peaks at about 25 ns and decreases again. The measurement illustrates the semi-Gaussian shape of the signal as it is produced after the shaping amplifier. Superimposed on the measured charge signal are semi-Gaussian functions [79]

$$h(t) = \frac{qA^n n^n}{C_{\mathrm{fp}} n!} \left(\frac{t}{\tau_{\mathrm{p}}} \right)^n e^{-nt/\tau_{\mathrm{p}}} \tag{4.85}$$

where C_{fp} is the feedback capacitance, A the DC gain of the charge integrator and τ_{p} the peaking time of the shaper. The semi-Gaussian fits have the orders $n = 1$, $n = 2$ and $n = 3$. The shaping time is a free parameter in the fit. The measurement is well described by the semi-Gaussian function of third order and 24 ns signal peaking time. The first order fit yields a signal peaking time of 22 ns. The signal shape in Eq. 4.85 allows one to determine the factors A_{series} and A_{parallel} by integration over the squared semi-Gaussian and squared deviation of the semi-Gaussian charge signal as described by Eq. 4.83 and Eq. 4.84. The numerical integration of the pulse shape gives $A_{\mathrm{series}} = 1/(32\ \mathrm{ns})$ and $A_{\mathrm{parallel}} = 34$ ns. Both factors were then used in Eq. 4.82 to calculate the equivalent noise charge as shown in Fig. 4.71 (dashed line).

Fig. 4.74 shows the single pad signal charge distribution measured on the silicon pad detector. The preamplifier current for the measurement shown was $I_{\mathrm{c}} = 150\ \mu$A. The distribution contains only events with TDC values in the time interval from 16 ns to 28 ns which is around the peak of the semi-Gaussian signal shape. The charge signal is Landau distributed. The most probable signal is 199 ADC, the mean signal is 256 ADC. Using the measured equivalent noise charge of 5.6 ADC one obtains a most probable signal to noise of 35-to-1 and a mean signal to noise of 46-to-1.

4.5.7 Results: Diamond Strip Detector with SCTA32

The 32 channel version of the SCTA/DMILL chip was available earlier than the 128 channel versions. The diamond strip detector D39 was tested as one of the first diamond detectors on this chip (results from the very first test with another diamond were reported in [4] and later in [3]). Fig. 4.75 shows the measured signal charge distribution from D39 with SCTA32 readout in the pion beam. The signal charge is the sum from 3-strips. The signal charge distribution from the cluster analysis is overlayed to the charge signal distribution from the transparent analysis. A cut on TDC values which are around the peak of the shaped signal is applied in both distributions. The mean and most probable values of the transparent signal distribution are 36 ADC and 26 ADC at a single strip noise of 6.2 ADC. Therefore the mean and most probable signal-to-noise ratios are 6-to-1 and 4.2-to-1. The ratio between mean and most probable is about 1.4 which is similar to the ratio measured with a source but smaller than the value of 1.7 measured using VA readout on this diamond in the beam. The transparent signal overlaps with 0 ADC due to noise broadening. The noise of about $(800 \pm 100)\ e$ was measured in the lab and assigns a mean charge signal of about $(5000 \pm 625)\ e$ to this diamond. In the cluster analysis a signal-to-noise threshold cut

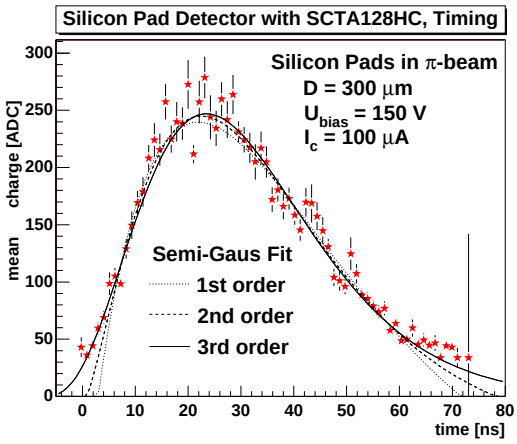

Figure 4.73: Mean signal from single pads in the silicon pad detector with SCT128HC readout as a function of the time between trigger and pipeline clock phase. The measurement is fitted with the semi-Gaussian function Eq.4.85 for the orders $n = 1$, $n = 2$ and $n = 3$.

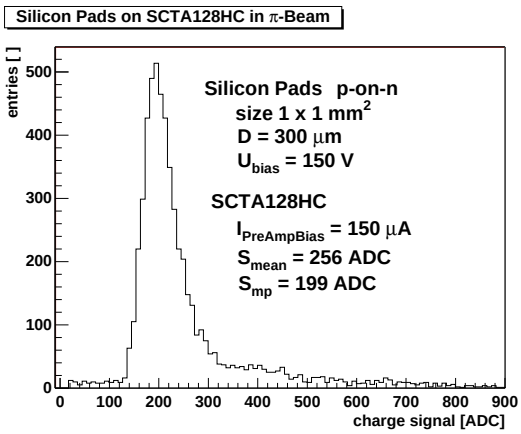

Figure 4.74: Signal distribution from single pads of the silicon detector with SCT128HC readout. The charge signals are taken from the seed pad. The mean value is calculated for charge signals bigger then 100 ADC.

of 3-to-1 was applied on the seed strip which explains less events around 0 ADC. However, the noise on neighbour strips in the cluster is sufficiently high to broaden the distribution at the rising edge with entries at around 0 ADC.

Fig. 4.76 shows the distribution of the residuals. The distribution is centered at 0 μm with normal distributed residuals and a standard deviation of 22.5 μm as obtained from a Gaussian fit to the residual distribution. The distribution shows many entries at high and low residuals which are caused by false estimations of hit positions due to relatively high noise on strips in hit clusters.

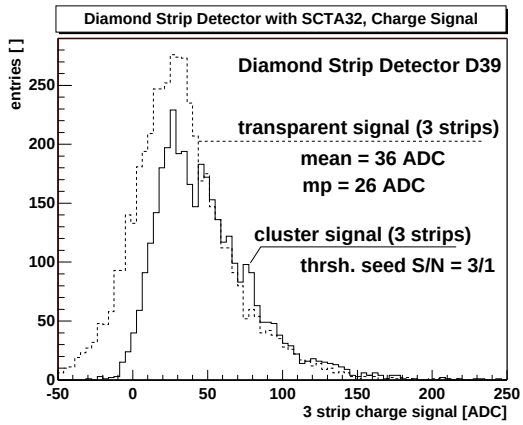

Figure 4.75: Distribution of the charge signals from 3 strips measured on the diamond strip detector D39 with SCTA32/DMILL readout. Both distributions from a transparent analysis and a cluster analysis are shown.

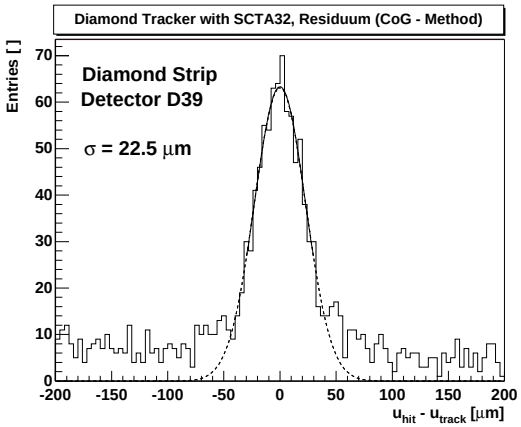

Figure 4.76: Distribution of the residuals measured on D39 with SCTA32/DMILL readout.

This test with analogue SCT/DMILL readout electronics, which was originally designed for silicon detectors, was encouraging to continue tests with further SCT readout.

4.5.8 Results: Diamond Strip Detector with SCTA128HC

The diamond strip sensor UTS-5 was tested using the 128 channel high capacitance (HC) version of the SCT/DMILL chip. This diamond was studied previously with VA electronics in the beam and with a source [Sec. 4.2]. UTS-5 was bonded to exactly the same SCTA128HC readout chip which was used in Sec. 4.5.6 for the measurement with the silicon pad detector. The chip was operated at the same pre-amplifier current as for silicon and the gain on UTS-5 is assumed to be equal to the gain in the silicon pad detector. The collector current was 100 μA. UTS-5 was operated at 1 V/μm.

Fig. 4.77 shows the 3-strip transparent signal as a function of time from the TDC in an interval from 0 ns to 100 ns. The same semi-Gaussian shape is observed as on the silicon pad detector as can be seen from the FWHM of ≈37 ns. The signal peaking time of 25 ns and the recommended time cut on the interval from 40 ns to 50 ns can be read from this figure. The corresponding signal distribution from the transparent and cluster analysis are shown in Fig. 4.78. The mean and most probable values of the transparent signal distribution are 50 ADC and 36 ADC at a single strip noise of 5.0 ADC. The mean and most probable signal-to-noise ratios are therefor 10-to-1 and 7.2-to-1. The ratio between mean and most probable is about 1.4 and agrees with the ratio obtained with a source on this sample, but is narrower than the VA measurement in the beam. Using the gain measurement [Fig. 4.72] one obtains a mean signal of 6000 e which is 30 % less than what is observed on this diamond in VA measurements in the lab or in the beam. The cluster signal starts out separated from 0 ADC due to the seed signal-to-noise threshold cut of 5-to-1.

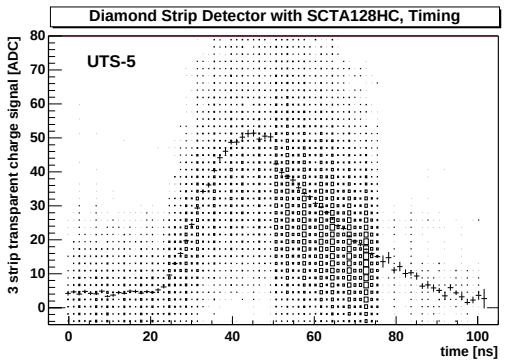

Figure 4.77: Transparent signal from 3 strips of the diamond detector UTS-5 with SCTA128HC readout as a function of the TDC time between trigger and pipeline clock phase. The mean values at each time bin are superimposed with crosses.

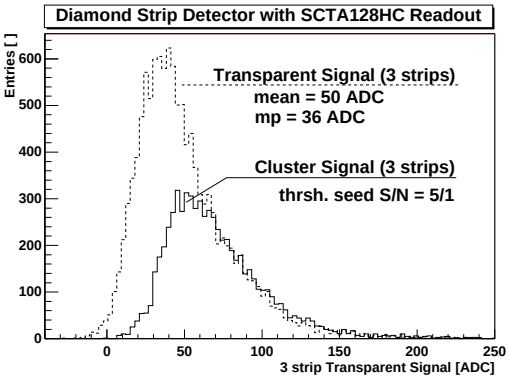

Figure 4.78: Charge signal distribution from the diamond strip detector (UTS-5) with DMILL/SCTA128HC readout electronics. The charge signals are the sum from 3 strips.

Fig 4.79 shows the distribution of the residuals. The distribution peaks at 0 μm and the Gaussian fit gives the spatial resolution of 16.5 μm. The tails of the distribution show a negligible amount of noise hits.

4.5.9 Summary and Discussion

Two diamond strip sensors and one silicon pad detector have been tested in the beam with fast, analogue SCT/DMILL readout electronics. Table 4.6 summarizes the beam results in terms of equivalent noise charge on a single strip, the most probable signal to noise ratio and the mean signal to noise ratio at the given parameters for the pre-amplifier bias current

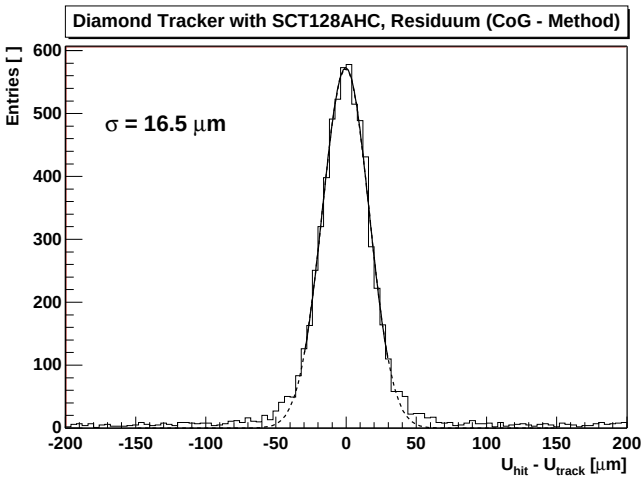

Figure 4.79: Residual distribution from the diamond strip detector UTS-5 with DMILL/SCTA128HC readout electronics. The K-strip center of gravity method was used for hit finding. The measured residual distribution is fitted by a Gaussian function (solid line) with a standard deviation of $\sigma = 16.5$ μm.

and the bias voltage of the detector. The most probable signal-to-noise of the diamond UTS-5 on SCTA128HC electronics was 7.2-to-1, its mean signal-to-noise was 10-to-1. The mean signal obtained from D39 and UTS-5 on SCTA32 and SCTA128HC electronics was lower than the mean signal obtained with the same sensors on VA2 electronics. The difference was between 20 % to 30 %. This observation requires confirmation in future beam tests.

device	SCT	I_c [μA]	ENC [e]	S_{mp}/N	S_{mean}/N	detector bias
Si-pads	128HC	100	680 ± 50	35	46	150 V
UTS-5	128HC	100	620 ± 50	7.2	10	1 V/μm
D39	32	22	800 ± 50	4.2	6	1 V/μm

Table 4.6: Summary on signal to noise ratios using SCT/DMILL readout in the beam.

Using the center of gravity method for hit position finding the spatial resolution was similar to the digital resolution for a 50 μm pitch strip detector. Improvements in signal-to-noise ratio and spatial resolution were seen in the SCTA128HC compared to SCTA32 readout, eventually due to a higher quality diamond. Further improvements in signal-to-noise may be expected using the low capacitance readout, SCTA128LC, and diamonds sensors with higher signal charge.

Chapter 5

Irradiations

The inherent properties of diamond indicate that it may be a radiation resistant sensor material. CVD diamond samples were irradiated above LHC particle fluences in order to study their radiation resistance. Fig. 5.1 shows the sample stand at the ISIS neutron irradiation facility a few minutes before several CVD diamonds were inserted for a 1 month long irradiation with neutrons.

Figure 5.1: Photograph of the neutron irradiation stand. The diamonds are in boxes at the base of the stand. The picture was taken during installation of the 11/97 irradiation at ISIS at the Rutherford Appleton Laboratory (RAL).

Contents

5.1 Introduction to Radiation Damage

Radiation hardness is required for particle detectors in future particle physics experiments at the LHC/CERN or Tevatron/FNAL. In particular solid state tracking devices have to retain a minimum signal-to-noise ratio after receiving large fluences of damaging radiation. Solid state devices are damaged by particle irradiation. Damage in solid state detectors causes, on one hand, an increase in leakage current and therefore an increase in noise and, on the other hand, a reduction in the amount of collected charge, which leads to a smaller signal. The signal-to-noise ratio therefore decreases with damage. The inherent properties of diamond indicate that it may be a radiation resistant sensor material. Excessive radiation induces point defects in the sensor material. The point defect concentration is one factor which determines electrical properties of the sensor. Defect types in general and the mechanism of defect creation under irradiation are briefly described below.

5.1.1 Point Defects

Many important properties of diamond depend heavily upon the concentration of point defects. The thermal and electrical conductivities, the carrier mobilities, the color and luminescence and also radiation hardness are affected by point defects [120]. A point defect is a 'zero-dimensional' deviation from the periodicity of the crystal lattice. A point defect is typically localized within the cubic cell, but can cause the lattice to be under tension (stress) over several lattice sites. Fig. 5.2 illustrates point defects in diamond. The illustrated defects are foreign substitutional and foreign interstitial atoms, self interstitials and vacancies. Point defects introduce energy levels for charged carriers in the band gap. These energy levels can act as acceptors, donors or charge traps. Point defects affect the lifetime of charge carriers. The lifetime of the carrier is related to the concentration of defects, m, by [65]

$$\tau_{\mathrm{def}}^{(\mathrm{R})} = \frac{1}{v_{\mathrm{th}}\sigma_{\mathrm{m}}m} \tag{5.1}$$

where v_{th} is the thermal velocity of charge carriers as given by Eq. 3.24 and σ is the cross section of the point defect for affecting the charge carrier.

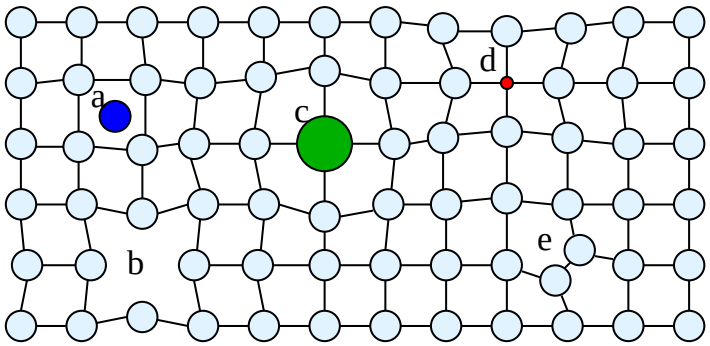

Figure 5.2: Schematic of point defects in the diamond lattice: a) foreign interstitial atom (*e.g.* H, Li), b) vacancy, c) and d) foreign substitutional atom (*e.g.* N,P,B), e) self interstitial [120].

5.1.2 Radiation Effects

Particle irradiation induces defects in solids which may alter the electrical characteristics of electrical devices and detectors. Radiation causes two types of effects: the first is ionization creating electron hole pairs. The pairs may separate by diffusion or due to an external electric field and migrate. They either leave the solid via contacts or get trapped in trapping centers. Trapping centers are often more abundant at surfaces or boundaries between surfaces. Ionization therefore causes *surface effects*. Effects due to ionization do not alter the crystal structure and are normally reversible.

The second type of effect, caused by irradiation, are *crystal defects* as illustrated in Fig. 5.3. Incident particles transfer energy to atoms in the lattice. An atom may get knocked from its lattice site, in the case of sufficient energy transfer from the incident particle. Such an atom is called a 'primary knock on atom' (PKA). The PKA leaves its lattice site (creating a *vacancy*), starts migrating in the lattice and may donate its kinetic energy to other lattice atoms which may cause secondary knock on atoms (SKA). The PKA eventually comes to rest at a free lattice site or at an *interstitial* lattice site. Vacancies or interstitials form *point defects* in the crystal. Point defects may recombine due to permanent migration (*beneficial annealing*). Secondary knock on atoms leave vacancies and form interstitials which then appear as *cluster defects*. It is possible that point defects 'catch' foreign atoms, that are always present by natural occurrence or intentional doping, hence causing *complex-defects*. The crystal defects occur in the bulk due to non-ionizing interaction of radiation in comparison to the surface effects caused by ionizing radiation. Crystal defects are often irreversible and remain as permanent radiation damage [121].

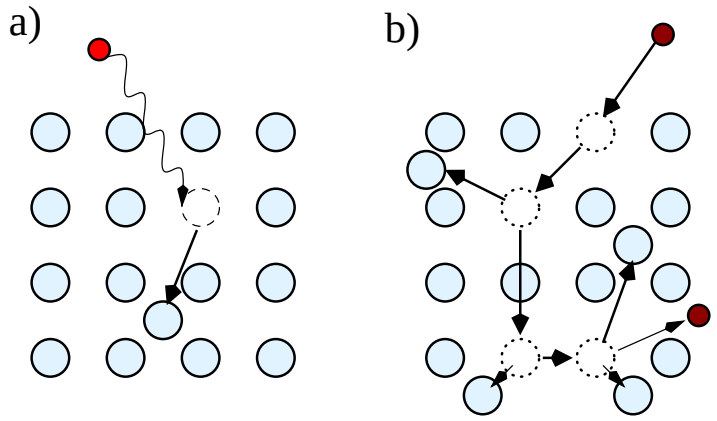

Figure 5.3: Model of atomic displacement: a) electromagnetic radiation (*e.g.* e, γ) knocks an atom from its lattice site and creates a vacancy-interstitial pair, b) a hadron (*e.g.* n, p, π) knocks an atom from its lattice site with creation of a cascade of secondary knock on atoms [122].

The concentration of point defects and cluster defects after irradiation depends on the energy spectrum of the radiation. The production rate of PKAs depends on the cross section for the interaction and the intensity of the incident radiation. The cross section is energy dependent. For example, irradiation of diamond with energetic particles (fast neutrons, deuterons, γ-rays and 1 MeV to 2 MeV electrons) can displace carbon atoms from their equilibrium lattice sites to interstitial positions, thus creating vacancies and interstitial atoms. When irradiated samples are annealed at high temperatures ($> 500\,^{\circ}\mathrm{C}$) vacancies can become mobile and can be trapped at other defects which create optical centers. The theoretical estimate for the formation of a vacancy-interstitial pair in diamond is ≈ 35 eV [120]. It

has been measured that the threshold energy for the production of defects in diamond by irradiation is between 37 eV to 47 eV [120].

After irradiation with a particle fluence, F, the *concentration of radiation induced point defects* is

$$m \propto F. \tag{5.2}$$

With the creation of point defects by irradiation additional mechanisms for carrier destruction are introduced which limit the carrier lifetime. The various independent mechanisms can be combined and described by a single lifetime, $\tau^{(\mathrm{R})}$, given by the 'Matthiessen-like' sum-rule [35, 36] as explained in Sec. 3.1.

Eq. 5.1 relates the concentration of point defects to the carrier lifetime. If the carrier had an initial lifetime, $\tau_0^{(\mathrm{R})}$, before irradiation one obtains from Eq. 3.36 a dependence of the lifetime on the fluence

$$\frac{1}{\tau^{(\mathrm{R})}} \overset{\text{Eq. 3.36}}{=} \frac{1}{\tau_0^{(\mathrm{R})}} + \frac{1}{\tau_{\mathrm{def}}^{(\mathrm{R})}} \overset{\text{Eq. 5.1}}{=} \frac{1}{\tau_0^{(\mathrm{R})}} + \kappa F \tag{5.3}$$

where the last term contains the *carrier lifetime damage constant*, κ [123, 65]. The carrier lifetime decreases like $(\kappa F)^{-1}$ for large fluence. Eq. 5.3 can be solved for $\tau^{(\mathrm{R})}$ and using Eq. 3.44 one obtains the carrier drift length as a function of the fluence

$$s(F) = \mu\tau^{(\mathrm{R})}|\vec{E}| = \frac{\mu\tau_0^{(\mathrm{R})}|\vec{E}|}{1 + \tau_0^{(\mathrm{R})}\kappa F}. \tag{5.4}$$

Hence the bulk averaged carrier drift length [Eq. 3.48] is

$$\bar{s}(F) = \begin{cases} \mu\bar{\tau}_0^{(\mathrm{R})}|\vec{E}| & : \quad \tau_0^{(\mathrm{R})}\kappa F \ll 1 \\ \dfrac{\mu|\vec{E}|}{\kappa F} & : \quad \tau_0^{(\mathrm{R})}\kappa F > 1 \end{cases}. \tag{5.5}$$

Two cases are distinguished: the case of low fluence and the case of large fluence. A fluence, F_{t}, may be defined

$$F_{\mathrm{t}} \overset{\mathrm{def}}{=} \frac{1}{\kappa\tau_0^{(\mathrm{R})}}. \tag{5.6}$$

The fluence F_{t} specifies at which fluence the carrier drift length may undergo a transition from the carrier drift length, $s_0 = \mu\tau_0^{(\mathrm{R})}|\vec{E}|$, of the unirradiated state to the carrier drift length at large fluence. Eq. 5.6 indicates that the fluence where a transition may occur depends on the carrier lifetime before irradiation: F_{t} decreases for larger $\tau_0^{(\mathrm{R})}$.

It was shown in Sec. 3.3.6.4 that the charge collection distance can be identified with the carrier drift length if $s < D$ for all positions, z, along the drift path

$$s(z) = d(z) \qquad \text{if} \qquad s(z) < D \quad \forall z \in [0, D]. \tag{5.7}$$

Under the assumption that the carrier drift length is smaller than the thickness of the material one obtains for the charge collection distance

$$\frac{\bar{d}(F)}{\bar{d}_0} = \begin{cases} 1 & : \quad F \ll F_{\mathrm{t}} \\ \dfrac{1}{\bar{\tau}_0^{(\mathrm{R})}\kappa F} & : \quad F > F_{\mathrm{t}} \end{cases}. \tag{5.8}$$

It should be noted that $\tau_0^{(R)}$ may depend on the position, z, along the direction of growth. Hence $F_{\rm t}$ may depend on z as well. It is therefore useful to define

$$\bar{F}_{\rm t} \stackrel{\rm def}{=} \frac{1}{\kappa \bar{\tau}_0^{(\rm R)}} \tag{5.9}$$

which allows one to rewrite Eq. 5.8 as follows

$$\frac{\bar{d}(F)}{\bar{d}_0} = \begin{cases} 1 & : \quad F \ll \bar{F}_{\rm t} \\ \dfrac{\bar{F}_{\rm t}}{F} & : \quad F > \bar{F}_{\rm t} \end{cases} . \tag{5.10}$$

One infers that the charge collection distance decreases as $1/F$ for $F > \bar{F}_{\rm t}$.

5.2 Irradiation with Protons

The dominant source of radiation at LHC will be charged hadrons coming directly from proton-proton interactions. It is therefore necessary to study the ionizing and non-ionizing effects of charged particles. In June 1997 CVD diamond samples were irradiated with 24 GeV/c protons at the Proton Synchrotron (PS) at CERN in Switzerland up to a total fluence of 5×10^{15} p/cm^2. *Results of the first proton irradiation of CVD diamonds at TRIUMF were reported in reference [8, 124]. Results from the proton irradiation at CERN were reported in reference [124] and are presented in more detail here.*

5.2.1 Interaction of Protons with Matter

Protons are hadrons with an electric charge. They can interact electromagnetically with matter (Coulomb-interaction) and due to their hadronic character they also interact with matter via the strong interaction. The nuclear interaction cross section for 24 GeV/c protons with hadrons (either neutrons or protons) is $\approx$ 40 mb [9]. Carbon has 12 hadrons in its nucleus and therefore a higher cross section which is expected to be between 400 mb and 500 mb. For comparison, the inelastic cross section of neutrons above 5 MeV with carbon is $\approx$ 400 mb as can be seen from Fig. 5.17 which is the same order of magnitude as the estimated proton carbon cross section.

The rate of proton interactions in carbon can be calculated using Eq. 5.13 multiplied by $A = 12.011$ (nuclei per carbon atom). Under the typical irradiation conditions with a proton flux of on average 4.2×10^9 $p/\mathrm{cm}^2/\mathrm{s}$ one obtains for a diamond sample with a thickness of 500 μm an average interaction rate of $\approx 2 \times 10^7/\mathrm{cm}^2/\mathrm{s}$.

5.2.2 Proton Synchrotron (PS) Irradiation Area

The proton synchrotron (PS) at CERN was used as the proton source for the irradiation. The PS delivered protons with a momentum of 24.2 GeV/c. The protons have a negligible momentum spread. Two or three proton spills were extracted per PS super cycle into the irradiation area. The PS super cycle had a length of 14 s. Each spill had a length of 300 ms. The average number of protons per spill was 2.9×10^{10} p/cm^2/spill. The proton beam had the shape of a narrow line with a height of 4 cm. It swept across the samples starting on one side and moving by about 1.5 cm. The PS irradiation facility has been used in parallel for irradiation of silicon detectors by the ATLAS experiment.

5.2.3 Experimental Method: Installation

A schematic view of the irradiation setup is shown in Fig. 5.4. The beam enters from the left and is directed by a beam splitter into the T7 beam line where the irradiation took place. The diamond samples were mounted with copper clips on ceramic PCBs in an aluminium box. Flux attenuation along the sample stack is negligible since the proton momentum is sufficiently high.

5.2.4 Experimental Method: Flux Monitoring

The flux was measured by two secondary emission chambers (SEC). These chambers give a signal charge proportional to the number of passing protons. The beam position could be verified using two glass plates in front and behind the samples which darkened at the beam spot. In order to monitor the presence and actual beam position a luminescence screen was

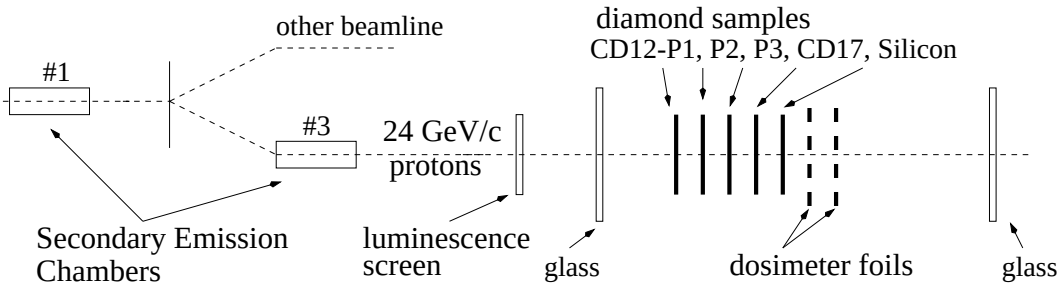

Figure 5.4: Schematic view of the proton irradiation setup. The samples were located about 3 m behind the end of the beam pipe exit.

used which was mounted a few centimetres in front of the irradiation stage. The luminescence light from the proton beam could be observed with a camera as soon as protons were present. The temperature during irradiation was stable between 23°C and 27°C.

A current signal was obtained from SEC3 after each spill. The current was the discharge of a capacitor which collected charge during the 300 ms spill. The current signal was recorded. Fig. 5.5 shows the current from SEC3 as a function of time during the first 60 hours. The measured current is about 1.5 μA for a typical spill and dropped to a few nanoampere at spill breaks when no protons were delivered. A few spill breaks of 1/2 hour to 1 hour are visible and the samples remained unirradiated during these periods.

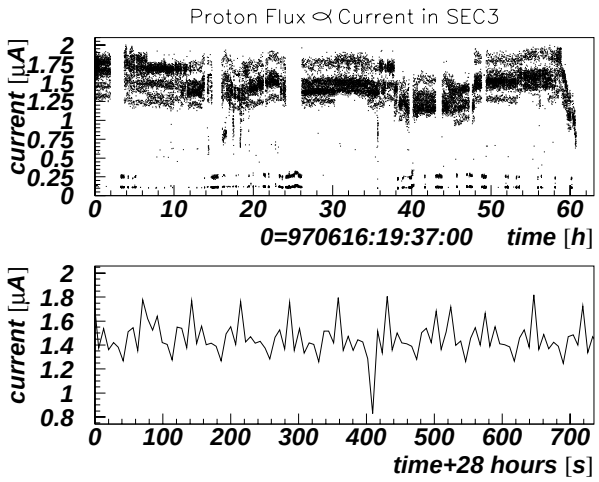

Figure 5.5: Top: current in the secondary emission chamber 3 (SEC3) during the first 60 hours. The current is proportional to the proton flux on the samples. Bottom: magnification of a time interval which illustrates the spill structure, a data point was taken every 7 seconds when a spill passed by.

5.2.5 Experimental Method: Dosimetry

The absolute proton fluence was measured using an aluminium foil activation method. The amount of ^{24}Na generated in the Al-foil under proton irradiation is proportional to the fluence. ^{24}Na decays with a half life time of 15 hours and emits photons of 1.368 MeV. The intensity of this γ-line was measured in a spectrometer and gives the proton fluences. A set of two foils was always used, one foil with a size of 5×5 mm^2 the other with 10×10 mm^2. These sizes corresponded to the area of the irradiated samples.

During the first 60 hours the PS delivered two spills per cycle. Fig. 5.6 shows the accumulated fluence during the first 60 hours as a function of time. The fluence increases linearly up to 0.91×10^{15} p/cm^2 on the 5×5 mm^2 dosimeters and 0.83×10^{15} p/cm^2 on the

10×10 mm^2 dosimeters. The proton flux on the 5×5 mm^2 samples is 4.2×10^9 p/cm^2/s corresponding to on average 2.9×10^{10} p/cm^2/spill. The fluence measured with the small foils is systematically higher than the fluence on the bigger foils since the intensity was higher in the middle of the beam. The samples were adjusted in the beam to receive a maximum flux which was measured to be in the lower center of the sweep area.

The second method for dosimetry was by numerically integrating the current from SEC3 [Fig. 5.5]. The integrated current is expected to be proportional to the fluence. If one normalizes the current sum to reach the fluence given by the foil activation method one indeed obtains a linear dependence and agreement between the intermediate foil measurements and the current sum. A third method for dosimetry was by counting pulses delivered from the secondary emission chamber SEC1. The number of counts per spill is proportional to the induced charge in this chamber. Summation of pulses from SEC1 gives the fluence as a function of time which is shown in Fig. 5.6 as well. The graphs for SEC1 and SEC3 interpolate the data taken with the foil activation method and can be used to predict the fluence at each time between foil measurements. All three methods agree within an error of $\pm 2 \times 10^{13}$ p/cm^2.

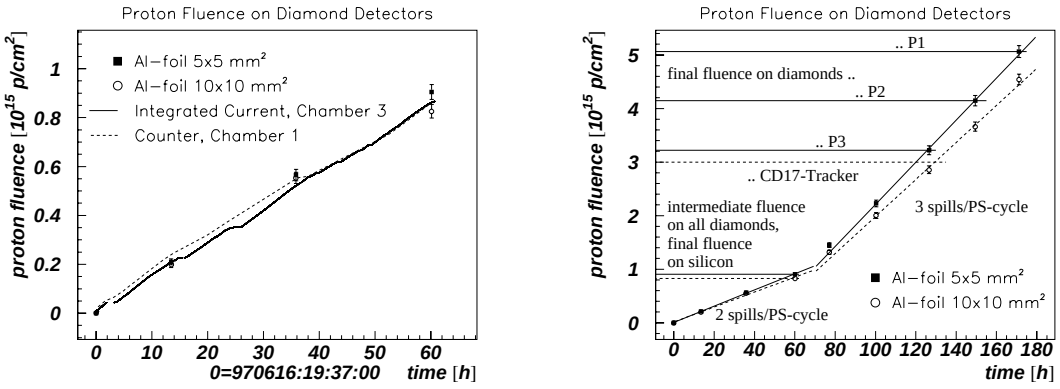

Figure 5.6: Proton fluence on diamond samples CD12-P1,P2,P3 and CD17 as a function of time up to 0.9×10^{15} p/cm^2 (left) and up to 5×10^{15} p/cm^2 (right). The proton fluence was measured every 20 hours using Al-foils. Two sets of markers correspond to the measured fluence on foils of different size. They differ slightly since the proton beam has its highest intensity in the center. The foil measurements below 60 hours (left) are confirmed by two other independent methods using SECs. The slope of the fluence increases above 70 hours (right) since the extraction changed from 2 spills to 3 spills per cycle. The graph (right) shows the final fluences reached on each sample.

Fig. 5.6 shows the fluence on samples for the irradiation period up to 5×10^{15} p/cm^2. After 70 hours the number of particle extractions was increased from two spills to three spills per 14 s cycle. The diamond strip detector CD17 received a fluence of 3×10^{15} p/cm^2. Sample CD12-P1 received the highest proton fluence of 5×10^{15} p/cm^2.

5.2.6 Experimental Method: Current Measurements

All diamond samples were biased during irradiation. The current during irradiation was measured with a setup shown in Fig. 5.7. The circuitry was similar to the one used for the neutron irradiation [Fig. 5.21] with 10 kΩ resistors instead of 10 MΩ in order to account for the higher current during irradiation. The bias voltage during irradiation was U=100 V, constant. The proton induced current was measured ON-spill, when a proton spill swept over the samples, and OFF-spill during spill breaks. Care was taken to distinguish both states

and to measure them correctly in time.

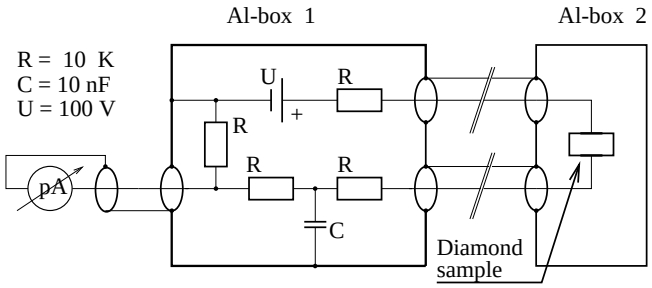

Figure 5.7: Circuitry for biasing diamond and silicon samples and measuring currents during proton irradiation.

The currents from several samples were recorded using a picoamperemeter (Keithley 6517 [66]) with a 10 channel scanner card (Keithley 6521 [66]). The acquisition was automated using a portable PC running a Labview program [67]. PC and picoamperemeters communicated via GPIBus. The data was transferred during acquisition to the analyzing host via Ethernet.

5.2.7 Experimental Method: Charge Collection Measurement

Fig. 5.8 shows a characteristic signal from an irradiated diamond CD12-P1 measured at an applied electric field of 1 V/μm in response to an electron from a ^{90}Sr β-source: the upper waveform, trace A, shows the shaped signal from the VA2, the lower waveform is the waveform average over several event samplings. The amplitude is 85.6 mV (read from the mean between both cursors at the peak of the signal). Using the electronic gain of 26 e/mV one obtains a mean collected charge of 2227 e which corresponds to a charge collection distance of 62 μm.

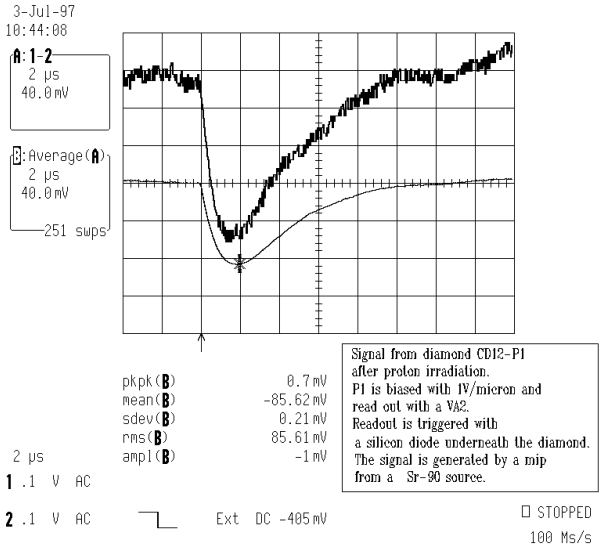

Figure 5.8: Signal response to a β particle as measured on CVD diamond sample CD12-P1 after proton irradiation. The signal is read out using one amplification channel of a VA2 readout chip. The shaped signal has a peaking time of 2 μs. The waveform of trace B is averaged over several events. The signal size can be read from the mean value between the cursors labeled as 'mean(B)'. The cursors are separated by 0.1 μs.

5.2.8 Irradiated Samples

The samples for this irradiation were provided by De Beers [34]. Two samples, CDS-12 and CDS-17 (in abbreviation also labeled CD12 and CD17), were cut from 4" diamond disks, both with a size of 10×10 mm^2. CD12 and CD17 were originally grown to a thickness of 738 μm and 743 μm, respectively. Both samples were processed before irradiation: Sample CDS-12 was lapped on its nucleation side by about 20 μm to a final thickness of $\approx$ 715 μm

and cut in four equal rectangular pieces CD12-P1,P2,P3 and P4 with a size of 5×5 mm^2. Pieces P1,P2,P3 were taken for irradiation, P4 remained unirradiated as a reference. Sample CD17 was lapped on its nucleation side by ≈ 300 μm and 50 μm on its growth side to a final thickness of 492 μm. Fig. 3.9 in Sec. 3.2 shows a photo of an irradiated CVD diamond sample and an irradiated silicon diode. The diamond samples were metallized on both sides with Cr/Au contacts. The irradiated diamond samples have a central dot with a guard ring. Sample CD17 was metallized with a dot and strip tracker mask on the growth side and a solid electrode on its back.

Table 5.1 lists the final fluences which were reached for each sample. All samples were removed for an intermediate characterisation at a fluence of 0.9×10^{15} p/cm^2. The silicon diode was taken out of the irradiation at that level. The diamond samples and the diamond strip tracker were reinserted and irradiated up to several 10^{15} p/cm^2. Sample CD12-P1 received the highest fluence of 5×10^{15} p/cm^2. The diamond strip detector CD17 received a fluence of 3×10^{15} p/cm^2.

sample name	thickness [μm]	center electrode size [mm^2]	final fluence [10^{12} p/cm^2]
CD12-P1	716	7.1	5064 ± 111
CD12-P2	726	7.1	4146 ± 99
CD12-P3	709	7.1	3222 ± 84
CD17	492	2.9	3000 ± 30
Si-Diode	350	16.0	905 ± 30

Table 5.1: Final proton fluences on samples.

5.2.9 Results: Induced Currents during Proton Irradiation

Protons interact in diamond and generate electron-hole pairs. The number of electron-hole pairs generated by one proton has on average a charge, $\bar{Q}^{(p)}_{\rm gen}$. Using the charge collection distance, $\bar{d}$, and assuming that the beam uniformly irradiates the contact area, A, one obtains the particle induced current, $I_{\rm pic}$, in diamond

$$I_{\rm pic} \approx \bar{d} \cdot \frac{A}{D} f_p \bar{Q}^{(p)}_{\rm gen}, \tag{5.11}$$

with the proton flux, f_p, and sample thickness D. This equation relates the charge collection distance to the particle induced current. The induced current depends on the bias voltage, U, via $\bar{d}(U)$. The bias voltage was $U = 100$ V.

Fig. 5.9 shows the proton flux, measured by the secondary emission chamber, and current measured on CD17 during the first 55 hours of the proton irradiation at CERN. Protons were only present during a spill of 300 ms. During this time the ON-spill current and the proton flux could be measured. The OFF-spill current was measured in breaks between spills. The difference between the ON- and OFF-spill current is the particle induced current. This current correlates with the proton flux. The OFF-spill current shown on the same scale as the ON-spill current is negligibly small. It remains constant during irradiation for all samples. The graph also shows that the induced current in diamond does not change with time and proton fluence which reached 1×10^{15} p/cm^2 [see Fig. 5.6] after 70 hours. At some points the induced current is low although protons were present (e.g. from 30 h to 35 h). This occured because beam steering magnets changed temporarily and shifted the beam spot by several millimetres to essentially miss the detectors. Fig. 5.10 shows the same measurement on the p-on-n silicon

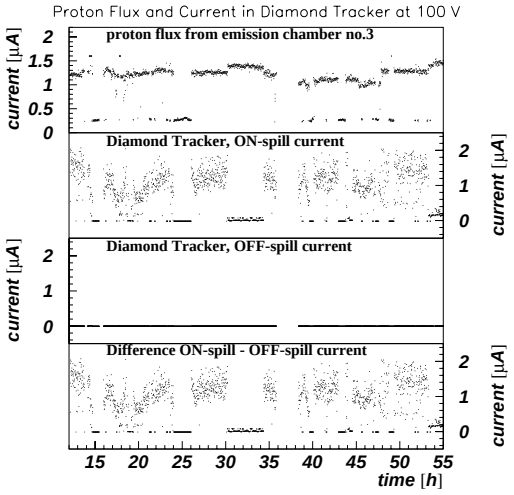

Figure 5.9: Proton flux as measured by the SEC and current on a 2.9 mm^2 contact pad on the diamond strip detector CD17 during proton irradiation. The thickness of the diamond detector is 490 μm. The current was measured ON- and OFF-spill.

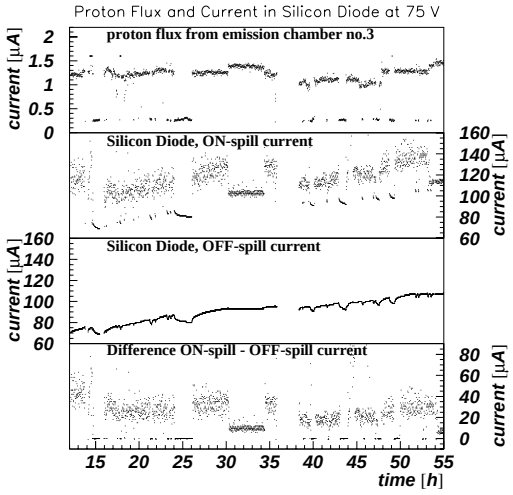

Figure 5.10: Proton flux and current in a silicon diode during proton irradiation for comparison with the current in a diamond detector.

diode behind the diamonds. The induced current, the difference between ON- and OFF-spill current, correlates with the proton flux and recognizes the beam shift mentioned above, as well. The dark current in silicon increases from its original value of 60 μA to 110 μA and is also visible as an offset to the ON-spill current. During the extended periods when the beam was off the silicon diode anneals and the dark current decreases exponentially but increases immediately and non-linearly when the beam comes back. It should be noted that the radiation damage induced OFF-spill current for the silicon diode is comparable to the difference between the ON-spill and OFF-spill currents pointing out the difficulty of using silicon detectors in high fluence regions.

Eq. 5.11 can be transformed to predict the charge collection distance at a given proton flux and an induced current. Using the characteristic flux of 2.9×10^{10} p/cm^2/spill and an induced current of (1.5 ± 0.3) μA [Fig. 5.9] in CD17 (which corresponds to 0.5 μC in the 0.3 s spill period) one finds a collected charge of (3320 ± 650) e which implies a charge collection distance of $\approx (87 \pm 17)$ μm for CD17 at 100 V in agreement with the ^{90}Sr measurement of (72 ± 4) μm at 100 V. A similar calculation for the silicon diode with a particle induced current of (40 ± 7) μA [Fig. 5.10] implies a charge of (16150 ± 3000) e which is less than one would expect for an unirradiated, fully depleted silicon diode of 300 μm thickness (≈ 27200 e). This is indicative of damage in the silicon diode above a fluence of 1.5×10^{14} p/cm^2.

5.2.10 Results: Charge Collection Distance

Fig. 5.11 shows a characteristic signal charge distribution measured on sample CD12-P1 before irradiation, after 0.9×10^{15} p/cm^2 and after 5×10^{15} p/cm^2. The sample was measured in its electron pumped state before irradiation and in the proton pumped state after irradiation. Pumping occurs at a relatively low dose *e.g.* from ^{90}Sr during a measurement of charge collection distance [125, 11] and during proton beam exposure. The charge distributions are fit by a convolution of Landau's energy loss distribution function for thin detectors

and a Gaussian associated with the noise. The measured noise in the characterization setup is about 350 e independent of the irradiation dose. The most probable charge signal, corresponding to the peak of the fit curve, and the mean signal increase slightly after a dose of 0.9×10^{15} p/cm^2 compared to before irradiation. This may be due to additional pumping by the proton beam. Other samples show no change in pulse height distribution at this fluence compared to before proton irradiation. After the highest fluence of 5×10^{15} p/cm^2 the most probable charge signal is decreased by 20% compared to before irradiation, while the mean value decreases by about 40% due to fewer events with high charge signals in the Landau tail.

Fig. 5.12 shows the pumped charge collection distance as a function of the applied electric field at different proton fluences on CD12-P2. In a range from 0 to ± 0.8 V/μm charge collection distance increases. Above $\approx \pm 0.8$ V/μm the velocity of charge carriers saturates and charge collection remains nearly constant.

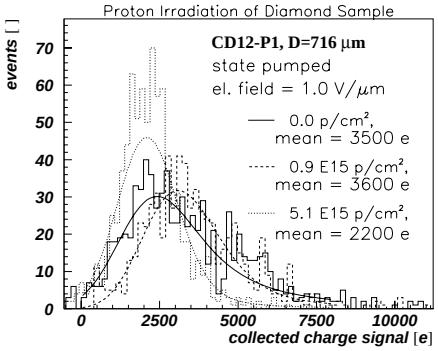

Figure 5.11: Measured charge signal distribution (histogram and fit) at 1 V/μm before proton irradiation, after 0.9×10^{15} p/cm^2 and after 5×10^{15} p/cm^2.

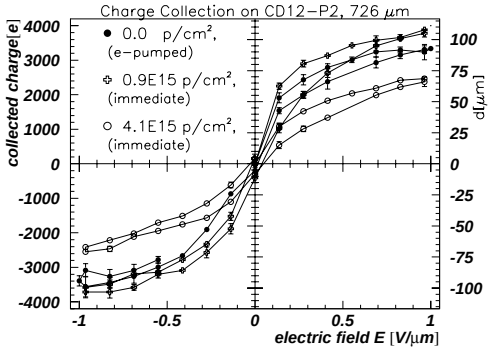

Figure 5.12: Charge Collection distance as a function of the applied electric field at different proton fluences on sample CD12-P2.

The voltage is applied in a loop starting at 0 V, increasing slowly to +1 V/μm, then decreasing to -1 V/μm and back to 0 V. The measured curve shows a hysteresis because of the inherent resistivity and capacitance of the diamond. Before proton irradiation charge collection distance of sample CD12-P2 is (92 ± 4) μm at 1 V/μm. After irradiation with 0.9×10^{15} p/cm^2 the charge collection distance is increased by about 10% compared to before proton irradiation. Other samples show less increase in charge collection distance at this fluence. CD12-P2 was irradiated up to 4×10^{15} p/cm^2. After this fluence its charge collection was decreased by about 27% to (68 ± 3) μm.

5.2.11 Results: Charge Collection versus Proton Fluence

Fig. 5.13 shows the charge collection distance as a function of the proton fluence. The measurements (left) were performed immediately after proton irradiation. Care was taken to keep the samples in absolute darkness for about 2 hours until their radio activity was sufficiently low to be safely characterized. The measurements (right) were performed in the electron pumped state. The samples were depumped under fluorescent light and then pumped under ^{90}Sr. The measurements shown were taken in the fully pumped state of each sample. The fully pumped (saturated) charge collection distance is equal to the value immediately after proton irradiation which means that the diamond pumped during irradiation. It is likely

that pumping during proton irradiation occurred within the first minutes since the proton flux was much higher than what could be achieved by the 37 MBq ^{90}Sr source in the lab.

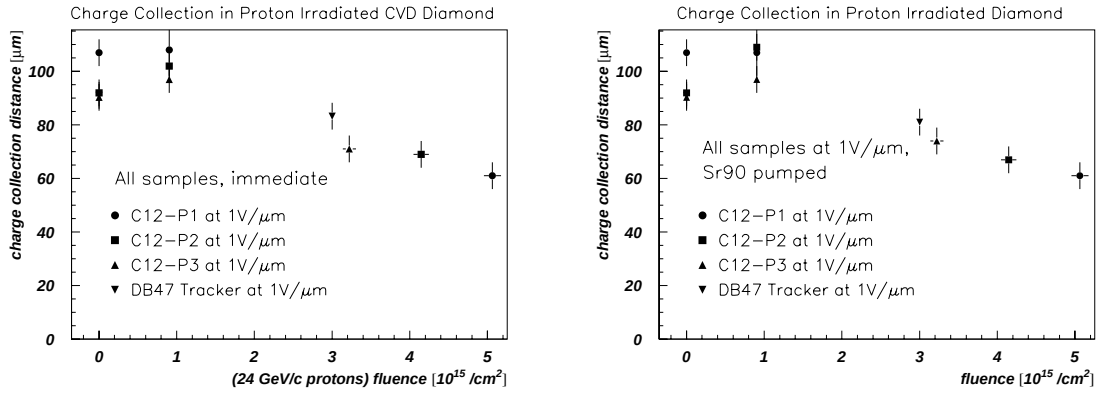

Figure 5.13: Charge collection distance in CVD diamond samples as a function of the proton fluence. Left: the samples were immediately measured after irradiation, care was taken to keep the samples in darkness. Right: the samples were depumped under fluorescent light and then measured several times under constant exposure to ^{90}Sr. After saturation (fully pumped) the Current voltage characteristic was measured as shown here.

Fig. 5.14 shows the relative charge collection distance as a function of proton fluence for the diamond samples. After irradiation with 0.9×10^{15} p/cm^2 the pumped values may be slightly increased compared to before proton irradiation. The next measurement at $3 \times$

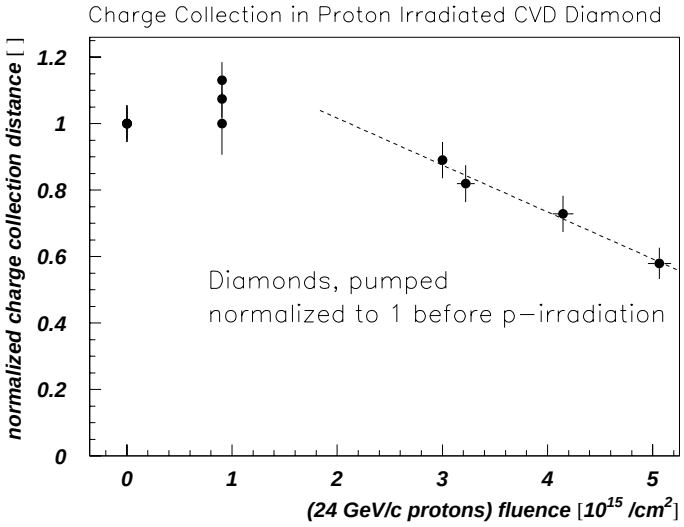

Figure 5.14: Charge collection distance in CVD diamond as a function of the proton fluence. The charge collection distance is normalized to its pumped value before irradiation.

10^{15} p/cm^2 shows a decrease by 10% compared to before proton irradiation. Measurements on the other samples at higher fluence show a decreasing charge collection distance. A linear fit to the values above 3×10^{15} p/cm^2 intersects the ordinate value one at a fluence of $\approx 2 \times 10^{15}$ p/cm^2. This indicates a transition between 1×10^{15} p/cm^2 and 3×10^{15} p/cm^2 where the

slope of the charge collection distance versus fluence changes. The charge collection distance normalized to the pumped value before proton irradiation appears to decrease linearly above $\approx 2 \times 10^{15}$ p/cm^2 and reaches 60 % of its initial value at 5×10^{15} p/cm^2. The linear decrease has a slope of 14 % per 10^{15} p/cm^2. As noted earlier the decrease of the most probable value is 20% at a fluence of 5×10^{15} p/cm^2. No decrease in charge collection distance below 1×10^{15} p/cm^2 is observed.

Table 5.2 lists the measured charge collection values at different proton fluences and compares the measurement immediately after irradiation with the pumped value after a depumping and pumping cycle. It shows the decrease in charge collection distance mentioned above and confirms that charge collection measurements are reproducible after depumping and pumping on all samples and that samples were in a pumped state during proton irradiation. The charge collection distances as a function of the applied electric field at different proton fluences for the various samples are shown in Fig. 5.15. The signal charge distributions are shown in Fig. 5.16.

sample name	fluence [10^{12} p/cm^2]	state	$\bar{Q}_{\mathrm{ind}}$ at 1 V/μm [e]	$\bar{d}$ [μm]
CD12-P1	0	pumped	3852	107
	905	immediate	3560	99
	5064	immediate	2196	61
		pumped	2232	62
CD12-P2	0	pumped	3312	92
	905	immediate	3672	102
	4146	immediate	2480	69
		pumped	2412	67
CD12-P3	0	pumped	3240	90
	905	immediate	3492	97
	3222	immediate	2556	71
		pumped	2660	74
CD17-Tracker	0	pumped	3276	91
	3000	immediate	2988	83
		pumped	2920	81
Silicon-Diode	0		30500	
	905	immediate	no signal	

Table 5.2: Mean induced charge, $\bar{Q}_{\mathrm{ind}}$, and charge collection distance, $\bar{d}$, of diamond samples and silicon diode at different proton fluences.

5.2.12 Summary and Discussion

CVD diamond detector samples were irradiated with 24 GeV/c protons up to a fluence of 5×10^{15} p/cm^2 at the proton synchrotron at CERN. No decrease in charge collection distance was observed below 1×10^{15} p/cm^2. Between 1×10^{15} p/cm^2 and 3×10^{15} p/cm^2 a transition from constant charge collection distance to a decreasing charge collection distance occured. Beyond a fluence of 2×10^{15} p/cm^2, the charge collection distance appeared to decrease linearly with a slope of 14 %/(10^{15} p/cm^2) to 60% of the initial value at 5×10^{15} p/cm^2. It is important to notice that the most probable charge signal of the detectors decreased by only 20% at the highest fluence compared to before irradiation. This indicates that for a fixed threshold cut below the most probable value there would be no loss of efficiency compared to before irradiation. The dark current on diamond samples before and after irradiation was unchanged, being of the order of a few picoamperes. The current during irradiation showed

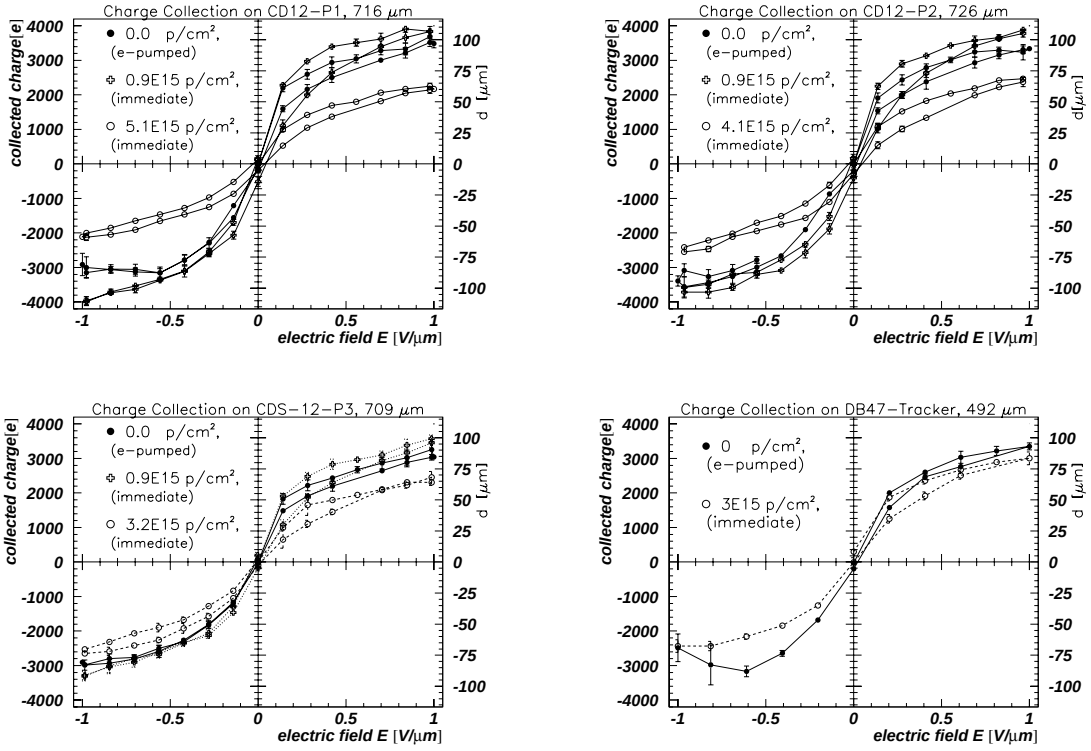

Figure 5.15: Charge collection distance as a function of the applied electric field at different proton fluences. Before irradiation samples were measured in their pumped state. The charge collection measurement after receiving a certain proton fluence was done immediately and without any exposure to light, which could have caused depumping.

a prompt response to protons and was proportional to the flux. In contrast to the fluence dependence observed in the leakage current in silicon detectors, the OFF-spill current for the diamond detectors was independent of proton fluence. The ON-spill current was of the order of microamperes and its response to protons did not change. The results indicate that the present state CVD diamond detectors are radiation hard up to proton fluences of at least 1×10^{15} p/cm^2.

5.3 Irradiation with Neutrons

CVD diamonds were irradiated with neutrons at the ISIS facility at the Rutherford Appleton Laboratory in England. Five ISIS run periods in 1/95, 10/95, 12/95, 11/96 and 11/97 were used for the irradiations. A typical ISIS run period had a length of 30 days. The neutron kinetic energy spectrum peaked at 1 MeV. Neutrons with such energy will be present close to the interaction region of high luminosity experiments at the LHC. Irradiations with thermal neutrons were performed at ISIS as well. Such irradiations are important since thermal neutrons will be present in the albedo background at LHC experiments. The leakage current in diamond was recorded before, during and after irradiations. The charge collection distance was measured before and after each irradiation period. Results from these neutron irradiations were reported in references [126, 127].

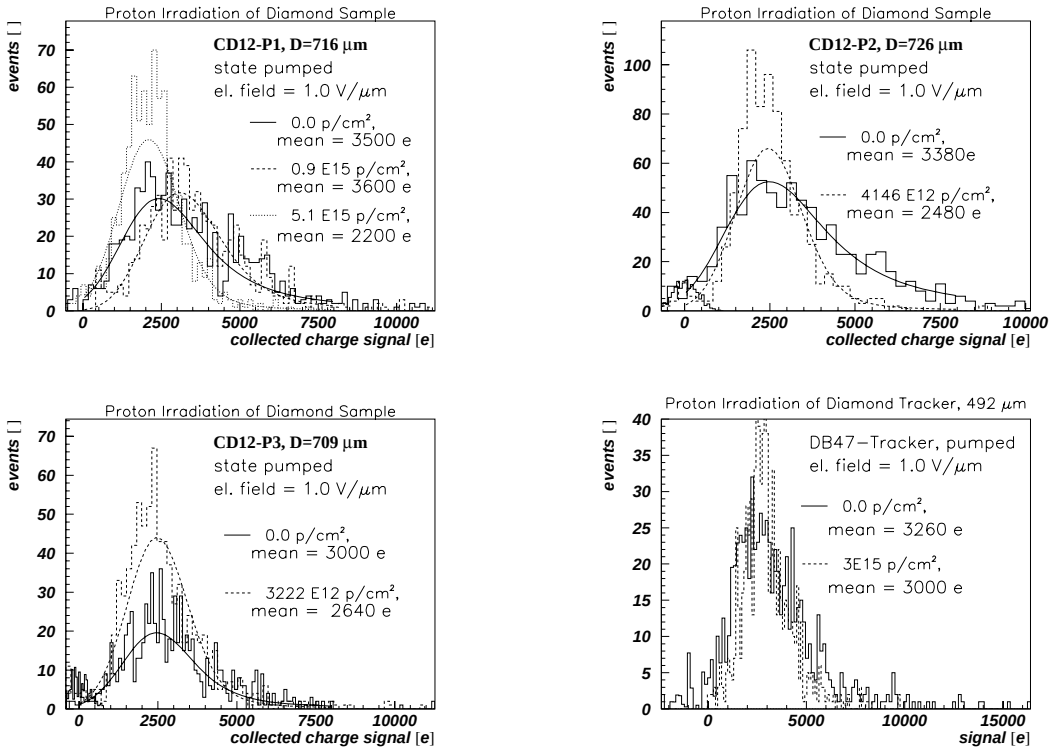

Figure 5.16: Charge signal distribution at a bias voltage of 1 V/μm from four irradiated diamond samples at different fluences immediately after proton irradiation.

5.3.1 Interaction of Neutrons with Matter

The neutron has no electric charge. Unlike charged particles, its dominant means of interaction with matter is through the strong interaction. Strong interactions are much 'rarer' in comparison to electromagnetic interactions of charged particles due to the short distance range of the strong interactions. Neutrons must approach a nucleus within $\mathcal{O}(10^{-13})$ cm in order to interact. When a neutron interacts, however, it may undergo a variety of nuclear processes depending on its energy [71]:

- Elastic scattering from nuclei, $A(n,n)A$. Elastic scattering is the most important mechanism of energy loss for neutrons in the MeV energy range.

- Inelastic scattering, $A(n,n')A^*$ or $A(n,2n')A^{n-1}$. In such reactions, the nucleus is left in an excited state which may later decay by $\gamma-$ray emission or another form of radiative emission. Inelastic reactions can occur if the neutron has sufficient energy to excite the nucleus, usually of the order of 1 MeV or more.

- Radiative neutron capture, $n + (Z,A) \rightarrow \gamma + (Z, A+1)$. The cross section for neutron capture is proportional to 1/velocity of the neutron. Therefore the capture is most likely at low kinetic energies.

- Nuclear reactions, (n,p), (n,d), (n,α), (n,t), $(n,\alpha p)$, etc.. In these reactions the neutron is captured and charged particles are emitted. These interactions occur in the eV to keV energy range. The cross section generally falls like 1/velocity. Resonances may occur depending on the element.

- High energy hadron shower production can occur at the very high energy range above 100 MeV.
- Fission, is most likely for thermal neutrons with kinetic energies below 10 keV. It can only occur in matter with proton number $Z > 56$.

Neutrons are classified according to their energy. *High energy neutrons* have energies above $\approx$ 100 MeV. Neutrons between a few 100 keV and several 10's MeV are called *fast neutrons*. Nuclear resonances occur between 0.1 eV and $\approx$ 100 keV and neutrons of that energy range are referred to as *epithermal neutrons*. At energies lower than the thermal agitation energy at room temperature (1/40 eV) neutrons are called *slow* or *thermal*. At even lower energies neutrons are called *cold* or *ultra-cold*. However, in this section neutrons with energies above 10 keV are called fast neutrons and neutrons with energies below 10 keV are referred to as thermal. This convention was chosen since the dosimetry distinguished between neutrons with kinetic energies below 10 keV and above 10 keV.

Fig. 5.17 shows the inelastic cross sections of neutrons in carbon and the inelastic cross section of neutrons with hydrogen. The cross sections for thermal neutrons are not included. The cross section for the individual nuclear reactions are visible.

The most prominent interaction is (n, γ) which sets in at $\approx$ 5 MeV. The total inelastic cross section is the sum of the cross sections, σ_k, of the individual processes

$$\sigma_{\text{tot}} = \sum_{k:\text{process}} \sigma_k. \qquad (5.12)$$

Using the cross section, σ_{tot}, and the neutron flux, f_n, the rate of neutron interactions with matter can be calculated

$$r = \sigma_{\text{tot}}\, f_n\, \varrho \frac{N_A}{A}\, V. \qquad (5.13)$$

The number of atoms in the sample is $\varrho\, V\, N_A/A$, with the mass density, ϱ, the sample volume, V, the Avogadro constant, N_A, and the molar mass, A. Under typical irradiation conditions with a fast neutron flux on average of $f_n \approx 10^8\ n/\text{cm}^2/\text{s}$, and a total cross section of $\sigma_{\text{tot}} \approx 100$ mb, one obtains for a 500 μm thick diamond sample an average interaction rate of $r \approx 1 \times 10^5/\text{cm}^2/\text{s}$.

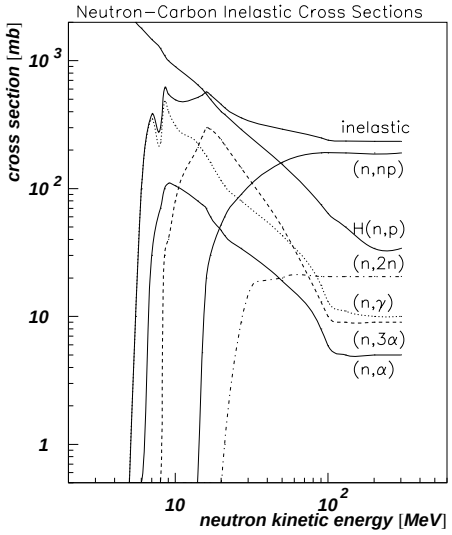

Figure 5.17: Inelastic cross sections of neutrons with carbon and the inelastic cross section of neutrons with hydrogen [128].

5.3.2 Neutron Irradiation Facility at ISIS

The diamond samples were irradiated at ISIS, the 800 MeV proton synchrotron at the Rutherford Appleton Laboratory. The ISIS facility provides a pulsed neutron source for neutron diffraction measurements in material science, biology, chemistry and physics. The neutron irradiation facility that was used here was a parasitic installation that ran in parallel with the beam program at ISIS. The neutrons at the irradiation facility were produced in a spallation process from a graphite block backed with copper. The graphite block was mounted in a collector box along the proton beam pipe between the injection and extraction lines of the proton synchrotron ring. This collector was designed to stop the 70 MeV protons from

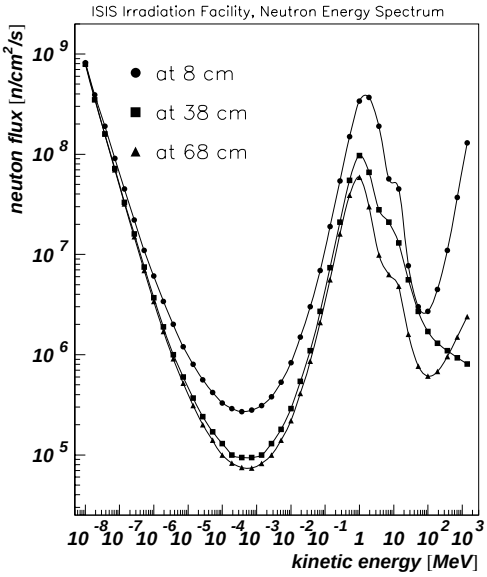

Figure 5.18: Kinetic energy spectrum of neutrons at ISIS taken at different heights. The height was measured relative to the base of the sample irradiation stand. This data was taken from the corresponding table in reference [129].

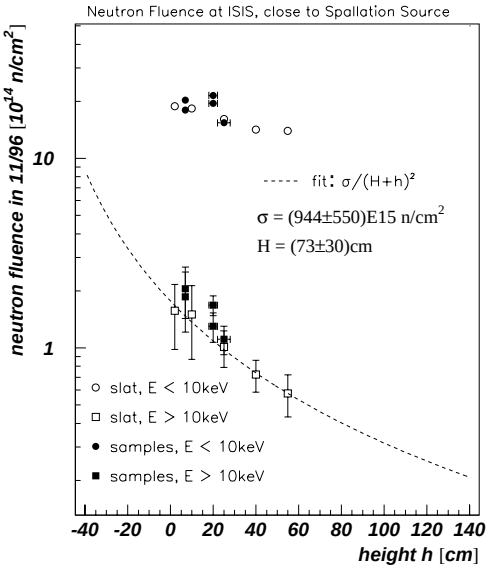

Figure 5.19: Measured neutron fluence versus distance from the graphite block. The fluence was accumulated in one irradiation period. The open markers are measurements from foils on the slat, solid markers are from foils which were attached to the sample boxes. The measurements are fitted with a $\propto 1/\text{distance}^2$ curve (dashed line).

the injector which were not captured by the radio frequency during the acceleration phase of the ISIS cycle. Those protons which were lost by the accelerating radio frequency fields could interact in the graphite block to produce neutrons. Fig. 5.18 shows the kinetic energy spectrum of neutrons measured at the location for samples above the spallation source [129]. The spectrum contains fast neutrons with kinetic energy above 10 keV. The spectrum of fast neutrons peaks at 1 MeV and decreases to half the maximum at 10 MeV. Neutrons with kinetic energy below 10 keV were present as well. For kinetic energies below 1 keV the spectrum rises. The integral under the flux curve gives the energy integrated flux.

In order to estimate the neutron flux two proton currents are important: the injected beam proton current, $I_{p,\text{inj}}$, and the trapped beam proton current, $I_{p,\text{trap}}$. The difference is lost by the accelerating RF field and 'scraped off' by the collector box where protons can interact with the graphite block to produce neutrons. The number, ΔN_p, is defined to be the number of protons which are lost by the accelerating field and interact in the graphite block. The protons produce ΔN_n neutrons in a time interval Δt. Then the lost proton current, $e\Delta N_p/\Delta t$, is proportional to the injected proton current, $I_{p,\text{inj}}$, and therefore $\Delta N_n/\Delta t \propto I_{p,\text{inj}}$. The neutron flux, $f_n = \Delta N_n/(\Delta A \Delta t)$, is given by the number of neutrons passing an area element $\Delta A = r^2 \mathrm{d}\Omega$ at distance r from the graphite block during the time Δt, where neutrons are emitted into solid angles $\Delta\Omega$. Hence one obtains the *neutron flux*

$$f_n(t) \propto \frac{I_{p,\text{inj}}(t)}{r^2}. \tag{5.14}$$

Integration of the neutron flux over the irradiation time interval from t_0 to the end of the irradiation at t gives the *neutron fluence*

$$F_n(t) \equiv \int_{t_0}^{t} f_n(t')\,\mathrm{d}t' \propto \frac{1}{r^2}\int_{t_0}^{t} I_{p,\mathrm{inj}}(t')\,\mathrm{d}t'. \tag{5.15}$$

The fluence depends on the distance, r, from the spallation source as $1/r^2$. Fig. 5.19 shows the measured fluence for fast and thermal neutrons as a function of the distance from the spallation source. The measurement from fast neutrons is fitted by a $1/r^2$ function (Eq. 5.15, dashed line). It can be seen that the measured data is well approximated by the fit function. The fluence obtained during an ISIS irradiation period of ≈ 30 days at the lowest mounting point for samples was several 10^{14} n/cm^2. The actual fluence was also dependent on the proton current and the stability of the beam operation during the irradiation period. The number of neutrons with energies below 10 keV was measured higher than the number of neutrons with energies above 10 keV. One reason for the large fluence of neutrons with energies below 10 keV is that the energy integrated neutron flux from Fig. 5.18 is larger for kinetic energies below 10 keV than it is for all neutrons with energies above 10 keV. Another reason for the large amount of thermal neutrons is that fast neutrons thermalize in successive scatterings in the surrounding material.

Eq. 5.15 indicates that recording the proton beam current allows the fluence values to be obtained for any time during irradiation if the integrated beam current value is normalized to the total fluence.

5.3.3 Experimental Method: Installation

The diamond samples were mounted on a sample stand as shown in Fig. 5.1: the sample stand is the light aluminium frame in front of the concrete. The boxes with samples inside were attached to the frame at various heights. The frame itself was sat vertically on the bench in the background, between the concrete blocks, and was dragged by a chain to the spallation source five meters away. The stand was placed directly above the spallation source, about 50 cm away from the source. The photo also shows a peltier cooling box mounted in the frame. This box allowed the samples to be cooled to -8°C in a nitrogen atmosphere. The peltier and fans survived the fluence at that location of at least one irradiation period without difficulties [130]. Those samples assigned to study the effects of thermal neutrons only were placed outside of the concrete wall, at the place where the photo was taken. An aluminium box containing the diamond samples for thermal irradiation is visible on the floor underneath the lamp.

Fig. 5.20 shows a drawing of the side view of the lower part of the sample stand and the mounting of the sample boxes. The lowest sample box was about 50 cm above the graphite block. Other boxes were mounted higher in the sample stand. The proton beam is shown to enter from the left. The protons had an energy of 70 MeV coming from the injector. The environment temperature was continuously measured during irradiation by a temperature sensor close to a beam magnet using existing ISIS monitoring software. The measured temperature was stable between $(18 \pm 1)^\circ$C and $(19 \pm 1)^\circ$C.

The region near the spallation source could not be accessed since the gamma irradiation level exceeded the allowable threshold in a radiation area by many orders of magnitude. The equivalent dose rate at the location where photo Fig. 5.1 was taken was 40 μSv/h maximum during installation (depending on the position relative to the beamline and bending magnets) [1]. The time required for installation was about 30 minutes. During the installation

[1] The unit *sievert*: 1 Sv = 1 J/kg $\times\, w$, is the equivalent absorbed dose, w is the biological radiation weighting factor, for γ, e, μ: $w = 1$.

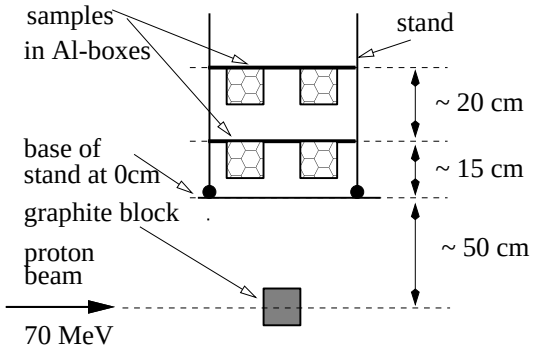

Figure 5.20: Side view of the sample stand and spallation target at ISIS. The samples were mounted at different distances from the collector box where the graphite block was mounted inside.

time the typically accumulated dose by a person was below 6 μSv which is lower than the maximum value given.

5.3.4 Experimental Method: Dosimetry

The total neutron fluence accumulated by each sample was measured after irradiation from the γ-activity of metal (cobalt) foils which were attached to the aluminium boxes containing the samples. The samples themselves and the aluminium boxes were γ radioactive after neutron irradiation (typically 40 μSv/h, 8 days after the end of the irradiation). The activity of an individual diamond sample was negligibly small (typically 40 Bq after 20 days). The main source of radioactivity was the gold contacts and the copper BNC connectors. The samples were removed from the boxes about half a month after the end of a neutron irradiation period. The γ-activity of the foils was measured when their activity was within the dynamic range of the γ-counter [131] which was typically one month after the end of the irradiation. The dosimetry was verified for one irradiation period by measuring the $1/r^2$ characteristics of the fluence (as described above and shown in Fig. 5.19). The measurement of fast neutrons agrees within errors with the $1/r^2$ behaviour. The error on the neutron dose measurement from foil dosimetry was typically 15 % to 30 %. The fluence of thermal neutrons was one order of magnitude higher than the fluence of fast neutrons since the neutron energy spectrum rises for energies below 1 keV.

The typical neutron flux for neutrons above 10 keV was of the order of 10^8 $n/\mathrm{cm}^2/\mathrm{s}$. For example during an 820 hour irradiation in 11/96 a final fluence of $(2 \pm 0.6) \times 10^{14}$ n/cm^2 was reached on a sample located at the base of the stand. This implies a neutron flux of $(6.8 \pm 2) \times 10^7$ $n/\mathrm{cm}^2/\mathrm{s}$.

5.3.5 Experimental Method: Current Measurements

During irradiation all diamond samples were biased with batteries at a voltage of 100 V between the electrodes. Biasing of samples in realistic operating conditions allows one to measure the induced currents during irradiation. Silicon diodes were biased above depletion voltage before irradiation in equivalent setups, like diamond, but with bias resistors of 10 kΩ, instead of 10 MΩ, in order to avoid the voltage drop at the higher silicon leakage current. Fig. 5.21 shows the schematic for voltage biasing and current measurement for one sample. Box 1 contained the biasing voltage with a picoamperemeter (Keithley 6517 [66]). Box 2, with the diamond sample inside, was located $\approx$ 80 m away inside the proton hall at the irradiation zone. The sample in box 2 was connected with two BNC lines to the biasing in box 1. Two BNC lines were used in order to minimize the noise current. The current through each sample was measured with an accuracy of a fraction of a picoampere during irradiation. The current was recorded manually in the first irradiation period [131]. In later

irradiations the currents were recorded using a 10 channel scanner card (Keithley 6521 [66]). The acquisition was automated using a portable PC running Labview [67]. The portable PC had battery power-backup in order to continue recording during short (< 3 hours) power failures.

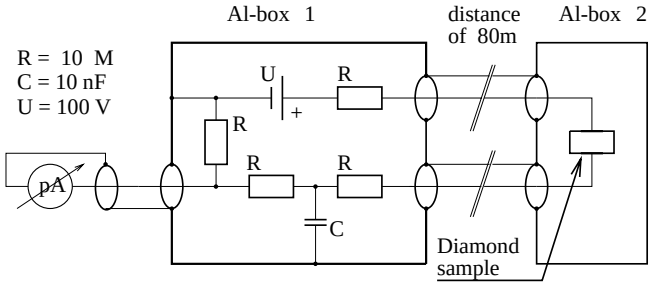

Figure 5.21: Circuitry for biasing diamond and silicon samples and measuring currents during neutron irradiation. The current was measured with fractions of picoampere accuracy over a cable distance of 80 m.

5.3.6 Experimental Method: Charge Collection Measurement

The charge collection distance was measured before and after each irradiation period. Fig. 5.22 shows a characteristic signal from an irradiated diamond sample, U7, measured at an applied electric field of 1 V/μm in response to an electron from a ^{90}Sr β-source: the upper waveform, trace A, shows the shaped signal from the VA2, the lower waveform is the waveform average over several event samplings. The averaged amplitude is 63 mV. Using the measured electronic gain of 25.5 e/mV one obtains a mean collected charge of 1610 e corresponding to a charge collection distance of 45 μm.

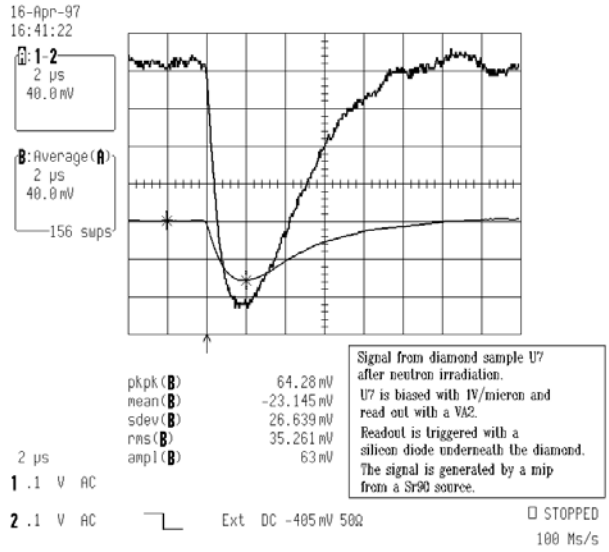

Figure 5.22: A high signal response to an electron from a ^{90}Sr β-source measured on CVD diamond sample U7 after neutron irradiation. The signal was read out using one amplifier channel of a VA2 readout chip. The shaped signal had a peaking time of 2 μs. The waveform of trace B is the average of trace A over several events. The signal size can be read from the peak-to-peak value between the cursors labeled as 'pkpk(B)'. The averaged amplitude is lower than the amplitude of the selected single event.

5.3.7 Irradiated Samples and Fluences

The CVD diamond samples were produced by Norton [33] and De Beers [34]. The samples were cut from diamond disks, similar to the disk shown in Fig. 4.21. After cutting, the samples had rectangular sizes between 5×5 mm^2 and 10×10 mm^2. The samples were metallized on both sides with circular electrodes with a diameter between 3 mm and 5 mm. The electrodes were made of Cr/Au or Ti/Au forming ohmic contacts to the diamond substrate.

Table 7.3 in Appendix 7.1 on page 232 lists all irradiated samples, their thickness, electrode type, size and neutron fluence received during an irradiation period. Diamond samples Y4 and YB were exposed to thermal neutrons only. The other samples received both thermal and fast neutrons. Several samples were irradiated twice or three times in order to reach fluences of several 10^{14} n/cm^2. The neutron fluences in Table 7.3 are from a single irradiation period. Several silicon diodes were irradiated for comparison. A typical fluence of 3×10^{14} n/cm^2 was reached in one irradiation period at the base of the sample stand. The error on the measured fluence was between 15 % and 30 %. Normally the measured fluences were consistent with the locations of the samples at the stand. Only one sample, Y1, may have had a systematic measuring error. The fluence in the initial irradiation of Y1 was inconsistent with the fluences obtained for other samples in irradiations of similar time period.

5.3.8 Results: Current during Irradiation

Fig. 5.23 shows the current through two diamond samples after installation in the irradiation area but before the start of the neutron irradiation. No neutrons were present at that time. The bias voltage was applied at the time $\approx$ 13.5 h. Between application of the bias voltage and start of the irradiation, the currents decreased exponentially and saturated at 44 pA and 65 pA. The contact area was 12.6 mm^2 for U6 and 19.6 mm^2 for YF. Therefore, the saturated current densities in the samples were 3.5 $\mathrm{pA/mm}^2$ and 3.3 $\mathrm{pA/mm}^2$ which are essentially equal. This current was higher by a factor ≈ 3 than that normally measured for the dark current in diamond. This indicates that the remaining γ-background induced charge in the diamond samples. The neutron irradiation started at the time $\approx$ 15.8 h and neutrons became present. It can be seen that the current in the diamond increased at the start of the irradiation.

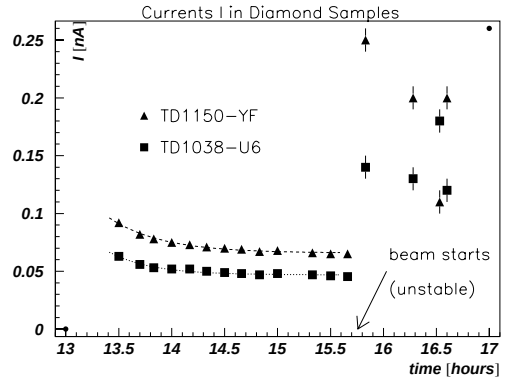

Figure 5.23: Current in diamond samples, YF and U6, a few hours before start of the irradiation in 10/95.

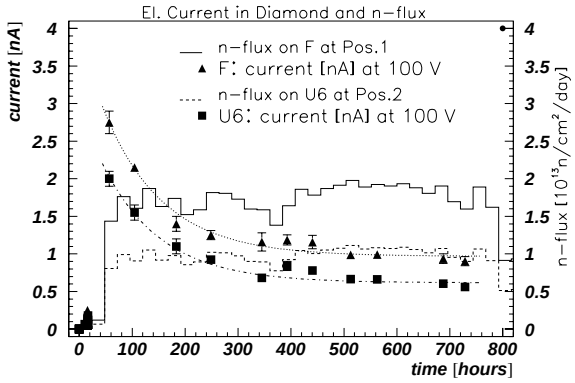

Figure 5.24: Induced current in diamond samples, YF (abbreviated as F) and U6, during n-irradiation 10/95. The current in both samples decreases exponentially with the same time constant.

Fig. 5.24 shows the induced current measured in U6 and YF during an irradiation period of $\approx$ 790 h ($\approx$ 33 d). Both samples were irradiated for the first time in this irradiation period. The current was measured manually every two days. As soon as the irradiation started and neutrons were present the currents raised to 2.0 nA and 2.75 nA corresponding to 158 $\mathrm{pA/mm}^2$ and 140 $\mathrm{pA/mm}^2$ which can be considered as equal. During irradiation

currents in both samples decreased. A decrease can not be due to decreasing biasing voltage since the batteries had the same voltage at the end of the irradiation as before. The measured induced current can be fitted by an exponential function

$$I_{\mathrm{ind}} = I_{\mathrm{sat}} + I_0\, e^{-(t-t_0)/\tau}. \tag{5.16}$$

The current in both samples decreased with the same time constant $\tau \approx 110$ h. At the beginning of the irradiation ($t = t_0 \approx 50$ h) the currents were $I_0 + I_{\mathrm{sat}} \approx 2$ nA in U6 and $I_0 + I_{\mathrm{sat}} \approx 2.7$ nA in YF. The exponential fit gives a saturation current of $I_{\mathrm{sat}} \approx 0.62$ nA in U6 and $I_{\mathrm{sat}} \approx 0.95$ nA in YF. The saturation currents correspond to current densities in U6 and YF of 49.2 pA/mm^2 and 48.5 pA/mm^2. Fig. 5.24 also shows the fast neutron flux in both samples, as deduced from the proton beam current according to Eq. 5.14. It can be seen that the flux of fast neutrons on both samples remained nearly constant during irradiation. It can also be seen that the flux on sample YF was higher by a factor 1.77 than the flux on U6. Although sample YF was exposed to a higher neutron flux than U6 the current densities and the exponential time constants were equal. This may indicate that the induced current and the exponential decrease are not related to the neutron flux. Both diamond samples had about the same charge collection distance as can be seen in the measured data below. The fact that the induced current densities were equal although they received different neutron flux leads to conclude that the current induced in diamond is not due to an interaction of neutrons in diamond. The only remaining source of radiation was photons. We conclude that the induced current in diamond during irradiation is mainly due to photons.

Fig. 5.25 shows the induced current measured in diamond sample U7 during a neutron irradiation in 12/95. The sample U7 was irradiated for the first time in 12/95. The current was measured every 5 minutes using a PC. The neutron flux was deduced from the proton current and is also shown. Before irradiation U7 was depumped under fluorescent light and had a dark current of ≈ 3 pA at 100 V. The current increased at the beginning of the irradiation to about 2.2 nA corresponding to a current density of 175 pA/mm^2. This behaviour is similar to the current measured on U6 manually in the previous irradiation as reported above [Fig. 5.24]. The induced current in U7 decreased exponentially as observed on U6. In addition one can see that the current often fell off. The fall-off is explained by spill breaks in the proton accelerator (see below). The current acquisition stopped recording after 660 hours. The irradiation continued until $t \approx 980$ hours. The logarithmic ordinate in Fig. 5.25 allows one an extrapolation of the current to 980 hours. The extrapolated induced current for the end of the 12/95 irradiation is (0.45 ± 0.1) nA corresponding to a current density of 36 pA/mm^2.

U7 was irradiated for a second time in 11/96. Fig. 5.26 shows the measured induced current in U7 in 11/96. At the start of the irradiation the induced current was about 0.48 nA corresponding to a current density of 38 pA/mm^2 which is equal to the induced current from the end of the irradiation in 12/95. Fig. 5.26 also shows the 'lost' proton current measured from the difference between the injected and the trapped beam proton currents. The lost proton current was proportional to the neutron flux. It can be seen that the current in U7 fell off during spill breaks. The current in U7 is correlated with the neutron flux. It can also be seen that the induced current in U7 did not decrease further during the 11/96 irradiation. The induced current saturated at 0.3 nA corresponding to 24 pA/mm^2.

Fig. 5.27 shows the induced currents in the samples N1 and N3 during neutron irradiation in 11/96. Both samples were irradiated previously in 12/95. The induced currents in both samples were constant during irradiation. Both samples already reached the saturated induced current during their first irradiation. Two other samples CD15-P3 and CD15-P4

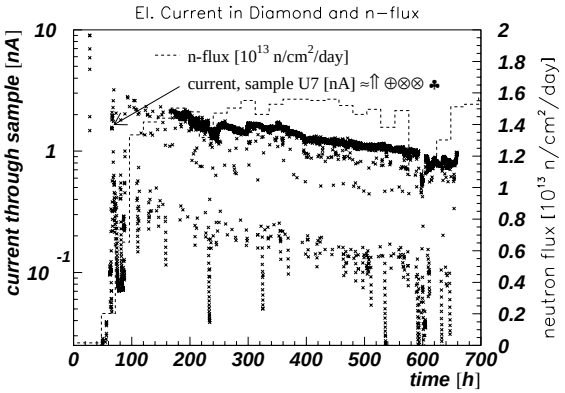

Figure 5.25: Induced current in CVD diamond samples, U7, during neutron irradiation 12/95. The neutron flux is shown as well. U7 was irradiated the first time in 12/95.

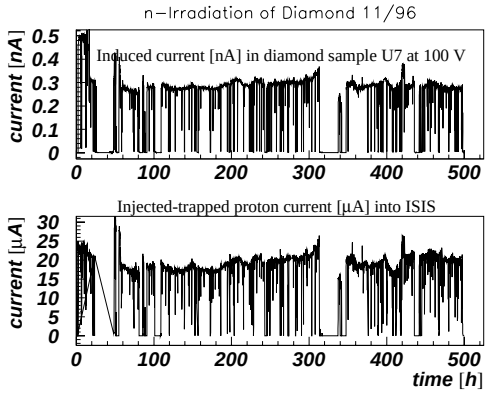

Figure 5.26: Induced current in sample U7 during irradiation in 11/96 (top) versus time during irradiation. Proton beam current which is proportional to the n-flux versus time (bottom). U7 was irradiated the second time in 11/96.

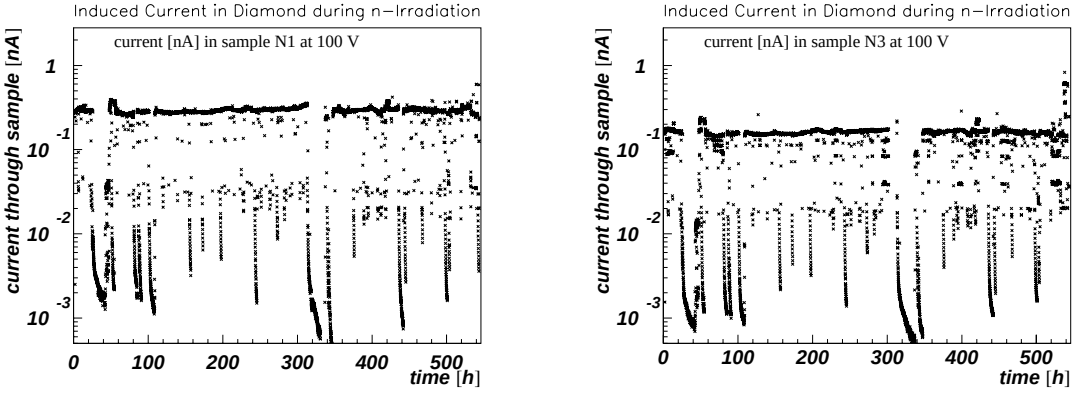

Figure 5.27: Induced currents in diamond samples N1 (left) and N3 (right) during neutron irradiation 11/96.

from a different manufacturer were irradiated the first time in 11/96 with the induced currents shown in Fig. 5.28. The currents decreased as well. They show the same correlation with the neutron flux as the current from other samples in the same irradiation. It can be seen that the beam-off current decreased in successive spill breaks during the irradiation period as well. Therefore, one concludes that not only the induced currents but also the dark currents decrease during irradiation.

Fig. 5.29 shows two current measurements in diamond, one current measurement in silicon and the neutron flux versus time during an irradiation in 11/97. The currents were measured on the diamonds U7, N3 and N1 which were all irradiated before, so that the induced current had already saturated. The currents in samples U7 and N3 were in parallel thus the current of ≈ 0.6 nA is the sum of both samples (consistent with the sum of ≈ 0.2 nA in N3 from Fig. 5.27 (right) and 0.3 nA in U7 from Fig. 5.26). U7 and N3 were mounted on the aluminium frame and exposed to fast and thermal neutrons. N1 was located ≈ 7 m away from the spallation source instead, outside the concrete wall where only thermal neutrons were

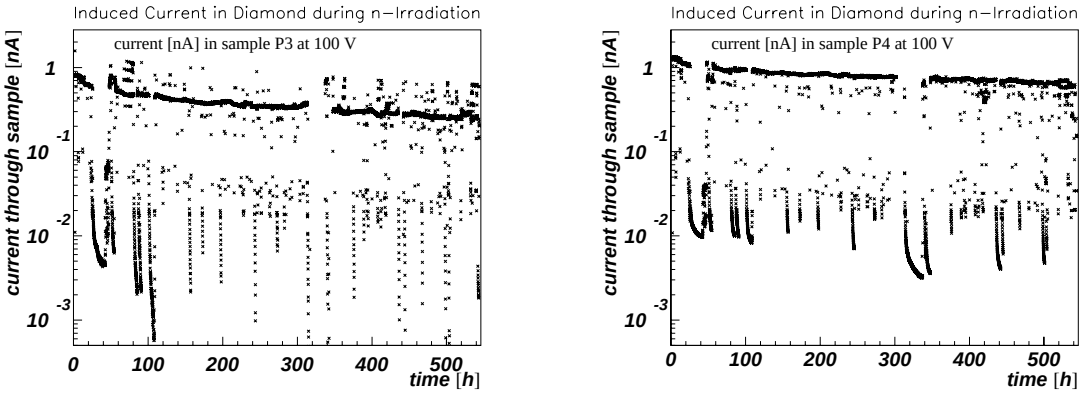

Figure 5.28: Induced current in diamond samples CD15-P3 (left) and CD15-P4 (right) during neutron irradiation 11/96.

present. The induced current in N1 was about 0.3 pA during beam-on periods and drops fractions of a picoampere below zero during spill breaks (not shown on the logarithmic scale). The induced currents follow the neutron flux. The induced current behind the concrete wall is lower by 3 orders of magnitude than the current in samples close to the spallation source.

A silicon diode was irradiated as well. The silicon diode had a thickness of 350 μm and a p-implant of 4×4 mm^2 in an n-bulk. The diode was biased with 61 V, sufficient to deplete the diode before irradiation. The bias voltage was still at 61 V at the end of the irradiation. The diode was kept in the peltier cooler in an N_2-atmosphere at -8 °C. The current in the cooled silicon diode increased during irradiation. It can be seen that the current did not follow the spill breaks as it was the case in diamond. The current in silicon was dominated by leakage current whereas the current in diamond was mostly an induced current. The current in silicon annealed during spill breaks. A short power-cut occurred at the time $\approx$ 580 h. After the main power returned, the current meter automatically re-initialized and the PC kept recording thanks to its battery. However, the accelerator was off for about 24 hours and the peltier silicon cooling was off for the time of the power cut. During this power cut the silicon diode warmed up to +18 °C which caused a leakage current increase in the silicon diode by a factor of 10. The leakage current returned to the value from before the power-cut after the cooling returned.

Another silicon diode, of the same type as above, was neutron irradiated at room temperature. The leakage current typical for a silicon diode before and after neutron irradiation (at room temperature) is shown in Fig 5.30. Before irradiation the current had the characteristic of a reversed biased diode: the current increased from 0 to 1 nA proportional to $\sqrt{U_{\rm bias}}$ between $U_{\rm bias}$ = 0 V and 70 V. The diode was fully depleted at 50 V (as known from a capacitance measurement). Above 80 V the current increased linearly to 6 nA at 100 V. This behaviour was normally observed on unirradiated silicon diodes from this manufacturer, CSEM, and is an avalanche effect. After irradiation with 3.2×10^{14} n/cm^2 and further 6 months at room temperature in darkness the current was 100 nA at 60 V, a factor 100 higher than before irradiation. It can be seen that, after irradiation, the current ranges from -1 μA to 1 μA for bias voltages between -300 V and 300 V. The current depends linearly on the voltage. After irradiation the silicon diode had the characteristic of an ohmic resistor with a resistance of R = 330 MΩ corresponding to a resistivity of ρ = 1.5 GΩcm. This example illustrates qualitatively how a silicon diode behaves if it is handled in exactly the same way as a diamond. However, it is known that silicon behaves 'better' given a more

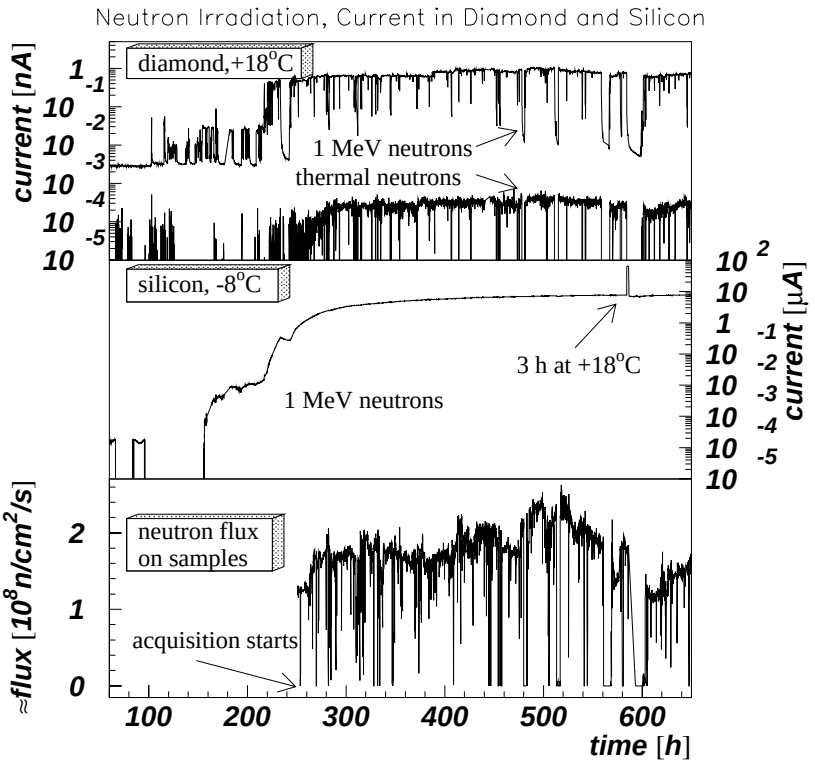

Figure 5.29: Top: total induced current in CVD diamond samples, U7 measured in parallel to N3, located at the base of the sample stand ('1 MeV neutrons'). Also top: induced current in N1, located outside the concrete ('thermal neutrons'). Middle: leakage current in the silicon diode, cooled to $-8\,^{\circ}\mathrm{C}$, located few centimetres above the diamond samples U7 and N3. Bottom: 1 MeV neutron flux at the location of U7 and N3 and the silicon diode. This data was measured in the neutron irradiation 11/97.

controlled treatment after irradiation than was done here.

Fig. 5.31 shows the mean signal due to electrons from ^{90}Sr measured in the silicon diode before and after irradiation. The mean signal charge was measured using the setup for measuring charge collection distances in diamond (VA2, 2 μs signal peaking time). Before irradiation a mean number of 35000 e was collected when an electron from the ^{90}Sr source traversed the fully depleted diode. This is about 10 % higher than expected if one assumes 26250 e as the most probable value for minimum ionizing particles in the 350 μm thick silicon diode. Below 50 V the diode was not depleted and only a fraction of the generated charge was collected. After irradiation with 3.2×10^{14} n/cm^2 no charge could be detected. In this figure the data is plotted at the applied voltage which does not take into account the voltage drop on the biasing resistors shown in the setup Fig. 3.27. At 200 V applied the effective voltage across the diode was still 100 V and no signal was observed from the diode at that voltage.

5.3.9 Results: Induced Current compared to Neutron Flux and Fluence

Fig. 5.32 shows a magnification of the induced current, I_{pic}, in the diamond sample and the difference between the injected and trapped proton current as a function of time. It can be seen that the induced current and the proton current are correlated: $I_{\mathrm{pic}} \propto I_{\mathrm{p,inj}}$. Even small (10 % level) changes in the proton current are seen by the diamond sample. The diamond sample acts as a monitor for the neutron or photon flux. Only those samples which were irradiated once before worked as a flux monitor. Integration of the induced current in diamond versus time gives the induced charge

$$Q_{\mathrm{pic}}(t) = \int_0^t I_{\mathrm{pic}}(t')\,\mathrm{d}t' \propto \int_0^t I_{\mathrm{p,inj}}(t')\,\mathrm{d}t' \overset{\text{Eq. } 5.15}{\propto} F_n(t)\,. \tag{5.17}$$

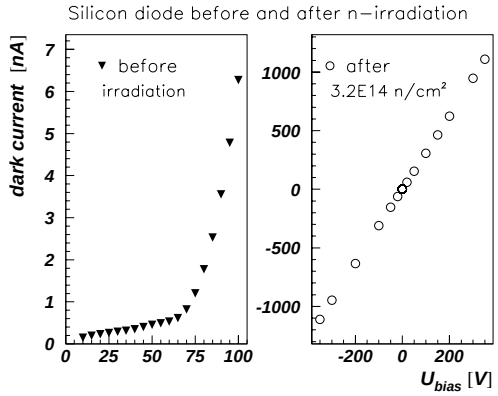

Figure 5.30: Current versus voltage characteristic in a silicon diode before and after n-irradiation. The diode received a fluence of 3.2×10^{14} n/cm^2.

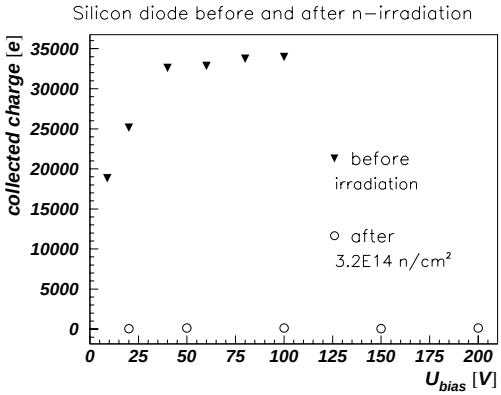

Figure 5.31: Charge collected in a silicon diode before and after n-irradiation.

That means that the induced charge is proportional to the proton beam fluence which allowed to deduce the neutron fluence.

Fig. 5.33 shows the measured induced charge in diamond and the measured neutron fluence as a function of time. The neutron fluence was measured by integration of the proton flux onto the spallation source. Both graphs have different slope, however, their ratio is nearly constant. Fig. 5.34 shows the current in the silicon diode and diamond sample U7 during neutron irradiation. The silicon diode was continuously at room temperature during irradiation. It can be seen that the current in the silicon diode increases non-linearly in time from a few nA to more than 60 μA. This current can be directly compared to the lower current (8 μA) in the cooled silicon diode in Fig. 5.29. Both silicon diodes were from the same silicon wafer and had equivalent geometrical dimensions. The superimposed current in diamond was at 300 pA constant in time when neutrons were generated. During beam-off periods, which are visible in diamond when the current has a few picoampere, a decreasing current in silicon was measured due to annealing. The leakage current in silicon versus neutron fluence, F_n, is normally described by the following empirical expression [65, 132]

$$I_{\mathrm{leak}}(F_n) = I_{\mathrm{leak}}(F_n = 0) + \alpha F_n \, A \, D \tag{5.18}$$

with the active area, A, and the sensor thickness, D. The value α is the leakage current constant which describes the slope of the leakage current as a function of the fluence. The measurement of the leakage current in silicon diodes during irradiation indeed shows a linear increase with neutron fluence up to about 1×10^{14} n/cm^2. The damage constant is in this range measured to be $\alpha = 1 \times 10^{-17}$ A/cm in agreement with measurements listed in [65]. The voltage required to deplete the silicon diode normally increases under irradiation. In the situation here the bias voltage could not be increased. Instead the voltage linearly decreased from originally 84 V to 72 V due to battery discharge as can be seen in the same figure. The silicon diode was certainly under-depleted for most of the irradiation.

Using the integrated induced current from the diamond U7 it was possible to measure the neutron fluence. Fig. 5.35 shows the leakage current in the silicon diode as a function of the normalized fluence deduced from the current induced in the diamond. The normalization fluence for U7 used is $F_n = 2.05 \times 10^{14}$ n/cm^2. Assuming linear relation between the induced current in diamond and the neutron fluence one finds a linear increase in the current in silicon

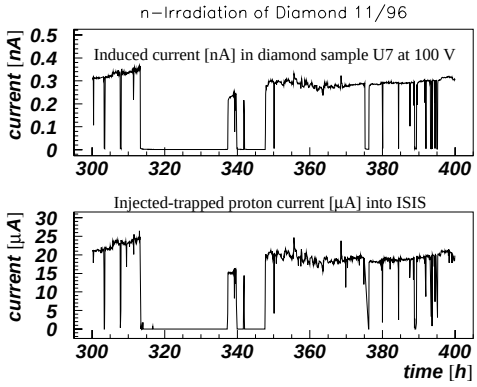

Figure 5.32: Top: induced current in sample U7 in 11/96 for an arbitrary time interval. Bottom: the difference between injected and trapped proton current that is proportional to the neutron flux. The current in diamond correlates with the neutron flux.

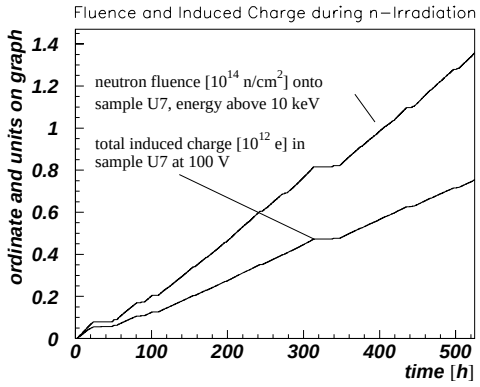

Figure 5.33: Neutron fluence and time integrated current in diamond versus time. The neutron fluence was measured by the number of protons which interact in the graphite block.

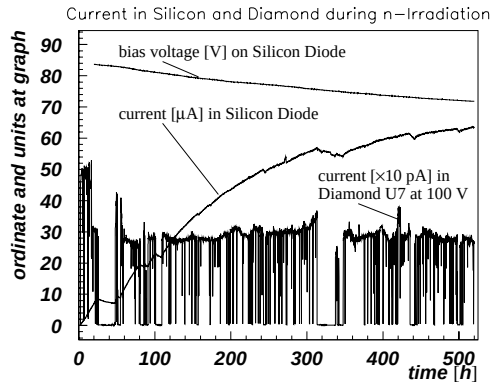

Figure 5.34: Leakage current and bias voltage in silicon diode S-16 and induced current in diamond U7 versus time during neutron irradiation (at room temperature). The diode is biased with a battery and its voltage decreases linearly due to the high current in the diode, whereas the voltage applied to the diamond stays constant at 100V.

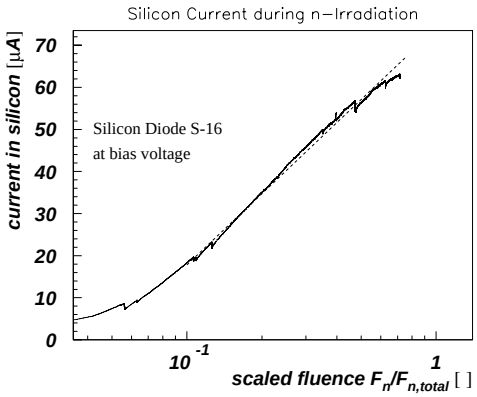

Figure 5.35: Current in silicon diode S-16 under irradiation at room temperature versus integrated current in diamond U7 during neutron irradiation. The solid line is the measurement, the broken line is a linear fit to the measured graph. The scaled fluence $F_n/F_{n,\mathrm{total}} = 1$ corresponds to $2.05 \times 10^{14}\ n/\mathrm{cm}^2$.

up to a scaled value of 0.6 which represents a fluence of 1.2×10^{14} n/cm^2.

5.3.10 Results: Dark Current

The dark current density, j_{dark}, on diamond samples depends on the bulk conductivity, σ_{bulk}, and on the surface conduction. Surface currents can not be neglected as shown in Sec. 3.2.3. However, here one may assume that the current is in a first approximation proportional to the applied electric field E and given by Ohm's law $j_{\mathrm{dark}} = \sigma_{\mathrm{bulk}} E$. The influence of fringe fields on the dark current and a non uniform field strength between the contacts are unknown and not considered. Fig. 5.36 shows a measurement of the dark current in diamond before and after irradiation as a function of the applied electric field. The dark current shows hysteresis which means that the current depends on the size of the voltage step and the time between steps. This effect is explained by resistivity and capacitance introduced by the contacts (Sec.3.2.3). The current before irradiation was typically higher by a factor 2 compared to after irradiation. The decrease in dark current measured in the lab confirms the decreasing current observed in the current measurements during irradiation.

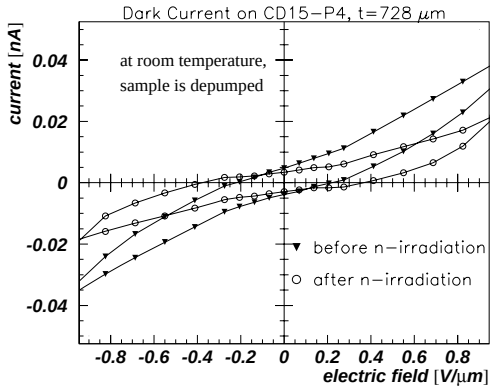

Figure 5.36: Dark current in diamond sample CD15-P4 as a function of the applied electric field before and after neutron irradiation. The sample was in the depumped state for both measurements. The current was measured in darkness, at room temperature and under normal atmospheric conditions.

Table 5.3 lists the conductivity of several diamond samples before and after irradiation. The conductivity was derived from the current measured at 1 V/μm. The dark current in diamond and therefore its conductivity depends on the pumping state. This effect can be seen on irradiated and unirradiated samples. The conductivity measured in both states decreased after irradiation compared to before irradiation. The difference in conductivity between pumped and depumped states after irradiation is smaller than before irradiation.

sample	σ_{before} $[10^{-11}\ \Omega^{-1}\mathrm{cm}^{-1}] \pm 10\%$		σ_{after} $[10^{-11}\ \Omega^{-1}\mathrm{cm}^{-1}] \pm 10\%$	
name	depumped	pumped	depumped	pumped
Y1	4.0	5.5	3.0	4.8
U6	5.5	14.3	3.0	4.0
U7	4.8	11.9	3.6	3.6
N1	2.7	13.3	1.2	2.3
N2	3.0	9.7	1.3	1.5
N3	-	11.1	2.8	2.8
CD15-P3	43.5	142.8	16.9	19.6
CD15-P4	62.5	250.0	33.3	38.5

Table 5.3: Conductivity, σ, before and after neutron irradiation 11/96.

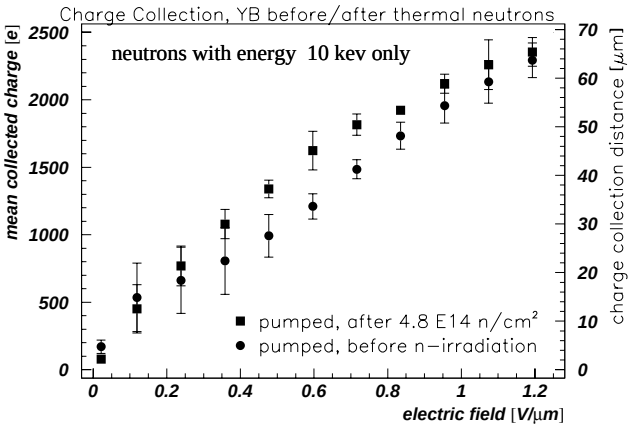

Figure 5.37: Charge collection distance on sample YB as a function of the applied electric field before and after irradiation with thermal neutrons.

5.3.11 Results: Charge Collection after Irradiation with Thermal Neutrons

Two samples, YB and Y4, were irradiated with thermal neutrons only. Both samples were placed outside of the concrete shielding, 7 m away from the spallation source. Fig. 5.37 shows the charge collection distance of YB as a function of the applied electric field before and after irradiation with thermal neutrons. The thermal neutrons fluence on YB was 4.8×10^{14} n/cm^2 in 10/95 with an immeasurable fraction of fast neutrons. The charge collection distance was (54 ± 3) μm at 1 V/μm before irradiation and (59 ± 3) μm at 1 V/μm after irradiation. The charge collection distance after irradiation increased slightly. Another sample (Y4) received thermal neutrons up to 2.7×10^{15} n/cm^2 and fast neutrons of 6.0×10^{13} n/cm^2. The charge collection after thermal irradiation also increased slightly compared to before irradiation. Since no decrease in charge collection distance was observed one can conclude that there is no radiation damage due to only thermal neutrons up to 2.7×10^{15} n/cm^2.

5.3.12 Results: Charge Collection after Irradiation with Fast Neutrons

Fig. 5.38 shows the charge collection distance from sample U6 as a function of the applied electric field before and after irradiation with 3.2×10^{14} n/cm^2 in 10/95. The sample was in both measurements in the electron pumped state. A charge collection distance of (52 ± 3) μm at 1 V/μm was measured before irradiation. After irradiation, the charge collection distance was (51 ± 3) μm at 1 V/μm which is the same as before irradiation. The measurement on U6 after its second irradiation in 11/96 (not shown), when it received an additional fluence of 1.7×10^{14} showed (50 ± 3) μm, the same as before irradiation.

Fig. 5.39 shows the signal charge distribution on the pumped sample U7 before neutron irradiation, after 7.5×10^{14} n/cm^2 and after 1.32×10^{15} n/cm^2. The mean value in the unirradiated state was 1900 e corresponding to a charge collection distance of (53 ± 3) μm. After its first irradiation the mean value was 1700 e (47 ± 3 μm) indicating a slight decrease compared to the unirradiated state. After the second irradiation the mean was 1130 e corresponding to a charge collection distance of (31 ± 3) μm. The mean signal decreased by 41 % compared to the unirradiated state. The most probable value decreased by about 30 % compared to before irradiation. The histogram is also narrower after the last irradiation compared to before irradiation.

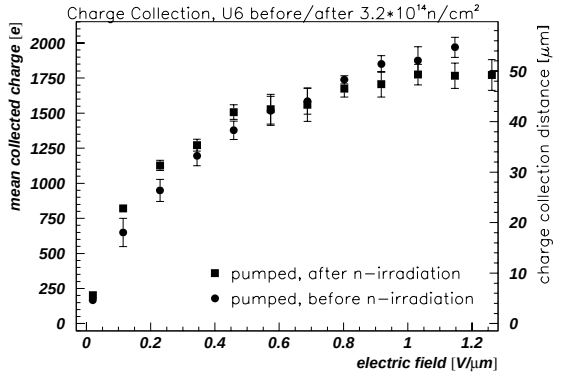

Figure 5.38: Charge collection distance on sample U6 as a function of the applied electric field before and after n-irradiation 10/95.

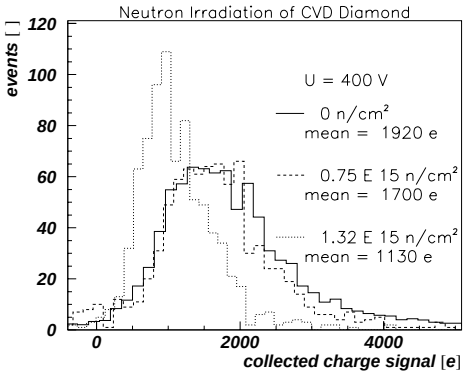

Figure 5.39: Signal distribution on sample U7 before and after two n-irradiations, measured after 11/96. The sample acquired a fluence of $\approx 1 \times 10^{15}$ n/cm^2. The mean signal decreased by 10%.

5.3.13 Results: Charge Collection versus Neutron Fluence

The charge collection distance corresponding to the mean value of the signal charge distribution was measured on all irradiated samples before and after each irradiation. Care was taken to fully pump the samples with electrons from a ^{90}Sr for the measurements shown here. A sample was considered as fully pumped when the charge collection distance was unchanged in several successive measurements of the signal charge mean value. One measurement of the mean value contained typically 800 trigger events.

Fig. 5.40 shows the charge collection distance as measured on two samples, U6 and U7, as a function of the neutron fluence. The initial charge collection distance was (53 ± 3) μm on U6 and (53 ± 3) μm on U7 as stated above. Up to 0.4×10^{15} n/cm^2 the there was no decrease in charge collection distance observed and the normalized charge collection distance was constant. There appears to be a transition between 0.4×10^{15} n/cm^2 and 0.5×10^{15} n/cm^2. A sizeable decrease is observed on these samples above 1.32×10^{15} n/cm^2 where the charge collection distance is decreased between 40 % and 45 %.

Fig. 5.41 shows the charge collection distance from three other CVD diamond samples, N1, N2 and N3, as a function of the neutron fluence. The initial charge collection distance was about 45 μm on N1 and N2 and 36 μm on N3. The charge collection distance was unchanged up to 4×10^{14} n/cm^2. There is a transition between 0.4×10^{15} n/cm^2 and 0.5×10^{15} n/cm^2 as seen earlier with the samples U6 and U7. A decrease of 55 % is observed on N3 at 7×10^{14} n/cm^2. The charge collection distance of N3 decreased further, though less rapidly, after 1.3×10^{15} n/cm^2. The tendency of decrease agrees with the measurements from U6 and U7.

Another series of samples, Y1, Y2, YE, YF, was irradiated with neutrons. Y1 was removed from the analysis due to its uncertain fluence value. The charge collection distance, as shown in Fig. 5.42, was initially between 45 μm and 50 μm. The charge collection distance was unchanged up to 3×10^{14} n/cm^2 on these samples. The charge collection distance for these samples shows a transition between 0.4×10^{15} n/cm^2 and 0.6×10^{15} n/cm^2.

Table 5.4 summarizes the charge collection distances of the samples as reported above. It contains the value from Y1 and from two more samples, CD15-P3 and CD15-P4. The last two samples are not included in the figures yet, since their first measurement has a large

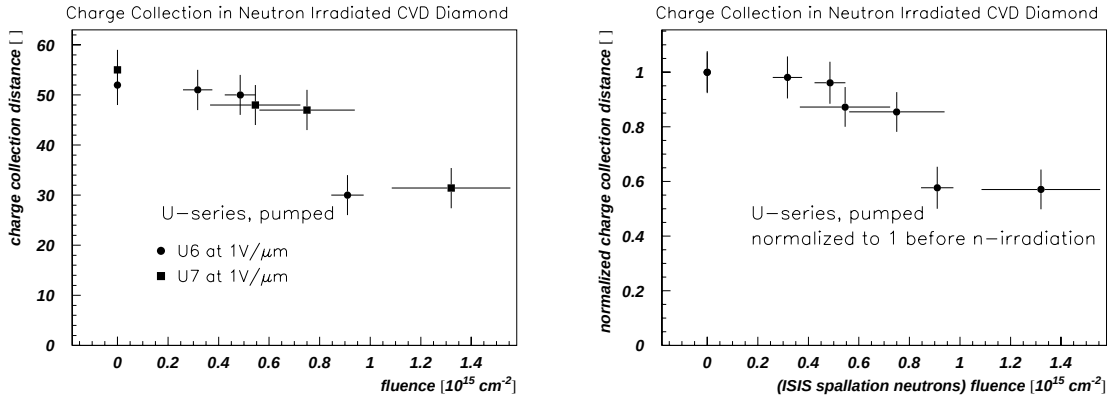

Figure 5.40: Charge collection distance in pumped CVD diamond samples U6 and U7 as a function of the neutron fluence. Left: the absolute charge collection distance. Right: the charge collection distance normalized to the initial electron pumped value of the sample before irradiation.

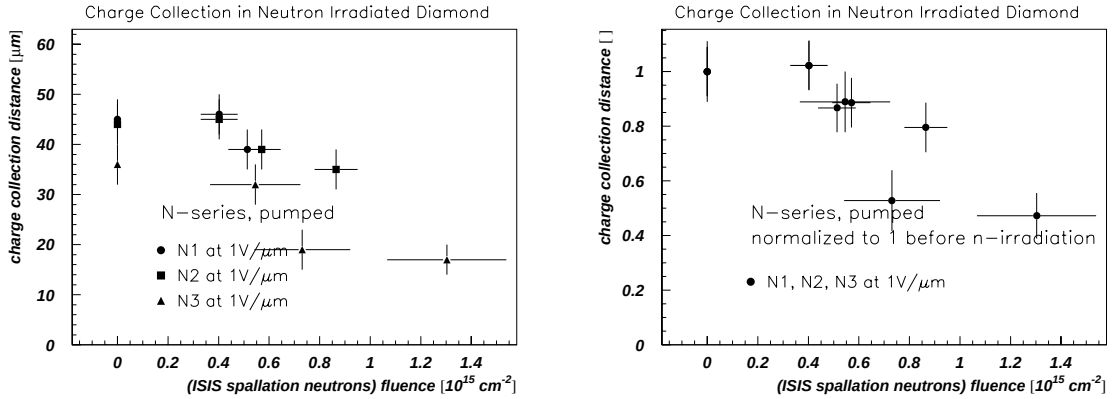

Figure 5.41: Charge collection distance in pumped CVD diamond samples N1, N2, N3 as a function of the neutron fluence. Left: the absolute charge collection distance. Right: the charge collection distance normalized to the initial electron pumped value of the sample before irradiation.

error. However, their charge collection distance as a function of fluence agrees with the data presented so far.

sample name	pumped *ccd* [μm] after each irradiation			
	0.	1.	2.	3.
Y1	≈42	40	35	29
U6	52	51	50	30
U7	55	42	47	31
N1	45	46	39	-
N2	44	45	39	35
N3	36	32	19	17
CD15-P3	87	96	72	
CD15-P4	86	55	45	

Table 5.4: Charge collection distance (*ccd*) in the pumped state measured on diamond samples after neutron irradiations. Each irradiation period is labeled by a number. The number 0 is before irradiation.

Fig. 5.43 overlays the normalized charge collection distances as a function of the fluence

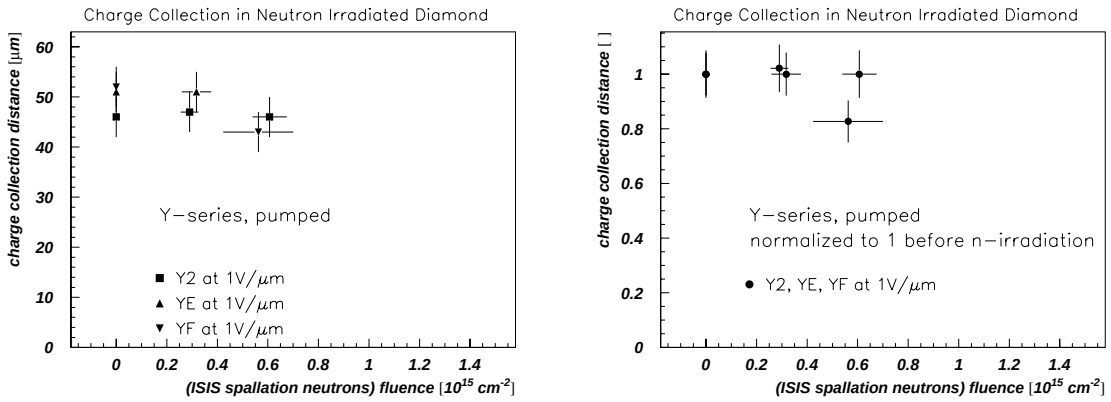

Figure 5.42: Charge collection distance in pumped CVD diamond samples Y2, YE and YF as a function of the neutron fluence. Left: the absolute charge collection distance. Right: the charge collection distance normalized to the initial electron pumped value of the sample before irradiation.

with the data reported above. The combination of data suggests no change in charge collection distance up to 0.4×10^{15} n/cm^2. The charge collection distance has a transition between 0.4×10^{15} n/cm^2 and 0.5×10^{15} n/cm^2. Assuming a linear decrease one finds the slope of about 60% per 1×10^{15} n/cm^2. The charge collection distance may follow the $1/F$-law as suggested by Eq. 5.8. More data is required in order to experimentally confirm such a decrease.

5.3.14 Summary and Discussion

CVD diamond samples were irradiated with neutrons at the ISIS irradiation facility. The induced current in diamond was observed to decrease exponentially during irradiation with a typical time constant of several hundred hours. The current eventually saturated. The induced current correlated with the proton beam flux. The current measured in the diamond samples is a real induced current, in contrast to the current in silicon where the measured current is mainly a leakage current. The current response in diamond to neutrons was prompt. When neutrons vanish, the current relaxed with a time constant determined by the impedance of the measurement setup. After saturation of the initial exponential decrease of the current it was found that the induced current can be used as a measure for the flux and the fluence. Based on the scaling of the induced current with the contact and the fact that the induced current density does not depend on the neutron flux one can conclude that the current is caused by photons from the γ-background. Diamond is sensitive to γ-radiation as could be qualitatively confirmed using an americium γ-source. The leakage current (dark current) was typically in the picoampere range. It decreased after irradiation as well.

The charge collection distance of the samples reported here were about 50 μm before irradiation. Irradiation with only thermal neutrons up to 2.7×10^{15} n/cm^2 did not change the charge collection properties. Many samples were exposed to fast neutrons with a kinetic energy peaking at 1 MeV. The charge collection distance on these samples was constant up to 0.4×10^{15} n/cm^2. Between 0.4×10^{15} n/cm^2 and 0.5×10^{15} n/cm^2 the transition of charge collection distance occured. At the highest fluence of 1.3×10^{15} n/cm^2 the charge collection distance decreased by 50 % compared to before irradiation. The most probable value of the signal charge distribution typically decreased by 30 % at 1.3×10^{15} n/cm^2. The most probable value decreased less than the mean value.

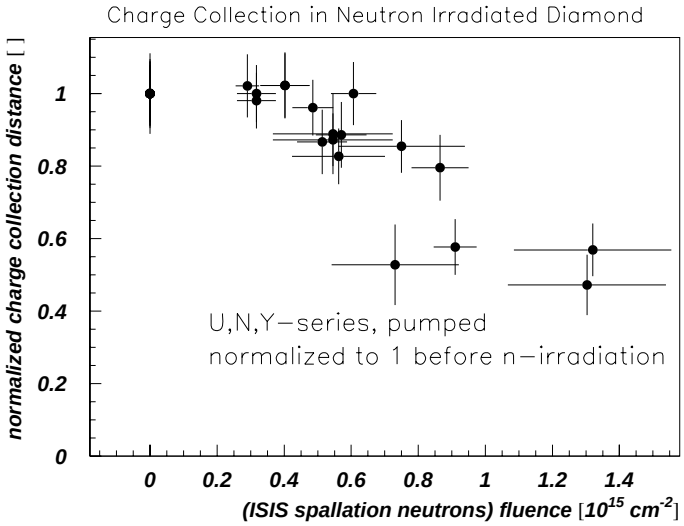

Figure 5.43: Charge collection distance in CVD diamonds of U,N and Y-series as a function of the neutron fluence. The charge collection distance is normalized to its pumped value before neutron irradiation.

It should be noted that these results are the first measurements obtained on CVD diamond sensors which have been irradiated above the expected neutron fluence in LHC experiments. The charge signal from silicon is usually sensitive to temperature due to temperature dependent annealing of defects. No annealing studies have been made on diamond so far. The samples were continuously kept at room temperature under 'drawer-conditions'. Defect studies using temperature stimulated current or luminescence methods could be of interest in order to quantify trap levels and their concentration as a function of fluence. These methods rely on heating the sample which could be of interest: silicon anneals at room temperature, annealing of defects in diamond may be possible at higher temperatures. However, anti-annealing at higher temperature may also occur. The carbide interface to diamond may degrade. The study with new electrical contacts after irradiation is of interest. Irradiated silicon sensors normally require higher depletion voltages after irradiation. The studies on diamond were done at the same bias voltage before and after irradiation and no attempt has been made yet to measure them at higher voltages. According to Eq. 5.8 the charge collection distance is proportional to the electric field. However, the electric field strength 1 V/μm is typically the field where the charge carrier velocity saturates. Therefore the slope of the charge collection distance versus voltage is small at 1 V/μm and no significant changes can be expected. Finally it may be emphazised that the fluences given here are the 'pure' ISIS fluences as obtained from the foil dosimetry.

5.4 Irradiation with Pions

The predominant source of radiation at LHC will be pions. They will contribute 78 % to the total charged hadron flux from the interaction region [Sec. 1.3.2]. The transverse momentum distribution of charged particles from proton-proton interactions peaks between 200 MeV/c and 300 MeV/c. Such pions cause ≈ 1.5 times more damage in silicon detectors than 1 MeV neutrons [132]. CVD diamond samples were irradiated with 300 MeV/c pions (π^+) at the Paul Scherrer Institute in Villigen. The first diamond samples were irradiated by reference [133]. The samples reported in this work were irradiated by the Vienna group [134]. The samples have been characterized before and after irradiation by reference [134] and reference [85]. The section here reports only on the results of the characterization at CERN.

5.4.1 Interaction of 300 MeV/c Pions with Matter

The pions under consideration here are positively charged (π^+). Like all charged particles they deposit energy according to their Coulomb interaction with matter [Eq. 3.68]. Pions with kinetic energies below 300 MeV/c are not minimum ionizing. The η-ratio of momentum to rest mass is below 2 which means that the energy deposited due to the electromagnetic interaction is above minimum ionizing (see Fig. 3.15). Pions may also interact strongly with nuclei. At ≈ 300 MeV/c, they can interact in resonance with nuclei forming the intermediate Δ-Baryon state. The Δ-Baryons, $\Delta(1232)P_{33}$, have a rest mass of about 1231 MeV/c and a width of about 100 MeV/c, depending on their electric charge [9]. The Δ-resonance decays to π and the nucleus where the nucleus may have left its lattice site, to conserve momentum in the interaction. The vacancy and the knock-on atom are point defects in the lattice and may result in degradation of the electrical properties of the detector. The cross section at the peak of the $\Delta(1231)$-resonance is ≈ 200 mb. At the typical flux of 2.5×10^9 $\pi^+/\mathrm{cm}^2/\mathrm{s}$, one obtains for a 500 μm thick diamond an average interaction rate of 5×10^8 $\pi^+/\mathrm{cm}^2/\mathrm{s}$. Pions with higher momenta have lower cross sections. However, their non-ionizing energy loss (NIEL), may be even larger depending on the material [135].

5.4.2 Irradiation Setup

Fig. 5.44 shows a drawing of the pion irradiation setup [133, 134]. The pion beam enters from the left. It passes a polyethylene shield in order to reduce the proton contamination of the beam below 1 %. The beam momentum was chosen to be 300 MeV/c with a 10 % momentum spread. Contaminations to the beam were removed with a dog-leg [2] in the beam line upstream of the samples. The electron and muon contaminations were reported to be less than 5% and 10 % respectively [133]. An ionization chamber was used to measure the pion flux. A typical pion flux was 2.5×10^9 $\pi^+/\mathrm{cm}^2/\mathrm{s}$. The samples were glued onto ceramic boards (Al_2O_3). The boards fit in a slide tray in the beam. The samples were centered in the beam using a photo film that darkened at the beam spot. A light tight box covered the slide tray such that the samples were in complete darkness during irradiation. The pion fluence on each sample was measured using the foil activation method. Each sample was equipped with Al-foils. The dosimetry used for pions was equivalent to the dosimetry used for the proton irradiation described in Sec. 5.2.

[2] A *dog-leg* structure sweeps out (from the beam axis) secondary particle produced in collimators. A dog-leg is a 'magnetic chicane'.

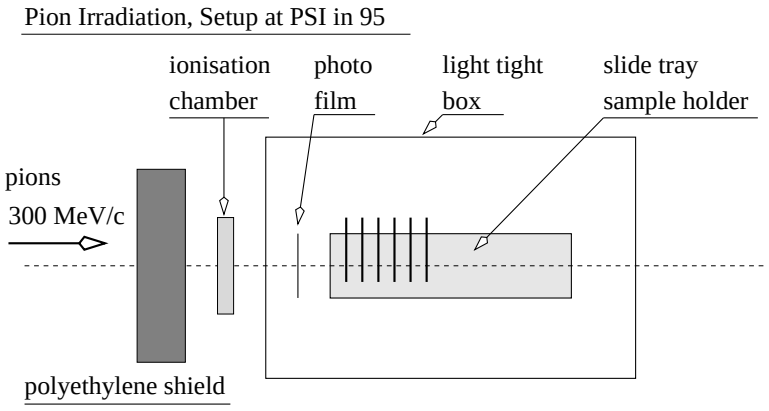

Figure 5.44: Schematic view of the pion irradiation setup from 1995 until 1997. The pion beam passes an ionization chamber. The chamber measures the pion flux. The samples were centered behind each other in the beam.

5.4.3 Samples and Fluence

The samples for irradiation were produced by Norton [33] and De Beers [34]. All samples were equipped with circular electrical contacts on both sides. The samples had a thickness between 300 μm and 800 μm. Table 7.2 in Appendix 7.1 lists all irradiated samples with their fluences received in several irradiation runs. The samples were biased during irradiation with voltages typically at 100 V. The current was monitored during irradiation. The samples were irradiated at room temperature.

5.4.4 ^{90}Sr-Pumping on Pion Irradiated Diamond

Irradiated diamonds require more time under the β-source to fully pump-up than before irradiation. The pump-up time increases for higher fluence. This observation has been made with neutron irradiated samples in the past [85]. The observation can be quantified by recording the 'pump-up' curves of the collected charge during exposure to electrons from the ^{90}Sr β-source. Fig. 5.46 shows two pump-up curves from one diamond sample before and after irradiation. The evolution of the mean collected charge versus time during constant illumination from the β-source has been fitted by Eq. 3.148 from Sec. 3.4.7, here evaluated for the mean induced charge

$$\bar{Q}_{\mathrm{ind}}(t) = \bar{Q}_{\mathrm{p}} \cdot \left(1 - r\, e^{-t/\tau}\right) \qquad \text{with} \qquad r \stackrel{\mathrm{def}}{=} \frac{\bar{Q}_{\mathrm{p}} - \bar{Q}_0}{\bar{Q}_{\mathrm{p}}} \tag{5.19}$$

Two observations can be made: The saturation value, $\bar{Q}_{\mathrm{p}}$, for $t \to \infty$ is higher before irradiation compared to after irradiation. The second observation is the time constant $\tau_{\mathrm{before}} = 54$ min, required for pumping, before irradiation is lower than the time constant $\tau_{\mathrm{after}} = 148$ min after irradiation. Care was taken to use the identical β-source in the same position in the measurement setup before and after irradiation in order to ensure the same electron dose rate.

Fig. 5.46 shows the time constant measured on several pion irradiated diamond samples as a function of the pion fluence. It can be seen that the time constant increases linearly with the pion fluence. A possible explanation is given by Eq. 5.2 which states that the defect concentration increases with fluence. These type of defects correspond to those traps which can be pumped by electrons from ^{90}Sr. A higher number of traps requires more time for pumping and passivating the traps.

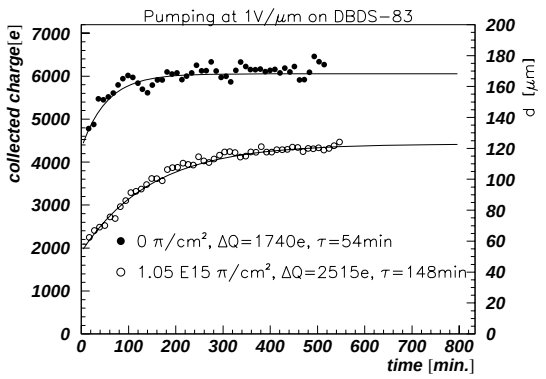

Figure 5.45: Collected charge from CVD diamond CD38 as a function of time during exposure to electrons from ^{90}Sr. The upper graph is before pion irradiation, the lower graph is after pion irradiation. The measured data is fitted with the function from Eq. 5.19.

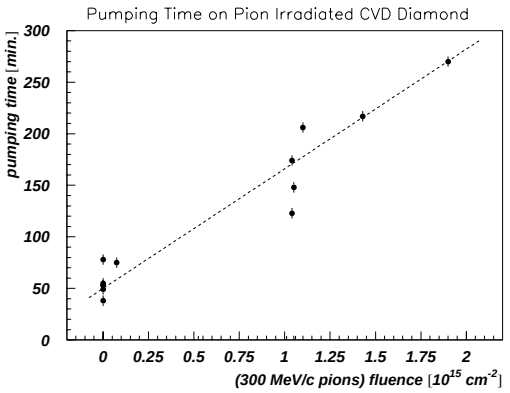

Figure 5.46: Pumping time, τ, (from Eq. 5.19) as a function of the pion fluence from several CVD diamond samples. The measured data is fitted by a linear curve (dashed line).

5.4.5 Charge Collection before and after Pion Irradiation

Fig. 5.47 shows the signal charge distribution measured several times on diamond sample U3 at three different pion fluences. The sample was measured the first time after receiving 0.5×10^{15} π/cm^2 with a mean signal charge of 2000 e at 1 V/μm corresponding to a charge collection distance of 56 μm. Care was taken to fully pump the sample with electrons from ^{90}Sr. Another measurement 7 months later shows an increase of the mean value by 10 %. The shape of the signal charge distribution was unchanged compared to the distribution before irradiation. The sample was then irradiated with 1.17×10^{15} π/cm^2 and the total fluence became 1.73×10^{15} π/cm^2. The signal charge distribution immediately after irradiation is shifted to lower values with a mean of 1670 e, corresponding to 46 μm. Another measurement 9 months later confirms the previous measurement. A third irradiation with only 0.8×10^{14} π/cm^2 on the same sample hardly changed the charge collection distance. Within the measurement error of at most 10 % on this sample, it is difficult to argue any significant decrease.

Fig. 5.48 shows the measured signal charge distribution on U3 and U4. The distribution of U4 has a significant number of pedestal entries due to the smaller contact area and eventual misalignment in the measurement setup. However, the mean signal charge can be obtained from the fit with the given interval. the mean value after irradiation with 0.42×10^{15} π/cm^2 decreased by 15 % compared to before irradiation.

Further irradiations have been made with CVD diamond of initially 100 μm and later up to 200 μm charge collection distance. Fig. 5.49 shows the signal charge distribution from four pion irradiated samples. The distributions before irradiation were typically wide and not Landau distributed. The fit has been made using a convolution of a Landau and a Gauss function. Three samples (CD29-P1, CD29-P2 and CD38) received a pion fluence of about 1×10^{15} π/cm^2. The distributions show that the relatively large charge signals are missing in the Landau tail after irradiation. The distributions are narrower after irradiation. The rising edge of the distribution is unchanged compared to before irradiation. The mean value decreased by 30 % to 35 %. The most probable values decreased by 20 % to 30 %.

Fig. 5.50 shows the charge collection distance of the diamond samples CD29 and CD28

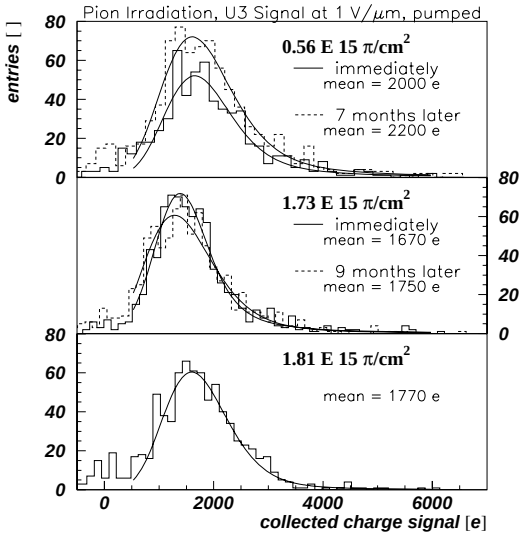

Figure 5.47: Charge signal distribution on a diamond sample with 55 μm charge collection distance before irradiation and after 1.8×10^{15} π/cm^2.

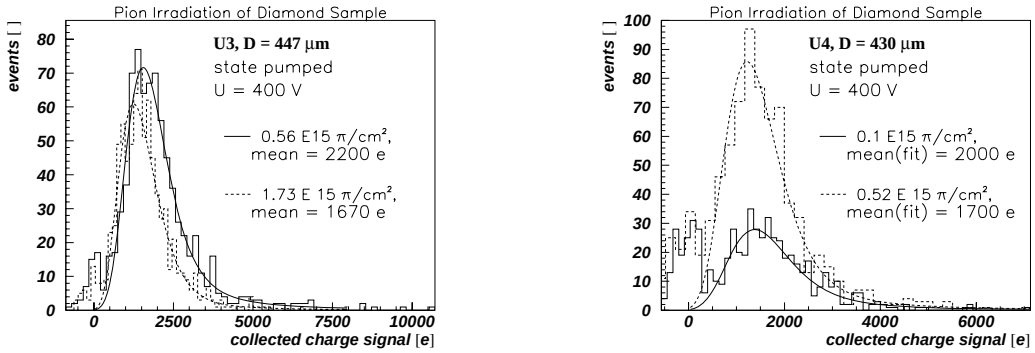

Figure 5.48: Charge signal distribution at a bias voltage of 1 V/μm on irradiated diamond samples at different fluences after pion irradiation.

as a function of the applied electric field before and after irradiation. The curves were taken in the fully pumped state. The mean values from this voltage scan at 1 V/μm are equivalent to the mean values from the signal charge distributions.

Fig. 5.51 shows the charge collection distance as a function of the pion fluence. The absolute charge collection distance decreases with fluence. The charge collection distance normalized to the initial value gives the relative change. For the given set of samples, the charge collection distance is unchanged up to 0.4×10^{15} π/cm^2. The charge collection distance makes a transition between 0.4×10^{15} π/cm^2 and 0.5×10^{15} π/cm^2. Beyond 0.5×10^{15} π/cm^2 the charge collection distance decreases with fluence. At the highest fluence of 1.83×10^{15} π/cm^2 the charge collection distance is decreased by 40 % compared to before irradiation. The relative decrease on samples with initially high charge collection distance is more pronounced than on samples with originally lower charge collection distance.

5.4.6 Summary and Discussion

CVD diamond samples were irradiated with 300 MeV/c pions (π^+). One observation made was the increase in pumping time under illumination with electrons from a β-source af-

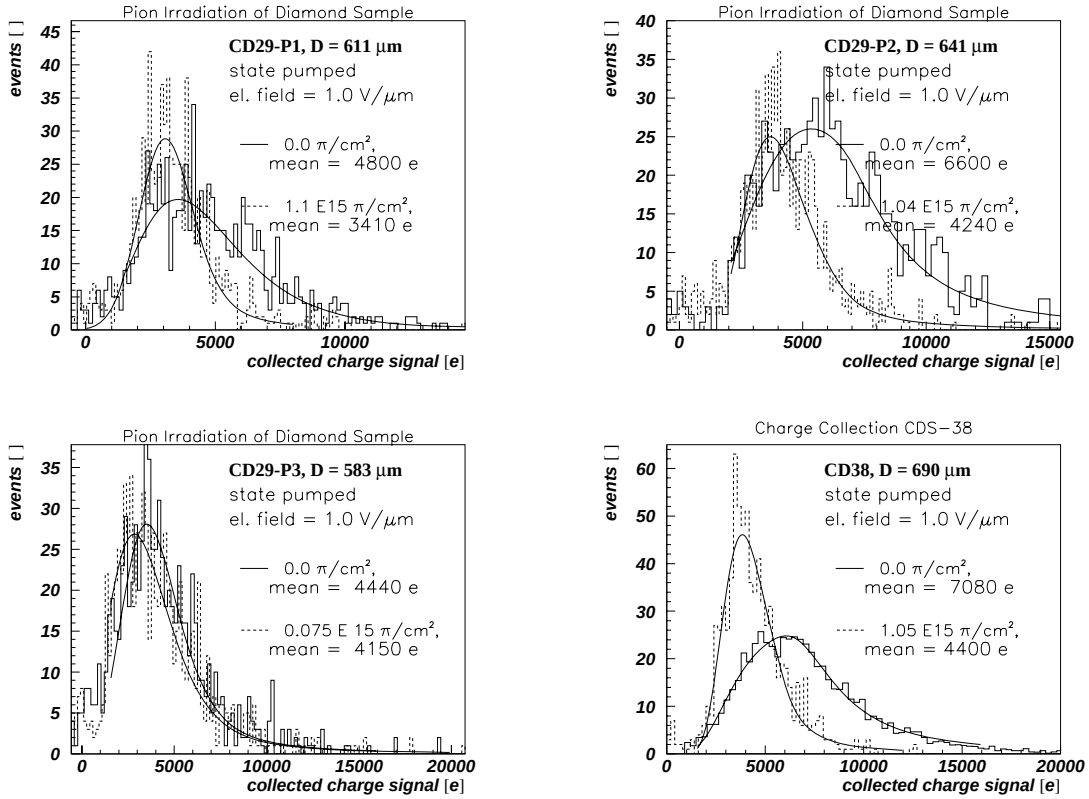

Figure 5.49: Signal charge distribution from pion irradiated diamond samples at an electric field of 1 V/μm. The measured distributions are fitted with a convolution of a Landau and a Gauss distribution.

ter pion irradiation. The time constant obtained from the pumping curves increased linearly with the pion fluences. This time constant is likely related to the concentration of defects. The increase in pumping time is explained by the increasing concentration of defects under irradiation with pions. Some defects can be passivated by exposing the diamond to electrons from the β-source and the charge collection distance increases. Other defects can not be passivated any more after irradiation and the charge collection distance eventually decreases. The charge collection distance was observed to be constant after exposure with pions up to about 0.4×10^{15} π/cm^2. Beyond 0.5×10^{15} π/cm^2 the charge collection distance decreased with fluence. At the highest fluence of 1.83×10^{15} π/cm^2 the charge collection distance was decreased by 40 % compared to the value before irradiation. The signal charge distribution after irradiation was observed to be narrower compared to before irradiation. The narrower width after irradiation may indicate more uniform charge collection laterally across the sample. The remarks made in the summary for neutron irradiated samples also apply here. The measurements require confirmation after eventual annealing and new contact preparation. Defect studies using TSC and TL and their correlation to charge collection distance could be helpful.

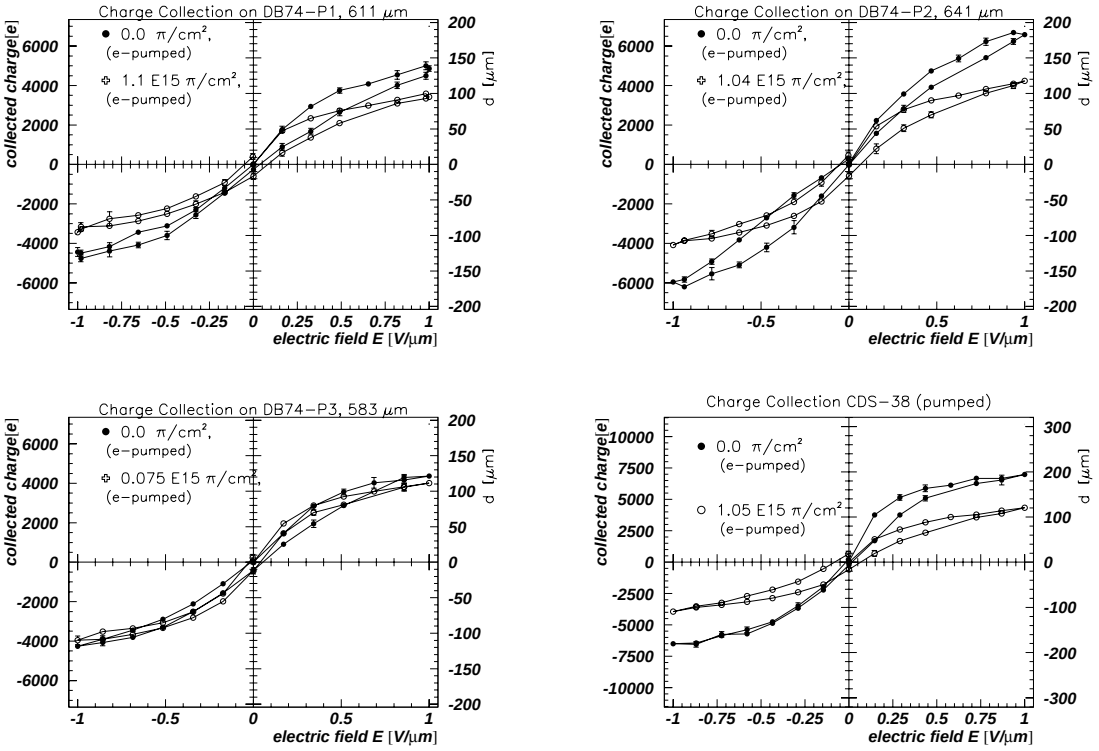

Figure 5.50: Charge collection distance as a function of the applied electric field at different pion fluences. The samples were in the pumped state during these measurements.

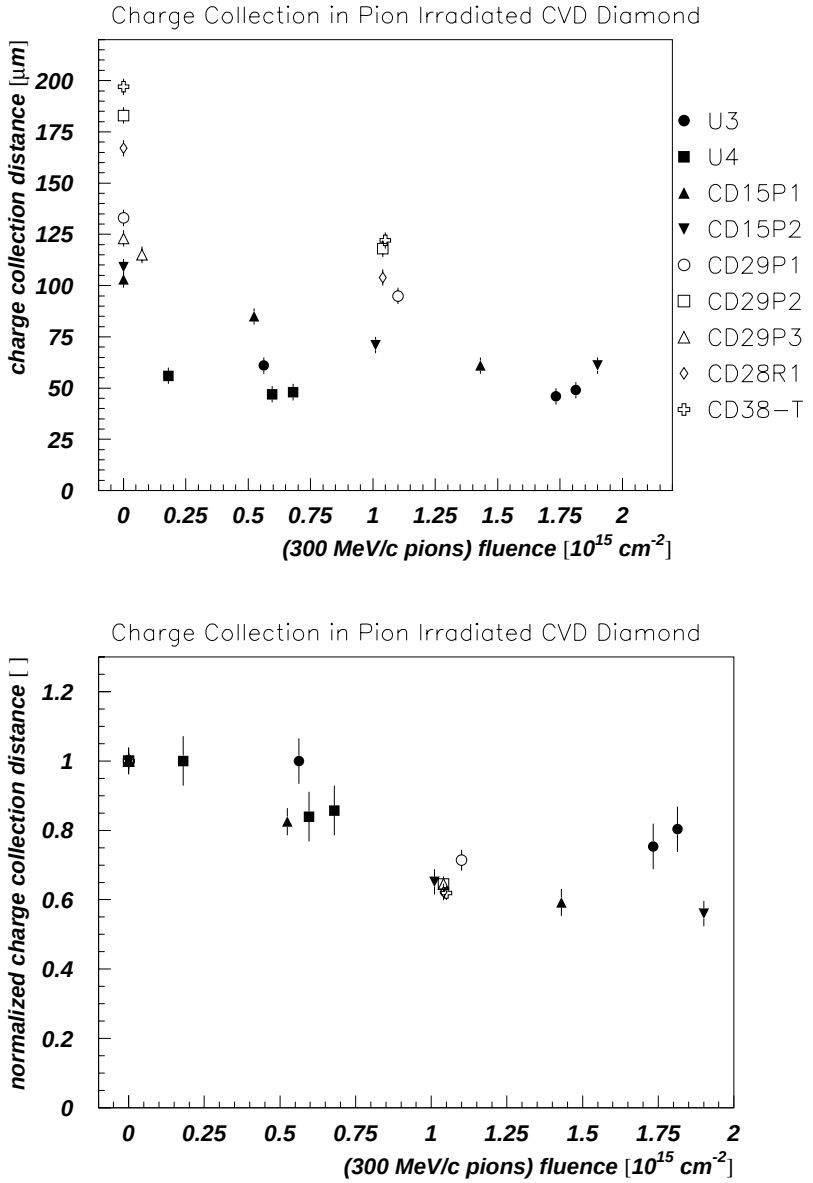

Figure 5.51: Charge collection distance in CVD diamond after irradiation at different pion fluences. On the lower graph the charge collection distance is normalized to its pumped value before irradiation.

Chapter 6

Summary

The goal of this work was to study the properties of CVD diamond for their application in particle tracking. This work included material studies, electrical characterizations and tests of diamond strip sensors in pion beams. The motivation for using CVD diamond is its potential radiation hardness. It was therefore essential to study electrical properties of CVD diamond under particle irradiations. A summary of the work performed and the important results are given here followed by the conclusion.

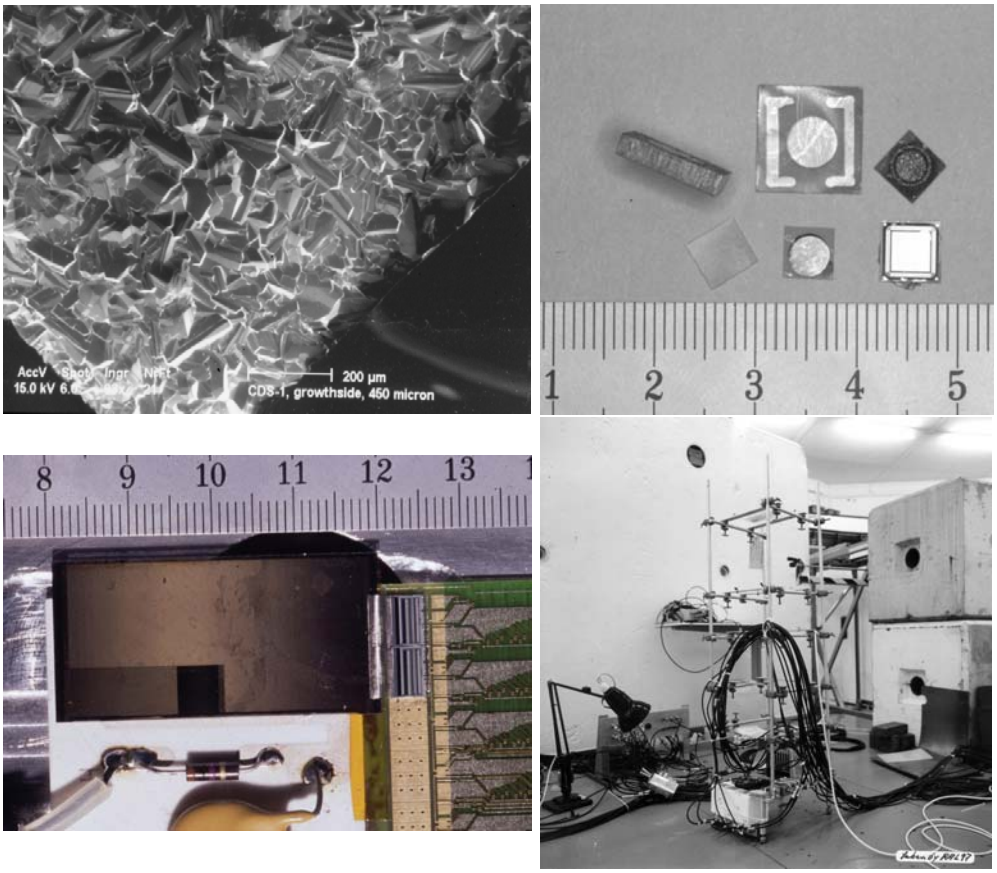

Figure 6.1: From upper left to the lower right: growth side of a CVD diamond, CVD diamond samples and a silicon diode with a variety of contact geometries, CVD diamond strip sensor and at the lower right the setup for the neutron irradiation.

Contents

6.1 Summary of Work Performed

During the course of this work I studied the electrical and material properties of CVD diamond. The material studies, including X-ray diffraction, micro-Raman spectroscopy and scanning electron microscopy, were performed using facilities of collaborators at RD42. The electrical properties including current, capacitance and charge collection distance were measured at CERN. For the charge collection distance measurements I built the setup described in Sec. 3.4.5. I automated the software for routine measurements of diamond samples. I built a second setup, similar to the one described, and installed it at the CVD diamond manufacturer. The charge collection distance measurements served as a quick and reliable method to characterize the electrical properties of CVD diamond samples. This setup was the basis for further work on strip sensors and irradiated samples. An important achievement of this work was the organization and the realization of beam tests at CERN and the analysis of the data taken. After patterning the diamond strip sensors at Ohio State University the sensors were delivered to CERN where I performed characterization, organized the bonding to the readout electronics and assembly in general and did installation and tests in the beam. I wrote new object oriented particle tracking and analysis software during this work. This code has been used for the beam data analysis described in this thesis. Numerous CVD diamond trackers were tested in the beam. I participated in beam tests of newly developed fast analogue electronics for the ATLAS SCT which was tested for the first time on diamond detectors. As a third important part of this work I performed irradiations of diamonds with neutrons and protons. I characterized all samples before and after irradiation at CERN. For the irradiations I automated the online current monitoring. The theoretical side of my work included the development of the tracking algorithm using the non-linear hit finding method in silicon and the development of the track fit and alignment method and its implementation in the code. For the understanding of signal formation in diamond sensors I gave an alternative proof of Ramo's theorem for charge induction due to moving charges. I showed that this theorem applies for the case of position dependent charge collection distance as it is the case in CVD diamond.

6.2 Results

The results of this work may be quantified in four areas: material characterizations, electrical characterizations, particle tracking and irradiations. The summary of results is given below.

6.2.1 Material Characterizations

CVD diamond is polycrystalline in nature. It has different grains sizes on the nucleation and on the growth side. This has been demonstrated by scanning electron microscopy. The grain size on the nucleation side was found to be of the order of a few microns. The grain size increases nearly linearly from the nucleation to the growth side. An average grain size on the growth side is 70 μm for a 500 μm thick diamond. It was found that the nucleation side of samples from one manufacturer exhibits gaps between grains whereas the nucleation side of samples from another manufacturer may have a non-diamond surface layer. As a result samples were almost always lapped on the nucleation side before preparation as a strip sensor. The polycrystalline nature was further investigated using X-ray diffraction. The amount of oriented grains was measured on the nucleation and on the growth side in a layer several tens of microns in depth. It was found that the nucleation side is less oriented then the growth side. The growth side is typically oriented in one crystal plane. The relative abundance

of oriented grains on the nucleation side changes during growth and may be different on the growth side. Four of five samples from one manufacturer had a preferential orientation of (220) on the growth side. The survey is not yet sufficient to correlate the orientations with other properties. The lattice constant of diamond has been measured based on a high intensity X-ray diffraction peak to be $a = (3.56604 \pm 0.0006)$ Å.

The material quality has been defined by the width of the diamond micro-Raman line. This line broadens when there is stress in the diamond lattice. The linewidth of a type IIa natural diamond was measured to be (2.0 ± 0.1)/cm. The linewidths of the CVD diamond samples here was on average 2.4/cm. A tendency of slightly broader lines for the nucleation side was seen. The linewidths seen here are relatively narrow and similar to those CVD diamonds with high material quality from previous growths by other manufacturers as reported in reference [11]. This indicates a high material quality with low amount of defects. The extended Raman spectra demonstrated absence of graphite impurities. However, it should be noted that a micro-Raman spectrum characterizes an area with a diameter smaller than 1 mm and it is possible that systematically focusing in grain boundaries would give on average broader lines. Focusing in grain boundaries has been tried several times but no line broadening was observed.

6.2.2 Electrical Characterizations

The most important result of the electrical characterizations is the improvement of the charge collection distance in CVD diamond. Whereas several years ago the charge collection distance scale from one manufacturer was at 30 μm we measure now routinely 200 μm charge collection distance, where the thickness of the samples is typically 400 μm to 1200 μm. On this scale it is possible to infere the average carrier drift length from the average charge collection distance: the average carrier drift length is equal to the average charge collection distance. It was confirmed that the charge collection distance depends on the position along the direction of growth. The charge collection distance was found to increase linearly from the nucleation side to the growth side. The charge collection distance is nearly zero on the nucleation side and twice the bulk average charge collection distance on the growth side. The charge collection distance is the basic quantity that controls the charge induced at the electrodes. It was shown that the mean induced charge for any distribution of local charge collection distances is proportional to the bulk average charge collection distance. The mean collected charge at the electrodes was typically above 6000 e at 1 V/μm. Samples with higher signal charge exceeding 8000 e (220 μm charge collection distance) were also available. The signal charge distribution from most diamonds was found to be separated from zero by about 1200 e which is typically 1/5 of the most probable value. For comparison in silicon the separation from zero is normally 3/4 of the most probable value.

For silicon of a single quality the FWHM of the signal charge distribution increases with the most probable value. The signal charge distribution in silicon has a ratio of the FWHM to most probable of approximately 0.5. For a sequential number of diamonds from a recent delivery it was found that the FWHM increases with the most probable value as well. For most CVD diamond samples the ratio of the FWHM to the most probable signal charge is about one. The width from silicon sensors is therefore lower than it was observed for the recent diamond samples. A possible explanation for the excess in width of CVD diamonds over that from silicon is the variation of the collected charge laterally across the material.

6.2.3 Tracking

The feasibility of CVD diamond strip sensors for particle tracking has been demonstrated in the beam. When operated with VA2 readout electronics the strip sensors had a mean signal-to-noise ratio between 30-to-1 and 90-to-1 depending on the electrical quality and the biasing electric field. The hit recognition efficiency was between 98 % and 100 % for thresholds below 1000 e. Using the K-strip center of gravity hit position algorithm the spatial resolution was between 14 μm and 16 μm at a strip pitch of 50 μm. Some trackers had an K-strip center of gravity resolution above 20 μm. Using a two strip center of gravity algorithm (which is equivalent to the two strip linear eta algorithm) a slightly better spatial resolution between 12 μm and 13 μm was obtained. 2×4 cm^2 CVD diamond trackers have been tested with most probable signal-to-noise ratio of 25-to-1 on 3.8 cm long strips. The spatial resolution was the same as on 1×1 cm^2 sensors. The noise was typically (100 ± 15) e on ≈ 7 mm long strips, (130 ± 20) e on 1.9 cm long strips and (165 ± 25) e on 3.8 cm long strips. Strip sensors operated with analogue SCT/DMILL readout electronics had higher noise as expected due to the fast signal peaking time of 25 ns. The measured noise was (620 ± 50) e on 7 mm long strips. Using the SCTA128HC a most probable signal-to-noise of 7.2-to-1 and a mean signal-to-noise of 10-to-1 have been measured in the beam. Using the center of gravity algorithm a spatial resolution of 16.5 μm has been obtained. Table 6.1 lists results obtained on a 1×1 cm^2 and a 2×4 cm^2 CVD diamond strip sensor with VA2 readout and a CVD diamond sensor with fast LHC type readout. For the spatial resolution the values obtained using the K-strip center of gravity algorithm are given. However, there are other algorithms that give better resolution as has been demonstrated by using the 2-strip center of gravity method in Sec. 4.2.10.

device	thickness [μm]	strips length	readout chip	τ_p	ENC [e]	S_{mean}/N	c.o.g. spatial resolution (K-strips)
UTS-5	432	0.7 cm	VA2	2 μs	100 ± 10	73	15.0 μm
CDS-55	452	3.8 cm	VA2	2 μs	165 ± 25	39	15.9 μm
UTS-5	432	0.7 cm	SCTA128HC	25 ns	620 ± 50	10	16.5 μm

Table 6.1: Selected results from one CVD diamond strip sensor with VA2 readout, one 2×4 cm^2 sensor with two VA2 readout chips and one sensor with LHC type readout electronics. The peaking time, τ_p, of the readout electronics, the measured equivalence noise charge (ENC), the mean signal to noise ratio and the K-strip center of gravity (c.o.g.) spatial resolution in the beam are given.

The lateral uniformity of the signal charge has been studied in a CVD diamond strip sensor using VA2 readout electronics. Variations of the signal charge have been observed. It was shown that the variation is a combination of statistical fluctuations and a variation of properties of the CVD diamond sensor. The variations have been shown to remain for 'infinite' number of events. The uniformity was defined as a quantity between 0 and 100 %. It was shown that a silicon sensor has 100 % uniformity. On this scale the uniformity of the tested CVD diamond sensor was between 60 % and 100 % depending on the binning chosen.

6.2.4 Irradiations

The need of radiation hard sensors at high luminosity experiments has been verified by an estimation of the particle flux from proton-proton interactions. The results for the fluxes and the annual fluences at a luminosity of 10^{34}/cm^2/s are summarized in Table 6.2. The

calculation was based on the primary amount of particles produced in single proton-proton collisions and the angular distribution of the product particles. This estimation agrees with simulations by ATLAS and CMS for distances between 7.5 cm and 20 cm from the interaction point. It is important to notice that the flux and the primary fluence decrease like $1/r^2$ from the interaction point which is essential for the survival of silicon sensors in the SCT and the SST detectors in ATLAS and CMS. The fluence given at radii between 4 cm and 11 cm are known to be a problem for the operation of silicon sensors. This is the reason for either working out the optimal operation conditions like cooling and increasing the bias voltage or pursuing defect engineering on silicon by optimizing certain impurities or search for new sensor materials which could withstand longer under irradiation.

radius		angle	charged flux	'annual' fluence ($= 10^7$ s)		
				charged	primary neutral	total
r	$r_\perp$	Θ	$\phi^c \pm 28$ %	$\Phi^c \pm 28$ %	$\Phi^n \pm 28$ %	$\Phi^t \pm 28$ %
[cm]	[cm]	[°]	[10^6/cm^2/s]	[10^{15}/cm^2]	[10^{15}/cm^2]	[10^{15}/cm^2]
4.0	4.0	90.0	70.2	0.70	0.47	1.17
11.0	11.0	90.0	0.09	0.09	0.06	0.16

Table 6.2: Results of the 'naive' model [Sec. 1.3.2] for the primary charged hadron flux ϕ^c close to the beam interaction point at nominal luminosity of 10^{34}/cm^2/s. The error is the statistical 1 σ variation of 28 % in the uncertainty of the number of interactions per bunch crossing.

The behaviour of CVD diamond under irradiation is different from the behaviour of silicon sensors. The irradiation of CVD diamonds at room temperature and under bias voltage shows that there is no increase in leakage current in diamond. The current measured is a particle induced current that is present as long as particles illuminate the diamond. The current immediately returns to the dark current value when the irradiation stops. This is very different from silicon where the leakage current increases and one observes beneficial annealing during stops of the irradiation and anti-annealing. The induced current as well as the dark current in diamond decrease during irradiation. The decrease was found in the neutron irradiation and is exponential with fluence. A similar decrease was found in pion irradiations. No decrease of the current was visible in the proton irradiation. In all irradiations diamonds were exposed to fluences where charge collection distance was shown to decrease. The charge collection distance was found to depend on the fluence. Table 6.3 gives the fluence up to where no decrease in charge collection distance was observed and the highest fluence of the irradiation together with the relative decrease of the charge collection distance and the most probable signal charge.

6.3 Conclusion

The CVD diamond samples used here had charge collection distances ranging from 30 μm to more than 200 μm corresponding to mean signal charges ranging from 1080 e to more than 7200 e. It was shown that one can infer the carrier drift length from the charge collection distance for the case of a drift length smaller than the sensor thickness. The carrier drift length is a measure of the electrical quality since it is proportional to the carrier mobility and to the carrier lifetime. The improvement of carrier drift length is therefore an improvement of the electrical quality. For an application as a particle sensor with relatively 'slow' signal

	no change in $\bar{d}$ up to fluence [cm^{-2}]	highest irradiated fluence [cm^{-2}]	decrease of $\bar{d}$ at highest fluence [%]	decrease of *m.p.* at highest fluence [%]
n(1 MeV)	0.4×10^{15}	1.3×10^{15}	50	30
p(24 GeV/c)	1×10^{15}	5×10^{15}	40	20
π^+(300 MeV/c)	0.4×10^{15}	1.9×10^{15}	40	30

Table 6.3: Summary of the behaviour of the CVD diamond samples under irradiation with protons (p), neutron (n) and pions (π^+). The fluence up to where no decrease in charge collection distance, $\bar{d}$, was observed and the highest fluence are given. The relative decrease of the charge collection distance and the relative decrease of the most probable (*m.p.*) signal charge at the highest fluence are given.

peaking time of the order of 2 μs with an equivalent noise charge of about 100 e a mean-signal-to noise ratio of 70-to-1 was obtained which is a very good result and enables particle tracking as demonstrated here. For applications at LHC a faster signal shaping of 25 ns is required due to the high interaction rate. The series noise in the readout of SCT electronics used here was about 620 e which would result in a mean signal-to-noise ratio between 10-to-1 and 12-to-1 for a diamond sensor with 200 μm charge collection distance. A slightly higher signal-to-noise ratio is desirable for a tracking application. This may be achieved by reducing the noise or further increasing the charge collection distance. The progress made so far in increasing the charge collection distance leads to the expectation that further improvement in charge collection distance is possible.

The uniformity of the electrical quality across the area of a CVD diamond disk is a second aspect of electrical quality. The results shown indicate variations of the charge collection distance laterally accross the sample. This does not necessarily imply a difficulty for a sensor with binary readout since any signal charge above threshold is sufficient to find the digital hit postion. For analogue readout the situation is more complex. Lateral uniformity may be important if it disturbes the hit position measurement. The analysis of uniformity performed here is not sufficient to draw a conclusion about the uniformity of CVD diamond in general. The variations in the mean charge collected shown here were found in a CVD diamond sample of high electrical quality based on charge collection distance only. The study of uniformity is therefore an additional mean of characterizing the electrical quality of CVD diamond. It would be advantageous to find a way to access the electrical quality parameter 'uniformity' with a method easier and faster to use than shown here. One possibility could be the characterization by the FWHM of the signal charge distribution.

Based on the results shown in Table 6.3 one can conclude that CVD diamond samples of the quality as they were available here are radiation hard without decrease in charge collection distance under irradiation with protons up to 1×10^{15} p/cm^2, with neutrons up to 0.4×10^{15} n/cm^2 and with pions up to 0.4×10^{15} π/cm^2. Taking into account that 78 % of radiation from primary interactions at LHC are pions one finds from Table 6.2 an annual pion fluence of 0.07×10^{15} π/cm^2 at 11 cm and 0.5×10^{15} π/cm^2 at 4 cm at the luminosity of 10^{34}/cm^2/s. This would allow one to operate a diamond sensor between one year and six years depending on the position between 4 cm and 11 cm at a luminosity of 10^{34}/cm^2/s. Further studies of radiation hardness of CVD diamond material with charge collection distance higher than 200 μm are necessary.

Chapter 7

Appendix

7.1 Irradiation Fluences

sample name	thickness [μm]	center electrode size [mm^2]	final fluence [10^{12} p/cm^2]
CD12-P1	716	7.1	5064 ± 111
CD12-P2	726	7.1	4146 ± 99
CD12-P3	709	7.1	3222 ± 84
CD17	492	2.9	3000 ± 30
Si-Diode	350	16.0	905 ± 30

Table 7.1: Proton irradiation: final proton fluences on samples.

sample name	thickness [μm]	electrode size [mm^2]	run	fluence [10^{14} π^+/cm^2]
NDF-2	710	19.6	9/95	1.6
			9/96	8.5
NDF-4	557	16	9/95	0.96
			9/96	6.9
NDF-5	570		9/95	0.79
P5	275		6/94	0.13
			9/95	2.8
U3	447	19.6	6/94	0.43
			9/95	5.2
			9/96	11.7
			11/97	0.8
U4	430	7.1	6/94	0.8
			9/95	1.0
			9/96	4.16
			11/97	0.84
CD15-P1	737	7.1	9/96	5.24
			11/97	9.06
CD15-P2	760	7.1	9/96	10.1
			11/97	8.9
CD28-R1	603	3.0	11/97	10.4
CD28-R2	611	3.0	11/97	10.6
CD29-P1	611	7.1	11/97	11.0
CD29-P2	641	7.1	11/97	10.4
CD29-P3	583	7.1	11/97	0.75
CD38-Tracker	690	-	11/97	10.5

Table 7.2: Pion irradiation: irradiated CVD diamond samples, their thickness, size of the electrode, irradiation period and pion fluences [136].

sample name	thickness [μm]	electrode size [mm^2]	period	measured fluence [n/cm^2] at energy	
				< 10 keV	> 10 keV
Y1 [a]	407	12.6	1/95	$(8.94 \pm 0.15) \times 10^{15}$	$(1.29 \pm 0.14) \times 10^{15}$
			10/95	$(1.57 \pm 0.03) \times 10^{15}$	$(5.62 \pm 1.39) \times 10^{14}$
			11/96	$(1.80 \pm 0.03) \times 10^{15}$	$(2.05 \pm 0.62) \times 10^{14}$
Y2	418	15.9	1/95	$(4.33 \pm 0.09) \times 10^{15}$	$(2.90 \pm 0.35) \times 10^{14}$
			10/95	$(1.48 \pm 0.03) \times 10^{15}$	$(3.17 \pm 0.58) \times 10^{14}$
Y4	414	19.6	1/95	$(2.25 \pm 0.4) \times 10^{15}$	$(6.00 \pm 0.95) \times 10^{13}$
			10/95	4.8×10^{14}	≈ 0
YB	419	15.9	10/95	4.8×10^{14}	≈ 0
YE	419	19.6	10/95	$(1.48 \pm 0.03) \times 10^{15}$	$(3.17 \pm 0.58) \times 10^{14}$
YF	414	19.6	10/95	$(1.57 \pm 0.03) \times 10^{15}$	$(5.62 \pm 1.39) \times 10^{14}$
U6	436	12.6	10/95	$(1.48 \pm 0.03) \times 10^{15}$	$(3.17 \pm 0.58) \times 10^{14}$
			11/96	$(2.15 \pm 0.04) \times 10^{15}$	$(1.68 \pm 0.20) \times 10^{14}$
			11/97	$(2.1 \pm 0.04) \times 10^{15}$	$(4.25 \pm 0.20) \times 10^{14}$
U7	433	12.6	12/95	$(2.01 \pm 0.04) \times 10^{15}$	$(5.45 \pm 1.79) \times 10^{14}$
			11/96	$(1.80 \pm 0.03) \times 10^{15}$	$(2.05 \pm 0.62) \times 10^{14}$
			11/97	$(2.26 \pm 0.05) \times 10^{15}$	$(5.72 \pm 1.4) \times 10^{14}$
N1	329	19.6	12/95	$(1.98 \pm 0.04) \times 10^{15}$	$(4.02 \pm 0.73) \times 10^{14}$
			11/96	$(1.54 \pm 0.03) \times 10^{15}$	$(1.11 \pm 0.19) \times 10^{14}$
			11/97	$\approx 5 \times 10^{14}$	≈ 0
N2	333	19.6	12/95	$(1.98 \pm 0.04) \times 10^{15}$	$(4.02 \pm 0.73) \times 10^{14}$
			11/96	$(2.15 \pm 0.04) \times 10^{15}$	$(1.68 \pm 0.20) \times 10^{14}$
			11/97(*)	$(1.8 \pm 0.04) \times 10^{15}$	$(2.95 \pm 0.39) \times 10^{14}$
N3	354	12.6	12/95	$(2.01 \pm 0.04) \times 10^{15}$	$(5.45 \pm 1.79) \times 10^{14}$
			11/96	$(2.03 \pm 0.04) \times 10^{15}$	$(1.86 \pm 0.65) \times 10^{14}$
			11/97	$(2.26 \pm 0.05) \times 10^{15}$	$(5.72 \pm 1.4) \times 10^{14}$
CD15-P3	755	7.1	11/96	$(1.95 \pm 0.03) \times 10^{15}$	$(1.30 \pm 0.23) \times 10^{14}$
			11/97	$(1.5 \pm 0.02) \times 10^{15}$	$(2.9 \pm 0.5) \times 10^{14}$
CD15-P4	728	7.1	11/96	$(2.03 \pm 0.04) \times 10^{15}$	$(1.86 \pm 0.65) \times 10^{14}$
			11/97	$(2.55 \pm 0.05) \times 10^{15}$	$(6.25 \pm 1.45) \times 10^{14}$
CD36-P1	640		11/97	$(1.5 \pm 0.02) \times 10^{15}$	$(2.9 \pm 0.5) \times 10^{14}$
CD36-P2	640		11/97	$(2.1 \pm 0.04) \times 10^{15}$	$(4.25 \pm 0.65) \times 10^{14}$
CD36-P3	640		11/97	$(2.55 \pm 0.05) \times 10^{15}$	$(6.25 \pm 1.45) \times 10^{14}$
S-9	350	16.0	10/95	$(1.48 \pm 0.03) \times 10^{15}$	$(3.17 \pm 0.58) \times 10^{14}$
S-10	350	16.0	10/95	$(1.57 \pm 0.03) \times 10^{15}$	$(5.62 \pm 1.39) \times 10^{14}$
S-16	350	16.0	11/96	$(1.54 \pm 0.03) \times 10^{15}$	$(1.11 \pm 0.19) \times 10^{14}$
S-24	350	16.0	11/96	$(1.54 \pm 0.03) \times 10^{15}$	$(1.11 \pm 0.19) \times 10^{14}$
SiStrip	350		11/96	$(1.54 \pm 0.03) \times 10^{15}$	$(1.11 \pm 0.19) \times 10^{14}$
Si9710	350		11/97(*)	$(1.8 \pm 0.04) \times 10^{15}$	$(2.95 \pm 0.39) \times 10^{14}$

Table 7.3: Neutron irradiation: neutron fluences on diamond samples and silicon (labels on silicon start with 'S'). The fluences were measured with Al-foil dosimeters at RAL [137]. The samples were irradiated at a stable temperature between 18 °C and 19 °C. Samples labelled with (*) were irradiated at -8 °C.

[a] The fluence on Y1 in 1/95 was probably measured to high.

7.2 Acknowledgements

I would like to acknowledge

The RD42-Collaboration

W. Adam, C. Bauer, E. Berdermann, P. Bergonzo, F. Bogani, E. Borchi, M. Bruzzi, C. Colledani, J. Conway, W. Dabrowski, P. Delpierre, A. Deneuville, W. Dulinski, B. van Eijk, A. Fallou, F. Foulon, M. Friedl, K.K. Gan, E. Gheeraert, E. Grigoriev, G. Hallewell, R. Hall-Wilton, S. Han, F. Hartjes, J. Hrubec, D. Husson, C. Jany, H. Kagan, D. Kania, J. Kaplon, R. Kass, K.T. Knöpfle, M. Krammer, P.F. Manfredi, R.D. Marshall, M. Mishina, F. Le Normand, L.S. Pan, V.G. Palmieri, H. Pernegger, M. Pernicka, A. Peitz, S. Pirollo, K. Pretzl, V. Re, J.L. Riester, S. Roe, D. Roff, A. Rudge, S. Schnetzer, S. Sciortino, V. Speziali, H. Stelzer, R. Stone, R.J. Tapper, R. Tesarek, G.B. Thomson, M. Trawick, W. Trischuk, R. Turchetta, A.M. Walsh, R. Wedenig, P. Weilhammer, H. Ziock, M. Zoeller.

In particular I like to say many thanks for help and support to my advisors Dr. Peter Weilhammer at CERN, Prof. Bogdan Povh at the MPI-K in Heidelberg and Prof. Harris Kagan at the Ohio State University in Columbus without whose help this work would have been impossible. I recognize the invaluable contributions from William Trischuk, Wojtek Dulinski, John Conway, Michael Zoeller, K.K. Gan, Rene Scholte and Rudolf Wedenig. I very much appreciated to work with Silvio Sciortino, Mara Bruzzi, Silvia Pirollo, Emilio Borchi, Hugo Bigeri and Laura Bonsi in Florence. It was a pleasure to work with Mike Edwards, Derek Hill, Bob Tapper, Richard Hall-Wilton, Bob Stone, Francois Lemeilleur, Maurice Glaser and Anyes Taffard during neutron and proton irradiations. I very much liked to work in our group together with Shaun Roe, Alan Rudge, Bob Bolter and Ogmundur Runolfsson. I also like to acknowledge the good collaboration with Geoffry Scarsbrook and Andrew John Whitehead.

I very much appreciated the presence of my office and lab neighbours Vincent Chabaud, Christian Regenfus, Stephan Spanier, Michael Doser, Kersten Braune, Florian Schopper, Caroline Schopper, Jörg Strobel, Adam Czermak, Norbert Danneberg, Christoph Posch and Petra Riedler. In the beginning it was very helpful for me to work with Klaus Vorwalter, Ivo Eschrich, Igor Konorov, Silvia Masciocchi and Walter Brückner. Finally it is a pleasure for me to remember everyone with whom I was living at the Ferme de Lespeneux.

The alps, growth side

Bibliography

[1] P. Chochula *et al.* "The DELPHI Silicon Tracker at LEP2", (1997). CERN-PPE/97-155.

[2] J.E. Field, editor. *"The Properties of Natural and Synthetic Diamond"*. Academic Press, (1997).

[3] W. Adam *et al.* (RD42-Collaboration). "Development of Diamond Tracking Detectors for High Luminosity Experiments at the LHC". Status Report/RD42, CERN, (June 1998). LHCC 98-20.

[4] W. Adam *et al.* (RD42-Collaboration). "Development of Diamond Tracking Detectors for High Luminosity Experiments at the LHC". Status Report/RD42, CERN, (Jan. 1997). LHCC 97-3.

[5] C. Bauer *et al.* (RD42-Collaboration). "Development of Diamond Tracking Detectors for High Luminosity Experiments at the LHC". LDRB Status Report/RD42, CERN, (Oct. 1995). LHCC 95-43.

[6] M.H. Nazaré *et al.* (RD42-Collaboration). "Development of Diamond Tracking Detectors for High Luminosity Experiments at the LHC". RD42-Proposal, CERN, (May 1994). DRDC 94-21/P56.

[7] W. Dulinski. "Electron Irradiation of CVD Diamond". RD42 Collaboration Meeting Notes, (June 1995).

[8] S. Han *et al.* (RD42 Collaboration). "Proton Irradiation Studies of CVD Diamond Detectors", (1996). RD42 Internal Note.

[9] Particle Data Group. "Review of Particle Properties". *Phys. Rev. D*, **50** (1994) 3.

[10] O. Madelung *et al.*, editor. *"Landolt-Börnstein, Zahlenwerte und Funktionen, Kristall- und Festkörperphysik, Band 22, Halbleiter"*. Springer, (1987).

[11] S. Zhao. *"Characterization of the Electrical Properties of Polycrystalline Diamond Films"*. PhD thesis, Ohio State University, (1994).

[12] L.S. Pan *et al.* "Particle- and Photo-induced Conductivity in Type-IIa Diamonds". *J. Appl. Phys.*, **74** (1993) 2.

[13] C. Canali, E. Gatti, S.F. Kozlov, P.F. Manfredi, C. Manfredotti, F. Nava, and A. Quirini. "Electrical Properties and Performances of Natural Diamond Nuclear Radiation Detectors". *Nucl. Instr. and Meth.*, **160** (1978).

[14] C.H.H. Wort, C.G. Sweeney, M.A. Cooper, G.A. Scarsbrook, and R.S. Sussmann. "Thermal Properties of Bulk Polycrystalline CVD Diamond". *Diamond and Related Materials*, **3** (1994) 1158-1167.

[15] H. Bichsel. "Straggling in Thin Silicon Detectors". *Rev. of Modern Physics*, **60**,3 (1988) 663-699.

[16] R.C. Alig *et al.* "Scattering by Ionization and Phonon Emission in Semiconductors". *Phys. Rev.*, **B22** (1980) 12.

[17] S.F. Kozlov, R. Stuck, M. Hage-Ali, and P. Siffert. "Preparation and Characteristics of Natural Diamond Nuclear Radiation Detectors". *IEEE Trans. Nuc. Sci.*, **22** (1975) 160-173.

[18] D.H. Perkins. *"Hochenergiephysik"*. Addison-Wesley, (1990).

[19] LHC Division. "Design Parameters of the LHC". `http://www.cern.ch` and `http://wwwlhc01.cern.ch/lhc/`, (1998).

[20] T. Mouthuy. "Radiation Dose Expected in LHC Inner Detectors". CERN/RD20/TN/6 or ASCOT/EAGLE INDET-NO (July 1992).

[21] A. Ferrari. "Radiation Calculations for the ATLAS Detector and Experimental Hall". CERN-EST-96-001 (1996) and CERN-TIS-RP-97-05, 48-60, (1997).

[22] CMS-Collaboration. "Technical Proposal". LHCC/94-38/P1, (1994).

[23] I.J. Aitchison and A.J. Hey. *"Gauge Theories in Particle Physics"*. Adam Hilger, (1981).

[24] ATLAS-Collaboration. "Technical Proposal". LHCC/94-43/P2, (1994).

[25] E. Fermi. "Versuch einer Theorie der β-Strahlen". *Z. Physik*, **88** (1934) 161.

[26] S.L. Glashow. "Partial Symmetries of Weak Interactions". *Nucl. Phys.*, **22** (1961) 579.

[27] S. Weinberg. "A Model of Leptons". *Phys. Rev. Lett.*, **19** (1967) 1264.

[28] ATLAS-Collaboration. "Inner Detector Technical Design Report", (1997). CERN/LHCC/97-17.

[29] ATLAS-Collaboration. in "CERN, Report of Activities in the Divisions", (1997). Annual Report 1997 - Vol.II.

[30] G.R. Stevenson. "On the Prediction of Radiation Levels in LHC Experiments". *Nucl. Phys.*, **A340** (1994) 572-579.

[31] CMS-Collaboration. "CMS Tracker TDR 5", (1998). CERN/LHCC 98-6.

[32] DELPHI-Collaboration. "Performance of the DELPHI Detector". *Nucl. Instr. Meth.*, **A378** (1996) 57-100.

[33] Norton. St. Gobain Diamond Film, Goddard Road, Northboro, MA 01532, USA.

[34] De Beers Industrial Diamond Division (UK) Ltd. Charters, Sunninghill, Ascot, Berkshire, SL5 9PX England.

[35] N.W. Ashcroft and N.D. Mermin. *"Solid State Physics"*. Saunders College Publishing, (1976).

[36] L.S. Pan and D.R. Kania, editors. *"Diamond: Electronic Properties and Applications"*. Kluwer, (1995).

[37] M.W. Geis and M.A. Tamor. *"Diamond and Diamondlike Carbon"*. Encyclopedia of Applied Physics. VCH Publishers, Inc., **5** (1993).

[38] A. Lettington and J.W. Steeds, editors. *"Thin Film Diamond"*. Chapman and Hall for The Royal Society, (1994).

[39] K.E. Spear. "Diamond - Ceramic Coating of the Future". *J. Am. Ceram. Soc.*, **72** (2) (1989) 171-191.

[40] O. Madelung *et al.*, editor. *"Landolt-Börnstein, Numerical Data .., Crystal and Solid State Physics, Volume 17, Semiconductors"*. Springer, (1982).

[41] L.S.G. Plano. in *"Diamond: Electronic Properties and Applications"*. editors L.S. Pan, D.R. Kania, Kluwer, (1995).

[42] P.K. Bachmann. "Towards a General Concept of Diamond Chemical Vapour Deposition". *Diamond and Related Materials*, **1** (1991) 1-12.

[43] W.G. Eversole. "Synthesis of Diamond". U.S. Patents 3,030,187 and 3,003,188, (1962).

[44] B.V. Deryagin *et al.* "Filamentary Diamond Crystals". *J. Cryst. Growth*, **2** (1968) 380-384.

[45] J.C. Angus *et al.* "Growth of Diamond Seed Crystals by Vapor Deposition". *J. Appl. Phys.*, **39** (1968) 2915-2922.

[46] B.V. Deryagin *et al.* "Synthesis of Diamond on Non-Diamond Substrates". *Dokl. Akad. Nauk SSSR*, **231** (1976) 333-335.

[47] B.V. Spitsyn *et al.* "Vapour Growth of Diamond on Diamond and Other Surfaces". *J. Cryst. Growth*, **52**, (1981) 219.

[48] D.V. Fedoseev, V.P. Varnin, and B.V. Deryagin. "Synthesis of Diamond in its Thermodynamic Metastability Region". *Russian Chemical Reviews*, **53**:5 (1984) 435.

[49] M. Kamo *et al.* "Diamond Synthesis from Gas Phase Microwave Plasma". *J. Cryst. Growth*, **62** (1983) 642-644.

[50] T. Bacci, M. Santoro, and S. Sciortino. "Deposition of Continous Diamond Films onto Molibdenum Substrates by DC Plasma CVD". In *EuroDiamond 96*. It. Phys. Soc., Conf. Proc., **52** (1996) 119.

[51] H. Niedrig, editor. *"Bergmann-Schäfer, Experimentalphysik, Optik"*. Walter de Gruyter, (1993).

[52] L. Bonzi and S. Sciortino. Thanks for the support during the SEM at the Dep. of Biology, Faculty of Math. Sci. and Physics at the Univ. Florence.

[53] J.A. Savage *et al.* "Properties of Free-standing CVD Diamond Optical Components". *Proc. Preprint, Window and Dome Technologies and Materials V*, **3060** (1997) 144-159.

[54] Joint Committee for Powder Diffraction. Jcpds-icdd, pdf-2 database, (1992).

[55] S. Sciortino and T. Bacci. Thanks for the support during X-ray diffraction measurements using the Phillips X-ray Diffraction Setup, PW1710/00 with PW1820/00, at the Univ. Florence, Dep. of Mechanics and Ind. Technology.

[56] T. Bacci *et al.* "Change in Surface Morphology of Diamond Films Deposited by DC Plasma Glow Discharge". *Mat. Sci. Engineering*, **B48** (1997) 268-278.

[57] J. Verhey *et. al.* "The Surface of Machined Silicon Wafers: a Raman Spectroscopic Study". *Semicond. Sci. Technol.*, **9** (1994) 404-408.

[58] S. Sciortino, F. Bogani, and M. Colocci. Thanks for the support during Raman Spectroscopy at the European Lab. for Non-linear Spectroscopy (LENS), Florence.

[59] P. Alers, H.E. Hintermann, and I. Hayward. "Correlations between Raman Scattering and Thermal Expansion Behavior for CVD and Natural Diamond". *Thin Solid Films*, **259** (1995), 14-17.

[60] K.H. Hellwege *et al.*, editor. *"Landolt-Börnstein, Atom- und Molekularphysik, 4.Teil, Kristalle"*. Springer, (1955).

[61] H. Raith, editor. *"Bergmann-Schäfer, Experimentalphysik, Festkörperphysik"*. Walter de Gruyter, (1992).

[62] A.C. Lewandowski and S.W.S. McKeever. "Generalized Description of Thermally Stimulated Processes without the Quasiequilibrium Approximation". *Phys. Rev.*, **B43** (1991) 10.

[63] L. Reggiani, S. Bosi, C. Canali, F. Nava, and S.F. Kozlov. "Hole-drift Velocity in Natural Diamond". *Phys. Rev.*, **B23** (1981) 6.

[64] M.A. Plano *et al.* "Polycrystalline CVD Diamond Films with High Electrical Mobility". *Science*, **260** (1993).

[65] E. Borchi and M. Bruzzi. "Radiation Damage in Silicon Detectors". *La Rivista del Nuovo Cimiento*, **17** (1994) 11.

[66] SA Keithley Instruments. `http://www.keithley.com`. Kriesbachstrasse 4, 8600 Dübendorf, Switzerland, Tel: ++41-01-821-9444.

[67] LabVIEW. Graphical software tool produced by National Instruments Corporation. `http://www.natinst.com`. Sonnenbergstr. 53, 5408 Ennetbaden, Switzerland, Tel: ++41-56-200-5151.

[68] J.D. Jackson. *"Klassische Elektrodynamik"*. Walter de Gruyter, (1983).

[69] S.P. Ahlen. "Theoretical and Experimental Aspects of the Energy Los of Relativistic Heavily Ionizing Particle". *Rev. Mod. Phys.*, **52** (1980) 1.

[70] U. Fano. "Penetration of Protons, Alpha Particles, and Mesons". *Ann. Rev. Nuc. Sci.*, **13** (1963), 1.

[71] W. Leo. *"Techniques for Nuclear and Particle Physics Experiments"*. Springer Verlag, (1994).

[72] L. Landau. "On the Energy Loss of Fast Particles by Ionisation". *J. Phys.*, VIII, (1944) 4.

[73] P. Weilhammer, (1996). private communication.

[74] U. Lachish. "The Role of Contacts in Semiconductor Gamma Radiation Detectors". *Nucl. Instr. Meth.*, **A403** (1998) 417-424.

[75] H. Schulz. *"Physik mit Bleistift Einführung in die Rechenmethoden der Naturwissenschaften"*. Springer, (1993).

[76] E. Nygård *et al.* "CMOS Low Noise Amplifier for Microstrip Readout". *Nucl. Instr. Meth.*, **A301** (1991) 506-516.

[77] O. Toker *et al.* "VIKING, a CMOS low noise monolithic 128 channel frontend for Si-strip detector readout". *Nucl. Instr. Meth.*, **A340** (1994) 572-579.

[78] Integrated Detector and Electronics (IDE) AS. "The VA Circuits". `http://www.ideas.no`. Pb.315, Veritasveien 9, N-1322 Høvik, Norway, Tel: ++47-6755-1818.

[79] W.M. Sansen and Z.Y. Chang. "Limits of Low Noise Performance of Detector Readout Front Ends in CMOS Technology". *IEEE Trans. Circuits Systems*, **37** (1990) 11.

[80] D. Nuehrmann, editor. *"Das große Werkbuch Elektronik"*. Franzis Verlag, (1989).

[81] LeCroy Corporation. `http://www.lecroy.com`. 2, rue du Pre-de-la-Fontaine, PO Box 3341, CH-1217 Meyrin 1 Geneva, Switzerland, Tel: ++41-22-719-2111.

[82] E. Borchi *et al.* "High Temperature Thermally Stimulated Currents Analysis of CVD Diamond Films". *Solid State Electronics*, **42** (1998) 4.

[83] K. Pajchel and D. Meier. We were using the thermoluminescence reader 3500 TLD at the radio protection group at CERN, (1997).

[84] R. Robertson *et al.* "Two Types of Diamond". *Royal Soc. London*, CCXXXII. (1934) 463-537.

[85] H. Kagan, M. Zoeller, and S. Zhao. Measurements of charge collection distances were also made at Ohio State University, Columbus, (1990-1998).

[86] M.A. Plano *et al.* "Thickness Dependence of the Electrical Characteristics of Chemical Vapor Deposited Diamond Films". *Appl. Phys. Lett.*, **64** (1994).

[87] S. Zhao *et al.* "Electrical Properties in CVD Diamond Films". *Mat. Res. Soc. Symp. Proc.*, **302** (1993) 257.

[88] L. Gatignon (liaison physicist). "Secondary Beamlines at the SPS". `http://nicewww.cern.ch/sl/eagroup/beams.html`, (1997).

[89] C. Colledani *et al.* "A Submicron Precision Silicon Telescope for Beam Test Purposes". *Nucl. Instr. Meth.*, **A372** (1997) 3.

[90] W. Dulinski. Designer of the Sirocco ADC readout for analogue multiplexed signal without zero suppression, (1997). This sirocco is similar to CAEN's model V 550.

[91] D. Meier. "DiamondTracking, Beam Reference Telescope Data Analysis Classes". `http://www.cern.ch/RD42/rd42cern/tracker/DiamondTracking/`, (1998).

[92] R. Brun and F. Rademakers. "ROOT - An Object Oriented Data Analysis Framework". `http://root.cern.ch`, (1996). AIHENP conference in Laussanne.

[93] L. Arnold *et al.* "Experimental Study of the spatial Resolution of Silicon Microstrip Detectors for the Inner Tracking System of the ALICE Detector". ALICE/97-12, Internal Note/ITS, (1997).

[94] H. Pernegger. *"The Silicon Ministrip Detector of the DELPHI Very Forward Tracker"*. PhD thesis, (english), Technical University Vienna, (1996).

[95] U. Kötz *et al.* "Silicon Strip Detectors with Capacitive Charge Division". *Nucl. Instr. Meth.*, **A235** (1983) 481-487.

[96] E. Belau *et al.* "Charge Collection in Silicon Strip Detectors". *Nucl. Instr. Meth.*, **214** (1983) 253-260.

[97] I.N. Bronstein and K.A. Semendjajew. *"Taschenbuch der Mathematik"*. Harri Deutsch, (1989).

[98] V. Chabaud *et al.* "Track Reconstruction for the NA11 SPS Experiment", (1981). internal write-up.

[99] F. Borchelt *et al.* (RD42-Collaboration). "First Measurements with a Diamond Microstrip Detector". *Nucl. Instr. Meth.*, **A354** (1995).

[100] G. Cavalleri *et al.* "Extension of Ramo's Theorem as applied to Induced Charges in Semiconductor Detectors". *Nucl. Instr. Meth.*, **92** (1971) 137-140.

[101] G. Cavalleri *et al.* "On the Induced Charge in Semiconductor Detectors". *Nucl. Instr. Meth.*, **21** (1963) 177-178.

[102] S. Ramo. "Currents Induced by Electron Motion". *Proc. I.R.E.*, (Sept. 1939) 584-585.

[103] W. Shockley. "Currents to Conductors Induced by a Moving Charge". *J. Appl. Phys.*, **9** (Oct. 1938).

[104] S. Han, H. Kagan, M. Trawick, and M. Zoeller. The metallization of CVD diamond samples and CVD diamond microstrip sensors has been prepared at Ohio State University, Columbus, (1996-1998).

[105] G. Lutz. "Correlated Noise in Silicon Strip Detector Readout". *Nucl. Instr. Meth.*, **A309** (1991) 545-551.

[106] R.J. Tesarek *et al.* "Performance of a Diamond-Tungsten Sampling Calorimeter". *Nucl. Instr. Meth.*, **A349** (1994) 96.

[107] E. Berdermann, K. Blasche, P. Moritz, H. Stelzer, and F. Zeytouni. "Diamond Detectors for Heavy Ion Measurements", (1998). Int. Winter Meeting on Nuc. Phys., Bormio.

[108] J.S. Conway *et al.* "RD42 Test Beam Analysis", (Oct, 1997). RD42 meeting minutes, Toronto.

[109] D.R. Beckman, A. Saint, D.N. Jamieson, and S. Prawer. "Spatially Resolved Imaging of Charge Collection Efficiency in CVD Diamond by the use of Ion Beam Induced Current". In *5^{th} Int. Conf. Nuclear Microprobe Technology and Applications*, (1996).

[110] A. Oh *et al.* "The Charge Collection Properties of CVD Diamond", (1998). submitted to Nucl. Instr. Meth. A.

[111] CEA, DSM, DAPNIA, Saclay-CEA, DTA, LETI, Grenoble-CEA, Bruyeres-Thompson, TMS-IN2P3, CPPM Marseille. "A Mixed Analog-Digital Radiation Hard Technology for High Energy Physics Electronics: DMILL (Durci Mixte sur Isolant Logico-Lineaire)". RD-Proposal, CERN, (1992). DRDC 92-31/P42.

[112] RD29-Collaboration. "DMILL, A Mixed Analog-Digital Radiation Hard Technology for High Energy Physics Electronics". Status Report/RD29, CERN, (Oct. 1993). DRDC/93-45/SR.

[113] RD29-Collaboration. "DMILL, A Mixed Analog-Digital Radiation Hard Technology for High Energy Physics Electronics". Status Report/RD29, CERN, (Nov. 1998). DRDC/98-37/SR.

[114] F. Anghinolfi *et al.* "SCTA - A Radiation Hard BiCMOS Analogue Readout ASIC for the ATLAS Semiconductor Tracker". *IEEE Trans. Nucl. Sci.*, **44** (1997) 3.

[115] W. Dabrowski, P. Jarron, and J. Kaplon. "Experimental Results for Bipolar Devices and Transimpedance Preamplifier Designed in DMILL Technology After a Total Dose of 10^{14} n/cm^2 and 12 Mrad", (1995). CERN/LHCC/95-56.

[116] J. Kaplon *et al.* "DMILL Implementation of the Analogue Readout Architecture for Position Sensitive Detectors at the LHC", (Oct.1998). 4^{th} Workshop on Electronics for LHC Epxeriments, INFN Rome.

[117] J. Kaplon and W. Dabrowski. "Design Layout of the SCT/DMILL Readout Chip". private communication, CERN, (August 1998).

[118] S.M. Sze. *"Physics of Semiconductor Devices"*. John Wiley and Sons, (1981).

[119] V. Radeka. "Low-Noise Techniques in Detectors". *Ann. Rev. Nucl. Part. Sci.*, **38** (1988) 217-277.

[120] W. Zhu. in *"Diamond: Electronic Properties and Applications"*. editors L.S. Pan, D.R. Kania, Kluwer, (1995).

[121] R. Wunstorf. *"Systematische Untersuchungen zur Strahlenresistenz von Silizium-Detektoren für die Verwendung in Hochenergyphysik Experimenten"*. PhD thesis, Universität Hamburg, (1992).

[122] G. Lindstroem. Transparencies at the 2^{nd} Int. Conf. Rad. Effects in Sem. Mat., Det. Dev., Florence, (1997). "Radiation Hardness of Silicon Detectors".

[123] A. Holmes-Siedle and L. Adams. *"Handbook of Radiation Effects"*. Oxford Univ. Press, (1993).

[124] D. Meier *et al.* (RD42-Collaboration). "Proton Irradiation of CVD Diamond Detectors for High Luminosity Experiments at the LHC". ., 2^{nd} Int. Conf. Radiation Effects Semiconductor Mat., Detectors and Devices, Florence, Preprint CERN-EP/98-79, (1998).

[125] W. Adam *et al.* (RD42-Collaboration). "Development of CVD Diamond Radiation Detectors". Proc. 5^{th} Symp. Diamond Mat., Electr. Chem. Soc., Paris, Preprint CERN-EP/98-80, (1997).

[126] D. Meier *et al.* (RD42-Collaboration). "Radiation Hardness Studies of CVD Diamond Detectors". 5^{th} Int. Conf. on Advanced Detector Technology, Como, 1996, (unpublished).

[127] D. Husson (RD42-Collaboration). "Neutron Irradiation of CVD Diamond Samples for Tracking Detectors". *Nuc. Inst. Meth.*, **A388** (1997) 421-426.

[128] R.A. Cecil *et al.* "Improved Predictions of Neutron Detection Efficiency for Hydrocarbon Scintillators from 1 MeV to about 300 MeV". *Nucl. Instr. Meth.*, **161** (1979).

[129] M. Edwards and D.R. Perry. "The Radiation Hardness Test Facility". *RAL Report*, RAL-90-065, (1990).

[130] B. Tapper Physics Department University of Bristol, (1997). Thanks for supplying the peltier cooler for the neutron irradiations.

[131] M. Edwards and D. Hill. Thanks for the support and measurements of neutron fluences from irradiations at ISIS/RAL.

[132] P.A. Aarnio *et al.* "Damage Observed in Silicon Diodes after low Energy Pion Irradiation". *Nucl. Instr. Meth.*, **A360** (1995) 521-531.

[133] C. Bauer *et al.* (RD42-Collaboration). "Pion Irradiation Studies of CVD Diamond Detectors". Preprint CERN-PPE/95-173, (1995).

[134] M. Friedl, J. Hrubec, and M. Krammer. RD42 Collaboration Note 12a, in April 1998 Meeting Minutes, (1998). "Pion Irradiation Studies of CVD Diamond Detectors".

[135] S. Lazanu *et al.* "Model Predictions for the NIEL of High Energy Pions in Si and GaAs". *Nuc. Inst. Meth.*, **A394** (1997) 232-234.

[136] J. Hrubec, 1995-1997. Pion fluences, private communication and RD42 minutes.

[137] M. Edwards and D. Hill. Measurements of neutron fluences from irradiations at ISIS/RAL.